Imbibition in a model open fracture

Capillary rise, kinetic roughening, and intermittent avalanche dynamics

Xavier Clotet i Fons

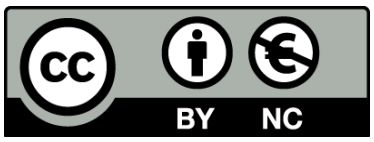

Imbibition in a model open fracture

Capillary rise, kinetic roughening, and intermittent avalanche dynamics

Ph.D. Thesis

Xavier Clotet i Fons

Ph.D. advisors:

Dr. Jordi Ortín Rull

Dr. Stéphane Santucci

Universitat de Barcelona

Programa de Doctorat en Física

Departament d'Estructura i Constituents de la Matèria

École doctorale de Physique et d'Astrophysique

Laboratoire de Physique (UMR CNRS 5672)

Agraïments

Primer de tot vull donar les gràcies als meus directors de tesi, el Jordi Ortín i l'Stéphane Santucci. Les discussions que hem tingut sobre física i sobre la ciència en general m'han encomanat la seva passió per fer recerca.

Al Jordi li vull agrair haver confiat en mi des del principi. Durant la supervisió del treball desenvolupat aquests anys, els seus consells sempre han estat molt valuosos: des dels experiments, on m'ha fet veure la importància de ser curós, a la redacció d'aquesta tesi, que ha revisat amb detall. També vull agrair-li haver-me animat sempre a *posar-hi la banya*, especialment en els moments difícils.

I want to thank Stéphane first for offering to be the coadvisor of my Thesis. It has been a great opportunity to work at Laboratoire de Physique with him. He passes his endless energy and motivation for physics on, making easier to solve any problem. He also makes you look on the bright side always. I also want to thank him his warm welcome in Lyon from the very first day.

També vull agrair als companys de laboratori tantes hores, problemes, discussions i solucions (i taques d'oli) compartides. El Ramon Planet em va ensenyar com funcionava el sistema experimental, em va explicar els trucs de funcionament i em va presentar les eines bàsiques d'anàlisi de dades. Fora del laboratori també hem compartit un munt d'estones agradables, especialment a Lió on m'ha acollit en totes les visites. He tingut la sort de compartir la major part d'aquests anys al laboratori amb la Laura Casanellas. Que necessàries algunes pauses a mitja tarda entre el soroll d'un experiment i l'oli de l'altre! El Jordi Soriano també ha tingut sempre un moment per donar-me un cop de mà al laboratori, o en l'anàlisi de dades, o en el que fos necessari.

Gràcies als companys de despatx, Carles Blanch, David Palau i Guillermo Rodríguez pel bon ambient que hi hem mantingut; especialment al Guillermo, amb qui ens hem suportat (també) durant la redacció de les tesis respectives. També als companys de departament amb qui hem compartit *deliciosos* dinars i cafès: Pau Bitlloch, Claudia Trejo, Xavier Fontané, Marta Manzanares, Oriol Rios, i perdoneu que no us mencioni a tots.

Il a été un plaisir aussi de partager mon séjour à Lyon avec des gens de l'ENS et La Doua. Merci beaucoup Osvanny Ramos, Marie-Julie Dalbe, Sébastien Lherminier,

Ania Modliska et, spécialement, Baptiste Blanc pour me faire sentir chez moi. La Clara Picallo es mereix una menció a part per tants sopars, excursions i consells.

Aquesta tesi no hagués estat possible sense el suport tècnic del Taller mecànic dels CCITUB amb el Manel Quevedo al capdavant, a qui li agraeixo la seva dedicació per trobar sempre la millor solució tècnica. També a l'Albert Comerma per les visites al laboratori, els consells i els muntatges electrònics.

Als meus pares, el Lluís i la Pilar, a ma germana, la Maria, i a tota la família vull agrair-los el suport incondicional durant aquests anys (i per preguntar de tant en tant si l'oli avançava bé) i per tots els anteriors que han fet que arribés fins aquí.

Finalment voldria agraïr als físics pel món que durant i després de la carrera ens hem dispersat des de Dunedin a Santa Cruz, passant per París, Granada, Edimburg, Amsterdam, Copenhaguen o Londres, o quedat al país, de Barcelona a Albesa, de Cambrils a Olot. Els cafès, els dinars, els skypes i les cerveses també han contribuït a fer créixer aquesta tesi i, encara més important, no només la tesi. També hi ha contribuït aquella gent de Manresa, amb menció especial per l'Aura, amb qui fa anys i panys que compartim penes i alegries. També els companys del quinto. Malgrat no poder mencionar tothom amb qui he passat part d'aquests anys i m'han donat un cop de mà (i em disculpo per això), no em voldria oblidar de la gent de muntanya, de l'Ararat al Punta Alta, amb qui hem compartit cims i aventures que sempre ajuden a veure-ho tot plegat més clar.

Aquesta tesi ha estat possible gràcies a la beca de Formació del Professorat Universitari que em va ser concedida pel Ministeri d'Educació, a un Ajut de Personal Investigador predoctoral en Formació que em va ser concedit per la Universitat de Barcelona, als programes Enveloppe attractivité i Accueil Doc que em van ser concedits per la Région Rhône-Alpes i al finançament rebut de la Generalitat de Catalunya (2009SGR00014) i del Ministeri d'Educació (FIS2010-21924-C02-02) al Grup de Recerca en Física no Lineal.

Xavier Clotet i Fons

Manresa, 27 d'abril de 2014

Contents

Part I

Thesis

Outline of the Thesis

The goal of this Thesis is to study the spatio-temporal dynamics of the oil-air interface front between displaced air and invading oil, in imbibition displacements through a model open fracture. Our research combines exhaustive experimental work with accurate data analysis based on methods of nonlinear statistical physics.

Imbibition is a process of fluid transport in a medium in which an invading fluid that preferentially wets the medium displaces the previously resident, immiscible fluid. Imbibition displacements can be classified according to two different driving protocols, that correspond to two different prescriptions at the boundary of the invaded medium. In *spontaneous imbibition* the interface is driven at constant pressure difference between the inlet and the outlet of the medium, and the flow rate is free to change in time. In *forced-flow imbibition* a constant flow rate of fluid is imposed at the inlet, and the pressure difference may change in time.

The Thesis is organized as follows. Chapter 1 reviews basic concepts used throughout our work and main previous results. We introduce the main properties of disordered media and a basic description of fluid displacements in this type of media, Sec. 1.1, and the illustrative case of capillary rise, Sec. 1.2. A description of the interfacial fluctuations of the front is discussed in Sec. 1.3. In Sec. 1.4 we provide a general overview of kinetic roughening. Finally, in Sec. 1.5 we briefly review the current state of knowledge about avalanche dynamics in spatially-extended non-equilibrium systems.

The experimental setup is presented in Ch. 2. We describe in detail its main elements: models of disordered medium and fluids, Secs. 2.2 and 2.3; driving protocols, Sec. 2.4; and image acquisition systems, Sec. 2.5. The preliminary data treatment, Sec. 2.6, and the experimental protocol followed, Sec. 2.7, are also explained.

The main results of the Thesis are presented in chapters 3 to 7.

Chapter 3 is devoted to the analysis of capillary rise (spontaneous imbibition) through our model open fracture. Specifically, we study the evolution of the mean position of the front in time, both analytically and experimentally.

The kinetic roughening of the interface in forced-flow displacements is studied in Ch. 4, with emphasis on the anomalous scaling scenario that corresponds to dominant capillary disorder.

The spatio-temporal dynamics of the front is analysed at the local scale in Ch. 5. We focus our study on the statistical properties of the fluctuations of local front velocities (Sec. 5.1) and of local avalanches (Sec. 5.2).

The study of the spatially-averaged, global velocity of the front is presented in chapters 6 and 7. We investigate the non-Gaussian character of the fluctuations of the global velocity (Sec. 6.1) and the spatio-temporal dynamics of the averaged front in terms of the statistical properties of global avalanches (Sec. 6.2). Finally (Ch. 7) we assess quantitatively the intermittent character of forced-flow displacements.

The general conclusions of the Thesis are drawn in Ch. 8.

Finally, to fulfil the requirements of the convention of cotutelle between the Universitat of Barcelona and the École Normale Supérieure de Lyon, in chapters 9 and 10 we enclose a summary of the Thesis in Catalan, and a short summary in French respectively. In these summaries we briefly review the introductory concepts, describe the experimental setup, and report the most relevant results. Three appendices are also included to provide useful additional information. In appendix A we describe the scaling scenarios predicted by the generic dynamic scaling ansatz for kinetic roughening. Appendix B provides `Matlab` scripts developed and used in this work. The implementation of a new experimental system is described in appendix C, and preliminary results are shown.

Chapter 1

Introduction

1.1 Flow in disordered media

The dynamics of porous and fractured media flows is relevant in many processes of interest that range from the micrometre to the kilometre lengthscales (Sahimi, 2011). These embrace physiological flows in biological membranes and vessels, flow of chemicals during filtration and osmosis, and geological processes (Dentz et al., 2011) like soil irrigation (Heber Green and Ampt, 1911), contaminant spreading (Frippiat and Holeyman, 2008), and oil recovery (Morrow and Mason, 2001; Teige et al., 2006).

Furthermore, flow in disordered media has been proved to be an interesting system to study fundamental physics problems. The heterogeneous structure of porous and fractured media can lead to complex spatiotemporal fluid invasion dynamics, with kinetic roughening (Dubé et al., 1999; Geromichalos et al., 2002; Soriano et al., 2002; Pauné and Casademunt, 2003), avalanches (Rost et al., 2007; Planet, 2009; Planet et al., 2011; Santucci et al., 2011), and non-Gaussian velocity fluctuations (Berkowitz et al., 2006; Rost et al., 2007; Planet, 2009; Planet et al., 2011) of the invading fronts. It thus brings forward fundamental questions in the context of out-of-equilibrium dynamical systems (Alava et al., 2004).

We can also find everyday examples of flow in disordered media: the spreading of a wine stain in the tablecloth, the rising of water through the trousers in a rainy day, or the impregnation of a biscuit when soaked in a cup of milk for instance. Moreover, the latter allowed Fisher (1999) to win the Ig Nobel Prize in 1999 for "calculating the optimal way to dunk a biscuit". He revealed the optimum dunking time for different kinds of biscuits based on Washburn's equation.

FIGURE 1.1: Everyday example of imbibition through a porous medium: soaking of a biscuit in a glass of milk. Fisher (1999) won the Ig Nobel Prize in Physics in 1999 for "calculating the optimal way to dunk a biscuit".

1.1.1 Disordered media

In order to provide a basic idea of how a fluid flows through a disordered medium, we consider two paradigmatic examples: a porous medium and an open fracture.

Porous media. A porous medium is a piece of solid matter characterized in terms of its pores or cavities. It can be defined as a portion of space occupied by heterogeneous or multiphase matter. The solid phase is called the solid matrix and it contains void or pore space inside (Bear, 1975). At least a second phase, which is either gaseous or liquid, is present filling these pores. The area of the void space per unit of bulk volume is relatively high, although the openings comprising the void space are rather narrow. Finally, some of the pores that constitute the medium should be interconnected –specially if we want to consider flow through the medium. Then, a porous medium morphology consists of the geometry that describes the shapes and sizes of the pores and the structure of their internal surface on one side, and the topology that quantifies the way pores and throats are connected together on the other (Sahimi, 2011).

To describe a porous medium one first usually measures its porosity, that is, the ratio of pore volume over the total volume of the medium, i.e. the volume fraction of its voids. Other geometric properties related to the pores like the size of the cavities and their specific surface area –the ratio of the internal surface area of the voids to the bulk volume of the medium–, and the tortuosity –that measures how a fluid particle diffuses in the medium– are used to characterize the medium. The local parameter that accounts for how easily a fluid flows through a porous medium is called permeability, and strongly depends on the porosity of the system. It might be convenient to consider the effective permeability of the medium κ when the mean evolution of the fluid is analysed –see Darcy's law below.

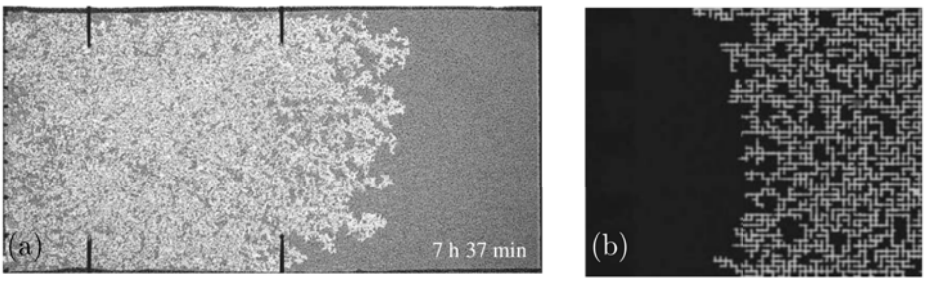

FIGURE 1.2: Fluid invasion (left-right) of two model porous media. (a) HS cell filled with glass beads where air is injected displacing a water-glycerol mixture –drainage process. From Tallakstad et al. (2009). (b) Oil injected through a network of channels to remove the air. Image from Cottin et al. (2010).

Pore space models are often used for estimating the flow and transport properties and other important dynamical features of porous media. Laboratory-scale systems must include heterogeneities at the microscopic –pore level– and macroscopic –bulk– scale. Two of the more representative examples that can be found in the literature are a Hele-Shaw cell –that consists of two parallel plates which are put apart a distance much smaller than their width and length– filled with glass beads (Måløy et al., 1985; Rubio et al., 1989; Erpelding et al., 2013), and a network of interconnected channels (Lenormand, 1990; Cottin et al., 2010). Examples are shown in Fig. 1.2.

Open fractures. Another example of a disordered medium is an open fracture. In this case, the piece of solid is separated by a fissure with a narrow gap. The spacing between the two walls of the crack is not the same along the medium but fluctuates. Here the fluid is able to flow from one end to the other of the solid without the need to avoid any obstacle. The types of fracture that one may observe are usually divided into single fractures, networks of fractures, and fractured porous media (Sahimi, 2011).

Open fractures are characterized by their geometrical and topological properties, and the structure of their internal surface. The geometry refers to the aperture of the cracks as well as their large-scale shape. The topology describes how fractures are connected one to another. Finally, the structure of the surface of fractures may be significantly rough, affecting the flow and transport properties through the medium.

Flow through an open fracture has been experimentally modelled using different systems. A Hele-Shaw cell with dichotomic gap spacing (Soriano et al., 2002; Soriano, 2003; Planet, 2009) or with continuous fluctuations of the spacing (Geromichalos et al., 2002; Boschan et al., 2009, 2011) are two representative examples of such models.

In the present thesis we study experimentally the flow of a silicone oil through a model open fracture. The model consists of two large parallel plates separated by a narrow gap

forming a Hele-Shaw cell. The gap spacing can either be constant or take two possible values randomly distributed in space. The lateral walls of the cell are sealed. Thus, the fluid is only allowed to flow from the inlet to the opposite end of the medium. Full details are given in Ch. 2.

1.1.2 Characterization of the flow

Let us now consider a medium filled with a resident fluid (1), and the slow invasion of a second, immiscible fluid (2) into the medium that will displace that previously resident fluid. In such a case, the Reynolds number is given by $\mathrm{Re} = (\rho_i \mathrm{v} L)/\mu_i \ll 1$, where ρ_i is the density of fluid i, v the mean velocity of the interface between the two fluids, L the characteristic size of the system, and μ_i the dynamic viscosity of fluid i. Since Re compares inertial to viscous effects, inertia is negligible in this situation. If we do not consider any gravity effect, only two physical mechanisms control the dynamics of the interface: viscous pressure and capillarity (Lenormand, 1990). The relative importance of these two kinds of forces is quantified by the capillary number:

$$\mathrm{Ca} = \frac{\mu_i \mathrm{v}}{\gamma_{12}}, \tag{1.1}$$

where γ_{12} is the fluid-fluid surface tension.

Another parameter is the contrast of viscosities:

$$c = \frac{\mu_1 - \mu_2}{\mu_1 + \mu_2}, \tag{1.2}$$

where μ_1 is the viscosity of the resident fluid and μ_2 the viscosity of the invading fluid. Depending on c, the interface between the two fluids can be stable or unstable. When $c < 0$, viscosity acts as a stabilizing mechanism of the interface. On the other hand, when $c > 0$, depending on the velocity of injection, the interface is unstable and viscous fingers appear (Saffman and Taylor, 1958).

We can also distinguish between two kinds of immiscible fluid-fluid flows through a disordered medium depending on their wetting properties.

Wetting refers to how a liquid deposited on a solid spreads out (de Gennes et al., 2004). It is measured by the spreading parameter:

$$S = \gamma_{SO} - (\gamma_{SL} + \gamma), \tag{1.3}$$

that is, the difference of surface energies of a substrate when dry and wet. γ_{SO}, γ_{SL}, and γ are the surface tensions at the solid/air, solid/liquid and liquid/air interfaces. We have total wetting for $S > 0$, when the liquid spreads completely out on the surface. For $S < 0$, the liquid forms a drop on the substrate with an equilibrium contact angle

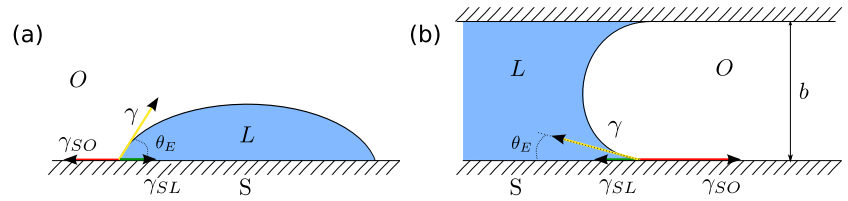

FIGURE 1.3: Two examples of Young's relation between the the solid/air γ_{SO}, solid/liquid γ_{SL} and the liquid/air γ surface tensions, and the equilibrium contact angle θ_E. (a) Drop of a partially wetting fluid L on a substrate S. (b) Fluid L invading a tube as $\theta_E < 90°$, and thus $I > 0$.

θ_E. This contact angle can be obtained by adding up the capillary forces acting on the contact line of the three interfaces, and equating the sum to zero. The projection onto the solid plane gives the Young's relation (Young, 1805):

$$\gamma \cos\theta_E = \gamma_{SO} - \gamma_{SL}. \tag{1.4}$$

The interplay of the different surface tensions is shown in Fig. 1.3.

Substituting equation (1.4) into (1.3) yields:

$$S = \gamma(\cos\theta_E - 1). \tag{1.5}$$

θ_E is then only defined for $S \leq 0$. In addition, in this equation we observe that the larger θ_E, the worse the wetting properties of the fluid.

However, the concept of a contact angle becomes much more problematic in the out-of-equilibrium situation of a moving contact line. In such a case, the angle strongly depends on scale, that is, on the distance from the contact line. A microscopic (or actual) contact angle can be defined, but the only uniquely defined macroscopic angle is the apparent contact angle θ (Bonn et al., 2009). Moreover, the apparent contact angle is known to depend on the velocity of the contact line. Then, when the fluid is in motion, θ is referred to as the advancing/receding dynamic apparent contact angle. Dynamic θ may also show hysteresis because of chemical heterogeneities or roughness of the substrate. From now on we will use simply *contact angle* to refer to apparent contact angle.

When the system is initially filled by a fluid whose wetting properties are better than the properties of the invading one, we observe a **drainage** process. An example could be the pavement of a road after a rainy day. In this case the water present in the asphalt –porous medium– is displaced by air –worse wetting properties than water– as a consequence of gravity. **Imbibition**, to the contrary, occurs when the invading fluid wets better the medium than the resident fluid. While in the first case an external

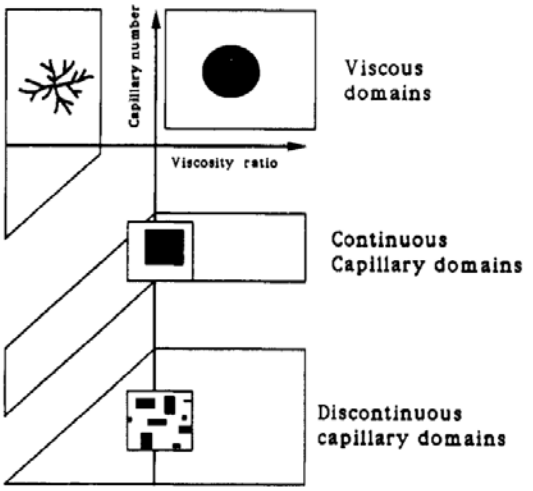

FIGURE 1.4: Theoretical phase diagram of the different scenarios for imbibition processes of a porous medium as a function of Ca and c. The size of the pore is small compared with channel diameters in the porous media considered. Figure reproduced from Lenormand (1990).

pressure is required in order to force the entering fluid through the disordered medium, during imbibition the fluid spontaneously invades the medium due to capillary forces.

Finally, we will differentiate between two possible imbibition processes. Alava et al., in their comprehensive review of the topic (Alava et al., 2004), divide imbibition phenomena in two: spontaneous imbibition, in which no external force is applied to the fluid to make it flow through the medium, and forced-flow otherwise. In our case, although we use the same adjectives, the definition is slightly different. We denominate **forced-flow imbibition** the case in which the flow rate of fluid imposed through the system is constant, $Q = \text{ct}$. **Spontaneous imbibition**, on the other hand, is used in the cases where the imposed pressure difference between the inlet and the outlet of the system is kept constant, $\Delta P = \text{ct}$. It is worth noting that in the former case there is global mass conservation (per unit time).

Lenormand (1990) studied the behaviour of the displacement of immiscible fluids in porous media. He distinguished different types of domains as a function of Ca and c. For imbibition in a porous medium, he set the theoretical phase diagram shown in Fig. 1.4. For small and intermediate Ca, capillary forces dominate the advancing of the front. Discontinuous domains are found for very small capillary numbers –fluid flows via the advancement of precursor films along the roughness of the walls. For intermediate Ca, continuous capillary domains are observed. For large values of Ca, viscous pressure controls the evolution of the fluid. In this regime more compact fronts are produced when $c < 0$. For $c > 0$, viscous fingering appears.

Darcy's law. The proportionality between the mean velocity of fluid through a porous medium and the pressure gradient is given by Darcy's law when considering a stationary, low Reynolds number flow.

The local form of Darcy's law is:

$$\vec{v} = -K\vec{\nabla}P = -\frac{\kappa}{\mu}\vec{\nabla}P, \tag{1.6}$$

where $\vec{v}$ is the velocity field of the fluid, P the pressure field, κ the local permeability of the medium, and μ the dynamic viscosity of the fluid.

We can derive it for the simple case of an open fracture with constant gap spacing from the stationary Stokes' equation[1]:

$$\nabla^2\vec{v} = \frac{1}{\mu}\vec{\nabla}P. \tag{1.7}$$

Then, we consider a Hele-Shaw cell with gap thickness b, much smaller than the lateral dimensions L. We assume that the flow is only in the direction of the pressure gradient, y, and it only depends on the perpendicular direction of advancement, z. The no-slip boundary condition at the walls is also fulfilled. From Stokes' equation we then obtain:

$$v_y = v_y(z) = \frac{1}{2\mu}\partial_y P z^2 - \frac{1}{8\mu}\partial_y P b^2. \tag{1.8}$$

If we now average the velocity profile over the height of the cell z, we get Darcy's law in one dimension:

$$\langle v_y \rangle = -K\partial_y P, \quad \text{where} \quad K \equiv \frac{b^2}{12\mu}. \tag{1.9}$$

Then, the local permeability for a Hele-Shaw cell of constant gap thickness is $\kappa = b^2/12$. This result can be generalized to three dimensions giving rise to

$$\vec{v} = \frac{\kappa}{\mu}(\vec{\nabla}P - \rho\vec{g}), \tag{1.10}$$

where gravity has been taken into account.

Darcy's law also applies at averaged (global) scales when considering a porous medium sufficiently homogeneous (Guyon et al., 2001). Then we can write:

$$\vec{v} = \frac{Q\hat{v}}{A} = \frac{\kappa}{\mu}(\vec{\nabla}P - \rho\vec{g}). \tag{1.11}$$

Now, $\vec{v}$ is the apparent average velocity[2] calculated on the basis of the total flow rate Q per unit area of sample A. $\hat{v}$ is the unit vector perpendicular to the cross-section A. In this case, the proportionality between $\vec{v}$ and the pressure gradient is the ratio of the effective permeability of the medium κ to the dynamic viscosity of the fluid μ.

[1] For a theoretical derivation of Darcy's law, see chapter 9 of Sahimi (2011).

[2] This $\vec{v}$ is a *macroscopic* velocity and differs from the actual local velocity of the fluid at each point of the sample. Specifically, in small pores or apertures the local velocity can be much higher.

To measure this effective permeability of a medium κ we can therefore take advantage of Darcy's law. We may perform steady-state flow rate experiments by imposing different pressure gradients and measuring the corresponding Q. The linear relation between the controlling parameter $\vec{\nabla}P$ and the measured Q gives the ratio κ/μ. If there were deviations from this linear relation, it would indicate that the flow is not in the regime of validity of Darcy's law (Sahimi, 2011). The measurement of κ in our experimental setup is described in Ch. 2.

1.2 Capillary rise

One of the simplest and illustrative realizations of imbibition is *capillary rise*. It consists of putting a narrow tube –a capillary– in contact with a reservoir of fluid. By the action of capillary forces the fluid will rise in the tube.

Back in the XV century, Leonardo da Vinci already described the process in his notes. He also associated capillary rise to the springs of water in natural fountains – although it was shown afterwards that it was unrelated to this phenomenon. Borelli, in the 2nd half of the XVII century, showed that the equilibrium height of the liquid was inversely proportional to the radius of the tube. In 1713, Francis Hauksbee was the first to systematically study the phenomenon, performing a series of careful experiments. This study allowed him to obtain four conclusions which were included in the Newton's treatise "Opticks" –although the name of the experimenter was not cited. First, the rise of the liquid occurs in air just as well as in vacuum. Second, it is not necessary a cylindrical geometry to observe the effect. Third, the effect is not specific for glass and water but also occurs with other solids and other liquids. Finally, the maximum height reached by the fluid inside a cylinder does not depend on the thickness of the tube but only on the inner radius (de Gennes et al., 2004). James Jurin got his name associated to capillary rise. He was a physician and natural philosopher who independently confirmed experimentally that the height achieved by the fluid is in inverse proportion to the radius of the tube (Jurin, 1717). Jurin hypothesized that the cause of the capillary rise was partly by the pressure of the stagnant liquid and partly by the *attraction of the periphery* immediately above it.

Where did that *attraction of the periphery* come from was not uncovered until a century later. In 1805, Thomas Young, in his "An Essay on the Cohesion of Fluids", described the origin of such a force as the consequence of the difference in surface energies between the dry (γ_{SO}) and the wet (γ_{SL}) interior of the tube. Pierre-Simon Laplace, in an appendix of his "Traité de Mécanique Céleste" (Laplace, 1805), established the mathematical relation among the different variables. The fluid would penetrate the tube whenever the difference $I = \gamma_{SO} - \gamma_{SL} > 0$. I is known as the imbibition or impregnation

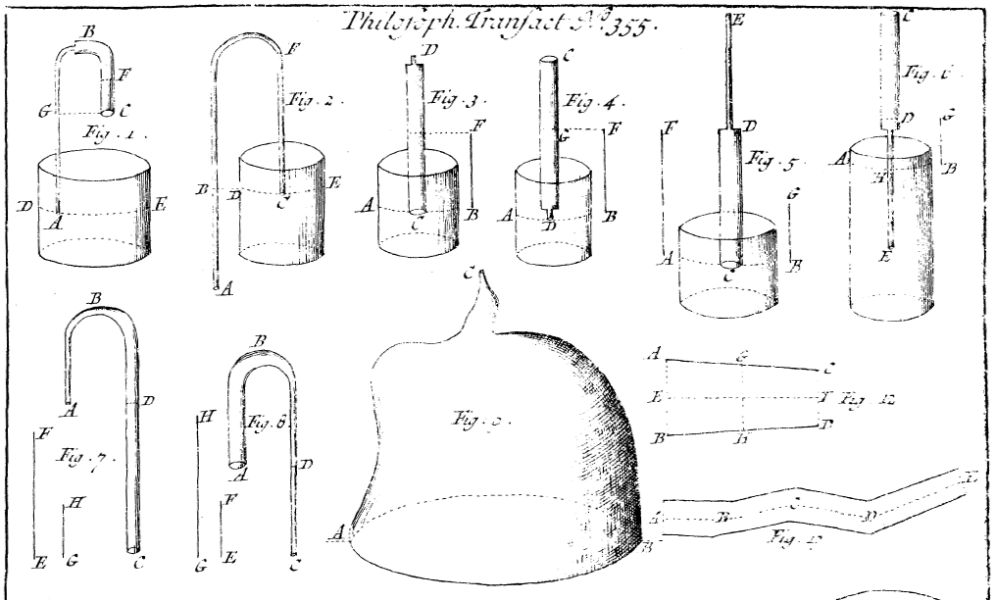

FIGURE 1.5: Sketches of the experimental setups used by J. Jurin for his study of the "Ascent and Suspension of Water in Capillary Tubes" published in 1717 (Jurin, 1717).

parameter (de Gennes et al., 2004). By means of Young's relation (Young, 1805) one can write

$$I = \gamma_{SO} - \gamma_{SL} = \gamma \cos\theta_E, \tag{1.12}$$

as a function of the surface tension of the liquid γ and its equilibrium contact angle with the surface θ_E. The interplay of the different surface tensions in this case is shown in Fig. 1.3 (right). Remarkably, it has been recently shown that Young's equation is also valid at the nanoscale (Seveno et al., 2013). By means of molecular-dynamics simulations, Seveno et al. provided evidence that the use of Eq. (1.12) is justified at these lengthscales.

Surface tension of the liquid is responsible for the increase in hydrostatic pressure across an interface between two fluids with a curved interface. This difference in hydrostatic pressure is given by the Laplace pressure:

$$\Delta P = \gamma C = \gamma \left(1/R + 1/R'\right), \tag{1.13}$$

where C is the curvature of the boundary, and R and R' are the two principal radii of curvature of the interface. In a capillary tube $R = R'$.

It is also important to define the lengthscale beyond which gravity becomes dominant in front of the surface tension of the fluid. The so called capillary length λ_c is obtained by comparing the Laplace pressure, proportional to γ/λ_c, and the hydrostatic pressure at a depth λ_c, $\rho g \lambda_c$, where ρ is the density of the fluid and g the acceleration of gravity

(de Gennes et al., 2004). It gives rise to

$$\lambda_c = \sqrt{\frac{\gamma}{\rho g}}. \tag{1.14}$$

1.2.1 Equilibrium height

We can first look at the maximum height achieved by the fluid within the tube when it is placed vertically. This maximum penetration of the fluid is known as the Jurin's or equilibrium height, h_{eq}. See a sketch in Fig. 1.6. We can compute it from different approaches.

• **Energies.** The energy of a column of liquid is given by $E = 2\pi bhI + \pi b^2 \rho g h^2/2$, where b is the inner radius of the tube and h the distance penetrated from the inlet. The first term corresponds to the surface energy, the energy cost of having the fluid in contact with the wall. The second accounts for the gravitational energy. By minimizing E as a function of h we obtain the equilibrium height of the front:

$$h_{eq} = \frac{2I}{\rho g b} = \frac{2\gamma \cos\theta_E}{\rho g b}. \tag{1.15}$$

• **Pressures.** We can also look at the variations of pressure in the tube to get the equilibrium height. Immediately underneath the surface the pressure is $P_A = P_0 - 2\gamma\cos\theta_E/b$, where P_0 is the atmospheric pressure. The underpressure just below the interface is due to capillary forces and given by Laplace's law (Eq. 1.13).

The pressure at $h = 0$ is $P_B = P_0$. Then, the pressure difference $P_A - P_B = \rho g h_{eq}$ is purely hydrostatic. By replacing the values of P_A and P_B we get the same expression of h_{eq} as Eq. (1.15).

• **Forces.** Finally, one could ask for the forces sustaining the column of fluid up to h_{eq}. The weight of the fluid above $h = 0$ is $F = \rho g \pi b^2 h_{eq}$. The capillary force per unit length is given by $I = \gamma \cos\theta_E$. As this force acts at the perimeter of the tube, the total force exerted is $F = 2\pi bI$. The balance of these two forces gives rise to the expression of h_{eq} obtained previously.

Given that the equilibrium height depends on $\cos\theta_E$, experiments of capillary rise where h_{eq} is measured are widely use to determine θ_E, the equilibrium advancing contact angle (Mumley et al., 1986*a*,*b*; Schäffer and Wong, 2000). The other parameters on which h_{eq} depends are usually either known, controlled, or easily measured via other methods.

It is worth noting that for $\theta_E > 90°$ the equilibrium height is negative. This means that the equilibrium position of the fluid inside the capillary is below the reservoir.

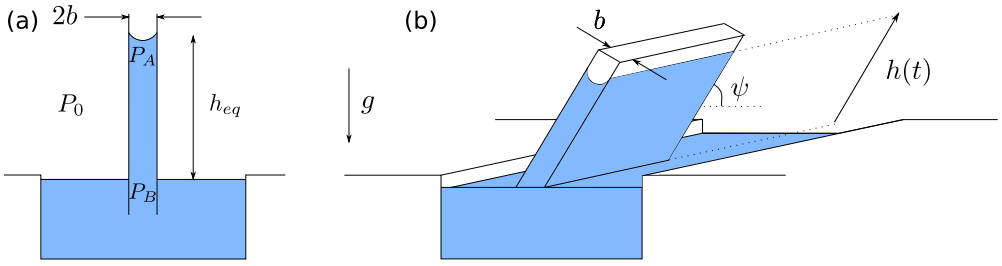

FIGURE 1.6: Sketch of capillary rise experiments. (a) A cylindrical capillary of radius b is immersed in a reservoir open at the atmospheric pressure P_0. P_A is the pressure underneath the front, P_B is the pressure at the surface of the reservoir. h_{eq} is the equilibrium height reached by the column of fluid. (b) Hele-Shaw of thickness b tilted an angle ψ with respect to the horizontal. $h(t)$ is the distance penetrated by the liquid as a function of time.

1.2.2 Capillary Rise Dynamics

The flow driven by capillarity and resisted only by viscous losses in the liquid, without gravity, was first analysed by Bell and Cameron (1906), who showed that the position of the imbibition front advances in time according to $h \sim t^{1/2}$. Heber Green and Ampt (1911) and Lucas (1918) and Washburn (1921) a few years later computed the proportionality constant for the case of a tube with a circular cross-section, and found that it depends on the radius of the tube and the properties of the liquid: viscosity, surface tension, and (advancing) contact angle.

Lucas and Washburn's result (LW) is the solution of a pressure balance equation based on a one-dimensional approximation of the flow. By adding the gravitational pressure contribution to the balance equation, Washburn (1921) was able to derive also a solution of the form $t(h)$ for capillary rise in a cylindrical tube restrained by gravity. In 1993 Barry et al., following the study of Heber Green and Ampt, and only a few years ago, in 2008, Fries and Dreyer, following the work of Lucas and Washburn, showed that the inverse of this solution could be written analytically in terms of the so called Lambert function, resulting in what is known as 'Extended Solution' (ES) (Barry et al., 1993; Fries and Dreyer, 2008*a*)[3]. The behaviour of this solution at short times, when gravitational pressure is negligible in front of capillary and viscous pressure, is of the LW form, $h(t) \sim t^{1/2}$. At longer times it crosses over to an exponential regime in which $h(t)$ tends asymptotically to a constant value –Jurin's or equilibrium height.

We will now derive these results from a pressure balance equation. The analysis that follows applies equally to a capillary tube of circular cross-section and small radius b than to a HS cell formed by two large parallel plates separated by a small gap of

[3]The two works were carried out independently. Barry et al. (2009) noticed that the results from Fries and Dreyer (2008*a*) had been previously found in Barry et al. (1993).

constant thickness b. Either tube or cell are tilted an angle ψ from the horizontal, while a gravitational field of intensity g points downwards in the vertical direction (Fig. 1.6). We consider the capillary-driven flow of a viscous liquid that gets into the tube or cell from one end and displaces the air initially present. We assume that:

- the flow is one-dimensional in the tube or cell,
- viscous and inertial effects in the displaced gas phase are negligible,
- inertial effects in the liquid reservoir are also negligible,
- viscous pressure losses are given by Poiseuille's law in the tube and by Darcy's law in the HS cell, and
- the capillary pressure at the liquid-air meniscus is constant and can be calculated from a constant contact angle θ and b.

Then, the equation of pressure balance at the mean height of the fluid front, $h(t)$, is:

$$\rho \frac{d}{dt}\left(h\dot{h}\right) = \frac{2\gamma\cos\theta}{b} - \rho g \sin\psi h - \frac{\mu}{\kappa} h\dot{h} + P, \tag{1.16}$$

where ρ is the density of the liquid, γ is the surface tension of the air-liquid interface, θ is the apparent (advancing) contact angle at the solid-liquid-air contact line, μ is the dynamic viscosity of the liquid, κ the permeability of the tube or cell, and P is an externally applied additional pressure at the liquid inlet. The overdot stands for time derivative. The LHS of this equation accounts for the variation of momentum –inertial term– in the invading liquid. The RHS is the sum of various pressure contributions: the first one is the capillary pressure, given by the Young-Laplace equation, that drives the flow in the case of wetting fluids ($\theta < 90°$); in addition to the capillary pressure, the liquid can also be driven into the medium by an external pressure difference, accounted for by the term P. The second and third terms account respectively for the gravitational pressure and for viscous losses of the liquid in the medium, and both resist the flow.

Neglecting the inertial term in the LHS, and assuming that the medium is placed horizontally ($\psi = 0°$) and the flow is driven only by capillary forces ($P = 0$), we are left with an equation of the form $h\dot{h} \sim$ constant, from which the LW result $h(t) \sim t^{1/2}$ is readily obtained. The solution with the coefficient of proportionality is then (Lucas, 1918; Washburn, 1921)

$$h(t) = 2\sqrt{\left(\frac{\gamma\cos\theta}{b}\right)\left(\frac{\kappa}{\mu}\right)\, t}. \tag{1.17}$$

In the absence of gravity, therefore, the front advances diffusively and does not arrive to a halt even though its velocity decays in time.

For a tilted tube or cell ($\psi \neq 0°$) gravity introduces a resisting term proportional to $h(t)$ which changes the nature of the solution. Neglecting again the inertial term and taking $P = 0$, the solution can be expressed in closed form as

$$h(t) = \left(\frac{\tilde{a}}{\tilde{b}}\right)\left[1 + W\left(-e^{-1-(\tilde{b}^2/\tilde{a})t}\right)\right], \tag{1.18}$$

where $x \equiv W(x)\exp(W(x))$ defines the Lambert function $W(x)$ and the parameters are $\tilde{a} = (\kappa/\mu)\,(2\gamma\cos\theta/b)$ and $\tilde{b} = (\kappa/\mu)\,(\rho g \sin\psi)$ (Fries and Dreyer, 2008*a*). This 'Extended Solution' predicts a LW behaviour at short times –capillary-viscous regime– that crosses over to an exponential behaviour at long times –capillary-gravity regime. According to this solution, an equilibrium height $h_{eq} \equiv 2\gamma\cos\theta/(b\rho g\sin\psi)$ $(= \tilde{a}/\tilde{b})$ is reached asymptotically.

Although the validity of these results has been repeatedly verified experimentally (LeGrand and Rense, 1945; Good and Lin, 1976; Fisher and Lark, 1979), it is important to realize that they were obtained under various assumptions that are not always fulfilled in experiments. In the first place inertial contributions to the pressure balance were neglected. However, a judicious choice of fluid properties can make inertia non-negligible, as demonstrated by Quéré and collaborators (Quéré, 1997; Quéré et al., 1999; Lorenceau et al., 2002). Inertia leads to underdamped oscillations of the front around the Jurin's height. Moreover, when inertia predominates –at very short times– Quéré (1997) found $h \sim t$ instead of $h \sim t^{1/2}$. This behaviour corrects the $t = 0$ singularity of the velocity that was first noticed by Bosanquet (1923). The transition from inertial to viscous flow in capillary rise has been recently studied by Fries and Dreyer (2008*b*). Oscillations around the equilibrium height due to inertia have been also demonstrated numerically by Hamraoui and Nylander (2002). Another source of discrepancy between the LW and ES solutions and the results of experiments may arise from the assumption of a constant capillary pressure. It is known that the contact angle at a moving contact line depends on its velocity (de Gennes, 1985). For perfectly wetting fluids –static contact angle $\theta_E = 0°$–, the dependence on velocity of the dynamic contact angle is usually accounted for by a friction term in the capillary pressure, $\cos\theta_D \propto (dh/dt)^x$, where the exponent x takes values in the range $0 - 1$. This additional resistive term has been invoked repeatedly to explain the systematic observation that the experimental curves $h(t)$ fall slightly below the corresponding theoretical predictions at intermediate times (Mumley et al., 1986*a*; Hamraoui et al., 2000; Hamraoui and Nylander, 2002; Chebbi, 2007; Martic et al., 2005; Fries and Dreyer, 2008*a*; Wolf et al., 2010) as shown in Fig. 1.7. For partially wetting fluids Zhou and Sheng (Zhou and Sheng, 1990; Sheng and Zhou, 1992) have shown that the contact line also experiences a frictional force, due to the excitation of capillary waves at the fluid-fluid interface. For two-phase displacements in

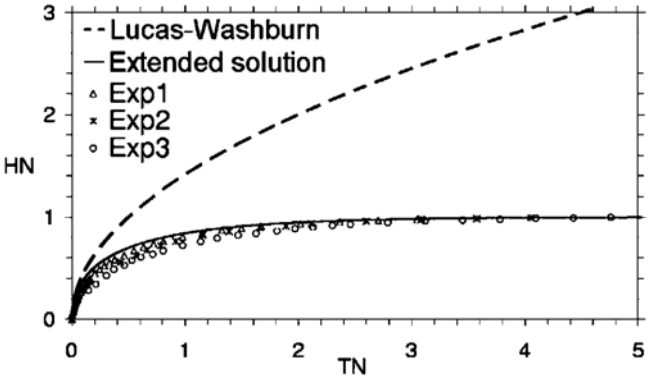

FIGURE 1.7: Comparison between the LW and ES solutions, and experimental data for capillary rise experiments with $\psi \neq 0°$. Data plotted in dimensionless form, $HN = h/h_{eq}$ and $TN = (\tilde{b}/h_{eq})t$. Reprinted from Fries and Dreyer (2008*a*).

porous media, finally, Weitz et al. (1987) showed that the capillary pressure drop across the interface scaled as $(dh/dt)^{1/2}$. Other features neglected in the original formulation, including the development of the flow field, entrance effects, and the viscous resistance of the gas phase in very long tubes have subsequently been considered as well (Szekely et al., 1971; Kornev and Neimark, 2001; Hultmark et al., 2011).

In Ch. 2, we will apply the same kind of formalism that led to Eq. (1.16) to capillary rise in our model disordered medium. The systematic overestimation of the experimental data by the LW and ES solutions without and with gravity will be addressed and discussed in detail.

1.3 Interfacial fluctuations

In the experiments presented in this Thesis, we deal with an oil-air interface advancing through a Hele-Shaw cell of either constant or dichotomic gap spacing that randomly fluctuates in space. We define the first case as Smooth (S) cell and the latter as Disordered (D) cell –details in Ch. 2. Let us now focus our attention on the interplay of forces that takes place at the front line in such experiments.

As commented previously, in this situation only two physical mechanisms control the dynamics of the imbibition front: viscous pressure and capillarity.

When we consider the Smooth cell, tiny fluctuations on the capillary pressure are only due to the small heterogeneities of the system –in the wetting properties of the substrate, for example. On the contrary, the capillary pressure in the Disordered cell fluctuates significantly as the gap spacing does so. Then, in the D cell the interface can get stuck where the capillary forces are small, and moves faster in other regions of the cell. Thus, the medium distorts the front producing a bent interface. The permeability or mobility of the medium also fluctuates as the front advances and explores different regions of the disorder. These two destabilizing forces act at two different length scales that crossover at $\ell_\times \propto \sqrt{\kappa}/\mathrm{Ca}$ (Pauné and Casademunt, 2003). Small scales are dominated by

capillary disorder while the fluctuations on the permeability become dominant at large length scales –see the discussion below.

On the other hand, two damping mechanisms act on the front to flatten it in the in-plane direction. These two forces are the surface tension acting along the interface –in the plane parallel to the substrate– and the viscous pressure drop associated with the fluid motion. Let us consider a perturbation $\delta h(x) = A\cos(kx)$ of lateral extent ℓ, with $k = 2\pi/\ell$, as shown in Fig. 1.8. The pressure jump across the interface is given by the Young-Laplace relation, and the viscous-pressure drop in a quasistatic approximation by Darcy's law:

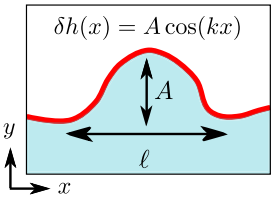

FIGURE 1.8: Schematic perturbation of the front.

- Surface tension: $[\![p]\!] = \gamma \dfrac{\partial^2 \delta h(x)}{\partial x^2} \sim \gamma A/\ell^2$.
- Viscous pressure: $\Delta p = (\mu/\kappa)\, \mathrm{v} A$.

As the two pressure jumps do not scale in the same way with the lateral size of the perturbation, ℓ, a characteristic crossover lengthscale can be derived:

$$\ell_c = \sqrt{\frac{\kappa}{\mu \mathrm{v}/\gamma}} = \sqrt{\frac{\kappa}{\mathrm{Ca}}}. \tag{1.19}$$

This lengthscale separates the range of perturbation sizes at which the surface tension is the main damping mechanism, $\ell < \ell_c$, from the perturbations that are essentially damped by the viscous-pressure drop, $\ell > \ell_c$.

Interfacial equation. We have just discussed the forces that act at the oil-air interface in a qualitative way. We now want to characterize the effect of these forces by means of the interfacial equation. This equation describes the growth of the q^{th} mode of the front in Fourier space. It is worth noting that the interface considered is a 2D projection of the actual 3D oil-air interface, with a more complex dynamics. Considering the linear approximation, i.e. small perturbations of the interface, the interfacial equation reads (Krug and Meakin, 1991; Dubé et al., 1999; Hernández-Machado et al., 2001)

$$\frac{\partial \tilde{h}_q}{\partial t} = \underbrace{-\frac{\gamma\kappa}{\mu}|q|q^2\tilde{h}_q}_{\text{Surface tension}} \underbrace{-\mathrm{v}(t)|q|\tilde{h}_q}_{\text{Viscosity}} + \text{quenched disorder}. \tag{1.20}$$

It is a linear equation in $\tilde{h}_q$, and non-local due to the $|q|$ terms. The surface tension term scales with $|q|q^2$ and has negative sign. Then, small-scale perturbations of the interface are mainly damped by surface tension. Larger-scale fluctuations, on the other

hand, are flattened out essentially by viscous pressure, which scales as $|q|$. The quenched disorder term is responsible for the roughening of the interface. This noise is *quenched* since it only depends on time through the position of the interface $h(x,t)$. It represents the different distorting forces present in the system.

Two similar formulations for the disorder terms were proposed for spontaneous (Dubé et al., 1999) and forced-flow imbibition (Hernández-Machado et al., 2001) –for large imposed fluxes. Pauné and Casademunt (2003) derived *ab initio* a general and complete interface equation including all the sources of noise present in an interface moving in a model of disordered medium. The medium studied was very similar to the one used in this thesis. It consisted of a Hele-Shaw cell with random gap spacing variations $\delta b = b - b_0$, where b_0 is the mean value. Smooth variations of gap thickness, $|\nabla b| \ll 1$, were assumed. In this system a dimensionless quenched noise ζ can be introduced as $b^2 = b_0^2\,[1 + \zeta(x,y)]$ with $\langle \zeta(x,y) \rangle = 0$.

The fluctuations of the front arise from local variations of capillary pressure, permeability, and available volume produced by this noise. In Fourier space, the *capillary noise* is

$$\frac{\gamma b_0}{12\mu}|q|\hat{\zeta}_h(q), \tag{1.21}$$

where $\hat{\zeta}_h(q)$ is the Fourier transform of $\zeta(x,h(x))$. This noise is conserved –it preserves the area of the front– and non-local. It arises from the fluctuations of gap thickness of the medium. The *permeability noise* is given by

$$\mathrm{v}(t)\hat{\zeta}_h(q). \tag{1.22}$$

This is a local, non-conserved noise. It results from the effect of the local variations of the gap thickness on the permeability and on the available volume for the fluid front. Finally, the *bulk noise* for forced-flow imbibition is

$$\hat{\Omega}_{LR}(q,t) = \frac{3\mathrm{v}}{2}|q| \int_{-\infty}^{\infty} dx' \int_{-\infty}^{0} dy \zeta(x, y + \mathrm{v}t) e^{-iqx'} e^{y|q|}. \tag{1.23}$$

It is a long-ranged, explicitly time-dependent, correlated noise. It takes into account the effect of the disorder in the whole area occupied by the fluid. This noise is relevant at small lengthscales. At these scales, though, the approximation used by Pauné and Casademunt (2003) to derive the interfacial equation may miss details of local interface pinning. Nevertheless, this noise term is expected not to affect the scaling behaviour of the fluctuations of the interface when considering imbibition of a wetting liquid against an inviscid fluid (Pauné and Casademunt, 2003).

Characteristic lengthscales. The characteristic lengthscales ℓ_c and $\ell_\times$ introduced phenomenologically above can now be derived more rigorously. From Eq. (1.20) we can define a crossover lengthscale by comparing the surface tension and the viscosity terms:

$$\ell_c \simeq \sqrt{\frac{\kappa}{\mathrm{Ca}}} \sim \sqrt{\frac{1}{\mu \mathrm{v}}}. \tag{1.24}$$

The second crossover lengthscale can be obtained by comparing the effect of the quenched noise at different lengthscales. The roughening of the interface at small scales is mainly due to capillary fluctuations. At large scales, the noise on the permeability is the main distorting mechanism. Comparing these two terms –Eqs. (1.21) and (1.22)– we get

$$\ell_\times \simeq \frac{b_0}{6\mathrm{Ca}} \sim \frac{1}{\mu \mathrm{v}}. \tag{1.25}$$

1.4 Rough interfaces

The fluid front invading the disordered cell gets rougher and rougher as it advances through the medium.

Most rough surfaces or interfaces are generated by out-of-equilibrium physical processes that may lead to scale-invariant structures (Krug, 1997). Specifically, during the growth of an interface, the competition of forces present at the front, that act at different length scales, plays a central role in developing long-ranged spatial correlations along the front, and scale invariance. These growth processes are studied in the framework of kinetic roughening theory. A more detailed description and some examples are given in appendix A.

In our experiments we follow the advancement in time of a fluid front through a quasi-bi-dimensional medium. In order to characterize it, we first need a single-valued function $h(x)$ which is extracted from the experimental images at each capturing time. Once we know $h(x,t)$, we can compute the mean position of the front measured at a window of observation of size ℓ:

$$\langle h(x,t)\rangle_\ell = \frac{1}{\ell}\int_\ell h(x,t)dx, \tag{1.26}$$

and its statistical width about the mean value:

$$w(\ell,t) = \overline{\langle [h(x,t) - \langle h(x,t)\rangle_\ell]^2\rangle_\ell^{1/2}}. \tag{1.27}$$

$\langle \dots \rangle_\ell$ indicates the average over the window, and the overline is an average over all the realizations of the disorder explored. The quantity $w(\ell,t)$ is usually referred to in the literature as the front width, and it characterizes the roughness of the interface (Barabási

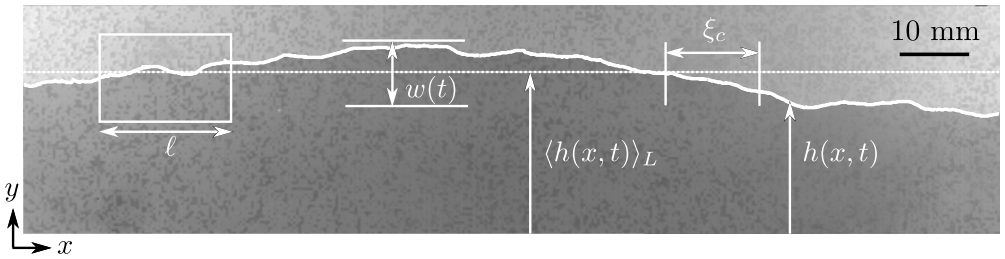

FIGURE 1.9: Interface from a real experiment. $h(x,t)$ is the position of the front, $\langle h(x,t)\rangle_L$ is the mean position averaged over the whole system L. ℓ is the size of the window of observation, $w(\ell,t)$ is the width of the interface at the scale ℓ, and ξ_c is the correlation length along the front.

and Stanley, 1995). A sketch of the relevant length scales is shown in Fig.1.9 on top of an interface from a real experiment.

In the reciprocal space, the power spectrum is also a convenient quantity to analyse the fluctuations of $h(x,t)$. It is defined as

$$S(q,t) = \overline{\hat{h}_\ell(q,t)\hat{h}_\ell(-q,t)}, \tag{1.28}$$

where

$$\hat{h}_\ell(q,t) = \frac{1}{\ell^{1/2}} \int_\ell dx \, [h(x,t) - \langle h(x,t)\rangle_\ell] \, e^{iqx} \tag{1.29}$$

is the Fourier transform of $h(x,t)$ when observing the system at a scale ℓ, where the average height has been subtracted.

1.4.1 Kinetic roughening

The theory of kinetic roughening relates the local, microscopic fluctuations that affect the motion of the interface to the macroscopic behaviour of this interface and its universal scaling properties (Krug, 1997). The fluctuations can be of thermal origin or due to quenched disorder.

Dynamic scaling

Family and Vicsek (1985) proposed a dynamic scaling for the global roughness $w(L,t)$ of an interface in a kinetic roughening process. Many examples can be found in literature showing such behaviour (Barabási and Stanley, 1995). However, in some growth models and experiments, a different scaling of the local and global roughness is observed, that is, different values of the roughness exponent at the global scale and at the local scale are found. This dynamic scaling was called *anomalous scaling* to differentiate it from the *ordinary* or Family-Vicsek scaling.

Ramasco et al. (2000) suggested a generic dynamic scaling ansatz for kinetic roughening processes. In that work, Ramasco et al. showed that all the types of scaling can be obtained from a unique generic scaling ansatz, which is formulated in the Fourier space. Let us consider a flat, uncorrelated interface at $t = 0$. As it grows in the presence of noise, it becomes rougher and rougher because physical coupling of different points in the interface spreads fluctuations. This evolving interface satisfies a generic dynamic scaling if it develops correlations along the front that span a length $\xi_c(t)$ in the x direction, and if $\xi_c(t) \sim t^{1/z}$, where z is the *dynamic exponent*. The growing ξ_c spans up to the system size L if no other characteristic length scale is present in the system. Once ξ_c has saturated, the interface is in a statistically-steady regime in which its width $w(\ell, t)$ does not increase and only fluctuations are observed. Ramasco et al. consider the Fourier transform of the height of the interface in a system of size L, $\tilde{h}(q, t)$, and propose that the power spectrum behaves as

$$S(q, t) = q^{-(2\alpha+1)} s(qt^{1/z}), \tag{1.30}$$

where the scaling function $s(u)$ is defined as

$$s(u) \sim \begin{cases} u^{(2\alpha+1)} & \text{for } u \ll 1, \\ u^{2(\alpha-\alpha_s)} & \text{for } u \gg 1. \end{cases} \tag{1.31}$$

The exponent α is the *roughness exponent* and α_s is the *spectral roughness exponent*. Their difference is usually referred to as the *anomalous exponent* $\theta = \alpha - \alpha_s$.

The *global width* of the interface is then obtained by integration of the power spectrum

$$w^2(L, t) = \frac{1}{L} \int dq S(q, t), \tag{1.32}$$

while the *local width* of the interface arises from the height-height correlation function $C(\ell, t)$:

$$w^2(\ell, t) \sim C(\ell, t) \sim \frac{1}{L} \int dq \, [1 - \cos(q\ell)] \, S(q, t). \tag{1.33}$$

Then the dynamic scaling behaviour is

$$w(\ell, t) \sim t^{\beta} g(\ell/\xi_c), \tag{1.34}$$

where the scaling function $g(u)$ is not unique and depends on the scaling scenario.

Scaling scenarios

From the values of the *global*, *spectral*, and *local roughness exponents*, α, α_s, and α_{loc}, one can distinguish among four scaling scenarios:

If $\alpha_s < 1 \Rightarrow \alpha_{loc} = \alpha_s$	$\alpha_s = \alpha \Rightarrow$ Family-Vicsek	Ordinary scaling
	$\alpha_s \neq \alpha \Rightarrow$ Intrinsic	Anomalous scaling
If $\alpha_s > 1 \Rightarrow \alpha_{loc} = 1$	$\alpha_s = \alpha \Rightarrow$ Super-rough	
	$\alpha_s \neq \alpha \Rightarrow$ Faceted	

In all cases, the global roughness –for $\ell = L$– scales as

$$W(L,t) \sim \begin{cases} t^{\beta} & \text{for } t \ll t_s, \\ L^{\alpha} & \text{for } t \gg t_s, \end{cases} \tag{1.35}$$

where β is the *growth exponent* and t_s is the saturation time. Since the correlation length $\xi_c \sim t^{1/z}$, the stationary regime is achieved for $t \gg t_s \sim L^z$, that is, the correlation length has spread along the whole interface. The three global exponents verify the scaling relation $\alpha = z\beta$.

The generic scaling ansatz that refers to the behaviour of power spectra of the interfaces, Eqs. (1.30) and (1.31), also applies to all cases. We observe, however, differences on the local roughness depending on the scaling scenario. In anomalous scaling scenarios, an *anomalous growth exponent* $\beta^* = (\alpha - \alpha_s)/z = \theta/z$ is defined. It is only observable when small windows are analysed as this growth regime appears in the range of times between the local saturation time, $t_\ell \sim \ell^z$, and the global saturation time, $t_s \sim L^z$.

The scaling functions $s(u)$, Eq. (1.31), and $g(u)$, Eq. (1.34), for the four scenarios are shown and discussed in appendix A.

1.4.2 Kinetic roughening in imbibition

The problem of imbibition and specifically the dynamics of the invading front has attracted a great deal of attention as a model system to study kinetic roughening. The experiments of Rubio et al. (1989) triggered intensive research on this topic both experimental and theoretical. The aim of those experiments and those from Horvath et al. (1991) and He et al. (1992) was to confirm the scaling universality class given by the celebrated KPZ equation (Kardar et al., 1986). Although KPZ is a local interfacial equation and the imbibition process is non-local, the hope was that this non-local nature of the problem could be neglected. However, it was shown that nonlocality had to be taken into account and so the KPZ equation was not appropriate (He et al., 1992). The first theoretical proposal for dealing with kinetic roughening in non-local Laplacian fields –such as pressure in imbibition dynamics– was done by Krug and Meakin (1991), followed by Dubé et al. (1999) and Hernández-Machado et al. (2001). In the dynamical equation for the interface fluctuations proposed by Krug and Meakin (1991), an intrinsic characteristic lengthscale naturally appears that separates the two relaxation

modes of the interface: surface tension and viscous pressure damping. The introduction of quenched disorder in a system with liquid conservation was done by Ganesan and Brenner (1998). Pauné and Casademunt (2003) studied in depth the effects of quenched disorder in two-phase fluid flow with arbitrary wettability and viscosity contrast in a Hele-Shaw cell with random gap spacing.

The growth exponent β was difficult to measure experimentally because the transient regime preceding the statistically-stationary state was too short in most of the experiments. The first β exponent measured was reported by Horvath et al. (1991). To avoid short growing times and to have a better control of the disorder, Soriano et al. (2002) developed a new model of disordered medium. In contrast to the Hele Shaw cell filled with glass beads used in the above mentioned experiments (Rubio et al., 1989; Horvath et al., 1991; He et al., 1992), this system was an open fracture. This new experimental setup allowed to explore a number of different disorder configurations and values of the controlling parameters in forced-flow imbibition, giving rise to different scaling scenarios (Soriano et al., 2002,a; Soriano, 2003). A similar setup was used by Planet et al. for spontaneous imbibition experiments (Planet et al., 2007; Planet, 2009).

A summary of earlier results of kinetic roughening of fluid interfaces in imbibition is presented in appendix A. In Table A.1 we specifically summarize the data obtained in imbibition experiments performed in setups equivalent to the one used in this Thesis, the expected theoretical values, and the results from simulations for equivalent imbibition front advancements.

In Ch. 4 we will study the effect on the kinetic roughening process of diminishing the fluid viscosity. We will study the kinetic roughening process for low-viscosity fluids, and we will compare the scaling scenario observed with earlier results for equivalent imbibition displacements obtained in experiments and phase-field simulations.

1.5 Avalanche dynamics

The problem of liquid imbibition bears many resemblances with other non-equilibrium critical phenomena in spatially-extended systems. The reason is that the lateral length of correlated motion, ℓ_c, diverges when the front velocity $v \to 0$. In this limit the imbibition front moves by discrete avalanches of all possible sizes and durations, limited only by the system size.

In general, the propagation of interfaces through disordered media displays a complex spatio-temporal dynamics. This complex dynamics is analysed in the literature at the local scale (when accessible) or at the averaged, global scale.

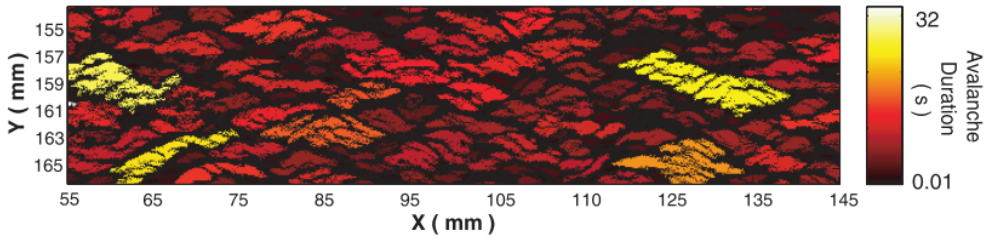

FIGURE 1.10: Spatial distribution of velocity clusters for velocities $v(x, y) > v_c$ in forced-flow imbibition experiments. Figure reproduced from Santucci et al. (2011).

1.5.1 Local avalanches

The complex dynamics of propagation of out-of-equilibrium interfaces at the local scale has been studied in a variety of systems. The motion of a contact line on an heterogeneous substrate (Moulinet et al., 2002) or front propagation in spontaneous imbibition in a weakly vibrated granular medium (Balankin et al., 2012) display burst-like dynamics at the local scale with avalanches widely distributed in size. The propagation of an interfacial crack along an heterogeneous weak plane studied by Måløy et al. (2006) and Tallakstad et al. (2011) also shows a front dynamics governed by local and irregular avalanches with very large size and velocity fluctuations. Magnetic fluxes show avalanche dynamics whose size distributions are controlled by the quenched disorder (Welling et al., 2005). And magnetic domain walls also exhibit a motion characterized by abrupt transitions that can be measured at the local scale using magneto-optics (Ryu et al., 2007; Magni et al., 2009). To name but a few.

Forced-flow imbibition local dynamics

The local dynamics of forced-flow imbibition fronts has been also studied experimentally and from a theoretical and numerical point of view.

Planet (2009) and Santucci et al. (2011) studied the propagation of imbibition fronts in a setup equivalent to the one used in this Thesis. The front was found to advance by means of spatially-localized avalanches spanning a wide range of sizes and durations. Local avalanches were defined as connected clusters of high velocities, above a given arbitrary threshold, in the local velocity map $v(x, y) > v_c$ (Fig. 1.10).

The distributions of sizes A, durations D, and lateral extent L_x of the avalanches were shown to follow the general form $P_x(x) = a_x x^{-m_x} e^{-x/\xi_x}$, i.e. a power law with an exponentially decaying cutoff (Fig. 1.11).

To obtain a reliable value of the power-law exponent of experimental distributions is complicated. Clauset et al. (2009) proposed the method of Maximum Likelihood (ML) to

fit the distributions of data exhibiting a lower cutoff. Baró and Vives (2012) presented a method also based on the ML estimator to obtain the exponent of distributions of experimental and numerical data which present distortions in the region of small events and also in the large-event region, that is, with upper and lower cutoffs. They specifically analysed the data by means of Maximum Likelihood exponent maps.

In the present Thesis we follow the procedure described by Pruessner (2010), Planet et al. (2010) and Pruessner (2012). For a power-law distribution of the quantity x with a cutoff, the general form is given by:

$$P_x(x) = a_x x^{-m_x} \mathcal{G}_x(x/\xi_x), \tag{1.36}$$

where $\mathcal{G}_x(x/\xi_x)$ is a generic function describing the decay of the power law as a function of the cutoff ξ_x. The expected value of this distribution is $\langle x \rangle = A_x \xi_x^{2-m_x}$ for $m_x < 2$. We can then obtain the distribution $\tilde{P}(u)$ of the rescaled variable $u = x/\xi_x$, measured in units of the cutoff. Since $\tilde{P}(u)du = P(x)dx$ with $du = 1/\xi_x dx$, the new distribution reads:

$$\tilde{P}(u) = \tilde{a}_u u^{-m_x} \mathcal{G}_u(u) \xi_x^{1-m_x}. \tag{1.37}$$

It can be arranged and rewritten in terms of the original experimental data x giving rise to:

$$\begin{aligned} P_x(x)\xi_x^{m_x} &= \tilde{a}_x \left(\frac{x}{\xi_x}\right)^{-m_x} \mathcal{G}_x\left(\frac{x}{\xi_x}\right), \quad \text{or} \\ P_x(x)\langle x \rangle^{\frac{m_x}{2-m_x}} &= b_x \left(\frac{x}{\langle x \rangle^{1/(2-m_x)}}\right)^{-m_x} \mathcal{G}_x\left(\frac{x}{\langle x \rangle^{1/(2-m_x)}}\right). \end{aligned} \tag{1.38}$$

The method is based on finding the power-law exponent m^* that provides the best collapse of $\mathcal{Y} = P_x(x)\langle x \rangle^{m_x/(2-m_x)}$ as a function of $\mathcal{X} = x/\langle x \rangle^{1/(2-m_x)}$. In order to quantify the quality of this collapse, we first fit $\mathcal{Y}_{\text{fit}} = A\mathcal{X}^{-m_x} e^{-\mathcal{X}/B}$ to the set of experimental data varying the exponent m_x and leaving A and B as free parameters. Then, we compute the error $\epsilon = \sum_i [\log(\mathcal{Y}_i) - \log(\mathcal{Y}_{\text{fit}})]^2$ as a function of m_x, where $\mathcal{Y}_i$ are the experimental distributions. The $\mathcal{Y}_{fit}$ that minimizes ϵ gives the best estimator of the exponent m_x.

This procedure was used by Santucci et al. (2011) to obtain the power-law exponents $\alpha_{L_x} = 0.82(15)$, $\alpha_A = 1.08(5)$, and $\alpha_D = 1.24(10)$ for the distributions of lateral extent, size, and durations of the local avalanches respectively. $P(A)$ are shown in Fig. 1.11 for experiments performed at various v, and compared to the distribution of sizes of the disorder islands.

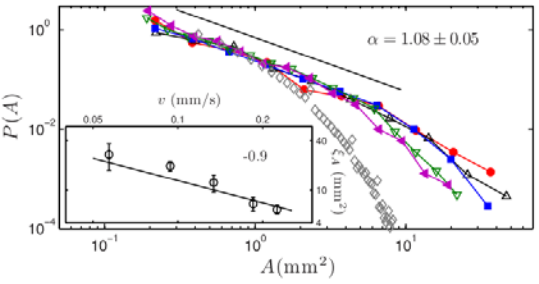

FIGURE 1.11: Avalanche size distributions for forced-flow imbibition experiments performed at different v. The diamond symbols give the size distribution of the disorder patches. Inset: divergence of the cutoff of the pdf with v. α corresponds to α_A in the notation used in this Thesis. Figure reproduced from Santucci et al. (2011).

The cutoffs of those distributions diverged as the mean imposed velocity of the front $\mathrm{v} \to 0$ (inset of Fig. 1.11), indicating the existence of a critical pinning/depinning transition at $\mathrm{v} = 0$ (Alava et al., 2004). The maximum lateral extent of avalanches ξ_{L_x} was found to depend on v as $\xi_{L_x} \sim \mathrm{v}^{-1/2}$, indicating that ξ_{L_x} is controlled by the lateral correlation length of the front $\ell_c = \sqrt{\kappa/(\mu \mathrm{v})}$. Santucci et al. (2011) observed that the local avalanches had an anisotropic shape. The maximum distance swept by the interface in the avalanche in the direction of advancement of the front ξ_{L_y} scaled as $\xi_{L_y} \sim \xi_{L_x}^H$ with $H = 0.81(5)$, where H is the anisotropy exponent. The cutoff of the pdfs of durations, ξ_D, was found to scale with an estimation of the maximum duration of the local avalanches as $\xi_D \sim \xi_{L_y}/\mathrm{v}$. Santucci et al. (2011) also showed that the propagation of the avalanches was ballistic, $L_x \sim D$. The scaling relations among critical exponents derived for the pinning point (described below) were also satisfied by the experimental values of the exponents found by Santucci et al. (2011).

Pradas et al. (2009), Pradas (2009), and López et al. (2010) studied numerically and theoretically the evolution of imbibition fronts through disordered media. In the capillary-disorder regime, when the front is uncorrelated at scales $\ell > \ell_c$, Pradas et al. (2009) proposed a scaling theory for the properties of the local avalanches. According to their theory, the size of the avalanches scales with their lateral length as $A \sim L_x^{d_{av}}$ for $L_x < \xi_c$, where d_{av} is the avalanche dimension exponent. The avalanche size can be estimated by the product of its lateral extents, $A \sim L_x L_y \sim L_x^{1+H}$, and thus $d_{av} = 1 + H$ (Santucci et al., 2011). The distributions of durations and sizes are also expected to scale as $A \sim D^{\gamma_{av}}$.

If we consider that the joint distribution of sizes, durations and lateral extent are scale invariant, it implies $P(A, D, L_x) = b^\sigma P(b^{d_{av}} A, b^{z_{av}} D, b L_x)$ for any factor $b > 0$. The marginal distributions $P(A)$, $P(D)$ and $P(L_x)$ are obtained integrating over the other two arguments. The following scaling relations among exponents are also obtained (Pradas et al., 2009):

$$\alpha_D - 1 = \frac{d_{av}}{z_{av}}(\alpha_A - 1), \quad \text{and} \quad \alpha_D - 1 = \frac{1}{z_{av}}(\alpha_{L_x} - 1), \tag{1.39}$$

where α_A is the power-law exponent of $P(A)$, α_D is the exponent corresponding to $P(D)$, and α_{L_x} corresponds to $P(L_x)$.

Pradas et al. (2009) relate the avalanche dynamics of the front with the local width of the interface fluctuations $w(\ell, t)$, described in Sec. 1.4. $w(\ell, t)$ scales with the local roughness exponent α_{loc} as $w(\ell, t) \sim \ell^{\alpha_{loc}}$, then, the size of a local avalanche can be written as $A \sim L_x w(L_x) \sim L_x L_x^{\alpha_{loc}} \sim L_x^{1+\alpha_{loc}}$, giving rise to $d_{av} = 1 + \alpha_{loc}$. In that work, the local dynamics is also linked to the fluctuations of the interface by means of the dynamic exponent z which is assumed to be $z = z_{av}$. Then, the following relations are also obtained:

$$L_x \sim D^{1/z} \quad \text{and} \quad A \sim D^{d_{av}/z}, \tag{1.40}$$

where $\gamma_{av} = d_{av}/z = (1 + H)/z$.

Another theoretical approach was proposed by Rost et al. (2007). In that work, the fronts studied displayed a lateral correlation length much smaller than the system size, $\ell_c \ll L$. In that case the avalanches could be considered as independent. Their duration is given by $D \sim w(L_x)/v(L_x)$, where $v(L_x)$ is the velocity of the region of lateral size L_x. Considering independent avalanches, the velocity scales as $v(L_x) \sim L_x^{-d/2}$ in $1 + d$ dimensions according to the central limit theorem. Then, the scaling $A \sim D^{\gamma_{av}}$ is given by $\gamma_{av} = (\alpha_{loc} + d)/(\alpha_{loc} + d/2)$. These results differ from the ones obtained by Pradas et al. (2009) as a consequence of $\ell_c \ll L$.

Pradas et al. (2009) performed phase-field simulations of forced-flow imbibition in two regimes: at high mean imposed velocities and at the static limit, where the lateral correlation of the front is comparable to the system size. Exponents $\alpha_A = 1.54(5)$ and $\alpha_D = 1.62(6)$ were found in both regimes independently of the mean velocity of the front, while the exponent γ_{av} took values $\gamma_{av} = 1.3$ and $\gamma_{av} = 1.1$ at high and low velocities respectively.

The discrepancies observed between experimental results by Planet (2009) and Santucci et al. (2011), and numerical results by Pradas et al. (2009) may arise from a number of reasons. Limited statistics in the experimental studies, or limited range of experimental parameters explored may result in the differences noticed. Those discrepancies may be also a consequence of studying the front dynamics experimentally with a driving velocity too high to be close enough to the critical pinning point, contrary to the quasi-static regime reached in the numerical studies. Finally, a fundamental difference between those experimental and numerical models of open fracture is the nature of disorder. A spatially-extended disorder patches with finite size were used by Planet (2009) and Santucci et al. (2011), contrary to the point-like defect simulated by Pradas et al. (2009).

In order to shed light on those discrepancies we have performed a systematic analysis of the local spatio-temporal dynamics of imbibition fronts, extending the range of

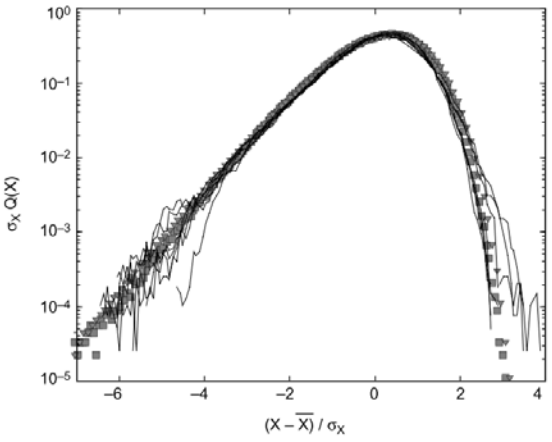

FIGURE 1.12: Collapse of the probability density functions of power fluctuations in turbulent closed flow (solid lines) and of instantaneous magnetization from simulations of spin wave approximation of the 2D XY model (symbols). Figure reproduced from Bramwell et al. (1998).

experimental parameters explored. In particular, a wider range of v has been analysed and, for the first time in this setup, oils of different viscosities have been used. In addition, we have carried out a large number of experiments leading to very large data sets required for accurate statistics. We have also introduced new analysis of the spatial and temporal correlations of front velocity. The results from these new experiments are shown, analysed and discussed in Ch. 5.

1.5.2 Global spatio-temporal dynamics

The avalanche-like propagation of interfaces through disordered media is not always accessible at the local scale. In these cases the evolution in time of a global, spatially-averaged quantity is analysed instead. As a result of the avalanche-like motion of the fronts at the local scale, the spatially-averaged signal is jerky, also showing burst-like dynamics.

Fluctuations of spatially-averaged quantities

The study of fluctuations of global quantities in spatially-correlated systems has attracted much attention in recent years. The seminal work of Bramwell, Holdsworth and Pinton (1998) showed that the power consumption of turbulent flow displays the same non-Gaussian fluctuations (BHP) as a model of finite size critical behaviour (two-dimensional XY model), and proposed that both systems share the same statistics because they are critical (Fig. 1.12).

That work triggered intensive theoretical and experimental research. The relationship of the BHP shape with both Gaussian and extremal statistics was analysed by Bramwell et al. (2000). Those non-Gaussian fluctuations of a spatially-averaged quantity from a spatially-correlated signal arise from the fact that the system cannot be divided into

mesoscopic regions that are statistically independent. Then, the conditions for the central limit theorem to be valid are not fulfilled and Gaussian fluctuations about the mean value should not be expected. Actually, these fluctuations are well fitted by generalized Gumbel (GG) distributions (Portelli et al., 2001; Bertin, 2005). GG distributions are defined by (Gumbel, 1958):

$$P_a(Y) = \frac{a^a b_a}{\Gamma(a)} \exp\left\{-a\left[b_a(Y+s_a) + e^{-b_a(Y+s_a)}\right]\right\}, \tag{1.41}$$

with

$$b_a = \sqrt{\psi^1(a)}/\sigma_Y \quad \text{and} \quad s_a = \langle Y\rangle + \left(\ln a - \psi^0(a)\right)/b_a, \tag{1.42}$$

where $\Gamma(a)$ is the gamma function and $\psi^m(a) = \frac{d^{m+1}}{da^{m+1}} \ln\Gamma(a)$ is the polygamma function of order m. If normalized data is considered, the two first moments of the distribution of Y are set: $\langle Y\rangle = 0$ and $\sigma_Y = 1$. Then, the only free parameter of Eq. (1.41) is a. This parameter is related to the asymmetry of the distributions by (Portelli et al., 2001):

$$Sk = \langle Y^3\rangle \sim 1/\sqrt{a}. \tag{1.43}$$

In addition, the asymmetry of GG-like distributions of averages of correlated variables is related to the number N_{eff} of effective degrees of freedom of the system under study (Portelli et al., 2001; Noullez and Pinton, 2002).

Such non-Gaussian fluctuations of an averaged-quantity have been observed in several experimental studies. For example, the fluctuations of injected power in electroconvection (Tóth-Katona and Gleeson, 2003), the fluctuations of the averaged order parameter in Fréedericksz transition in liquid crystals (Joubaud et al., 2008), or bioluminescent emission of bacterial colonies (Delle Side et al., 2013) were found to be described by GG-like distributions. In forced-flow imbibition experiments Planet et al. (2009) studied the fluctuations of the global spatially-averaged velocity of the oil-air interface, and showed that they follow generalized Gumbel distributions determined only by the skewness of the experimental data. In addition, the relation of the asymmetry of the distributions with the effective number of degrees of freedom of the front, $N_{\text{eff}} = \ell/\ell_c$, was verified for different windows of observation of size ℓ and different mean velocities of the front v, that determine $\ell_c \sim 1/\sqrt{\text{v}}$.

In the present work we go further on the study of the fluctuations of the global velocity of fluid fronts in forced-flow imbibition. We specifically analyse the dependence on different oil viscosities of the GG-like distributions found, and check the validity of the relation between N_{eff} and asymmetry of the distributions (Ch. 6).

Global avalanches

The response of a system to slow, external driving by exhibiting intermittent, scale-free avalanche dynamics is known as *crackling noise* (Sethna et al., 2001). A wide number of systems show such behaviour. Barkhausen noise due to the motion of magnetic domain walls in ferromagnetic materials was shown to exhibit avalanche dynamics widely distributed in size (Urbach et al., 1995; Colaiori, 2008). Vives et al. (1994) showed the absence of intrinsic scales in the avalanche dynamics of martensitic transformations by measuring their acoustic emission. The evolution of planar crack fronts (Bonamy et al., 2008; Barés et al., 2013) or fracture of disordered materials in 3D (Baró et al., 2013; Kun et al., 2014) also display features associated with crackling noise. Wang et al. (2013) have recently shown that active cargo transport in living cells show burst-like dynamics, resulting in avalanches in the advancement of the molecular motors involved in active vesicular transport along microtubules.

Imbibition fronts also display crackling-noise behaviour. For forced-flow experiments, Planet et al. (2009, 2010, 2011) showed that the spatially-averaged velocity of the front is jerky and displays avalanche-like dynamics. These bursts of fast motion are widely distributed both in sizes S and durations T, and follow a power law with an exponential cutoff. Using the method described in Sec. 1.5.1, the power-law exponent $\alpha = 1.00(15)$ of $P(S)$ and $\tau = 1.25(25)$ of $P(T)$ were found to be independent of the experimental conditions in a range of imposed mean velocities $0.057 < \mathrm{v} < 0.225$ mm/s for silicone oil of dynamic viscosity $\mu = 50$ cP and analysed at large windows of observation ℓ. The joint distribution $P(S,T)$ also displayed a scaling relation $S \sim T^{\gamma}$ with $\gamma = 1.33(12)$ (Planet et al., 2009, 2010). Considering faster experiments, with $0.267 < \mathrm{v} < 0.645$ mm/s, Planet et al. (2011) obtained $\alpha = 0.97(5)$, $\tau = 1.16(10)$, and $\gamma = 1.3(1)$, which are equivalent to their previous results. Contrary to the values of the exponents, the exponential cutoffs of the distributions evolved systematically with v. In all cases, ξ_S and ξ_T diverged as $\mathrm{v} \to 0$. This divergence also suggested the presence of a pinning/depinning transition at $\mathrm{v} = 0$.

It is worth considering that in imaging experiments, as a consequence of observing the system through a finite window of size ℓ, the observed distributions may be strongly distorted by a limited field of view (Chen et al., 2011). Specifically, when the window size is smaller than the characteristic size of the system (in our case the lateral correlation length along the front ℓ_c) windowed data lead to distributions which present a bump before the decay, and with a smaller power-law exponent.

In Ch. 6 (Sec. 6.2) the statistical properties of global avalanches in forced-flow imbibition experiments are analysed. The evolution of the cutoffs has been characterized in detail thanks to the large data sets collected. Moreover, changing the viscosity of the

oils has allowed to reveal the role played by μ and v independently. The effect of the window of observation is also systematically studied.

Shape of averaged global bursts

The average shape of the bursts of fast motion is also an important signature of avalanching systems (Sethna et al., 2001; Papanikolaou et al., 2011). This problem has been vastly studied for Barkhausen noise signals, as reviewed in Secs. 4.7 and 5 of (Colaiori, 2008). Spasojevic et al. (1996) recognized a generic shape of a single Barkhausen noise burst. Kuntz and Sethna (2000) suggested the average burst shape to be universal and to provide a sharper method to check the models against experiments than the common comparison of critical exponents. Mehta et al. (2002) compared experimental data of the average avalanche shape from Barkhausen noise to theoretical predictions from two variants of the nonequilibrium zero-temperature random field Ising model finding differences among them. The universal scaling function of a burst shape was studied theoretically by Baldassarri et al. (2003), where they stated that the statistical information about temporal correlations is contained in the avalanche shape. The asymmetry of the shape observed in Barkhausen noise experiments is explained by Zapperi et al. (2005) and Durin et al. (2007) in terms of inertia, associating an effective mass to the domain wall moving under the action of the external field. Papanikolaou et al. (2011) suggested that all the relevant statistical information can be obtained from the joint two-point time-velocity distribution. In that article they solved exactly two mean-field models (random field Ising and ABBM models (Alessandro et al., 1990)) and compared them to experimental results. The asymmetry found in the shape of the bursts was attributed to distortions of the measuring system. Filtering out this noise they found good agreement between theoretical and experimental results.

Different scaling functions for the average avalanche shape have been proposed. For large classes of stochastic processes, Baldassarri et al. (2003) found that the average shape of avalanches of duration T follows $\langle V(t/T)\rangle = T^{\tilde{\alpha}} f(t/T)$, where $\tilde{\alpha}$ is the wandering exponent of the process. An inverted parabola was derived analytically by Papanikolaou et al. (2011) for the ABBM model in the limit of vanishing drive rate and demagnetizing factor. Very recently Laurson et al. (2013) presented a general scaling form for the average avalanche shapes for non-mean-field systems exhibiting crackling noise, that depends on the universality class of the avalanche dynamics. Let us recall that the size of an avalanche of duration T, $V_\ell(t|T)$, is given by

$$S(T) = \int_0^T V_\ell(t|T)dt, \tag{1.44}$$

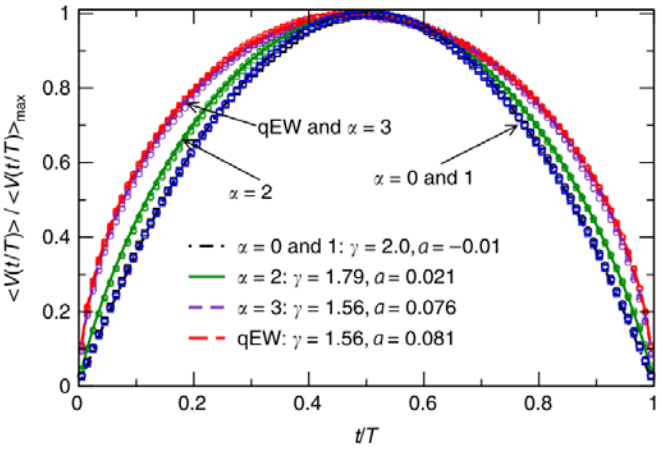

FIGURE 1.13: Average avalanche shapes from interface depinning models for different elastic kernels, ranging from the infinite range model ($\alpha = 0$) to the local quenched Edward Wilkinson equation. Parameters γ and a characterizing the shapes are quoted in the figure. Figure reproduced from Laurson et al. (2013).

and the average size and duration of the bursts scale as $S \sim T^{\gamma}$. Then, the amplitude of the average avalanche shape scales as $\langle V_\ell(t|T)\rangle \sim T^{\gamma-1}$ and, in a general form:

$$\langle V_\ell(t/T)\rangle \sim T^{\gamma-1} f(t/T), \tag{1.45}$$

where time is rescaled by the avalanche duration, and $f(x)$ is the scaling function that defines the average avalanche shape. Laurson et al. (2013) assumed that the average early-time growth of an avalanche is given by a power law of time, $\langle V_\ell(t/T)\rangle \sim t^{\delta}$ for $t \ll T$. The validity of Eq. (1.45) implies $\delta = \gamma - 1$. The last ingredient of the formulation by Laurson et al. (2013) is the inclusion of an asymmetric term in order to allow small temporal asymmetry in the average avalanche shape. The general scaling form proposed then reads:

$$\langle V_\ell(t/T)\rangle \sim T^{\gamma-1} \left[\frac{t}{T}\left(1-\frac{t}{T}\right)\right]^{\gamma-1} \left[1 - a\left(\frac{t}{T}-\frac{1}{2}\right)\right]. \tag{1.46}$$

It depends on two parameters only: the scaling exponent γ relating the average avalanche size of the avalanche S to its duration T, and an asymmetry parameter a that characterizes the temporal asymmetry of the avalanches.

The average avalanche shape (1.46) was verified numerically at the depinning transition of elastic interfaces driven in disordered media (Fig. 1.13), and compared to planar crack front propagation experiments, showing a good agreement (Laurson et al., 2013).

In Ch. 6 (Sec. 6.2.5) the average shape of global avalanches of imbibition fronts is analysed and compared to the proposed scaling function (1.46).

1.5.3 Intermittency

Intermittency is a key concept in hydrodynamic turbulence, associated with the occurrence of bursts of intense motion within more quiescent fluid flow (Frisch, 1996). It leads to strong deviations from Gaussian statistics that become larger and larger when

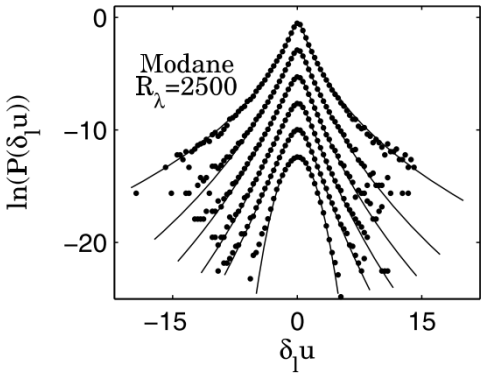

FIGURE 1.14: Evolution through length-scales of the pdfs of longitudinal velocity increments $\Delta v(r)$ from small (top) to large (bottom) scales. Figure reproduced from Chevillard et al. (2012).

considering fluctuations at smaller and smaller scales (Fig. 1.14) (Castaing et al., 1990; Chevillard and Meneveau, 2006).

Intermittency is observed in many dynamical systems. In addition to the studies of hydrodynamic turbulence (Castaing et al., 1990), intermittency has been also observed in systems involving transport by a turbulent flow (Falkovich et al., 2001), in granular systems (Radjai and Roux, 2002), in magneto-hydrodynamic turbulence in geophysics (Michelis and Consolini, 2004), in the solar wind (Alexandrova et al., 2007), in stock-price fluctuations (Kiyono et al., 2006), in seismic series (Manshour et al., 2009), and in plasma turbulence (Milligen et al., 1995; Mier et al., 2008) for instance. In the context of interfacial dynamics, small-scale intermittency was recently observed in gravity-capillary wave turbulence (Falcon et al., 2007, 2010; Deike et al., 2011). Lagrangian velocities of porous media flows were shown to exhibit also persistent intermittent properties in numerical simulations by de Anna et al. (2013).

While coherent structures such as strong vortices are known to be responsible for those deviations in hydrodynamic turbulence (Batchelor and Townsend, 1949), most of the systems enumerated strongly differ from high Reynolds number hydrodynamic turbulence. In theses cases understanding the physical mechanism of intermittency remains a challenge. Falcon et al. (2007) and Falcon et al. (2010) suggested that a more general explanation of intermittency could be related to the properties of the fluctuations of the energy flux that are shared by different systems displaying an energy cascade.

Quantifying intermittency

The principal contributions to the analysis of intermittent signals arise from research in the field of hydrodynamic turbulence. The pioneering work of Frisch and Parisi (1985) introduced a multi-scale description of the irregular nature of longitudinal velocity data $v(t)$ in fully developed turbulence (Frisch, 1996, and references therein). In particular, they studied the fluctuations of the jerky signal $v(t)$ by means of the increments of velocity $\Delta v(\tau) = v(t_0+\tau) - v(t_0)$ at time t_0 as a function of time lag τ. To characterize the

non-local behaviour of these singular fluctuations they introduced the p-order structure functions:

$$\mathcal{S}_p(\tau) = \langle |\Delta v(\tau)|^p \rangle, \tag{1.47}$$

where $\langle \cdots \rangle$ is the average over t, and studied their power-law behaviour at short time lag τ

$$\mathcal{S}_p(\tau) \sim \tau^{\xi_p}. \tag{1.48}$$

The exponents ξ_p scale linearly with p when the fluctuations are homogeneous at all scales. On the contrary, the non-linear dependence of ξ_p on p corresponds to non-homogeneous fluctuations, and it is a hallmark of intermittency (Frisch, 1996; Falcon et al., 2010a).

Castaing et al. (1990) proposed another approach to the problem in their seminal work. They analysed the probability density distributions of velocity differences between two points separated a distance r, $\Delta v(r)$, and developed a new model for the shape of the pdf. That model depends on two parameters only that describe the intermittent properties of the flow, and can be extracted directly from the fitting of this pdf to the experimental data.

Relevant information to characterize intermittency can be also obtained from the analysis of the moments of the distribution of velocity increments $\Delta v(\tau)$ (Frisch, 1996; Chevillard et al., 2012). Specifically, the flatness (or peakedness) of the pdfs, that measures the relative importance of the tails, gives information about the intensity of the intermittent character of the signal. It is measured by the kurtosis of $P(\Delta v(\tau))$:

$$K \equiv \frac{E\left(x - \langle x \rangle\right)^4}{\sigma^4}, \tag{1.49}$$

where $E\left(x - \langle x \rangle\right)^n$ is the n-th central moment of the distribution of x (Δv in this case), and σ the standard deviation. For a Gaussian distribution $K_G = 3$ while $K > K_G$ for pdfs with large tails.

The distributions of increments of the signal may also display some asymmetry, $Sk \neq 0$. Such asymmetry is quantified by computing the skewness of the pdfs as

$$Sk \equiv \frac{E\left(x - \langle x \rangle\right)^3}{\sigma^3}. \tag{1.50}$$

In fully developed turbulence the asymmetry of the pdfs is a associated to the flux of energy across different scales (Castaing et al., 1990; Frisch, 1996; Arnéodo et al., 2008). In 3D Sk is found to be negative while in 2D turbulence, where an *inverse-cascade* is observed, the asymmetry of the distributions is positive (Boffetta and Ecke, 2012).

Chapter 2

Experimental setup, protocol, and preliminary data analysis

A similar experimental system as the one used during this Thesis was first designed and used by Soriano (2003). It was motivated by the first experiments on imbibition in porous media (Rubio et al., 1989; Horvath et al., 1991; He et al., 1992; Dougherty and Carle, 1998) and theories (Kardar et al., 1986; Krug, 1997; Ramasco et al., 2000) for kinetic roughening of driving interfaces in disordered media.

That setup was initially used to study the morphology of the fronts, i.e. the kinetic roughening process that develops when an interface is set in motion through a disordered medium. The acquisition of a fast camera allowed to perform studies of the dynamics of those fronts. Specifically, the dynamics of the oil-air interfaces in the statistically stationary regime was studied by Planet (2009) for a number of experimental conditions.

Thanks to the potential of the setup, we have been able to improve and introduce new features to the experimental system: a better control of the inclination system, and a new support of the acquisition system. These features have opened a way to perform new kinds of analysis such as a systematic study of the effect of an effective gravity against the evolution of fronts in capillary rise, or the improvement of the spatial and temporal resolutions in kinetic roughening experiments. In addition, different fluids have been used to explore a wider range of experimental conditions.

In this chapter we present the experimental setup in detail. We first summarize the setup configurations used in this Thesis. Then, the models of disordered medium, the fluids, the driving protocols, and the image acquisition system used are described. The methods of analysis of the images recorded are reported as well as the preliminary data treatment. Finally, the experimental protocol is described.

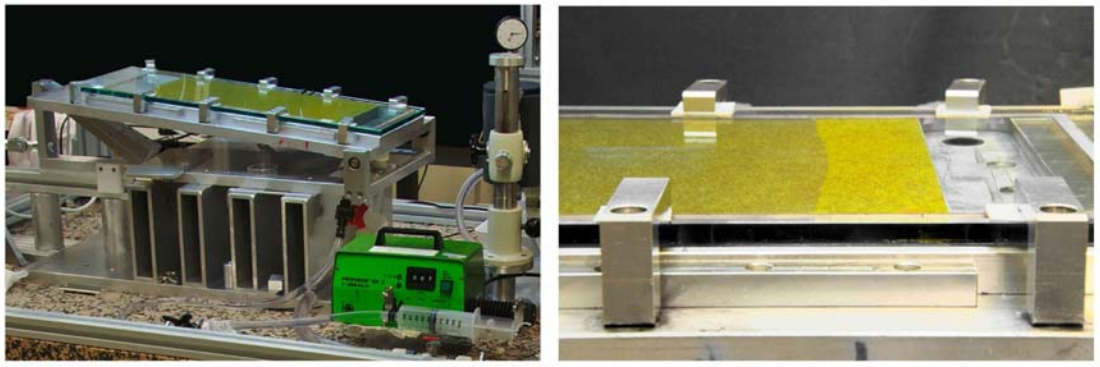

FIGURE 2.1: Pictures of the experimental setup. Left: overview of the cell connected to the syringe pump used for forced-flow experiments. Right: close-up picture of the advancement of the fluid front from the inlet on the right.

2.1 Overview of the setup configurations used

In the present work we study the evolution of a fluid front through a disordered medium. In particular, our experiments emulate the invasion of an open fracture of controlled, variable aperture by a wetting, viscous fluid. The experimental setup, shown in Fig. 2.1, consists of a Hele-Shaw (HS) cell made of two parallel plates separated by a narrow gap spacing. The specific aperture of the cell is controlled by fiber-glass plates with controlled disorder (Sec. 2.2). The fluid (Sec. 2.3) is driven through the system displacing the air initially present at either constant pressure difference between the inlet and the outlet of the HS cell or constant flow rate (Sec. 2.4). We record the advancement of the front from the top with one of the two different cameras described in Sec. 2.5. The preliminary analysis of the fronts is detailed in Sec. 2.6. In addition, the HS cell and the acquisition system can be tilted in order to introduce an effective gravity affecting the front propagation.

All the different setup configurations used in this Thesis are listed in Table 2.3 at the end of this chapter, which provides details on the model disordered medium, flow control protocols, acquisition system, and methods of analysis used for each type of experiment.

A sketch of the whole experimental setup is shown in Fig. 2.2. The different parts that will be described in the following sections are shown. The acquisition system **A** represented in the top panel, uses the *Slow cameras* (Sec. 2.5). The two cameras in sequential order are pointing towards the HS cell. In the bottom panel, the *Fast camera* is shown. Indirect lighting on the cell is used in all the experiments to avoid undesired reflections on the top glass plate of the cell, and to achieve a good contrast between the oil and air phases. To this end, a white reflecting plate is placed at the level of the camera lens. Up to four LED units are used to light up the white plate which indirectly illuminates the cell. The system used to control the fluid flow is also represented (**B**).

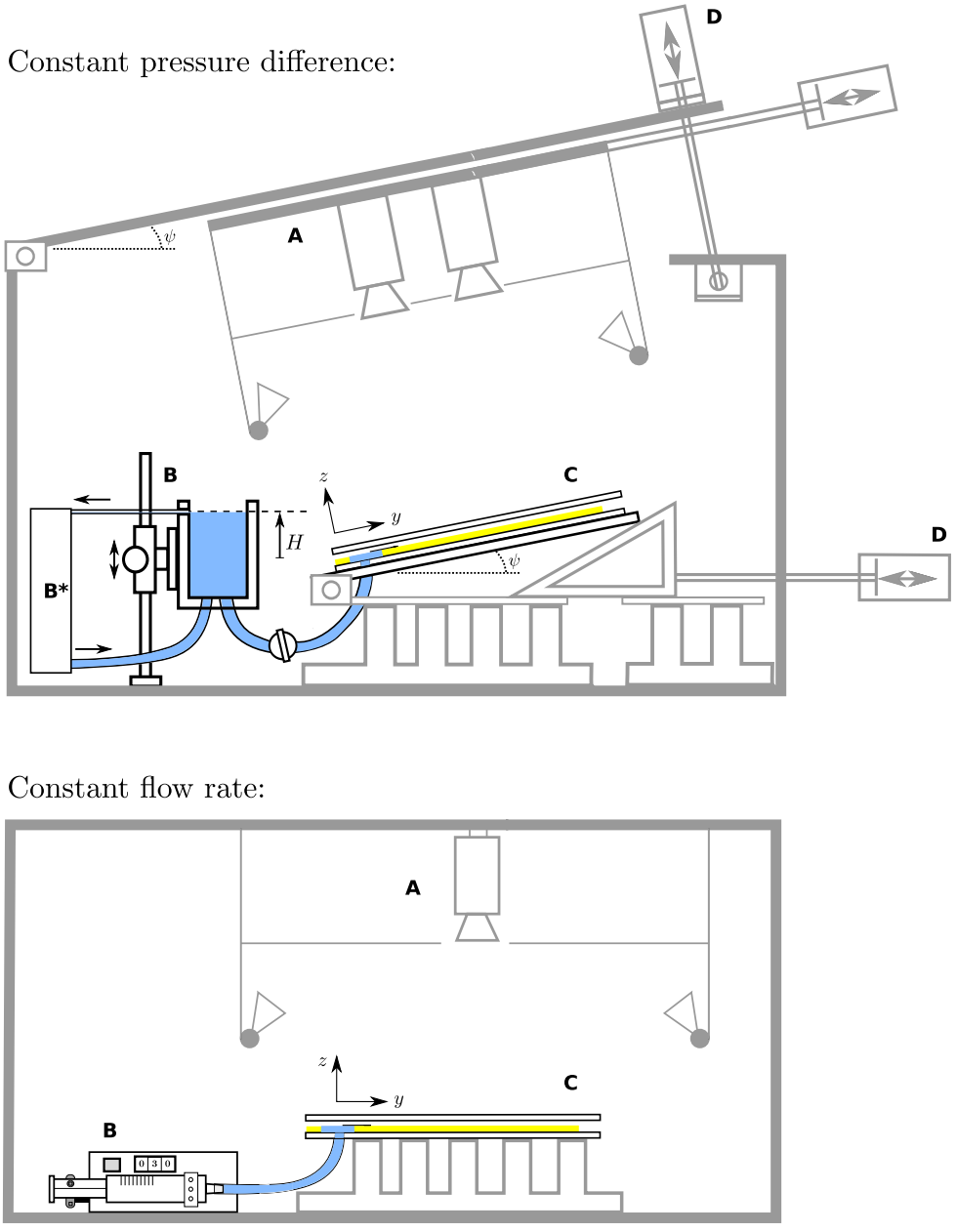

FIGURE 2.2: Sketches of the experimental setup. **A** corresponds to the acquisition system, **B** to the driving system, **C** to the Hele-Shaw cell, and **D** to the inclination system. In the constant pressure difference configuration shown in the top panel, two cameras in sequential order (**A**) record the evolution of the front through the HS cell (**C**). The constant pressure difference between the inlet and the outlet of the cell is achieved by means of the reservoir (**B**) connected to the Hele-Shaw cell (**C**) and to the recirculating system (**B***). The cell and the acquisition system can be tilted an angle ψ by using two motors (**D**). In the constant flow rate configuration shown in the bottom panel, the fast camera (**A**) records the advancement of the interface. The syringe pump (**B**) injects oil into the cell (**C**) at constant Q. In both cases the Hele-Shaw cell (**C**) is illuminated by indirect lighting (LEDs pointing up towards a white reflecting plate).

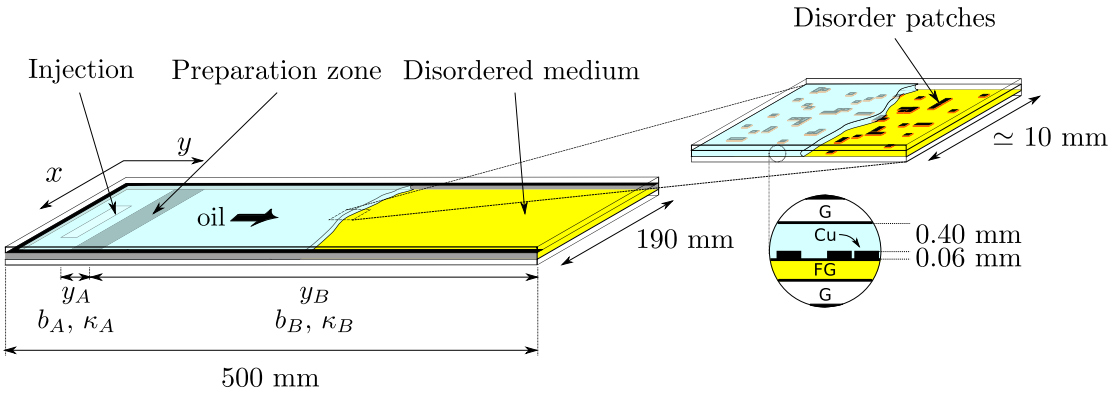

FIGURE 2.3: Sketch of the model disordered medium used. The right end of the cell is open to air. The oil penetrates from the injection region, fills the preparation zone (A) and invades the porous medium model (B) displacing the resident fluid (air) that remains at atmospheric pressure. y_A and y_B denote the extension of each region in the streamwise direction. b_A and b_B are the corresponding gap spacings, and κ_A and κ_B the corresponding permeabilities. The zoomed region shows the disorder patches and their orientation with respect to the fluid front for a D or D* cell (in the latter disorder patches would be larger). The lateral zoom is a view of the disordered HS cell showing the parallel glass plates (G) and the fiberglass substrate (FG) with the copper obstacles (Cu).

Specifically, in the top panel the constant pressure device is depicted. The height of the oil reservoir can be tuned, thus varying the distance from the inlet to the free surface of the liquid H, and so the applied ΔP. To keep the level of the oil constant, the reservoir is connected to a recirculating system (**B***). The reservoir is also connected to the Hele-Shaw cell. In the bottom panel, the forced flow driving system is shown. In this case, a syringe pump is used to inject the fluid into the cell at constant flow rate. Finally, **C** corresponds to the model of disordered medium. The HS cell is schematically represented with the two parallel plates (white) and the fiberglass substrate (yellow). The HS cell and the acquisition system can be tilted an angle ψ by means of the inclination system **D**, as shown in the top panel of the figure.

2.2 Models of disordered media

The models of disordered media used in this Thesis mimic an open fracture. They consist of Hele-Shaw cells of 205 × 555 mm^2 –width × length–, made of two parallel plates separated by a narrow gap spacing. The top plate is a 10 mm-thick piece of glass while for the bottom plate either a 15 mm-thick glass plate or a 15 mm-thick steel plate have been used. A sketch is shown in Fig. 2.3.

A fiberglass substrate is attached to the bottom plate and determines the type of disordered medium used. Throughout this work we have studied two kinds of disorder. The first one is a smooth cell of constant gap thickness $b = 0.46$ mm. We call this

Plate	y_A (mm)	b_A (mm)	κ_A (mm^2)	y_B (mm)	b_B (mm)	κ_B (mm^2)
S	20	0.40	0.0133	420	0.46	0.0176
D	0-20	0.40	0.0133	410	0.439*	0.0146
D*	10	0.40	0.0133	420	0.439*	0.0146

TABLE 2.1: Nominal or measured values of lengths (y), gap spacings (b), and permeabilities (κ) of the preparation zone (A) and the model region (B) for the different cells used. **Spatially averaged value of the gap thickness in region B.*

cell S, for smooth. The second one, D or D* for disordered, is a cell with a dichotomic gap spacing randomly distributed in space. The spatial fluctuations in gap thickness are provided by copper patches of size 1.50×1.50 mm^2 –for D*– or of 0.4×0.4 mm^2 –for D– and height $\Delta b = 0.06$ mm, randomly distributed over the fiberglass substrate. Both in D and D* plates the copper patches fill 35% of the total area. The patches do not overlap, and they are oriented parallel to the boundaries of the cell as shown in the zoom of Fig. 2.3. In this cell the gap thickness takes two different values, $b = 0.46$ mm and $b - \Delta b = 0.40$ mm, causing fluctuations of the capillary pressure along the imbibing front. These cells mimic a very simple open fracture that features a two-dimensional non-zero aperture field of either constant (S) or variable aperture (D and D*) distributed along a plane (Adler and Thovert, 1999).

Typically the fiberglass substrate attached to the bottom plate has a preparation zone –A– between the liquid inlet and the measurement region –B–, as shown in Fig. 2.3. The cell in this zone has constant gap thickness $b_A = 0.40$ mm. The streamwise extension y_A of this zone is given in Table 2.1, as well as other nominal values of the cell properties. The preparation zone is intended to have a reproducible initial condition: a plane fluid front in the spanwise direction.

All plates have a copper frame around their perimeter, of the same height as the disorder patches and 8 mm width. On top of this frame a PVC frame of precise thickness is placed to close hermetically the cell during the experiments.

Plate manufacturing. The technique used to obtain the fiberglass plates is the one used for printed circuit boards. This allows a high control of the disorder. The program `PlatesDesign` –see appendix A in (Soriano, 2003)– has been used for the design of the plates D and D^*. It randomly distributes disorder patches of the chosen lateral size –0.40 mm (D) or 1.50 mm (D*)– over a square matrix until the occupation fraction imposed is reached. The patches are allowed to connect only to the four nearest neighbours –SQ disorder type in (Soriano, 2003). The designs are sent to *Circuitos Impresos 2CI, SL*[1] for production. Due to the fabrication process the actual size of the non-adjacent disorder

[1] http://www.2cisa.com/

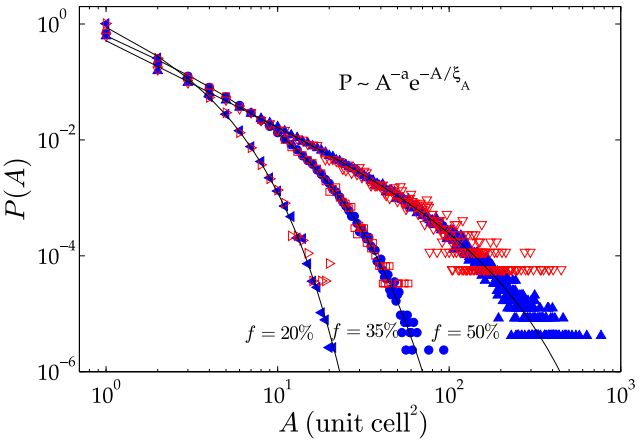

FIGURE 2.4: Distribution of sizes of the islands of disorder patches numerically generated (8 for each configuration) in D (solid symbols) and D^* (empty symbols) plates. Different occupation fractions f are shown. Solid lines correspond to fits of the form displayed. Figure reproduced from Planet (2009).

patches is slightly smaller –about 10 %, see (Soriano et al., 2002; Soriano, 2003). We oxidised the plates to avoid contrast problems arising from the brightness of the copper islands compared to the fiberglass background. The protocol is as follows: 1) the brand new plate is covered with a layer of *Green patina aging solution*[2] during 10 minutes, 2) the plate is dried with paper and left uncovered during 5 minutes, 3) the remainders of the oxidiser are removed by applying distilled water for several minutes and drying with paper towels, 4) finally the plate is covered with silicone oil to definitely stop the oxidation. If the result is not perfectly satisfactory at the end of 3), one may repeat steps 1) and 2) or just 2) for shorter times.

Characterization of the disorder. The disorder used is uncorrelated both in x and y above the characteristic size of the patches. The distribution of sizes of the disorder islands is shown in Fig. 2.4 for different occupation fractions. All of them are distributed following a power-law with exponential cutoff, $P \sim A^{-a}e^{-A/\xi_A}$. The value of the cutoff of the sizes is larger as the fraction of patches increases. For the occupation ratio f used in this Thesis –35 %– the distribution only displays the exponential decay, with a characteristic truncation scale $\xi_A = 8.4 \pm 0.1$ unit cells $= 1.34 \pm 0.16$ mm^2 (Planet, 2009)[3].

Actual porous media and HS models are characterized by their (effective) permeability κ. According to Darcy's law the gap-averaged –two component– fluid velocity is related to the pressure gradient in the medium by $\vec{v} = -(\kappa/\mu)\vec{\nabla}p$, where μ is the dynamic viscosity of the fluid –as shown in Sec. 1.1.2. In smooth HS cells, averaging the Poiseuille profile across the gap of the cell results in $\kappa = b^2/12$. In disordered media κ

[2]Oxidiser used in art works or restoration. Brand: *Modern Masters*. Bought at Gomara (crossing of C/ Xuclà and C/ Elisabets, Barcelona). Also available at: http://shop.modernmasters.com/.

[3]For $f = 0.20$, $\xi_A = 2.1 \pm 0.1$ unit cells; for $f = 0.50$, $\xi_A = 103 \pm 10$ unit cells. The exponents are $a = 0.96 \pm 0.16, 1.22 \pm 0.14, 1.46 \pm 0.10$ for $f = 0.20, 0.35, 0.50$, respectively (Planet, 2009).

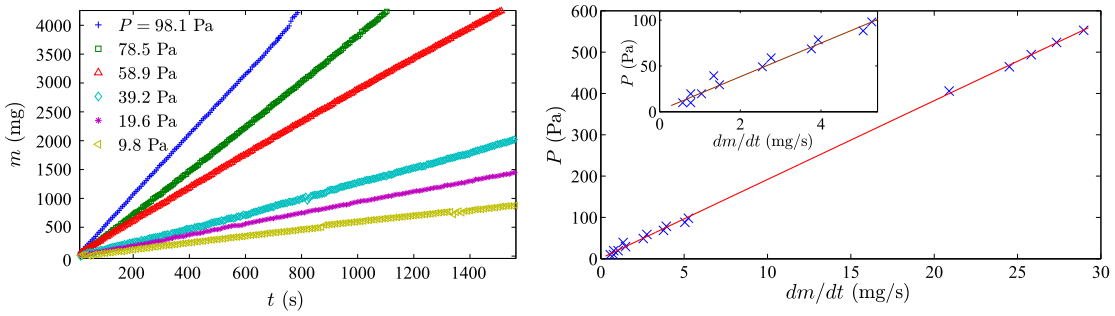

FIGURE 2.5: Left panel: mass of fluid collected at the outlet of the disordered HS cell as a function of time for several imposed pressure differences. Right panel: imposed pressure difference P vs mass flow rate in the D* cell. The solid line is a least-squares linear fit of slope 18.36 Pa·s/mg. Inset: zoom of the main plot in the range of pressures used in the capillary rise experiments –discussed in Chapter 3.

can be obtained empirically using Darcy's law. The values of the permeabilities of the S, D and D*-cells are given in Table 2.1. $\kappa_A = b^2/12$ applies to the preparation zone and κ_B to the disordered medium model. For the S plate $\kappa_B = b^2/12$ also, while for the D and D* plates κ_B has been measured independently.

Measurement of the permeability. To measure the permeability of the disordered HS cell (D*) we have carried out fluid displacements under constant applied pressure. It corresponds to the configuration represented in the top panel of Fig. 2.2, with $\psi = 0°$ – horizontal cell. For every applied pressure P we have measured the flow rate of a silicone oil of kinematic viscosity $\nu = \mu/\rho = 50$ mm^2/s through the cell. To this purpose we have let the oil flow through the entire cell and collected it in a container placed at the outlet, standing on top of an electronic balance. This setup allows to measure the mass of oil flowing through the cell per unit time. We have taken measurements for several pressure differences between 9.8 and 551.8 Pa. The results for the range of pressures $9.8 - 98.1$ Pa used in the capillary rise experiments are shown in the left panel of Fig. 2.5.

From Darcy's law, the applied pressure is related to the mass flow rate at the outlet by

$$P = -\frac{\mu}{\rho A}\left(\frac{1}{\kappa_A}\frac{b_B}{b_A}y_A + \frac{1}{\kappa_B}y_B\right)\frac{dm}{dt}\,, \tag{2.1}$$

where A is the cross-sectional area of the channel. It is important to point out that the geometric factor b_B/b_A, arising from volume conservation of oil, allows to express the pressure drop in region A as a function of the mass flow rate in region B.

The $m(t)$ curves are linear, as predicted by Eq. (2.1) for fixed P. From the slopes of these curves we obtain the plot of P vs dm/dt shown in the right panel of Fig. 2.5. The experimental points are well fitted by a straight line of slope 18.36 Pa·s/mg, from

Oil	ρ (kg/m^3)	ν (mm^2/s)	γ (mN/m)
Rhodorsil 47V 10	959	10	20.1
Rhodorsil 47V 50	965	50	20.7
Calsil Fluido 47V 100	965	100	20.9
Mixture (42 % R.47V 10, 58 % R.47V 500)	965*	169*	20.9*
Calsil Fluido 47V 350	970	350	21.0

TABLE 2.2: Nominal values of the density ρ, kinematic viscosity ν, and oil-air surface tension γ at 25 °C of the silicone oils used. *Estimated or measured values.

which a value $\kappa_B = 0.0146$ mm^2 is finally obtained using Eq. (2.1). This value is sensibly different from $b_B^2/12$ ($= 0.0161$ mm^2).

Inclination of the system. We can introduce an effective gravity by tilting the cell an angle ψ. It will oppose the front advancement when $\psi > 0$ and favour it when $\psi < 0$. The possibility to tilt the cell was originally introduced by Planet (2009). In the course of the present work the inclination system has been improved and automatized. The supports of cell and image acquisition system –cameras and illumination– have been replaced by a new aluminium structure from Phoenix Mecano Company. A programmable motor connected to a wedge allows to control the inclination of the cell with a precision of 0.1°. A second motor is responsible for the inclination of the recording system as shown in the top panel of Fig. 2.2. In both cases, the motors are RK Rose+Keiger with RK MultiControl Duo as controllers. This new structure allows us to tilt the whole setup from negative angles –cell tilted in the direction of propagation of the fluid– to large positive angles by reprogramming the motor or using modified wedges. Finally, a third motor has been introduced to control the linear displacement of the recording system along the y direction of the cell. Motor and controller are also manufactured by RK Rose+Keiger.

2.3 Fluids

In this Thesis we have studied the two-phase flow displacements of different silicone oils through the system described above. For the first time, oils of different viscosities have been used in this system. The fluids are silicone oils of dynamic viscosities $\mu \simeq 10$ cP (Rhodorsil 47V 10), $\mu \simeq 50$ cP (Rhodorsil 47V 50), $\mu \simeq 100$ cP (Calsil Fluido 47V 100), and $\mu \simeq 350$ cP (Calsil Fluido 47V 350). An oil with dynamic viscosity $\mu \simeq 170$ cP was also obtained by mixing 42 % of Rhodorsil 47V 10 and 58 % of Rhodorsil 47V 500. The density of these silicone oils is close to 1000 kg/m^3, an their oil-air surface tension ranges between 20 and 21 mN/m. The nominal values are quoted in Table 2.2.

Oil properties depend on temperature. Our HS cell is not equipped with a thermal bath, but the temperature of the room is kept at a controlled temperature: 23±3 °C. Temperature fluctuations in this range imply variations in oil temperature of up to 2 °C, which do not affect perceptibly experiments performed at otherwise identical conditions.

The equilibrium contact angle θ_E of the oil-air-surface contact line is zero or practically zero for the three types of surfaces that the oil is in contact with: glass, fiber-glass, and copper (Soriano, 2003). Nevertheless, to ensure perfect wetting the cell is prewetted with a very thin layer of oil before each experiment. The effect of a dry surface is specially noticeable for S cells: small impurities in wetting properties may strongly affect the front, specially at low velocities.

Concerning the dynamics it is known that the contact angle at a moving contact line depends on its velocity (Joanny and de Gennes, 1984; de Gennes et al., 2004). In this Thesis, the effect of contact angle variations on the temporal evolution of the mean position of the front has been studied for spontaneous imbibition with S and D cells –see Chapter 3. In general, though, since maximum variations in velocity occur because of gap thickness variations, fluctuations of contact angle have been considered included in the capillary disorder.

2.4 Driving protocol

The oil can penetrate the cell in different controlled ways. Imbibition phenomena have been classified in two main groups: spontaneous and forced-flow –see Sec. 1.1.2. In this Thesis we have explored both drivings conditions. In the following, these two driving systems are explained in detail. We have also designed a pressure-controlled perturbation system which is described in appendix C.

Constant pressure difference

This configuration allows us to perform spontaneous imbibition experiments. In spontaneous imbibition the injection of fluid through the cell takes place under a constant pressure difference between inlet and outlet, $\Delta P = \text{ct}$.

A sketch of the setup is shown in the top panel of Fig. 2.2. The constant-pressure device consists of a large oil reservoir that can be displaced vertically with ±0.5 mm resolution. The height of the fluid in this reservoir is kept constant by means of a recirculation system that continuously injects oil into the reservoir and recovers the oil overflowing from the outlet in the top part of the reservoir. The level of oil in the reservoir is at height H from the entrance of the cell, connected to the bottom reservoir by a plastic tubing of large cross-section.

The height difference between the oil level in the reservoir and the entrance of the cell H causes a pressure difference $\Delta P \simeq \rho g H$ between the inlet and the outlet (at atmospheric pressure). Tiny viscous losses due to the fluid flow through the tube (22 mm diameter) connecting the reservoir and the cell can be neglected. The recirculating system does not cause appreciable fluctuations in pressure at the cell inlet (Planet, 2009).

Constant flow rate

In forced-flow imbibition experiments we impose a constant flow rate of fluid through the cell, $Q = \text{ct}$. A sketch of the setup is shown in the bottom panel of Fig. 2.2. To do so, we use a B. Braun syringe pump with a syringe of 100 ml volume and 35 mm diameter. The range of flow rates explored approximately corresponds to mean front velocities from 0.04 to 0.6 mm/s –for the D cell– that can be imposed with precision of 0.005 mm/s.

The mechanical fluctuations of the pump were shown not to produce appreciable fluctuations in the mean front velocity for imposed velocities larger than 0.05 mm/s (Planet, 2009). However, the slower the fluid is pushed into the cell, the easier is to observe such perturbations. Thus, for the slowest velocity explored in the present Thesis, v = 0.036 mm/s, we introduced a damping mechanism between the syringe pump and the cell. The mechanism consists of a small elastic cavity –a balloon– connected to the tube that goes from the pump to the inlet of the disordered system.

2.5 Image acquisition systems

The advancing of the front through the medium is recorded from the top. LED indirect lighting is used to have a high contrast between the cell filled with oil and the air region in the images –see Sec. 2.6 below. Two different types of camera have been used for video recording. In both cases the images obtained are in grey scale of 8 bits.

Slow cameras

In this configuration, the motion of the oil-air front is recorded using two CCD cameras in sequential order. The cameras, JAI CV-M10BX, are equipped with a motorized lens system Computar M10Z1118MP of focal length ranging from 11 to 110 mm and aperture 1:1.9. Diaphragm, focal length, and focus are electronically controlled.

A video grabber PCVision JAI M10 is used to record the images. The acquired images have 574×768 square pixels ($x \times y$). Placing the cameras at the positions used for the experiments reported in Chapter 3, the typical resolution is $r = 0.36$ mm/pixel

–the actual resolution is measured for each experiment and may vary slightly. The maximum acquisition rate is 5 fps (frames per second).

A software CAMERAS, designed by Soriano (2003), allows us to control the cameras and record the images to the computer. The program can record images at constant time delay between frames, or at logarithmically increasing time delays. The latter option is specially convenient for studying the morphology of growing interfaces, or for spontaneous imbibition experiments in which the mean velocity at the beginning of the invasion process is much larger than at the end.

Fast camera

To record images at higher spatial and temporal resolution we use a Redlake MotionPro X3 camera. It is equipped with a CMOS sensor of 1280×1024 square pixels, and can take images up to 1000 fps at maximum resolution. The camera has 4 GB of internal memory. This implies a compromise between temporal and spatial resolutions, and duration of the experiment. The lens used is a Nikkor AF 50 mm of maximum aperture 1.4.

This camera has been used at different heights from the cell, giving rise to different spatial resolutions. Typical resolutions range from 0.10 mm/px to 0.20 mm/px –see Table 2.3 for details.

The camera is controlled with the IDT Motion Studio to perform experiments at constant frame rate. The program `CameraAcquisition.m` has been developed to control the camera via MATLAB required for experiments at varying frame rates –see appendix B. It allows, for example, to acquire images at logarithmically increasing time delays.

2.6 Methods of analysis

We are interested in the spatio-temporal evolution of the oil-air interfaces. Thus, from the recorded images we have to extract the fronts $h(x,t)$. Two different edge-detection methods have been used. In both cases a background image is recorded before the starting of the experiment. This background is subtracted from all the images to get rid of lighting inhomogeneities, undesired reflections from the top glass plate or the disorder patches, and the disorder pattern. These new subtracted images are then binarized so that the oil phase is white –or black– and vice versa for the air phase. See Fig. 2.6.

`Subpixel`

This program, developed by Soriano (2003), extracts the interfaces by following the front from one end of the interface to the other. It explores the images from the air

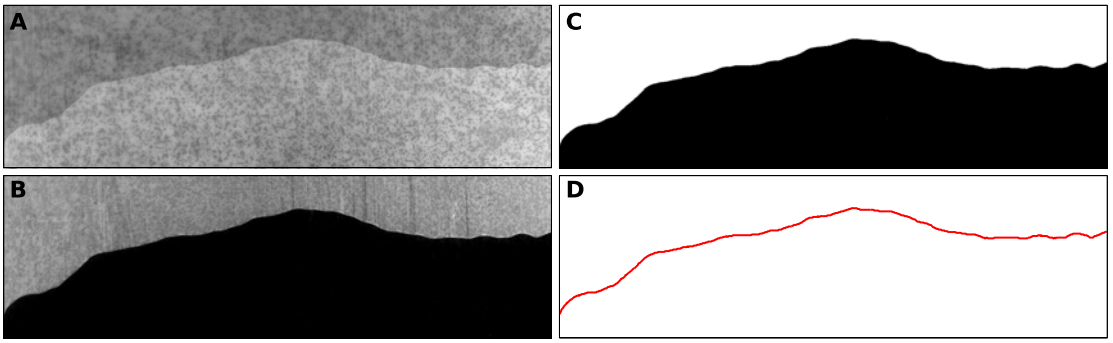

FIGURE 2.6: Example of the process to extract the front $h(x)$ from an image taken using the fast camera. **A**: original image (136×40 mm). **B**: image **A** with the background subtracted. **C**: binarized image. **D**: front extracted.

region –white, for instance– towards the oil region –black. Once it finds a black pixel, the algorithm leaves it on the right, turns counter-clockwise, and advances following the black edge towards the next pixel, and so on and so forth until it reaches the other end of the front.

The fronts extracted that way may have overhangs, or multivaluations. In such cases, overhangs are eliminated by taking the highest value of $h(x)$.

`Interfaces_wt`

To obtain the front position $h(x)$ this script –see appendix B for details– does not follow directly the front. Instead, for each image, it explores all x from the position $h(x) = 0$. There the image is black (or white). Advancing along the given x, the front will be found at the point $h(x)$ where the image changes to white (black). This procedure assumes no overhangs in the front so that $h(x)$ is single-valued for all x.

Data treatment

The profiles $h(x,t)$ obtained from the experimental images are the object of our study. We perform two kinds of analysis on these data: morphological and dynamical studies.

Morphology. We extract the statistical width of the fronts w as a function of the window of observation of lateral size ℓ and as a function of time. $w(\ell,t)$ for a region of lateral size ℓ at time t is given by:

$$w(\ell,t) = \left\langle \frac{1}{N}\sum_{i=1}^{N} h^2(x_i,t) - \left(\frac{1}{N}\sum_{i=1}^{N} h(x_i,t)\right)^2 \right\rangle_j^{1/2}, \tag{2.2}$$

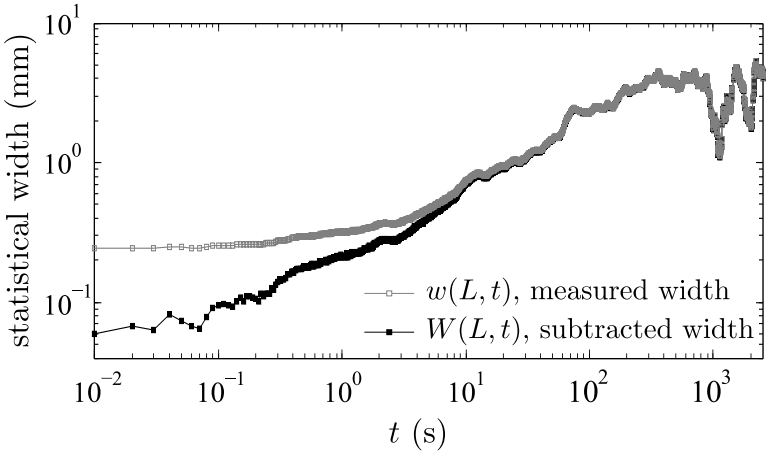

FIGURE 2.7: Effect of the intrinsic width on the statistical width of the fluctuations of the front.

where $N = \ell/\delta\ell$, with $\delta\ell$ the sampling interval, and $\langle\cdots\rangle_j$ is the average over the $j = L/\ell$ windows of size ℓ along the whole front of size L. $\delta\ell$ is equal to the spatial resolution r if no interpolation has been applied to the interface, or larger otherwise.

To avoid artefacts caused by the boundaries of the cell during the propagation of the fluid we consider a corrected interface, in which the *general trend* introduced by the boundaries is subtracted. In the case of our cell, the boundaries pull the fluid because the oil tends to advance along the side walls. This effect becomes more important at low velocities.

In morphological studies, we record the full evolution of the front from an initially flat interface until the statistically stationary regime of constant width. Although we can obtain reasonably flat initial interfaces at $t = 0$, they always have an intrinsic width $w_i = w(\ell, 0)$. This instrinsic width adds to $w(\ell, t)$ all along the experiment. At small times, when $w(\ell, t)$ is comparable to w_i, it strongly affects the behaviour of the front width making impossible to observe the growth at small time scales. To overcome this problem we shall consider the subtracted width, W, defined from:

$$W^2(\ell, t) = w^2(\ell, t) - w_i^2. \tag{2.3}$$

This is a common procedure used in the study of the roughening of growing interfaces (Jeffries et al., 1996; Tripathy and van Saarloos, 2000). A comparison between the width of the front and the subtracted width is shown in Fig. 2.7.

Another useful characterization of kinetic roughening is based on the behaviour of the Fourier power spectrum of the invading fronts. To compute the power spectra, we need to force periodic boundary conditions for each interface by subtracting the straight line that connects its two ends. This is a common procedure to avoid an artificial exponent -2 that appears in the power spectrum $S(q, t) \sim q^{\alpha_s}$ for large wavevectors q (Schmittbuhl et al., 1995).

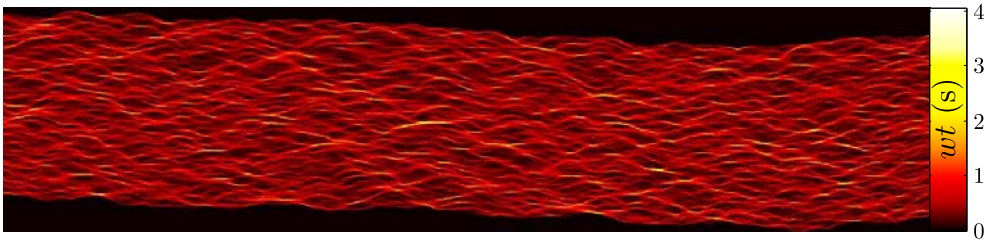

FIGURE 2.8: Typical waiting time matrix. The acquisition rate was 100 fps. Only 2 % of the elements of wt lasted less than 0.1 s (10 δt). The colour bar shows the waiting times in seconds. The value 0 (black) corresponds to regions not explored by the front. The image size is 136×31 mm^2.

Dynamics. To study the dynamics of the invading front, we construct a *waiting time matrix*, $wt(x, y)$, by computing the amount of time spent by the interface $h(x, t)$ at each position (x, y) of the ROI (image recorded). This method was developed by Måløy et al. (2006) to study the propagation of an interfacial crack along a heterogeneous weak plane.

In order to obtain $wt(x, y)$ we first assign to each recorded image a *front matrix* $F(x, y)$ of the size of the ROI. Each element of F is zero except the elements $(x, y = h(x, t))$ corresponding to the position of the front, where $F(x, y) = 1$. An example of a front matrix is shown in panel **D** of Fig. 2.6. The white region corresponds to $F = 0$, and the red line –the front– to $F = 1$. The waiting time matrix is then generated by adding up all the front matrices corresponding to one experiment:

$$wt(x, y) = \sum_t F(x, y). \tag{2.4}$$

An example of a waiting time matrix is presented in Fig. 2.8.

The *local velocity map* is now straightforwardly obtained by computing

$$v(x, y) = \frac{r}{wt(x, y) \cdot \delta t}, \tag{2.5}$$

where r is the spatial resolution of the recorded images and δt the time lapse between images.

To apply this method of analysis the waiting time matrix is required not to have any hole, that is, a zero value. A hole in wt means that we have not been fast enough to record the interface passing through that point. As a consequence, we cannot obtain the local velocity there. This constraint determines the minimum frame rate required.

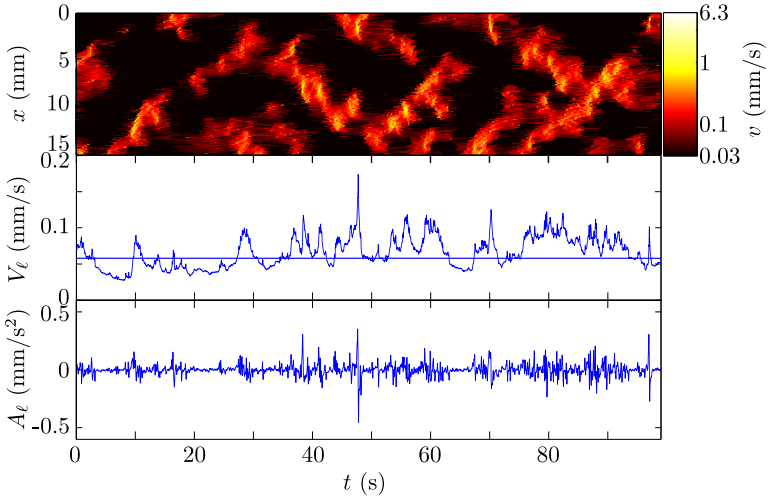

FIGURE 2.9: Top: Typical activity map, $v(x,t)$, observed on a scale $\ell = L/8$. Middle: Global velocity, $V_\ell(t)$, computed from the activity map. The horizontal line is the mean velocity on the activity map. Bottom: Corresponding time-derivative, $A_\ell(t)$.

The uncertainty in the values of the waiting time matrix is $\delta wt = \pm 1$. The propagation of this uncertainty to the values of the local velocity is then

$$\delta v = \frac{r}{\delta t}\left|\frac{-1}{wt^2}\right|\delta wt \quad \Longrightarrow \quad \frac{\delta v}{v} = \frac{1}{wt}, \tag{2.6}$$

where Eq. (2.5) has been used. Then, each element of the waiting time matrix equal or smaller than 10 introduces a 10 % error or more in the local velocity $v(x,y)$. Therefore, the higher the acquisition rate, the smaller the uncertainty in determining $v(x,y)$. However, since our fast camera has a given available memory, a compromise must be reached between temporal resolution, spatial resolution, and duration of the experiment.

It is important to notice that we have to discard some of the first (and last) interfaces recorded. Specifically, all the interfaces that share one point in common with the first (last) interface have to be removed, since information regarding the waiting time might be incomplete.

Another useful representation of the local velocities is the spatio-temporal or *activity map* $v(x,t)$. It is computed from the local velocity map $v(x,y)$ and the temporal information from the interfaces $y = h(x,t)$. Then, the *spatially-averaged (global) velocity* at scale ℓ is directly computed from:

$$V_\ell(t) = \frac{1}{\ell}\int_\ell v(x,t)dx. \tag{2.7}$$

An example of the portion of size ℓ of an activity map, its spatially-averaged velocity $V_\ell(t)$, and the corresponding acceleration $A_\ell(t)$ is shown in Fig. 2.9.

This scheme summarizes the procedure for preliminary treatment of the data, in studies of spatio-temporal dynamics:

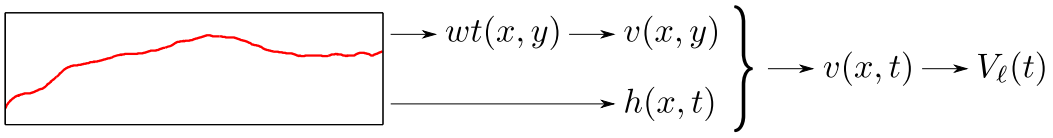

2.7 Experimental protocol

Finally, the experimental protocol followed to perform the experiments is described in this section.

1. Cleaning of the disorder plate. The fiberglass plate is usually cleaned with paper towel soaked with the same silicone oil as the one used for the experiment. The aim is to remove remaining oil from previous experiments, dust, or any other impurities deposited on the plate. The glass plates can be eventually cleaned with water and soap, and then acetone.

2. Placement of the plate in the system. The fiberglass plate is affixed to the bottom plate of the cell, taking advantage of capillary adhesion. A thin layer of oil is first placed on the bottom plate of the cell. Then, the fiberglass plate is slid over the oil while pressing towards the cell.

3. Prewetting of the plate. The fiberglass plate is prewetted with a very thin layer (thinner than one fifth of the height of the copper patches) of the same oil used in the experiment to avoid possible wetting inhomogeneities.

4. Placement of the spacers. A PVC spacer cut in the form of a rectangular frame is placed on the copper rectangular frame that surrounds the fiberglass plate. Its purpose is both to separate the top and bottom plates of the cell and to close the cell hermetically everywhere except at the outlet. Two or three small spacers of PVC (typically 2×3 mm) are also placed on the (bigger) copper islands of disorder along the cell, to avoid bending of the top glass plate.

5. Closing of the cell. The top glass plate is placed on top of the spacers.

6. Last verifications. Before starting the experiment, the inclination of both cell and cameras must be checked to avoid any parallax problem. The illumination must be verified also to ensure a proper contrast in the images.

7. Recording system. The program to control the cameras is configured.

8. Flat interface. In all the experiments presented, a first flat interface is required. In the plates with a *preparation zone* it is sufficient to bring the fluid front gently to the edge of this copper region and the experiment is ready to start. For plates

without preparation zone, the fluid is pushed into the cell at high velocity (either via a high ΔP or a large v) and stopped. This interface is flat and the experiment can start from this point. Together with these two methods, the cell may be tilted against the advancement of the front to ensure an initially-flat front. Once this initial condition is obtained, the cell is tilted back to the desired ψ and the experiment is ready to start.

Chapter	Silicone oil	Disordered medium	Flow control	Image acquisition	Analysis
Spontaneous imbibition: capillary rise					
3		S- and D*-type	Constant pressure difference	Slow cameras ($r = 0.36$ mm/pixel)	`Subpixel`
	$\mu = 50$ cP	$\psi = 5°$	$\Delta P = 116.8, 67.8, 38.3, 18.7, -0.9, -40.1$ Pa	Logarithmic: $5 - 0.25$ fps	
	$\mu = 50$ cP	$\psi = 6.24°, 4.15°, 3.32°, 2.35°$	$\Delta P = 18.7$ Pa	Logarithmic: $5 - 0.25$ fps	
	$\mu = 50$ cP	$\psi = 0°$ (only D*)	$\Delta P = 147.2, -9.8, -49.1$ Pa	Logarithmic: $5 - 0.25$ fps	
Forced-flow: morphology					
4		D-type	Constant flow rate	Fast camera ($r = 0.182$ mm/pixel)	`Interfaces_wt`
	$\mu = 10$ cP	$\psi = 0°$	v $= 0.13$ mm/s	Logarithmic: $100 - 0.5$ fps	
Forced-flow: dynamics					
5, 6, 7		D-type	Constant flow rate	Fast camera ($r = 0.106$ mm/pixel)	`Interfaces_wt`
	$\mu = 10$ cP	$\psi = 0°$	v $= 0.130, 0.219$ mm/s	Ctt.: 100, 100 fps	
	$\mu = 50$ cP	$\psi = 0°$	v $= 0.036, 0.053, 0.131, 0.223, 0.353, 0.553$ mm/s	Ctt.: 50, 100, 100, 100, 200, 200 fps	
	$\mu = 100$ cP	$\psi = 0°$	v $= 0.051, 0.131$ mm/s	Ctt.: 50, 100 fps	
	$\mu = 169$ cP	$\psi = 0°$	v $= 0.053, 0.130$ mm/s	Ctt.: 50, 100 fps	
	$\mu = 350$ cP	$\psi = 0°$	v $= 0.131$ mm/s	Ctt.: 100 fps	

TABLE 2.3: Specifications for the different experimental studies presented in this work. The chapter where the corresponding results are shown, the oils and type of disorder used, the experimental conditions explored, the acquisition system used (and its spatial and temporal resolution), and the software used for the analysis are indicated.

Chapter 3

Capillary rise in Hele-Shaw models of disordered media

Capillary rise of fluids in porous media results from capillary-driven ascensional flow (imbibition) counteracted by gravity. Capillary rise is of primary importance in natural and industrial processes, from rise of sap in plants to capillary water absorption of concrete in buildings. Accordingly, these flows have been the subject of numerous investigations, dating back to more than a century ago (Bell and Cameron, 1906; Lucas, 1918; Washburn, 1921).

In this chapter we focus our attention on the mean displacement of fronts in spontaneous imbibition through our model open fracture. Experiments are performed with and without the presence of gravity, i.e. tilting the cell against the advancement of the front or keeping it horizontal. Compared to capillary rise in circular tubes, capillary driven flows in Hele-Shaw (HS) cells have been less studied. We find that our results of the spatially-averaged position of the imbibing front, $h(t)$, show systematic deviations from the Lucas (1918) and Washburn (1921) solution (LW) at any time, and from the Fries and Dreyer (2008*a*) Extended Solution (ES) at short and intermediate times, discussed in Sec. 1.2.2, in both smooth and disordered HS cells. The deviations are attributed to energy dissipation at the small preparation zone that precedes the measurement region in the cell entrance. In the following we show that an additional resistive term proportional to dh/dt must be included in the pressure balance equation to account for this extra source of energy dissipation. This new term modifies the nature of the governing differential equation, but an analytical solution $h(t)$ can still be found, which is in very good agreement with the experimental results. Small discrepancies still observed at short times, that increase with dh/dt, are attributed to a remaining dynamic dependence of the capillary pressure on front velocity, and to experimental uncertainties.

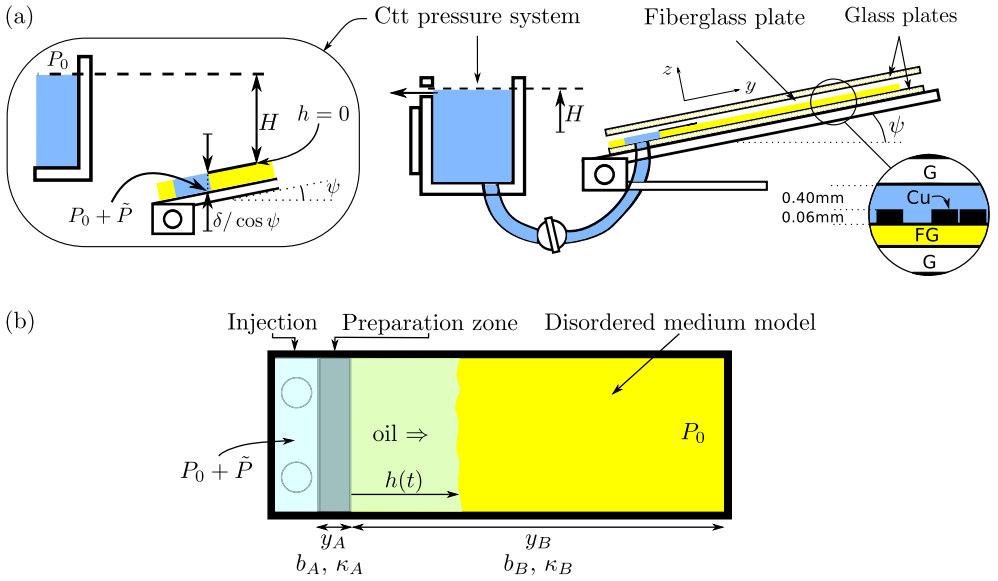

FIGURE 3.1: Sketch of the experimental setup used in this chapter. The two control parameters H and ψ are depicted in panel (a). The zoom on the left shows that the height H must be supplemented with the two small contributions $y_A \sin\psi$ and $\delta/\cos\psi$ to account for the exact applied pressure $\tilde{P}$. The zoom on the right is a lateral view of the disordered HS cell showing the parallel glass plates (G) and the fiberglass (FG) substrate with the copper obstacles (Cu). (b) Top view of the cell. The right end of the cell is open to air. The oil penetrates from the injection points at pressure $P_0 + \tilde{P}$, fills the preparation zone (A) and invades the porous medium model (B) displacing the resident fluid (air) that remains at P_0. y_A and y_B denote the extension of each region in the streamwise direction. b_A and b_B are the corresponding gap spacings, and κ_A and κ_B the corresponding permeabilities. $h(t)$ is the mean position of the fluid front, measured from the right end of the preparation zone.

3.1 Experimental procedure

The specific experimental configuration used in the present chapter is sketched in Fig. 3.1. Further details have been given in Ch. 2.

The models of disordered medium are S and D* and the fluid is Rhodorsil 47V 50 –described in detail in Secs. 2.2 and 2.3. The cell can be tilted an angle ψ, and it is connected to a constant pressure device, both shown in Fig. 3.1. The constant pressure device allows to impose a pressure difference $\tilde{P}$ between the pressure at the liquid inlet and the outer atmospheric pressure. As shown in the left panel of Fig. 3.1(a), this pressure difference is given by $\tilde{P} = \rho g(H + \delta/\cos\psi + y_A \sin\psi)$, where ρ is the density of the invading fluid, g is the acceleration of gravity ($g = 9.81$ m/s^2), H is the height of the liquid in the constant pressure reservoir connected to the inlet measured with respect to the entrance of the measurement region B, $\delta/\cos\psi$ takes into account the thickness of the fiber-glass substrate, $\delta = 1.9$ mm, and $y_A \sin\psi$ the difference in height across the preparation zone. The cell inclination provides an effective gravitational field

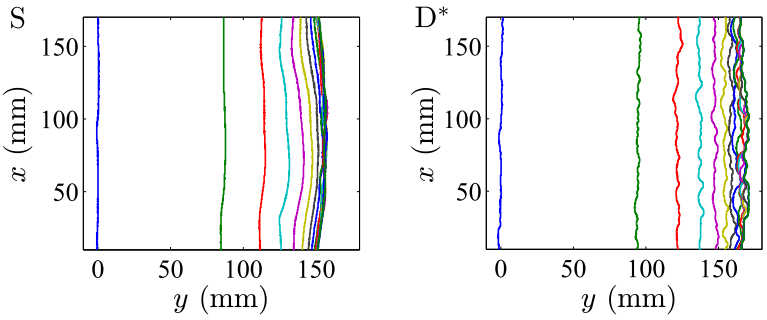

FIGURE 3.2: Examples of the oil-air interfaces recorded in the S (left) and D* (right) cells, for $\psi = 5°$, $H = 5$ mm. The time interval between consecutive interfaces in this plot is 250 s.

$g^* = g \sin\psi$ on the invading fluid. The flow is thus controlled by the parameters H and ψ. We have investigated H ranging from -6 mm to 10 mm, with precision ± 0.5 mm, corresponding to external pressure differences from about -32 Pa to 134 Pa for $\psi = 5°$, and ψ ranging from 2.3° to 6.3°, with precision $\pm 0.1°$, corresponding to values of g^* from 0.39 m/s^2 to 1.08 m/s^2.

The motion of the oil-air front is recorded using the two slow CCD cameras (Sec. 2.5) in sequential order, with spatial resolution $r = 0.36$ mm/pixel and logarithmic acquisition rate from 5 to 0.25 frames per second. Typical examples of the experimental fronts recorded are shown in Fig. 3.2.

3.2 Pressure balance equation

We first analyse the differential equation governing front displacement. The balance of forces at the mean height of an invading front through either a capillary tube of circular cross-section and small radius b, or a Hele-Shaw cell formed by two large parallel plates separated by a small gap of constant thickness b, has been already presented in detail in Sec. 1.2.2. Considering a capillary-driven flow of a viscous liquid that moves into a tube or cell from the inlet and displaces the air initially present, one obtains the pressure balance equation for the mean height of the fluid front, $h(t)$:

$$\rho \frac{d}{dt}\left(h\dot{h}\right) = \frac{2\gamma\cos\theta}{b} - \rho g \sin\psi h - \frac{\mu}{\kappa} h\dot{h} + P, \tag{3.1}$$

where ρ is the density of the liquid, γ is the surface tension of the air-liquid interface, θ is the apparent (advancing) contact angle at the solid-liquid-air contact line, g is the acceleration of gravity, the angle ψ measures the inclination of the tube or cell with respect to the horizontal, μ is the dynamic viscosity of the liquid, κ the permeability of the tube or cell, and P is an externally applied additional pressure at the liquid inlet. The overdot stands for time derivative.

Equation (3.1) is valid when five premises are fulfilled: the flow is one-dimensional in the tube or cell, viscous and inertial effects in the displaced gas phase are negligible,

inertial effects in the liquid in the reservoir are also negligible, viscous pressure losses are given by Poiseuille's law in the tube and by Darcy's law in the HS cell, and the capillary pressure at the liquid-air meniscus is constant and can be calculated from a constant contact angle θ and b. This equation gives rise to the Lucas-Washburn solution (1.17) when the displacement of the fluid is through an horizontal cell, or to the Extended-Solution 1.18 when the fluid advances against gravity.

We found a systematic discrepancy between these solutions and our experimental data in both cases, with and without gravity (Sec. 3.3). Specifically, LW and ES solutions were found to overestimate the experimental position of the front in all cases. This systematic discrepancy led us to rewrite the pressure balance equation for our system, in particular, considering the geometrical properties of our cell.

3.2.1 Pressure balance formulation in HS models of porous media

We write down here the particular form of the pressure balance formulation based on a one-dimensional description of the flow –Eq. (3.1)– that applies to our HS cells. In order to obtain an accurate expression of the viscous pressure losses we first take into account the specific details of the geometry of the S and D* cells shown in Fig. 3.1(b). Secondly, we replace the capillary pressure term $2\gamma\cos\theta/b$ by a generic capillary pressure term Y that, in the S cell, takes into account dynamic variations of the contact angle, and in the D* cell velocity-dependent capillary pressure fluctuations caused by the fluctuations in gap thickness.

In a Hele-Shaw cell the pressure drop caused by viscous losses follows from Darcy's law (1.6). We assume that the flow takes place in the y direction only, and integrate Darcy's law along the cell up to the mean front height $h(t)$. In doing this we take into account the different parts of the cell –the preparation zone (A) and the model medium (B)–, and the condition of incompressibility. The pressure difference due to viscous losses between the inlet and the mean interface position reads then:

$$p_{vl} = \int_0^{y_A+h} \frac{\partial p}{\partial y} dy = \int_0^{y_A+h} \left(-\frac{\mu}{\kappa}\dot{h}\right) dy = -\mu \left(\frac{1}{\kappa_A}\frac{b_B}{b_A} y_A + \frac{1}{\kappa_B} h\right) \dot{h}. \tag{3.2}$$

It is important to point out that the geometric factor b_B/b_A, arising from volume conservation of oil, allows us to express the pressure drop in region A as a function of the mean front velocity $\dot{h}$ in region B.

In the pressure balance equation that gives rise to the the LW and ES solutions, the capillary pressure is taken as constant. The constancy of the capillary pressure relies on the constancy of the apparent (advancing) contact angle. It is known, however, that the advancing contact angle depends on the velocity v of the contact line and on its previous history. The dependence on v is often expressed in terms of the capillary

number, $\mathrm{Ca} = \mu v/\gamma$ (Mumley et al., 1986*b*; Hoffman, 1975; Bonn et al., 2009). Since in capillary rise v evolves from very large initial values to negligible values as the equilibrium height is reached, an important variation of the dynamic contact angle and hence of the capillary pressure in the course of fluid invasion is to be expected. Similarly, a large range of velocities, an thus of capillary pressures, are explored also in imbibition in a horizontal cell, where the mean front velocity decays approximately as $t^{-1/2}$. Moreover, in the presence of spatial fluctuations in gap thickness, as in cell D*, it is reasonable to expect that the capillary pressure will also experience local fluctuations.

To account for deviations of the capillary pressure from a constant value $2\gamma\cos\theta/b_B$ we replace this term by a generic capillary pressure Y. We expect Y to be dependent on mean front velocity and on the previous history of the contact line. Our final expression for the pressure balance equation reads now:

$$\rho\frac{d}{dt}\left(h\dot{h}\right) = Y - \rho g\sin\psi h - \mu\left(\frac{1}{\kappa_A}\frac{b_B}{b_A}y_A + \frac{1}{\kappa_B}h\right)\dot{h} + P, \tag{3.3}$$

where the LHS is the inertial term, Y is the generic capillary pressure, $-\rho g\sin\psi h$ is the gravitational pressure, $-\mu\left(\frac{1}{\kappa_A}\frac{b_B}{b_A}y_A + \frac{1}{\kappa_B}h\right)\dot{h}$ is the viscous pressure drop, and $P = \tilde{P} - \rho g\sin\psi\, y_A$ is the external pressure difference applied, defined as to make evident that the gravitational pressure in the preparation zone cancels out.

Making $\dot{h} = 0$ in Eq. (3.3) we see that the equilibrium height in this case is given by

$$h_{eq} = \frac{1}{\rho g\sin\psi}\left(Y_0 + P\right), \tag{3.4}$$

where Y_0 stands for the value of Y at equilibrium ($\dot{h} \to 0$) for each particular flow history.

It is important to notice the presence of a term proportional to $\dot{h}$ in Eq. (3.3), which comes from viscous dissipation in the preparation zone, and is absent in the original Eq. (3.1) that led to LW (1.17) and ES (1.18) solutions. Any viscous loss in capillary transport with a constant transport length –independent of h or t– can be modelled that way. Even if the unknown generic contribution Y is taken constant, this term proportional to $\dot{h}$ is going to change the nature of the solution $h(t)$ in a qualitative way. As discussed in Sec. 1.2.2, a term of the generic form $\dot{h}^x$ has been invoked in capillary rise in tubes to explain deviations of the experimental results from the LW and ES solutions. It has been attributed to velocity-dependent friction losses at the contact line. In our formulation it appears naturally as the result of having an entrance or preparation zone in the cells. We will see that even though this zone is relatively small –in comparison to h_{eq}, for instance– the associated viscous losses are by no means negligible.

3.2.2 Analytical solutions

Absence of gravity. We deal first with displacements in the absence of gravity, i.e. in a horizontal cell ($\psi = 0°$). In order to derive an analytical solution of Eq. (3.3) we neglect the inertial term and consider $Y = 2\gamma\cos\theta/b_B$ with constant θ. The solution reads:

$$t = \frac{\mu}{\frac{2\gamma\cos\theta}{b_B} + P}\left(\frac{1}{\kappa_A}\frac{b_B}{b_A}y_A h + \frac{1}{2\kappa_B}h^2\right), \tag{3.5}$$

where $t = 0$ is defined by the condition $h = 0$. The inverse of this equation gives an evolution curve $h = h(t)$ of the form:

$$h(t) = \sqrt{\left(\frac{\kappa_B b_B}{\kappa_A b_A}y_A\right)^2 + \frac{2\kappa_B}{\mu}\left(\frac{2\gamma\cos\theta}{b_B} + P\right)t} - \frac{\kappa_B b_B}{\kappa_A b_A}y_A. \tag{3.6}$$

It is not difficult to check that this solution reduces to the LW solution when $y_A = 0$ and $P = 0$, and to the solution derived by Hilpert (2009*a*) if the cell is uniform ($\kappa_A = \kappa_B$ and $b_A = b_B$).

Presence of gravity. We turn our attention now to the case with gravity. In order to derive an analytical solution $h(t)$ of Eq. (3.3) –again neglecting inertia and assuming $Y = 2\gamma\cos\theta/b_B$ with constant θ– it is convenient to make h and t dimensionless. The natural way to make h dimensionless is to measure it in units of h_{eq}:

$$h^* \equiv h/h_{eq}. \tag{3.7}$$

Applying this change of variable to Eq. (3.3) it is possible to obtain a solution of the form $t = t(h^*)$:

$$t = -\frac{1}{\rho g\sin\psi}\left[\frac{\mu}{\kappa_B}h_{eq}h^* + \mu\left(\frac{1}{\kappa_A}\frac{b_B}{b_A}y_A + \frac{1}{\kappa_B}h_{eq}\right)\ln(1-h^*)\right]. \tag{3.8}$$

This solution suggests defining a dimensionless time as:

$$t^* \equiv t\frac{\rho g\sin\psi}{\mu\left(\frac{1}{\kappa_A}\frac{b_B}{b_A}y_A + \frac{1}{\kappa_B}h_{eq}\right)}. \tag{3.9}$$

The solution (3.8), written in dimensionless variables, reads then:

$$t^* = -\frac{1}{1 + \frac{\kappa_B b_B}{\kappa_A b_A}\frac{y_A}{h_{eq}}}h^* - \ln(1-h^*). \tag{3.10}$$

This solution recovers Washburn's solution for imbibition in the presence of gravity when $y_A/h_{eq} \to 0$. It reduces also to the solution derived by Hilpert (2009*b*) if the cell is uniform ($\kappa_A = \kappa_B$ and $b_A = b_B$). It can also be inverted, following the procedure used by Fries and Dreyer (2008*a*). To this purpose, we define

$$\frac{1}{\tilde{c}} \equiv \left[1 + \frac{\kappa_B b_B y_A}{\kappa_A b_A h_{eq}}\right] \tag{3.11}$$

and add it to both sides of Eq. (3.10). Taking the power e of both sides and multiplying them by $-\tilde{c}$ we get:

$$-\tilde{c}e^{-\tilde{c}-t^*} = \tilde{c}(h^* - 1)e^{\tilde{c}(h^*-1)}. \tag{3.12}$$

Using the property of the Lambert function that $Z = Xe^X \iff X = W(Z)$ the analytical solution of Eq. (3.3) with $Y = Y_0$ reads finally:

$$h^* = 1 + \frac{1}{\tilde{c}} W\left(-\tilde{c}e^{-\tilde{c}-t^*}\right). \tag{3.13}$$

This solution differs from Fries and Dreyer ES in the parameter $\tilde{c}$, which takes into account the effect of the preparation zone on the dynamics of the imbibition front. The parameter $\tilde{c}$ depends on h_{eq} and thus, in contrast to the ES, the dimensionless solution (3.13) is not universal.

3.3 Results

3.3.1 Capillary rise experiments

Experiments were performed, on the one hand, at a constant inclination angle $\psi = 5°$ and reservoir heights $H = 10$, 5, 2, 0, -2, and -6 mm, and, on the other, at constant reservoir height $H = 0$ mm and inclination angles $\psi = 2.35°$, $3.32°$, $4.15°$, $5.05°$, and $6.28°$. For each pair of values (ψ, H) we carried out 3 displacements for the S plate and 2 displacements for each of the two possible orientations of the D* plate. We recorded the front position as a function of time, $h(x,t)$, and averaged it in the direction x to obtain the mean front position $h(t)$. Finally the different experimental curves $h(t)$ obtained for the same pair of values (ψ, H) and the same plate were averaged.

Curves $h(t)$ measured in the series of experiments at constant angle ψ are plotted on the left panels of Fig. 3.3. Both in the smooth (a) and in the disordered configuration (b) we observe the three regimes expected for h vs t. At short times the experimental data follow the LW behaviour $h \sim t^{1/2}$. At long times there is an exponential saturation to the Jurin's height, which is seen to depend systematically on the applied pressure P. These two behaviours cross over at intermediate times. The two panels on the right show that h_{eq} depends linearly on P, as predicted by Eq. (3.4). Remarkably, the slope

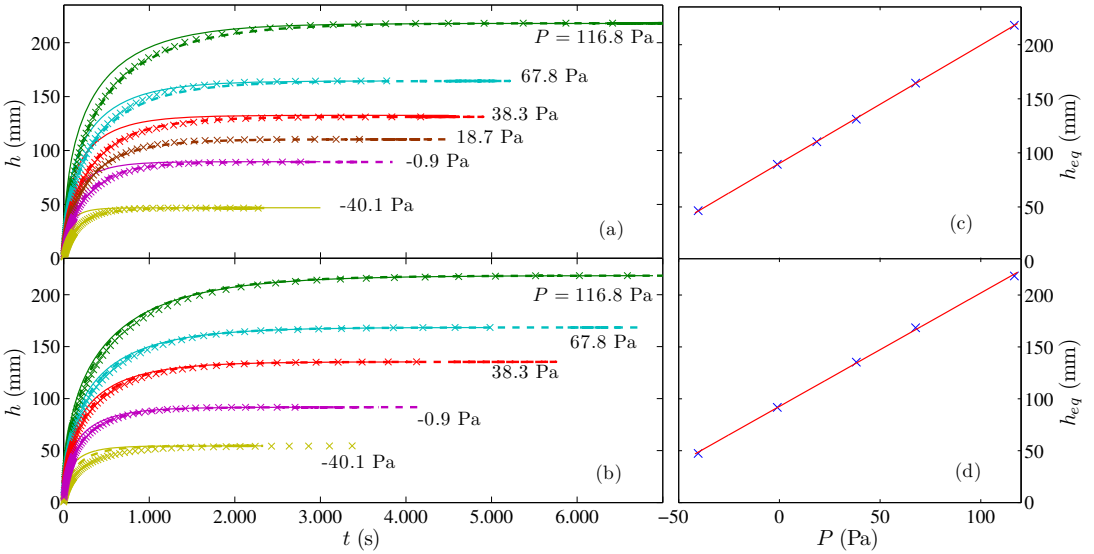

FIGURE 3.3: Left panels show the mean height of the imbibition front vs time for fixed inclination $\psi = 5°$ and different pressures P in the S (a) and D* cells (b). Crosses represent the experimental data (one out of ten points plotted). Solid lines are the ES (extended solution) of Eq. (3.1) and dashed lines the solution (3.13) of Eq. (3.3), both rescaled to match the experimental equilibrium heights h_{eq}. The right panels show the dependence of h_{eq} on applied pressure P in the S (c) and D*(d) cells (crosses) and their linear fits (solid lines).

of the linear fits of h_{eq} vs P is identical for both data sets, 1.09 mm/Pa. It is slightly below the value $1/(\rho g \sin\psi) = 1.17$ mm/Pa, which means that Y_0 must include a tiny linear dependence on P. The intercepts of the linear fits are 90.1 mm for the S cell and 92.4 mm for the D* cell.

In this same figure the measured data for $h(t)$ is compared to the ES of Fries and Dreyer and to the solution of Eq. (3.3) given in dimensionless variables by Eq. (3.13). We have plotted the solutions in the form $h(t) = h^*(t)h_{eq}$ to force the experimentally measured value of h_{eq} at long times. This is equivalent to adjust Y_0 to match the equilibrium heights. We notice a significant and systematic deviation of the ES (solid lines) from the experimental results at short and intermediate times, in both S and D* cells. The deviation is always such that the experimental data fall below the ES. The solution (3.13) adapted to our specific setup –dashed lines– provides in contrast a very good prediction of the $h(t)$ curves in the S cell. In the D* cell the agreement is not so good, but still represents an improvement over the ES curves.

The results for the series of experiments at constant pressure P are plotted on the left panels of Fig. 3.4. The behaviour of the experimental data is qualitatively the same than in the series of experiments at constant angle just discussed. The two panels on the

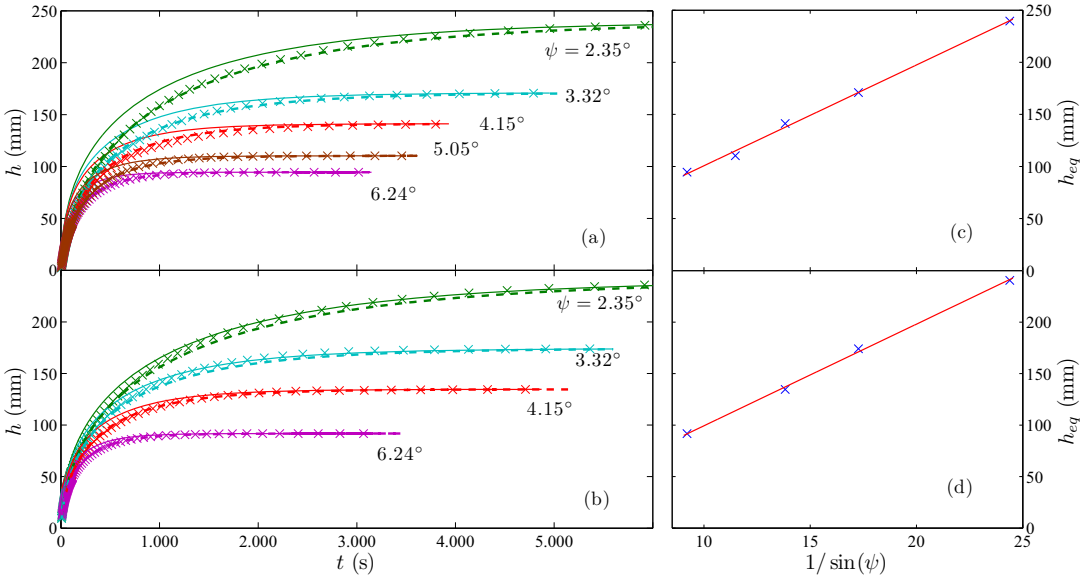

FIGURE 3.4: Left panels show the mean height of the imbibition front vs time for fixed pressure $P = 18.7$ Pa and different inclination angles ψ in the S (a) and D* cells (b). Crosses represent the experimental data (one out of ten points plotted). Solid lines are the extended solution of Eq. (3.1) and dashed lines the solution (3.13) of Eq. (3.3), both rescaled to match the experimental equilibrium heights h_{eq}. The right panels show the dependence of h_{eq} on $1/\sin\psi$ in the S (c) and D*(d) cells (crosses) and their linear fits (solid lines).

right show that h_{eq} depends linearly on $1/\sin\psi$, as predicted by Eq. (3.4). The slopes are 9.67 mm (S cell) and 9.87 mm (D* cell), and the intercepts are 4.0 mm (S cell) and 0.7 mm (D* cell).

Comparison to the ES (solid lines) and to the solution (3.13) (dashed lines) reveals again that the ES overestimates the position of the front at all times, in both the S and D* cells. Again, the solution (3.13), that accounts for viscous losses in the preparation zone, provides a very good prediction of the $h(t)$ curves in the S cell. In the D* cell the result is less clear. For 6.24° and 4.15° the measured data is well represented by Eq. (3.13) at all times. For 3.32° and 2.35°, however, Eq. (3.13) reproduces the data satisfactorily at short and intermediate times, but the ES seems to work slightly better at long times.

It is worth mentioning that the curves corresponding to the solution (3.13) are similar to the ones that result from the analytical solution by Hilpert (2009*b*), who presented a generalization of the ES for capillary rise that allows for a non-zero initial condition for the position of the infiltration front. The latter however are not as close to the experimental data as ours. The similarity comes from the fact that permeabilities and gap

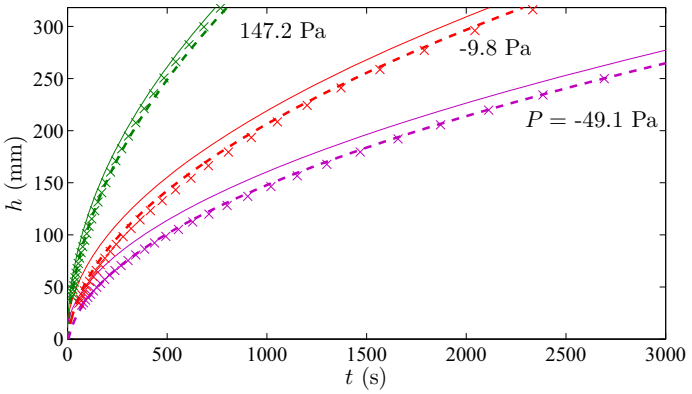

FIGURE 3.5: Mean position of the imbibition fronts vs time, measured in displacements in the D* cell in the absence of gravity (horizontal cell) at different imposed pressures. Experimental results are represented by crosses, and compared to LW predictions (solid lines) and to our own prediction (3.6) that accounts for viscous dissipation in the preparation zone (dashed lines).

spacings in the preparation zone and in the measuring region do not differ significantly, but the differences can still be noticed in the $h(t)$ curves.

3.3.2 Imbibition displacements in a horizontal cell

We have also carried out a series of imbibition experiments keeping the cell horizontal ($\psi = 0°$). Figure 3.5 shows three displacements of this kind (crosses) carried out at different applied pressures in the D* cell. In the absence of gravity the dynamics is governed only by capillary and viscous forces, and the front never reaches an equilibrium height. The solid lines show the LW solutions for each set of experimental parameters. Notice that in contrast to the measurements in inclined cells, where h_{eq} was used to match the experimental and analytical results at long times, the comparison here is made without adjustable parameters. The comparison shows that the LW solutions overestimate the experimental data at all times. However, if viscous dissipation in the preparation zone is taken into account, the theoretical curves given by Eq. (3.6) –dashed lines– become much closer to the experimental data. Similar agreement would be obtained using the analytical solution by Hilpert (2009*a*) for infiltration in horizontal tubes, that allows for a non-zero initial condition for the position of the infiltration front. As before, however, the latter does not reproduce the experimental data so accurately because the permeabilities and gap spacings in the preparation zone and the measuring region are not exactly the same.

3.4 Analysis and discussion

3.4.1 Contributions to the pressure balance equation

In this section we discuss the relative importance of the different contributions to the pressure balance Eq. (3.3). Except for the generalized capillary pressure Y, the value

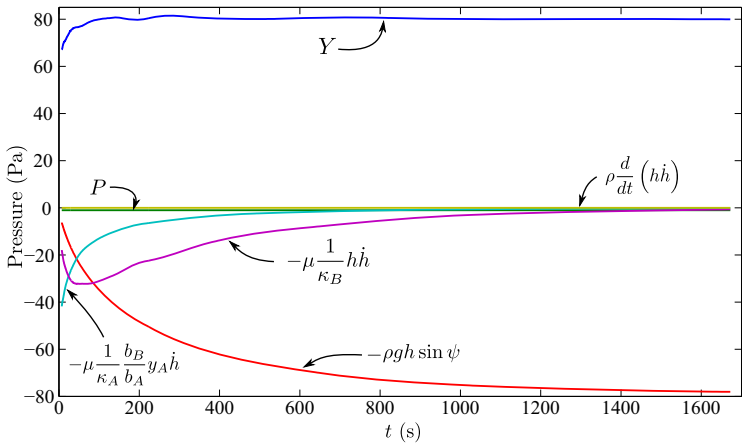

FIGURE 3.6: Contributions to the pressure balance Eq. (3.3) computed from $h(t)$ measured in the disordered HS cell under the experimental conditions $\psi = 5°$, $H = -2$ mm ($P = -0.9$ Pa).

of these contributions as a function of time can be computed from the measured $h(t)$ –obtained, as mentioned, by averaging over realizations that correspond to the same experimental conditions (ψ, H) and the same plate– and its time derivative $\dot{h}$ computed numerically. To this purpose we take the nominal values of the different material and geometric parameters quoted in Table 2.1 (Sec. 2.2).

Figure 3.6 displays the different pressure contributions as a function of time for one particular data set, obtained with $\psi = 5°$, $H = -2$ mm, and the D* cell. The inertial contribution $\rho\, d(h\dot{h})/dt$ is found to be at least three orders of magnitude smaller than all other non-zero contributions in the whole range of front velocities, and can therefore be safely neglected. Next, there is a constant contribution, the applied constant pressure P. The magnitude of the gravitational pressure $-\rho gh\sin\psi$ grows monotonically in time, replicating the behaviour of $h(t)$ and resisting front advance. The two other resisting contributions are the viscous dissipation in the medium, $-(\mu/\kappa_B)h\dot{h}$, whose magnitude increases as $h(t)$ departs from zero and later on decays as the front slows down, and the viscous dissipation in the preparation zone, $-(\mu/\kappa_A)(b_B/b_A)y_A\dot{h}$, whose magnitude decays monotonically at the rate of the front velocity. The sum of all these contributions finally gives the magnitude of the unknown capillary pressure, $Y(t)$, shown also in the figure.

3.4.2 Generalized capillary pressure Y

The generalized capillary pressure Y in Eq. (3.3) will in general have a static and a dynamic contribution.

Type of cell	P (Pa)	ψ (°)	Measured h_{eq} (mm)	Y_0 (Pa)	θ_0 (°)
S	116.8	5	218.0	69.7	39.2
S	67.8	5	164.5	73.1	35.7
S	38.3	5	131.2	74.0	34.7
S	18.7	5	110.3	75.7	32.7
S	-0.9	5	89.4	77.5	30.6
S	-40.1	5	46.5	80.1	27.1
D*	116.8	5	218.4	70.1	42.0
D*	67.8	5	168.5	76.4	35.9
D*	38.3	5	135.3	77.5	34.7
D*	-0.9	5	91.7	79.4	32.6
D*	-40.1	5	47.3	80.7	31.2
S	18.7	2.35	239.6	82.0	24.3
S	18.7	3.32	171.0	82.8	23.1
S	18.7	4.15	141.2	85.9	17.4
S	18.7	5.05	110.3	75.6	32.9
S	18.8	6.24	94.5	86.6	15.8
D*	18.7	2.35	240.6	78.0	34.2
D*	18.7	3.32	174.1	80.2	31.7
D*	18.7	4.15	134.6	76.9	35.4
D*	18.8	6.24	91.8	79.3	32.8

TABLE 3.1: Measured equilibrium heights h_{eq}, corresponding values of the static capillary pressure Y_0, and equilibrium advancing contact angles θ_0 derived from Y_0, for the various experimental conditions investigated.

The static contribution, Y_0, is the value of Y at equilibrium ($\dot{h} \to 0$). It can be computed by equating the equilibrium height measured experimentally to the nominal value that results from Eq. (3.4). The values of Y_0 computed in this way are given in Table 3.1 for all the measured displacements. It is worth mentioning that Y_0 depends linearly on the imposed pressure P in both types of cells, as foreseen in Sec. 3.3.1. The dependence is very mild, however. The slope is -0.07 for the displacements in the S cell and -0.04 in the D* cell.

In the displacements carried out in the S cell we attribute the values of Y_0 to the capillary pressure jump that results from the advancing contact angle when the fronts arrive to a halt. The slight dependence of Y_0 on P is then a result of the different flow histories. Indeed, displacements at higher P involve larger $\dot{h}$ and thus larger advancing contact angles. When the fronts reach h_{eq}, the (equilibrium) advancing contact angles may retain a dependence on P because the contact angle is known to exhibit hysteresis and thus to retain memory of its previous history (de Gennes, 1985). This is consistent with the observation that Y_0 decreases with P. If the equilibrium capillary pressure is written as $Y_0 = 2\gamma \cos\theta_0 / b_B$, the corresponding equilibrium advancing contact angles

θ_0 take the values listed in Table 3.1. This method of determining θ_0 from h_{eq} is widely used in vertical capillaries (Mumley et al., 1986*a*,*b*; Schäffer and Wong, 2000).

In the D* cell the fronts become rough (Fig. 3.2) and thus the approximation of a one-dimensional flow is much more crude. Nevertheless, the values of Y_0 follow the same trend than in the S cell. Moreover, in the D* cell the concept of a dynamic contact angle for the interface as a whole has no meaning. Different parts of the front have different vertical and in-plane curvatures. If an *effective* equilibrium advancing contact angle is still defined through the relation $Y_0 = 2\gamma \cos\theta_0 / b_B$, the resulting values are the ones listed in Table 3.1. They are quite similar to the ones found in the S cell for each displacement (ψ, H).

As for the dynamic contribution to Y, it is important to recall that the curves $h(t)$ measured in the S cell are very well reproduced by Eq. (3.13), rescaled by the asymptotic value h_{eq}. This means that a constant capillary pressure Y_0 is enough to reproduce the measured $h(t)$ in the S cell.

However, this is not the case for the displacements carried out in the disordered cell D*. To estimate the dynamic contribution to Y we have computed systematically the unknown capillary pressure Y for all the experiments performed in the D* cell as a function of the front velocity $\dot{h}$. In order to avoid large fluctuations at low $\dot{h}$, that come from numerical uncertainties in computing $\dot{h}$ from the measured $h(t)$, we have represented $Y_s - Y$, where $Y_s = 2\gamma/b_B$ is the upper bound (or static value) of the capillary pressure. The result is shown in the left (constant inclination) and right (constant applied pressure) panels of Fig. 3.7, in double-logarithmic plots. For constant inclination experiments the general trend is that the capillary pressure is nearly constant at low front velocities, and depends linearly on P as mentioned earlier. At large front velocities, instead, it grows roughly as a power of $\dot{h}$. For the experiments at constant P the qualitative trend is similar, but the values at low front velocities are not well correlated with the inclination angles and, on the other hand, the crossover to a power law at large $\dot{h}$ displays a pronounced dip. The power-law behaviour at large $\dot{h}$ is compatible with a dependence $\sim \mathrm{Ca}^{\beta}$ with β in the range $0.5 - 1$. A value $\beta = 0.5$ has been reported by Zhou and Sheng (1990) and Sheng and Zhou (1992) for the frictional force experienced by the contact line between two immiscible fluids in a capillary tube, and by Weitz et al. (1987) for the capillary pressure drop between two immiscible fluids in a porous medium. Larger values of β in the range mentioned earlier have been found by several authors, as reviewed by Schäffer and Wong (2000).

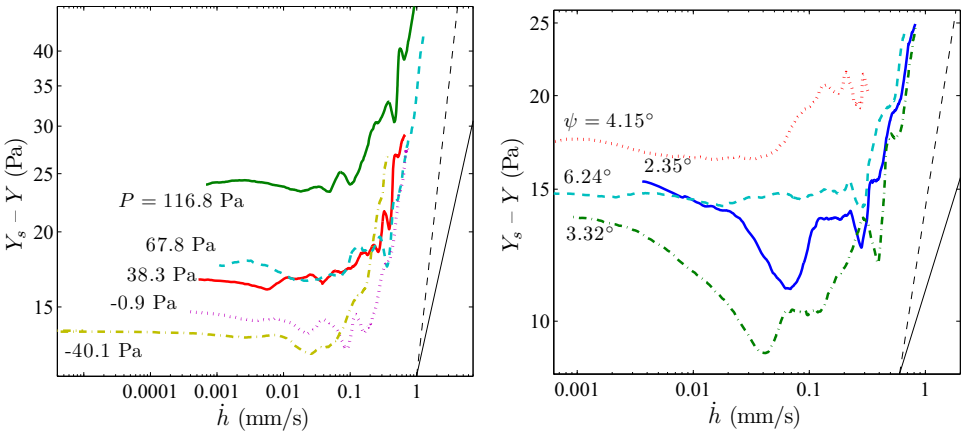

FIGURE 3.7: Computed values of the difference $Y_s - Y$ between $2\gamma/b_B$ and the unknown capillary pressure Y vs the mean velocity of the front, $\dot{h}$, in the D* cell. Results for measurements at constant angle $\psi = 5°$ are shown in the left panel, and at constant pressure $P = 18.7$ Pa in the right panel. The straight lines are power laws $Y_s - Y \sim \dot{h}^\beta$ with $\beta = 1$ (dashed) and $\beta = 1/2$ (solid), and have been included to guide the eye.

3.5 Conclusions

We have presented an exhaustive experimental investigation of capillary-driven imbibition displacements of air by a silicone oil in large HS models of porous media, namely a smooth cell (S) and a cell with a two-valued gap thickness fluctuating in space (D*). In both cells, displacements under different applied pressures and different inclinations –including the particular, qualitatively different case of keeping the cell horizontal, for which gravity is ineffective– have been studied.

The results show that the spatially-averaged interface height, $h(t)$, follows a diffusive behaviour $\sim t^{1/2}$ in the initial stages of the displacements. In capillary rise displacements –in the presence of gravity– this behaviour crosses over to an exponential one at long times, such that an equilibrium height h_{eq} is reached asymptotically. These results are in very good qualitative agreement with the predictions of Lucas (1918) and Washburn (1921) and with the Extended Solution derived by Fries and Dreyer (2008*a*) for capillary rise in circular capillary tubes. A careful comparison of the ES and the experimental curves shows however a measurable quantitative disagreement in the crossover regime at short and intermediate times. The experimental curves fall systematically below the predicted ES in this regime.

We have reformulated the original pressure balance equation leading to the LW and ES results, in order to include an additional resisting term proportional to $\dot{h}$. The physical origin of this term is the pressure drop caused by viscous dissipation in the first region of the cell, the preparation zone. This zone is intended to allow for a reproducible

and carefully controlled initial condition of the fluid front before it invades the model medium. The presence of this term modifies the nature of the solution, but we have shown that the new equation can also be solved analytically for $t(h)$, and inverted to provide $h(t)$, in the two relevant cases: with and without gravity.

This new solution agrees nicely with the experimental results at all times, particularly for the smooth HS cell (S). For the HS cell D*, in which capillary pressure fluctuates in space due to the imposed fluctuations in gap thickness, small deviations can still be resolved experimentally. Translating them into an unknown capillary pressure, Y, our results show systematically that this capillary pressure can be modelled by a $\dot{h}$-independent driving contribution that depends linearly on P, supplemented by a pressure drop that follows roughly a power-law of $\dot{h}$ at large velocities –initial times. The latter is compatible with a dependence $\sim \mathrm{Ca}^{\beta}$ with β in the range $0.5 - 1$.

Chapter 4

Kinetic roughening in forced-flow imbibition

In the previous chapter we have analysed the advancement of the mean position of a fluid front in spontaneous imbibition. We observe that fronts advancing through the disordered cell are not flat during the whole experiment but get rough as the fluid penetrates the medium. Now we characterize the evolution of the roughness fluctuations of the invading front.

In order to focus only on the fluctuations of the advancing front $h(x,t)$, we analyse forced-flow imbibition experiments, where the mean position of $h(x,t)$ increases linearly in time. We specifically study the scale-invariant properties of the oil-air interface during the kinetic roughening process that occurs as a consequence of the competition of forces acting on the interface at different lengthscales (Krug, 1997).

Previous results of kinetic roughening in a setup equivalent to the setup used in the present Thesis are shown in appendix A. Family-Vicsek, intrinsic anomalous, and super-rough scaling scenarios were observed in experiments of spontaneous imbibition (Soriano et al., 2005; Planet et al., 2007) depending on the relative importance of the applied pressure. In forced-flow experiments, at low injection rates (capillary regime) the scaling scenario was recently found to be super-rough (Planet et al., 2014). It is worth mentioning that, while fluid incompressibility imposes local mass conservation (in 3D) in both spontaneous and forced-flow imbibition displacements, the latter is subjected also to global mass conservation due to the imposed constant flow rate. This feature may have an effect on the scaling behaviour of the invading fronts.

In this chapter we analyse the scaling properties of the front in forced-flow imbibition for an oil of dynamic viscosity $\mu = 10$ cP for the first time in this setup. The flow rate imposed corresponds to a mean front velocity v $= 0.13$ mm/s. Two disorder plates D were chosen for the study and 17 different disorder configurations were explored.

Compared to previous results, we used the fast camera which allows higher temporal and spatial resolutions. The setup and the properties of the oil used have been described in detail in Ch. 2.

4.1 Morphological analysis: base-line correction

In the morphological analysis of growing interfaces in kinetic roughening processes, base-line correction may be necessary in order to prevent the appearance of artefacts. There are two kinds of artefacts inherent in the geometrical description of the resulting self-affine object that affect the large and local scales respectively (Schmittbuhl et al., 1995). Large scale effects may arise from misorientation of the image acquisition system with respect to the interface frame, that introduces a global inclination of the front. The power spectrum is specially sensitive to this artefact, resulting in a slope $S \sim q^{-2}$, corresponding to the Fourier transform of a linear ramp –as commented in Sec. 2.6. At the local scale, spatial resolution defines the minimum observable variation of the interface. It affects the analysis at the smallest windows ℓ and also the power spectrum at large q, and thus its scaling behaviour. The effect of the boundary conditions may also play an important role in determining the scaling exponents of the system. When the general trend induced by the boundaries is known, it can be removed from the interfaces.

Our experimental system presents two features that may justify the correction of the interfaces. First, the alignment of the camera with the cell is crucial. Specifically, to perform morphological studies of the front the first (flat) interface must be parallel to the edge of the image. A rotation of 1° of the image plane with respect to the cell implies a difference larger than 3 mm in height from one end of the interface to the other. In this case it would be justified to subtract a linear base-line from the interfaces. In addition, this correction would avoid artefacts in the computation of the power spectrum of the interfaces that give rise to the artificial exponent -2 previously commented. Second, the HS cell may also introduce some undesired effects on the morphology of the front. The boundaries of the cell pull the fluid because the oil tends to advance along the side walls. This effect may cause the front to deform into a parabolic shape. In this case we could subtract a second order polynomial from the raw data. This modification of the interface would also correct the misorientation of the camera with respect to the cell.

We analyse the effect of such corrections in our data to discriminate whether it is worth it and legitimate to apply them. In Fig. 4.1 interfaces for two different experiments (`a` and `b`) are plotted for two different times of the advancement of the front ($t = 0.1$ s and $t = 2500$ s). Raw interfaces are compared to interfaces *corrected* by subtracting a first or second order polynomial. The linear correction barely affects the morphology of the front at either small or large times. The effect of subtracting a parabola is also

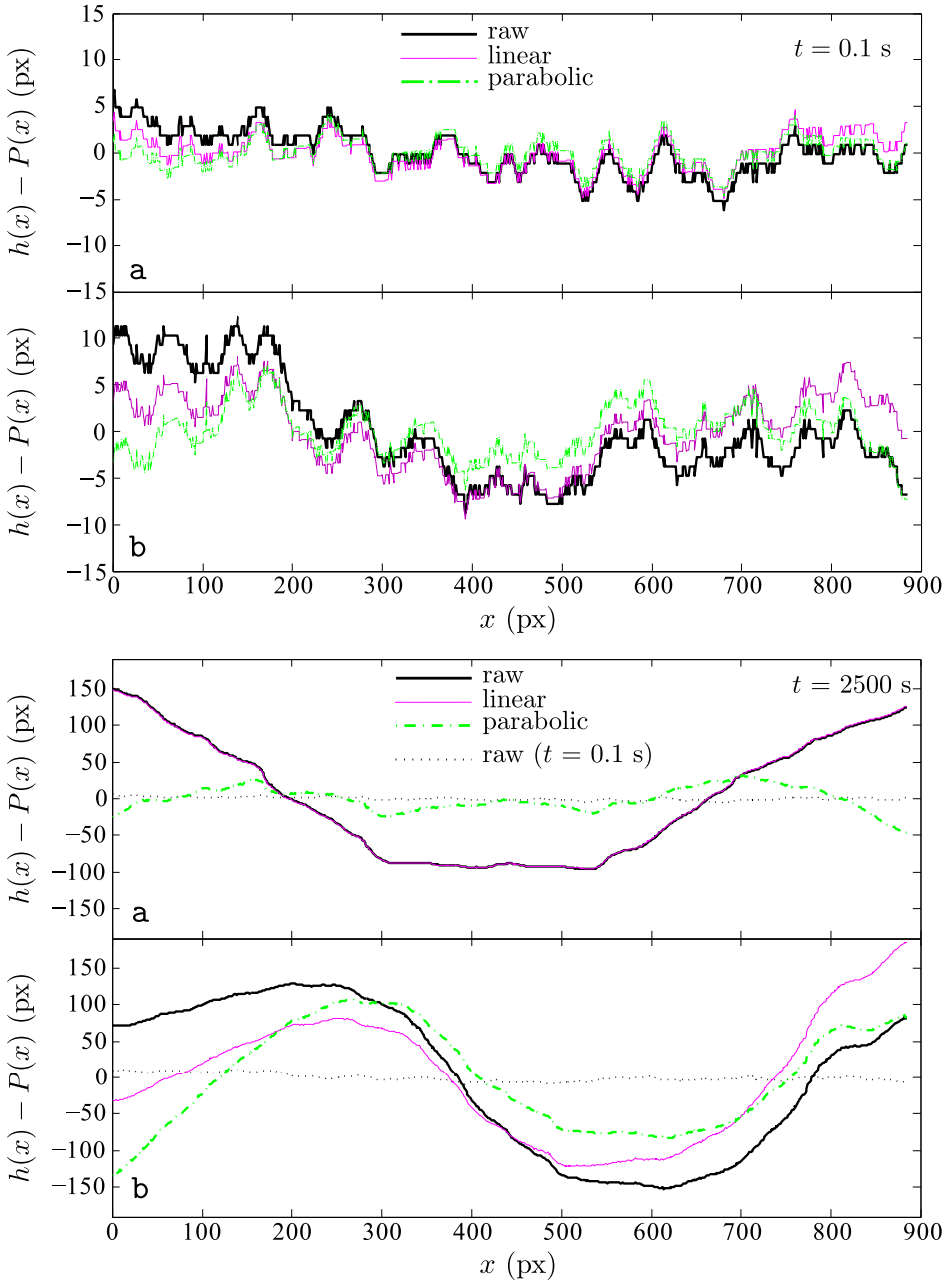

FIGURE 4.1: Effect of subtracting polynomials of first (linear) and second (parabolic) order $P(x)$ from raw interfaces $h(x)$ for two experiments (a,b) at times $t = 0.1$ and 2500 s. The mean position has been subtracted from the raw interfaces. For experiment a at time 2500 s, linear subtraction overlaps with raw data.

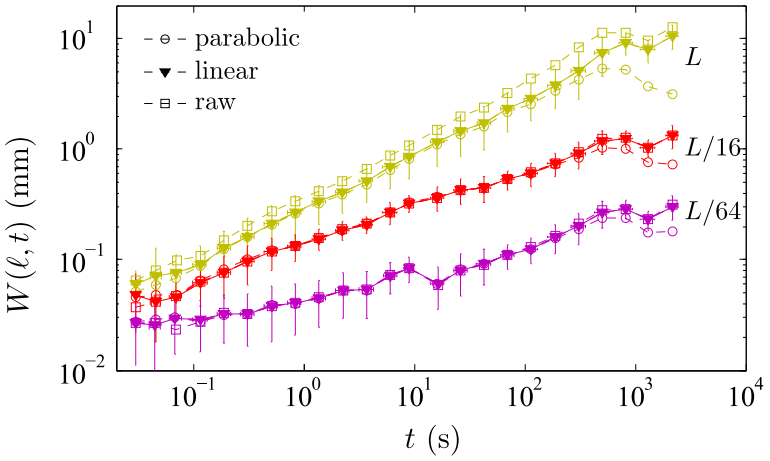

FIGURE 4.2: Statistical width of forced-flow imbibition fronts for three different windows of observation, and three different base-line corrections. Error bars correspond to data obtained after subtracting a linear function. The system lateral width is $L = 160.7$ mm.

small at short times. However, it can modify completely the shape of the front at large times. The general aspect of the interface of experiment `b` is only slightly changed by the correction. However, the interface of experiment `a` is dramatically modified. The large Fourier modes of the front are completely removed, thus changing the nature of the interface.

The effect of the proposed corrections on the statistical properties of the front is shown in Figs. 4.2 and 4.3. Scaling of the front width $W(\ell, t)$ in time is practically not modified by the corrections. Figure 4.2 shows the evolution of $W(\ell, t)$ vs t for three windows of observation. For each ℓ raw data is compared with the result of linear and parabolic subtraction. Differences are observed only beyond the characteristic time at which the statistical width saturates. Therefore the growth exponent β, extracted from the power-law growth in time of $W(\ell = L, t)$, does not change using corrected or raw data.

The behaviour of $W(\ell, t)$ vs ℓ, however, is highly affected by the corrections, specially at long times. The top panel of Fig. 4.3 shows the differences observed at three different times. In all cases the separation between corrected and raw data curves is evident for large ℓ. In addition, the larger t, the larger the difference between parabola-corrected data and raw and linearly-corrected data. Specifically, for the largest time shown, $t = 2500$ s, the power-law regime varies completely, from an exponent $\alpha_{loc} \simeq 0.8$ to 0.95. The bottom panel of the same figure shows $W(\ell, t)$ vs ℓ at $t = 2500$ s for the different experiments analysed (crosses) and their average value (full symbols). The analysis of the interfaces from which a linear fit has been subtracted is shown on the left. In this case all experiments follow the same trend, and so does their average. The evolution

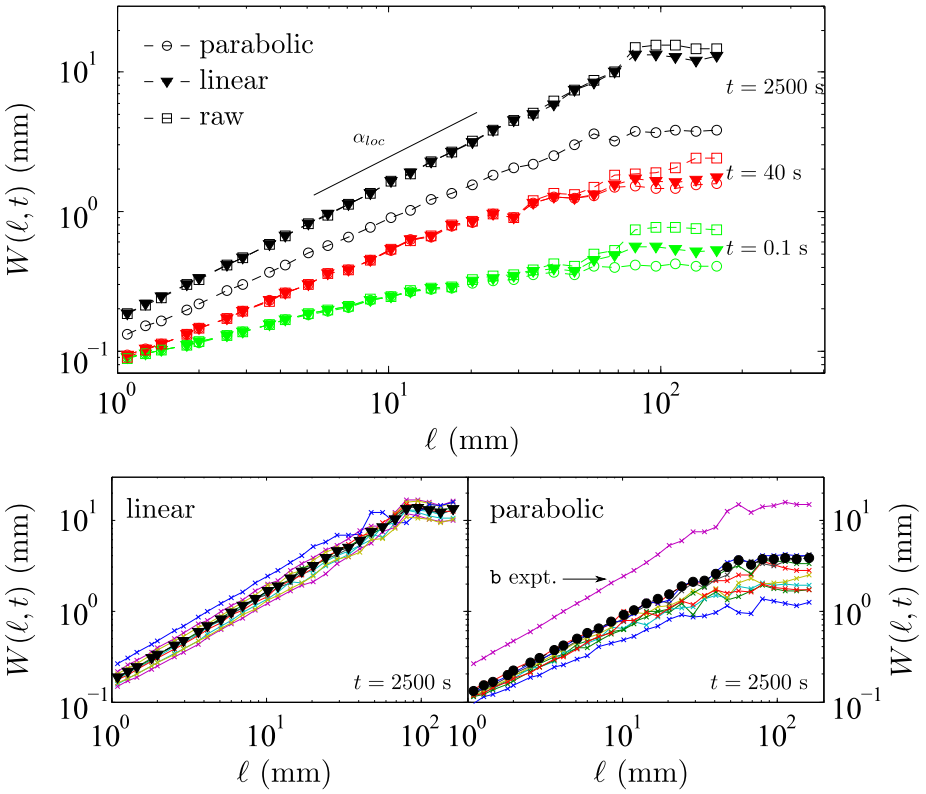

FIGURE 4.3: Statistical width of the interfaces as a function of ℓ. Top: $W(\ell, t)$ is displayed for three times t. The width has been computed with the raw interfaces, subtracting a linear fit, or subtracting a parabolic fit. Big differences are observed for $t = 2500$ s. Bottom: $W(\ell, t)$ for $t = 2500$ s when the linear (left) or parabolic (right) corrections are applied. Crosses represent data points from all experiments analysed. The average width is plotted in full symbols. Experiment `b` changes substantially the average $W(\ell, t)$ for parabolic polynomial subtraction.

of the statistical width for the interfaces from which a parabola has been subtracted is shown on the right panel. Differences at large ℓ are bigger than in the linear-fit case. Even though the majority of the experiments show similar behaviour, one curve separates from all others (corresponding to experiment `b` shown in Fig. 4.1).

We could infer that experiment `b` is pathological. However, observing the left panel, it seems clear that the experiment is also compatible with the others. Large wavelength modes of the interface are expected at long times as the front becomes rougher. Parabolic shapes are favoured by the geometry of the cell, thus making them the most probable modes. These shapes, however, are not artefacts but have physical meaning. From these results, then, we conclude that the second order polynomial correction of the front is not appropriate in our case. Therefore, the analysis presented in the following sections will be based on interfaces corrected by a base-line.

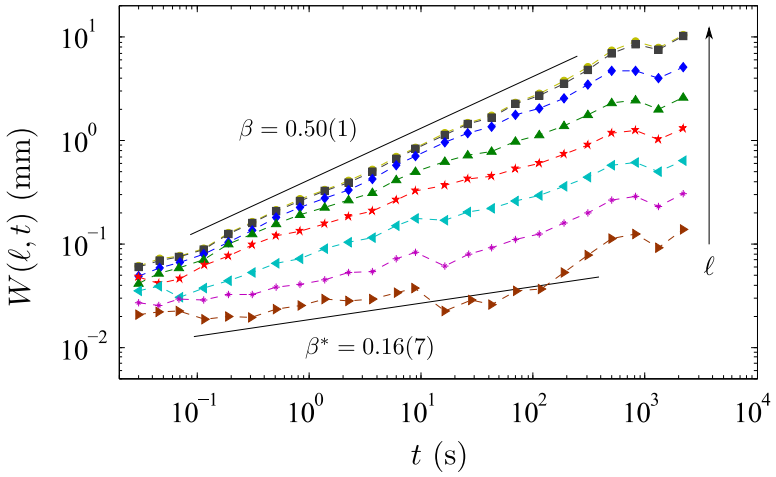

FIGURE 4.4: Double-logarithmic plot of the mean statistical width of the interface as a function of time. Different curves correspond to windows of observation $\ell = L/n$ with $n = 1, 2, 4, 8, 16, 32, 64, 128$. The growth exponents β and β^* are obtained from a linear fit of the log-log plots.

4.2 Scaling exponents

The critical fluctuations of interfaces in a kinetic roughening process are characterized by the scaling exponents described in Sec. 1.4. These exponents are obtained from the behaviour of the statistical width of the front $W(\ell, t)$ with time t or window of observation ℓ, and the behaviour of the power spectrum of the fluctuations $S(q, t)$ with q and t.

Figure 4.4 shows the evolution of the averaged subtracted width of the front $W(\ell, t)$ as a function of t in a double-logarithmic plot. Different windows of observation were analysed: from the system size $L = 160.7$ mm to $L/128 = 1.26$ mm. The width of the front increases following a power law in all cases until it saturates at large time t_s. For the larger scales of observation, the power-law regime extends over almost four decades in time. Interestingly, the power-law exponent for the largest window of observation L is different from the exponent that describes the behaviour at intermediate times for the smallest $\ell = L/128$. This is a signature of *anomalous scaling*.

We extract the growth exponent β from the largest window of observation L. From a linear fit of the data within the scaling regime in double-logarithmic scale we obtain $\beta = 0.50 \pm 0.01$. The local growth exponent is extracted at $\ell = L/128$ giving $\beta^* = 0.16 \pm 0.07$.

Power spectra as a function of q for these data are shown in Fig. 4.5 for different times of analysis: from $t = 0.02$ s to $t = 2000$ s. For large values of q and down to the characteristic $q_\times$, all curves collapse within error bars. Below a characteristic $q_\times$ which depends on time, $q_\times \sim t^{1/z}$, $S(q, t)$ saturates. A linear fit in double-logarithmic scale

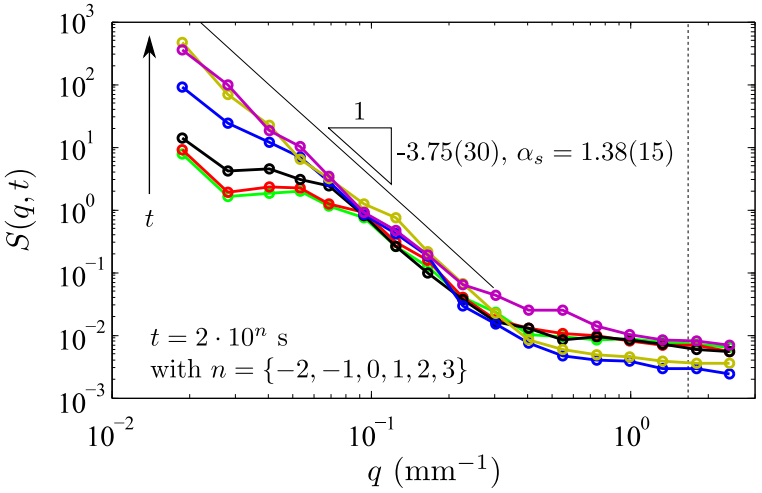

FIGURE 4.5: Double-logarithmic plot of the power spectrum as a function of q at different times. The power-law scaling of $S(q,t)$ with q is equal to $-(2\alpha_s - 1)$, where α_s is the spectral exponent. The vertical dashed line is plotted at the characteristic size of the disorder, $q_d = 1/\ell_d = 1/0.6$ mm^{-1}.

gives the power-law exponent of the power spectra vs q. According to the *general scaling ansatz* –presented in Sec. 1.4.1– this exponent corresponds to $-(2\alpha_s + 1)$. Therefore, $\alpha_s = 1.38 \pm 0.15$.

The collapse of the power spectra for $q > q_\times$, and thus without a systematic vertical shift at different times t, discards intrinsic-anomalous and faceted-interfaces scenarios. Then, the only possible scaling scenario is super-rough. It is confirmed by the measured spectral roughness exponent $\alpha_s > 1$.

We also look at the behaviour of the width of the front $W(\ell, t)$ with the scale of observation ℓ. Figure 4.6 shows the evolution of the subtracted width in a double-logarithmic plot for six different times. $W(\ell, t)$ increases following a power law in all cases until it saturates. For $t = 2500$ s the scaling regime extends over almost two decades in both W and ℓ. The scaling of the fluctuations of the front with ℓ in the statistically stationary regime (large times, when $t > t_s$) gives the local roughness exponent $\alpha_{loc} = 0.97 \pm 0.01$. This result is compatible with the expected $\alpha_{loc} = 1$ of super-rough fronts.

Finally, we can collapse the $W(\ell, t)$ curves by using the values of the exponents obtained, $\beta = 0.50 \pm 0.01$ and $\alpha = 1.38 \pm 0.15$, and the scaling relation $z = \alpha/\beta$. The main plot of Fig. 4.7 shows a good collapse of the data.

4.3 Discussion

Considering the experimental conditions explored, v = 0.13 mm/s and μ = 10 cP, the crossover lengthscale between the two damping mechanisms of the fluctuations of

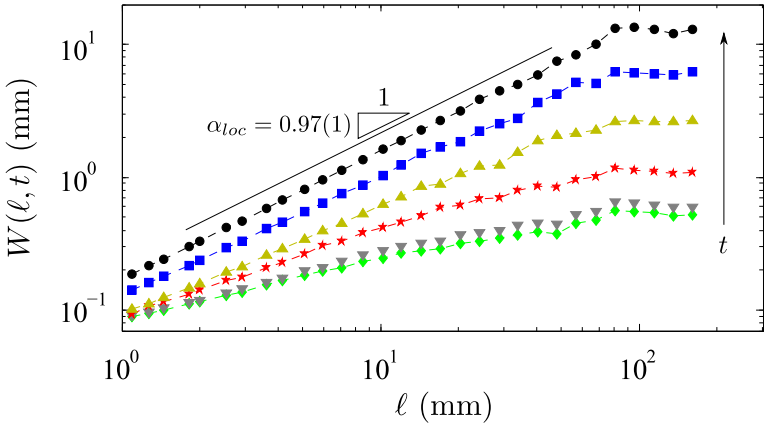

FIGURE 4.6: Double-logarithmic plot of the mean statistical width of the interface as a function of the scale of observation ℓ for times $t = 0.1$, 1, 10, 100, 400, 2500 s. The local roughness exponent α_{loc} is obtained from a linear fit of the log-log data at long times.

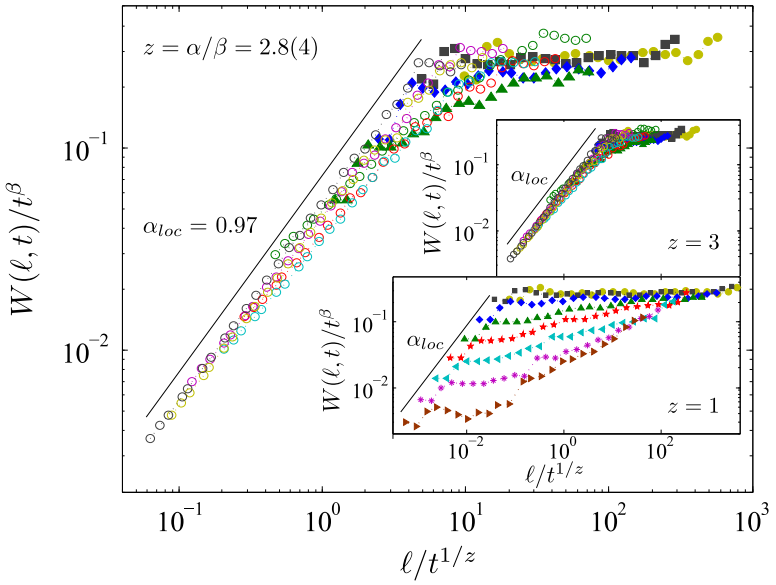

FIGURE 4.7: Collapse of $W(\ell,t)$ in a double-logarithmic plot. Data in main plot have been rescaled using $\beta = 0.50$ and $z = \alpha/\beta$, with $\alpha = 1.38$. The insets show the two limit cases $z = 3$ and $z = 1$, with $\beta = 0.50$. The straight line is a guide to the eye with the slope $\alpha_{loc} = 0.97$ obtained in Fig. 4.6.

	Roughness exponents		Growth exponents		Dynamic exponent
	α	α_{loc}	β	β^*	z
Present results (experimental)	1.38(15)	0.97(1)	0.50(1)	0.16(7)	2.8(4)
Forced-flow (experimental)	1.26(11)	0.82(5)	0.42(2)	0.15(3)	3.0(2)
Spontaneous (experimental)	1.26(15)	0.96(30)	0.41(2)	0.10(3)	3.0(4)
Spontaneous (numerical)	1.50(2)	0.95(3)	0.49(3)	0.20(4)	3.0(1)

TABLE 4.1: Scaling exponents obtained in the present chapter (Present results) compared to exponents measured in super-rough scaling scenarios in imbibition: forced-flow experiments (Planet et al., 2014), spontaneous imbibition experiments (Planet et al., 2007), and spontaneous imbibition phase-field simulations (Pradas and Hernández-Machado, 2006; Pradas, 2009).

the interface –surface tension and viscous pressure drop (Alava et al., 2004)– is $\ell_c = \sqrt{\kappa/\mathrm{Ca}} \simeq 15.3$ mm. The lengthscale at which the two main sources of disorder –capillarity and permeability (Pauné and Casademunt, 2003)– cross over in this situation is $\ell_\times \simeq b_0/(6\mathrm{Ca}) \simeq 1165$ mm. The size of the system is $L = 160.7$ mm, so that $L \ll \ell_\times$. Hence, fluctuations of permeability are negligible in this regime, and front roughening is governed by capillary pressure fluctuations.

Regarding the damping mechanisms of the interfacial fluctuations let us recall the interfacial equation discussed in Sec. 1.3. Considering only the damping terms, a linear approximation in Fourier space reads:

$$\frac{\partial \tilde{h}_q}{\partial t} = -\frac{\gamma\kappa}{\mu}|q|q^2\tilde{h}_q - \mathrm{v}|q|\tilde{h}_q, \tag{4.1}$$

where $\tilde{h}_q$ is the amplitude of the Fourier mode of wave number q of $h(x,t)$.

We can now obtain a theoretical prediction of the dynamic exponent z by imposing scale invariance to the equation under a transformation $x \to bx$, $h \to b^\alpha h$ (in Fourier space $q \to b^{-1}q$, $\tilde{h} \to b^{\alpha+1}\tilde{h}$), and $t \to b^z t$. When surface tension dominates over viscous pressure damping (at low v) we obtain $z = 3$. Conversely, in the regime in which viscous pressure dominates over surface tension damping, $z = 1$. These two limiting cases are analysed in the insets of Fig. 4.7. We observe a data collapse for $z = 3$ but a clear dispersion of the curves for $z = 1$. Hence, the figure confirms that surface tension dominates the damping of the fluctuations. This result also agrees with the dynamic exponent obtained using the scaling relation $z = \alpha/\beta = 2.8 \pm 0.4$, shown in the main plot of the same figure.

A super-rough scaling scenario has been observed in imbibition in forced-flow experiments (Planet et al., 2014), spontaneous imbibition experiments (Planet et al., 2007), and spontaneous imbibition phase-field simulations (Pradas and Hernández-Machado, 2006; Pradas, 2009). The exponents obtained in the present chapter are compared to

those found in the literature in Table 4.1. They show a good agreement within error bars. Interestingly, the results presented in this work for v = 0.13 mm/s and μ = 10 cP are equivalent to the results obtained in a setup equivalent to the setup used in the present Thesis with v = 0.13 mm/s but for a different μ = 50 cP (Planet et al., 2014).

According to Pradas and Hernández-Machado (2006) and Pradas (2009), in the capillary-disorder regime super-roughness is observed when the physical conditions explored imply a low contrast between the opposing forces acting on the interface, i.e. when capillary pressure and driving pressure are comparable.

4.4 Conclusions

We have studied the spatio-temporal fluctuations of the advancing oil-air front during forced-flow invasion of a laboratory model of an open fracture. A constant flow rate implies global conservation of fluid mass per unit time, as well as a linear increase in time of the average position of the front. We have specifically analysed the scale-invariant properties of the interface in a kinetic roughening process, from an initially flat interface to a final, statistically-invariant rough front. Our experiments have been performed with a low viscosity oil for the first time in this setup.

The results show super-roughness scaling. This is the result expected indeed for forced-flow at v = 0.13 mm/s and μ = 10 cP, since the contrast of capillary pressure to applied driving pressure is low (Pradas, 2009).

The correlation length of the interfacial fluctuations along the front increases with time as $t^{1/3}$, denoting that surface tension is the controlling damping mechanism of the process.

We have also checked the effect of subtracting different base-lines from the interfaces. Application of a linear correction to the raw data is justified in order to avoid misorientation of the image acquisition system with the cell. Parabolic corrections, however, should be discarded since they can introduce uncontrolled artefacts that change the roughening properties of the fronts.

Chapter 5

Local spatio-temporal dynamics

In the previous chapter we have studied the morphology of the oil-air interface invading our model of disordered medium in forced flow, and characterized its kinematic roughening process. During this process the spatial fluctuations of the front height $h(x,t)$ grow in time until a statistically-steady state is reached, when fluctuations saturate. In the present and following chapters we study the dynamics of the interface at this statistically-stationary state of saturated front roughness.

In this chapter we specifically focus our attention on the spatio-temporal dynamics of the interfaces at the local scale, that is, at the scale of the spatial resolution, typically much smaller than the correlation length ℓ_c and the characteristic length of the disorder ℓ_d. We base our study on the analysis of the local waiting time fluctuations along the front during its propagation. This method was originally developed to study the dynamics of interfacial cracks (Måløy et al., 2006) and successfully applied to characterize the avalanche dynamics observed in forced-flow imbibition (Planet, 2009; Santucci et al., 2011).

In the present work we go further on the experimental analysis of the dynamics of imbibition fronts at the local scale. First of all, we have largely increased the number of experiments: for each given experimental condition (v, μ) we have performed 15 to 20 experiments with different disorder realizations. This leads to very large data sets, required for accurate statistics and a proper statistical analysis. Moreover, we have increased the range of experimental parameters analysed. Imposed flow rates corresponding to mean velocities of the front spanning more than one decade in the lowest accessible range have been studied, and, more importantly, we have systematically changed the oil viscosity for the first time. Therefore, we have been able to explore forced-flow imbibition dynamics in a wide range of capillary numbers.

The fluctuations of the local velocity signal are analysed both in space and time. We find that the correlation length along the front, ℓ_c, plays a crucial role in controlling

TABLE 5.1: Experimental conditions explored. Dynamic viscosity of the fluids μ, imposed mean velocity v, and their corresponding capillary numbers Ca, nominal correlation length along the front ℓ_c, and percentage of the lateral system size that is correlated, ℓ_c/L, are quoted.

Experimental conditions				
μ (cP)	v (mm/s)	Ca ($\times 10^{-4}$)	ℓ_c (mm)	ℓ_c/L (%)
10	0.126	0.63	15.3	11.2
	0.219	1.09	11.6	8.5
50	0.036	0.90	12.7	9.4
	0.053	1.32	10.5	7.7
	0.131	3.27	6.7	4.9
	0.227	5.68	5.1	3.7
	0.353	8.84	4.1	3.0
	0.553	13.84	3.3	2.4
100	0.051	2.46	7.7	5.7
	0.131	6.26	4.8	3.5
169	0.053	4.27	5.8	4.3
	0.130	10.49	3.7	2.7
350	0.131	21.71	2.6	1.9

the dynamics of the system. Local avalanches have been defined as clusters of high velocity in the velocity map $v(x, y)$. They are widely distributed both in space and time, following power-law distributions with exponential cutoffs. The cutoffs of the distributions diverge as Ca $\to$ 0, when the system becomes fully correlated. We have also put effort into relating the underlying disorder landscape to the evolution of the oil-air interface. Results are compared to earlier experimental studies (Planet, 2009; Santucci et al., 2011) and phase-field simulations (Pradas, 2009; Pradas et al., 2009; López et al., 2010).

For the experiments we have specifically used the D-type disorder plates and velocities ranging from v = 0.036 to 0.55 mm/s and five different oils of viscosities dynamic μ = 10, 50, 100, 169, and 350 cP. The actual values and their corresponding capillary numbers and nominal correlation lengths are quoted in Table 5.1. Details regarding the setup and the properties of the oils used are described in Ch. 2.

5.1 Fluctuations of $v(x, y)$

The experiments presented in this chapter are performed in the statistically stationary regime of the fluid invasion, that is, when the statistical width of the interface saturates in average and does not grow in time. Figure 5.1 shows the evolution in time of the subtracted statistical width of the front $W(L, t)$, where $W^2(L, t) = w^2(L, t) - w_i^2$. As described in Sec. 2.6, $w(\ell, t)$ is the interfacial statistical width about the mean value: $w(\ell, t) = \overline{\langle [h(x, t) - \langle h(x, t)\rangle_\ell]^2\rangle_\ell}^{1/2}$, where ℓ (= L here) stands for the size of the window

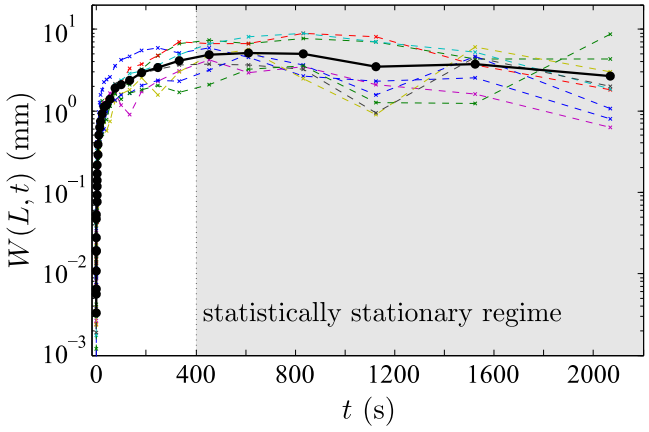

FIGURE 5.1: Log-lin plot of the subtracted width of the interface vs time, for v = 0.13 mm/s and μ = 10 cP. $W(L, t)$ increases in time until it saturates. Dashed lines correspond to individual displacements, and solid dots to their average. The statistically stationary regime is shaded in the plot.

of observation, $\langle \dots \rangle_\ell$ indicates average over the window, and the overline is an average over different realizations of the disorder. w_i is the intrinsic width of the interface.

Local velocities of the front –at the scale of the spatial resolution– are obtained via the procedure developed by Måløy et al. (2006), based on the analysis of the local waiting time of the front. As described in detail in Ch. 2 (Sec. 2.6), the waiting time matrix $wt(x, y)$ gives the amount of time spent by the interface at each position (x, y) of the measuring window. Then, the *local velocity map*, i.e. the velocity at each position (x, y), is directly obtained from:

$$v(x, y) = \frac{r}{wt(x, y) \cdot \delta t}, \tag{5.1}$$

where r is the spatial resolution and δt the increment of time between consecutive images. Another convenient representation is the (local) *activity map*, that is, the spatio-temporal map of local velocities $v(x, t)$, which is computed from $v(x, h(x, t))$.

Figure 5.2 displays local velocity maps for three experiments performed at the same imposed mean velocity v = 0.13 mm/s but different viscosities μ = 10, 50, 350 cP. In all cases regions of high velocities (above v) alternate with regions of low velocities. We clearly observe that these velocity fluctuations around v become larger at smaller viscosities. In particular, regions of local velocities $v \gg$ v become bigger and pinned regions with $v \ll$ v clearly appear. Besides, low-viscosity fronts are rougher than high-viscosity fronts.

The spatio-temporal maps of local velocities for the same three experiments shown in Fig. 5.2 are displayed in Fig. 5.3. Larger velocity fluctuations are evident again at lower viscosities. The clusters of high velocities follow a ballistic propagation in time, as observed in the characteristic v-shaped, darker regions in the map. The lateral extent of these clusters (in the x direction) is related to the lateral correlation length of the front ℓ_c, as will be shown in Sec. 5.2. This branching in v-shapes of the high local velocity clusters defines a time direction, revealing time-irreversibility of the system at the local scale.

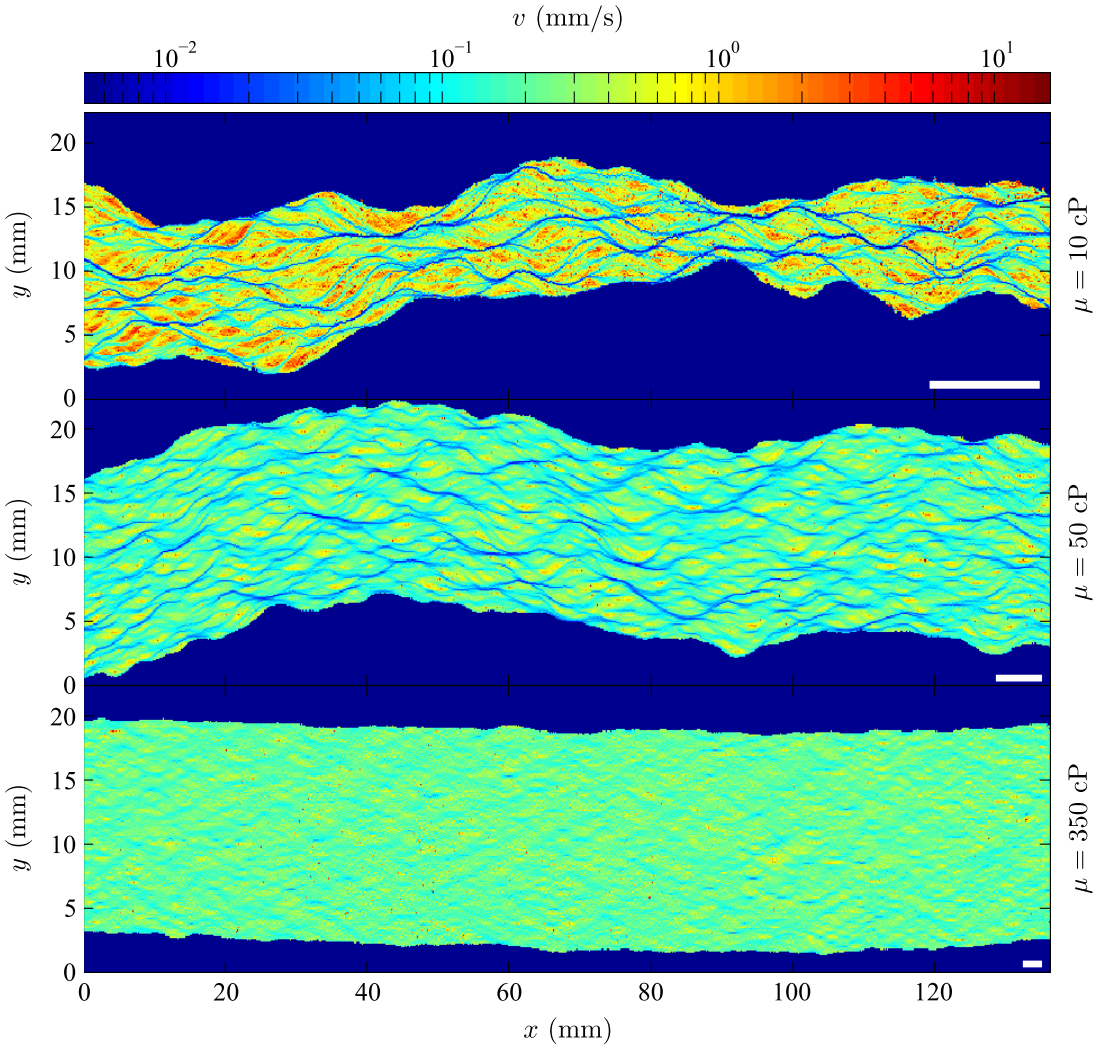

FIGURE 5.2: Velocity maps of three experiments performed at the same v = 0.13 mm/s but different $\mu = 10$, 50, 350 cP (top, middle, bottom). The colourcode for $v(x, y)$ is the same in all cases. The bottom-right white line gives the nominal correlation length $\ell_c = 15.3$, 6.7, 2.6 mm for each experimental condition.

An equivalent behaviour to decreasing μ is observed when v is reduced, and thus equivalent evolution of velocity and activity maps. This suggests that the capillary number $\mathrm{Ca} = \mu \mathrm{v}/\gamma$ (which compares viscous to capillary forces) may control the fluctuations of v. In the following sections we will analyse the front dynamics quantitatively in terms of Ca.

5.1.1 Statistical distributions of local velocities

We first study the statistical distributions of local velocities upon changing the experimental controlling parameters, μ and v. Figure 5.4 shows the distributions of local

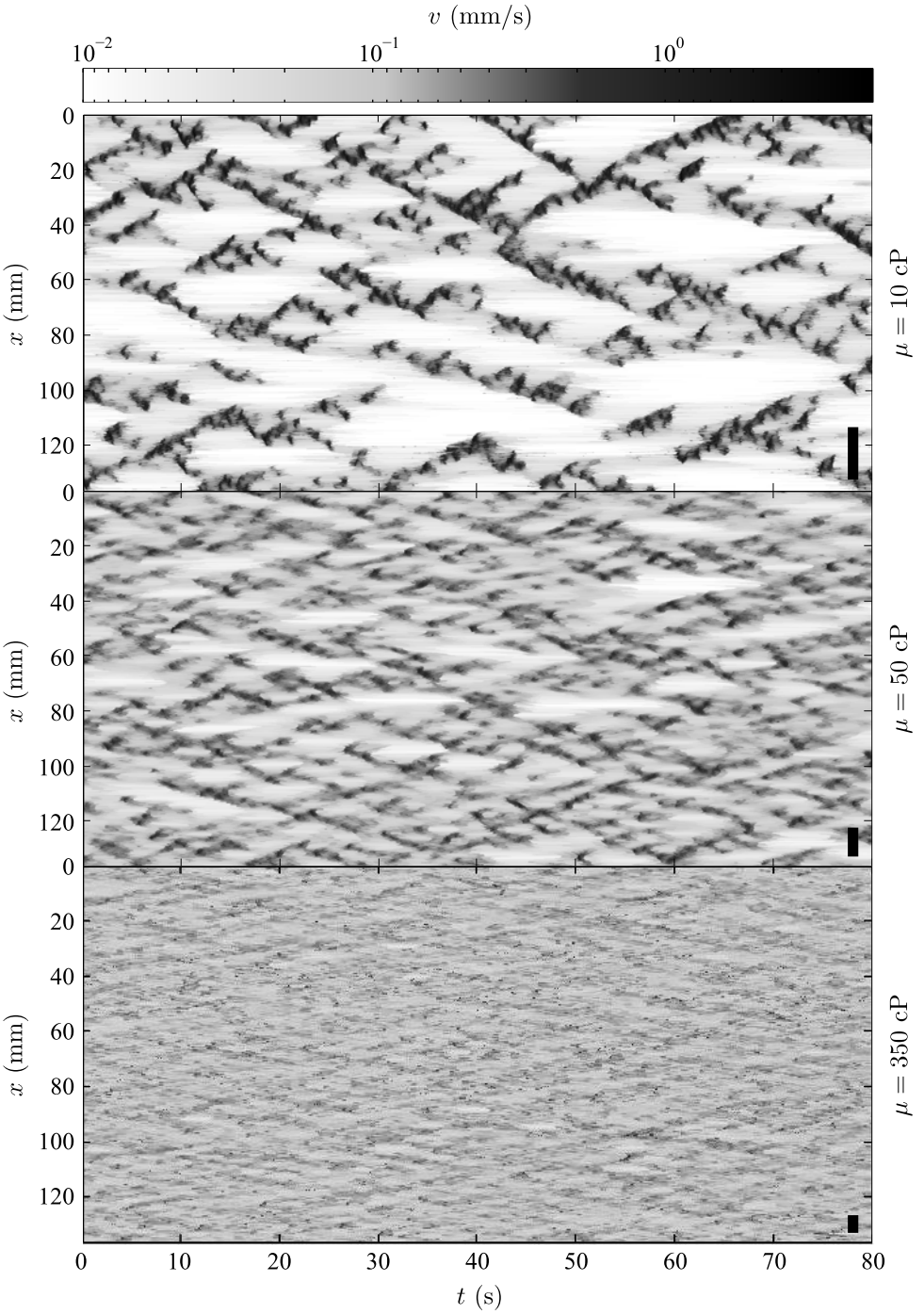

FIGURE 5.3: Spatio-temporal (activity) maps of the same three experiments shown in Fig. 5.2. v = 0.13 mm/s in all cases but $\mu = 10$, 50, 350 cP (top, middle, bottom). The greycode for $v(x, y)$ is the same in all cases. The bottom-right black vertical line gives the nominal correlation length $\ell_c = 15.3$, 6.7, 2.6 mm for each experimental condition.

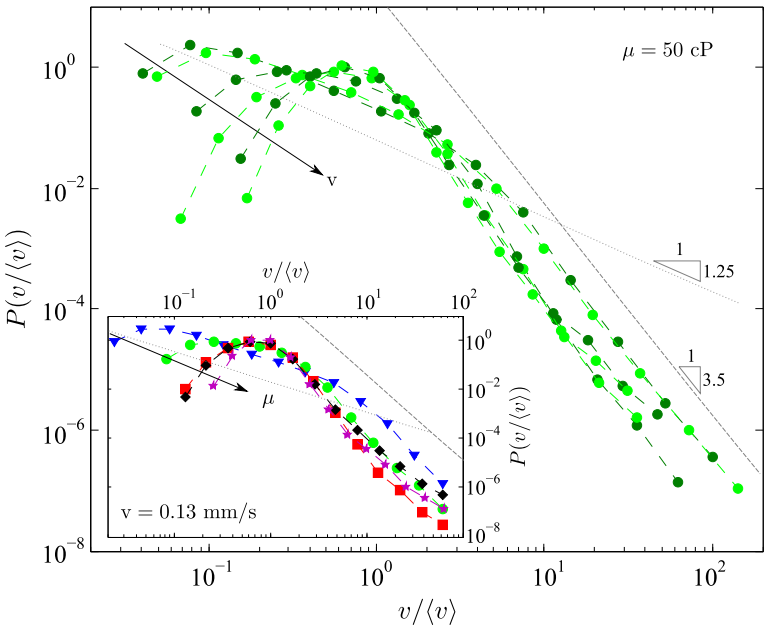

FIGURE 5.4: Distributions of local velocities rescaled by their mean value $P(v/\langle v\rangle)$. Main plot: distributions corresponding to experiments performed with the same oil but different v = 0.036, 0.053, 0.13, 0.23, 0.35, 0.55 mm/s. Inset: distributions corresponding to experiments with different oils of viscosities μ = 10, 50, 100, 169, 350 cP. Dashed and dotted lines are guides to the eye.

velocities rescaled by their mean value $P(v/\langle v\rangle)$. We choose this quantity in order to compare experiments performed at very different v –covering more than one decade. First of all local velocities are widely distributed, spanning a large range of more than three decades. As observed previously in Fig. 5.2, the distributions of local velocities span a wider range for lower μ or v. In all cases distributions show a steep decay at large values of v. This behaviour can be approximated by a power-law decay proportional to $(v/\langle v\rangle)^{-3.5}$. In experiments performed at large v or μ, the pdfs show a maximum slightly below the mean value. However, as v or μ are lowered, the distributions develop a power law around $\langle v\rangle$ and their maximum shifts towards $v < \langle v\rangle$. This power law is well fitted by $(v/\langle v\rangle)^{-1.25}$ in all cases. It spreads over almost two decades in the experiments of lowest viscosity and velocity.

This systematic evolution of the distributions $P(v/\langle v\rangle)$ with μ and v is analysed in terms of the capillary number Ca $\sim \mu$v. The distributions in the left panel of Fig. 5.5 correspond to four different values of Ca including the two extreme values studied Ca $= 6.3 \times 10^{-5}$ and 2.2×10^{-3}. The evolution of the distributions with Ca is clear: as the capillary number is reduced, local velocities span a wider range, developing a power-law regime around $\langle v\rangle$. Conversely, the distributions become more peaked as Ca increases. Remarkably, the pdfs of experiments performed at similar Ca almost collapse on the same curve. This provides strong evidence that the capillary number controls the statistical behaviour of the local velocities of the front.

The evolution of $P(v/\langle v\rangle)$ with Ca can be quantified by measuring the standard deviation of the distributions or their most probable value, for example. These quantities are shown in the right panels of Fig. 5.5. The standard deviation of the velocities rescaled

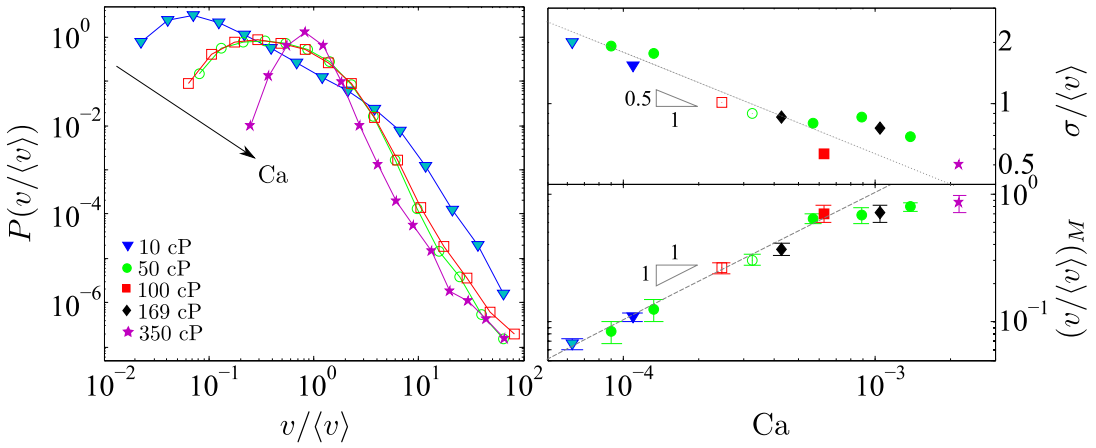

FIGURE 5.5: Left: distributions $P(v/\langle v\rangle)$ for displacements at various Ca $= 6.3\times10^{-5}$, 2.5×10^{-4}, 3.3×10^{-4}, 2.2×10^{-3}. Right: standard deviation of $v(x, y)$ rescaled by the mean value (top) and most probable value of $P(v/\langle v\rangle)$ (bottom) vs Ca. Dashed lines correspond to power laws with the exponents shown, plotted as guides to the eye. In all cases, different symbols (either open or solid) correspond to different dynamic viscosities. The same colour code is used in the left and the right panels.

by $\langle v\rangle$ increases as Ca is reduced (top right panel). The behaviour can be approximated by a power law $\sigma/\langle v\rangle \sim \mathrm{Ca}^{-0.5}$. As for the most probable value of the distributions $(v/\langle v\rangle)_M$ we observe that the maximum of $P(v/\langle v\rangle)$ shifts towards smaller values $v < \langle v\rangle$ as Ca is reduced.

From these results we can infer that the fluctuations of the local velocities of the front are controlled by the capillary number Ca.

We can also study the statistical distributions of the normalized local velocities defined as:

$$Y = \frac{v - \langle v\rangle}{\sigma}. \tag{5.2}$$

The pdfs for all experiments are shown in Fig. 5.6. Again, all of them show a peak around the mean value and an abrupt decay at large v, as previously observed in Fig. 5.4. Interestingly all data collapse for $Y > 1$, that is, when fluctuations are one σ larger than the mean velocity of the experiment. We will come back to this observation when local avalanches are analysed in Sec. 5.2.

5.1.2 Spatial and temporal correlations of $v(x, h(x, t))$

Spatial correlation along the front

In the statistically stationary regime, interfaces are expected to be correlated along the front up to a distance ℓ_c (Alava et al., 2004). As we have shown in detail in Sec. 1.3, this length is given by $\ell_c = \sqrt{\kappa/(\mu \mathrm{v})}$. Planet et al. (2009) verified experimentally that

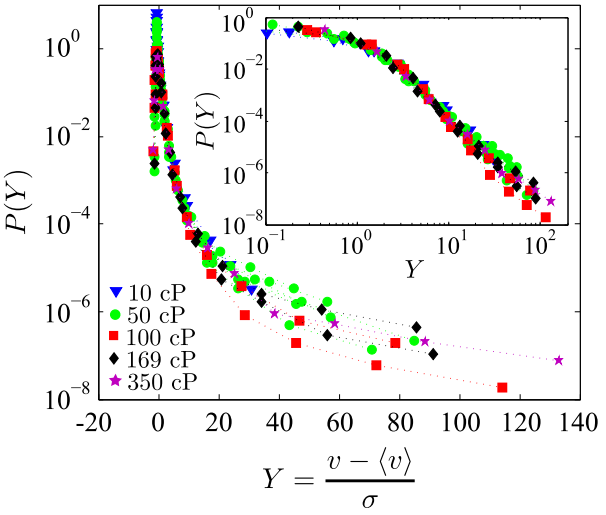

FIGURE 5.6: Distributions of normalized local velocities –at the scale of spatial resolution– in a semilog plot (main) and a log-log plot for the positive values (inset). Results are shown for all experiments, but different v are not differentiated.

imbibition fronts display indeed lateral spatial correlations that obey $\ell_c \sim 1/\sqrt{\mathrm{v}}$. We now examine this spatial correlation for a wider range of experimental conditions by computing the autocorrelation function of the local velocities along the front:

$$C_v(\Delta\ell) = \overline{\left\langle \Big(v(\ell+\Delta\ell) - \langle v(\ell)\rangle\Big)\Big(v(\ell) - \langle v(\ell)\rangle\Big) \right\rangle_\ell}. \tag{5.3}$$

$\langle v(\ell)\rangle$ is the average velocity within the window of size ℓ, $\langle\cdots\rangle_\ell$ is the average over all windows $\ell \in [0, L-\Delta\ell]$ along the interface, and $\overline{\cdots}$ is the ensemble average over interfaces recorded at different times.

Figure 5.7 shows the systematic evolution of C_v with imposed flow rate for a given viscosity (left panel), and the evolution of C_v with viscosity for a given mean velocity (right panel). By definition $C_v = 1$ –maximum correlation– for $\Delta\ell = 0$, and becomes 0 when the signal becomes completely uncorrelated. We observe that the autocorrelation of the local velocities decays with $\Delta\ell$ in all cases, reaches a minimum below zero –i.e. maximum anticorrelation– at $\Delta\ell^*$, and then increases again towards zero, until the signal becomes fully uncorrelated at large $\Delta\ell$.

The evolution of the lengthscale $\Delta\ell^*$ is plotted as a function of the nominal correlation length ℓ_c in Fig. 5.8 (solid symbols). The lengthscale $\Delta\ell^{min}$ at which the signal becomes fully uncorrelated is also displayed in the figure (open symbols). For all experimental conditions (μ, v) explored $\Delta\ell^*$ and $\Delta\ell^{min}$ are proportional to ℓ_c. The values of $\Delta\ell^*$ are systematically smaller than ℓ_c while the values of $\Delta\ell^{min}$ are systematically larger than ℓ_c. This result confirms that ℓ_c controls indeed the lateral spatial correlation of the interface. For the first time, it shows experimentally that μ and v play the same role on controlling ℓ_c.

Equivalent information can be extracted from the analysis of the statistical width $W_v(\ell)$ of the fluctuations of v over windows of size ℓ along the front. $W_v(\ell)$ increases

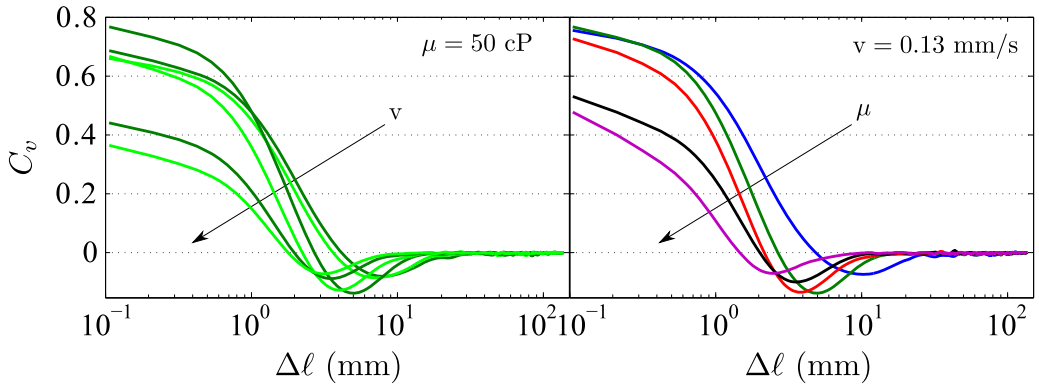

FIGURE 5.7: Autocorrelation of local velocities along the front. Left: experiments performed at different imposed mean velocities v = 0.036, 0.053, 0.13, 0.23, 0.35, 0.55 mm/s. Right: experiments using different oils of dynamic viscosities μ = 10, 50, 100, 169, 350 cP.

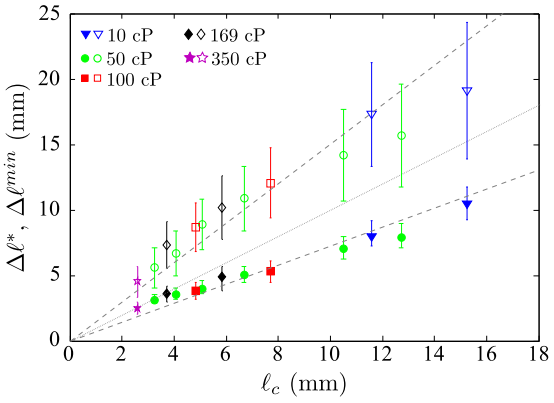

FIGURE 5.8: Lateral length scales of the maximum anticorrelation ($\Delta\ell^*$, solid symbols) and decorrelation ($\Delta\ell^{min}$, open symbols), extracted from Fig. 5.7, vs the nominal correlation length ℓ_c. Different velocities are plotted for each μ, with $\ell_c \sim 1/\sqrt{\text{v}}$. Dashed lines are guides to the eye. The dotted line has slope 1.

with ℓ until it saturates above a characteristic lenghtscale ℓ^* as observed in Fig. 5.9. The transition between the scaling and the saturated regimes is smooth, making more difficult to extract ℓ^* from this plot than to obtain the characteristic length $\Delta\ell^*$ from C_v. However, Planet et al. (2011) used this method to show that $\ell \sim 1/\sqrt{\text{v}}$ in experiments with one single oil, i.e. one single viscosity. Here we extend this result to experiments performed in more varied conditions (velocities and viscosities). The characteristic lengthscale ℓ^* evolves similarly with μ and v, and the results are compatible with $\ell^* \sim \ell_c$. Nevertheless, we observe that μ and v play a different role on the local dynamics of the front, and, specifically, on the amplitude of the velocity fluctuations, $W_v(\ell)$. Fluctuations are larger the smaller μ but, on the contrary, fluctuations are also larger the larger v, as observed on the top and bottom panels of Fig. 5.9, respectively.

Temporal correlation

We now analyse the temporal correlation of local velocities –at the scale of the spatial resolution– by computing the autocorrelation of the signal $v(x, t)$ in time, and taking

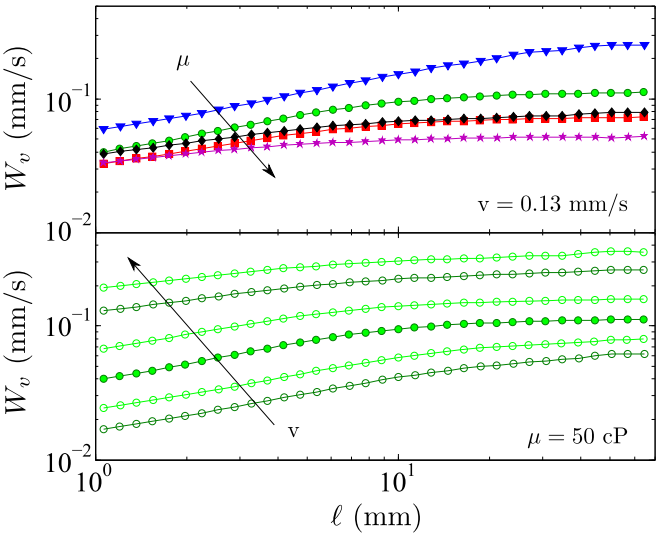

FIGURE 5.9: Statistical width of local velocities as a function of the window of observation ℓ. Top: experiments using different oils of viscosities μ = 10, 50, 100, 169, 350 cP. Bottom: experiments performed at different imposed mean velocities v = 0.036, 0.053, 0.13, 0.23, 0.35, 0.55 mm/s.

the ensemble average over different positions x along the front:

$$C_v(\Delta t) = \overline{\left\langle \Big(v(t+\Delta t) - \langle v(t)\rangle\Big)\Big(v(t) - \langle v(t)\rangle\Big)\right\rangle_t}. \tag{5.4}$$

$\langle v(t)\rangle$ is the average velocity within the temporal window Δt, $\langle\cdots\rangle_t$ is the average over all the temporal windows of $v(x,t)$ such that $t \in [0, t_{\max} - \Delta t]$, and $\overline{\cdots}$ is the ensemble average over velocity signals analysed at different position x and different realizations of the experiment.

$C_v(\Delta t)$ is shown in Fig. 5.10 for different experimental conditions. Its qualitative behaviour is similar to the spatial autocorrelation function displayed in Fig. 5.7. C_v decays as Δt increases until it reaches a minimum value below zero –maximum anticorrelation– at Δt^*. For larger time lags, local velocities become uncorrelated in time and $C_v \to 0$. On the left panel of figure 5.10 the evolution of C_v clearly shows that Δt^* is achieved at larger time lags the slower the front advances. On the right panel, the evolution of C_v with oil viscosity seems less clear. However, a careful analysis (inset) reveals that Δt^* increases for lower viscosities. Finally, although the range of imposed velocities explored ($\mathrm{v}_{max}/\mathrm{v}_{min} = 15$) is smaller than the range of viscosities ($\mu_{max}/\mu_{min} = 35$), Δt^* varies much more with v than with μ.

Figure 5.11 displays the evolution of Δt^* for all experimental conditions explored as a function of the capillary number $\mathrm{Ca} \sim \mathrm{v}\mu$. It makes clear that velocity and viscosity do not play the same role in controlling Δt^* –unlike it happens with $\Delta \ell^*$ discussed before. The dashed line goes through experiments performed at different v but same μ and is proportional to a power law $\mathrm{v}^{-1.4}$. Experiments at the same v but different μ correspond to the dotted line, that goes as $\mu^{-0.4}$.

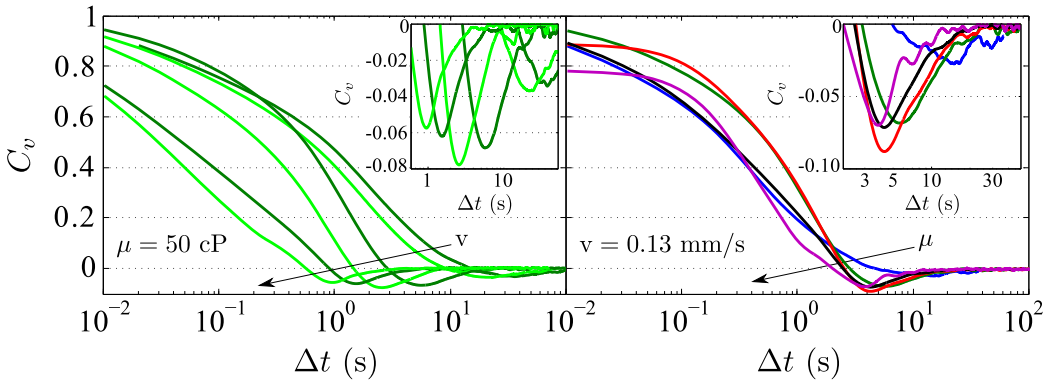

FIGURE 5.10: Autocorrelation of local velocities as a function of time lag Δt. Left: experiments performed at different flow rates corresponding to v = 0.036, 0.053, 0.13, 0.23, 0.35, 0.55 mm/s. Right: experiments using different oils of viscosities μ = 10, 50, 100, 169, 350 cP. Insets are zooms around the minima.

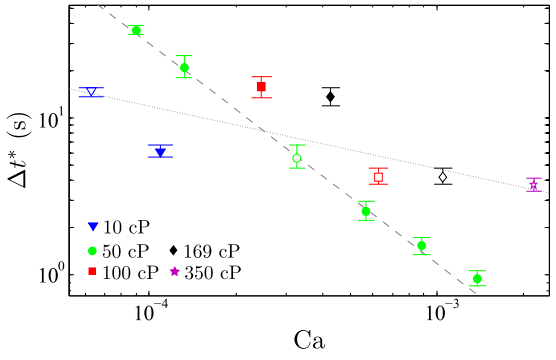

FIGURE 5.11: Maximum anticorrelation time Δt^* extracted from Fig. 5.10 as a function of the capillary number Ca. Dashed and dotted lines are guides to the eye proportional to $v^{-1.4}$ and $\mu^{-0.4}$, respectively. Open symbols correspond to experiments performed at v = 0.13 mm/s.

The autocorrelation of the front in time is noisier at large values of Δt than $C_v(\Delta \ell)$ for large $\Delta \ell$. Then, it is more difficult to extract a characteristic decorrelation time corresponding to $C_v(\Delta t)$ becoming zero. Thus, although we may have underestimated its actual value, we have chosen Δt^* as the characteristic decorrelation time of the front.

Spatial correlation in the direction of propagation

We finally study the correlation of $v(x, y)$ in the direction of propagation of the front. In this case we do not consider the temporal information of the position of the front explicitly. Instead, we analyse directly the correlation of the velocities of the interface in y, and compare it with the underlying quenched disorder. Figure 5.12 displays the autocorrelation functions $C_v(\Delta y)$ for experiments performed with different oil viscosities (solid lines). Again, in all cases the correlation decays with Δy until it reaches a minimum, negative value –maximum anticorrelation. After the minimum, C_v increases and saturates to 0 –fully uncorrelated signal. The curves plotted for $\Delta y > 1$ have been smoothed. At these scales the curves fluctuate but follow a systematic general trend. The average value of the fluctuations is well captured by the smoothed curves.

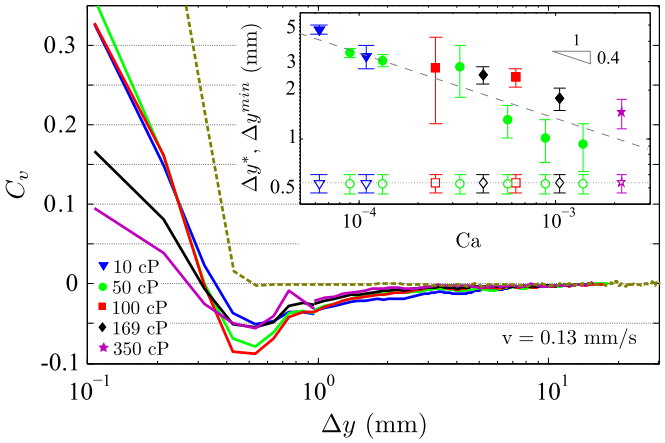

FIGURE 5.12: Autocorrelation of local velocities in the direction of propagation y for experiments performed using different oil viscosities (solid curves). The spatial correlation of the disorder is also shown (dashed line). Inset: Δy^* (open symbols) and Δy^{min} (full symbols) vs Ca. The dotted line corresponds to the length-scale Δy of decorrelation of the disorder. The dashed line is a guide to the eye proportional to $\mathrm{Ca}^{-0.4}$.

We define Δy^* as the value of Δy where C_v reaches its minimum. We also define a second quantity, Δy^{min}, as the value of Δy where (the smoothed) C_v becomes 0 after the minimum. These quantities are plotted in the inset of the figure as functions of the capillary number. Δy^* (open symbols) remains constant over all the range of Ca explored. On the contrary, Δy^{min} decreases with Ca. Its behaviour, analysed in Sec. 5.2.1, can be approximated by $\mathrm{Ca}^{-0.4}$.

We can compare these results to the underlying disorder in the cell. We consider the disorder landscape as a matrix with elements $d(x, y)$ equal to 1 on the disorder patches and 0 otherwise. Then the autocorrelation function of $d(x, y)$ in the direction of propagation of the front (dashed line in Fig. 5.12) can be compared to the autocorrelation function C_v of the fronts (solid lines in the same figure). In tune with the nominal lateral extent of the disorder patches (0.4 mm) and with the characteristic lateral extent of the clusters of disorder patches ($\ell_d = 0.6$ mm), the disorder is highly correlated up to $\simeq 0.3$ mm, from where the autocorrelation of $d(x, y)$ decays abruptly and becomes zero at $\Delta y_d = 0.54 \pm 0.05$ mm.

The value Δy_d at which the disorder becomes fully uncorrelated is compared to the experimental values Δy^* and Δy^{min} in the inset of the figure. A strong influence of the disorder patches on the local dynamics of the interface in the propagation direction y is clearly observed: the maximum anticorrelation is achieved at $\Delta y^* = \Delta y_d$, indicating that the largest fluctuations of the local velocity occur within the characteristic size of the disorder patches ℓ_d. However, the relaxation of those large fluctuations is controlled by the capillary number.

5.2 Local avalanches

In the previous section we have studied the fluctuations of the velocities of the fluid front measured at the scale of the spatial resolution. In particular we have found that

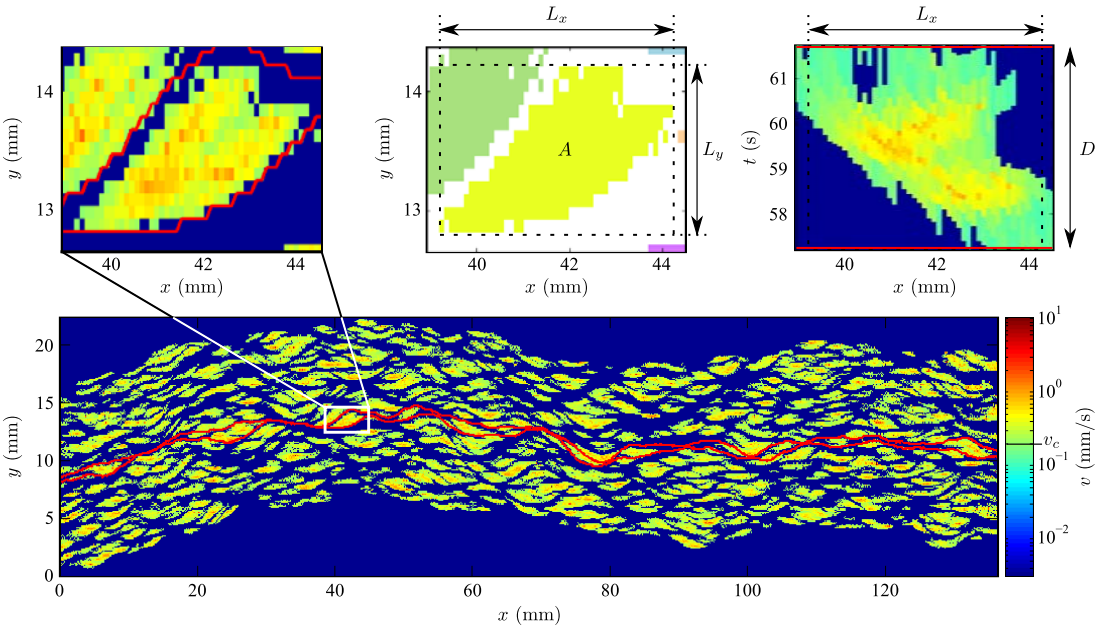

FIGURE 5.13: Definition of local avalanches. Bottom: velocity map after clipping: local velocities $v < v_c$ are all plotted in dark blue. The first and last interfaces in contact with the avalanche highlighted are shown. Top left: close-up of the selected avalanche. Top middle: definition of area, A, and lateral sizes, L_x and L_y, of the avalanche. Top right: close-up of the same avalanche on the activity map $v(x,t)$. The duration D of the avalanche and L_x are displayed. Experimental conditions: v = 0.13 mm/s and $\mu = 50$ cP.

imbibition interfaces present large spatial and temporal correlations. These strong fluctuations and large correlations lead to a burst-like dynamics as observed earlier on the velocity maps of Fig. 5.2.

We now study the spatio-temporal dynamics of imbibition fronts in terms of local avalanches. We define **local avalanches** as *spatially-connected clusters of velocities* $v(x,y)$ *higher than a given velocity threshold* v_c.

The threshold used throughout this chapter is

$$v_c = \langle v \rangle + c\sigma, \tag{5.5}$$

where $\langle v \rangle$ is the mean velocity of the front during the experiment –the temporal and spatial average of the activity map $v(x,t)$–, σ its standard deviation, and c an arbitrary constant.

Local avalanches are characterized by their size A, given by the area of the cluster of high velocities; their duration D, given by the time interval elapsed from the moment that a first interface enters the cluster of high velocities to the moment that a last interface leaves the cluster; and their lateral extent L_x and L_y in the directions x and y. The definition of these quantities is shown in Fig. 5.13.

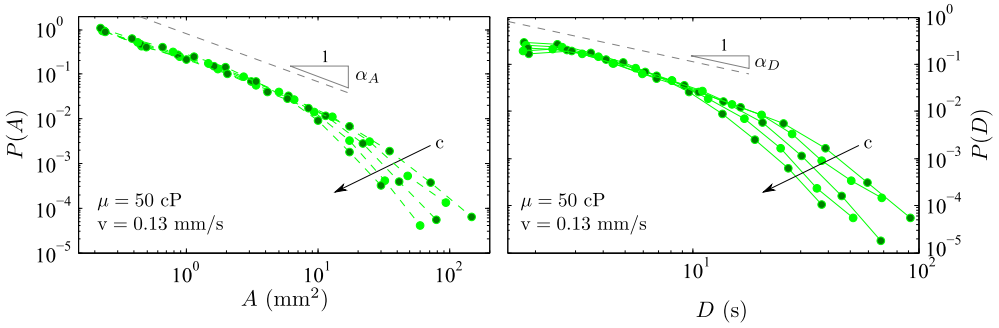

FIGURE 5.14: Distributions of sizes (left) and durations (right) of local avalanches for one experimental condition and different clip levels $c = 1, 1.5, 2, 2.5, 3$. α_A and α_D are the power-law exponents obtained for $P(A)$ and $P(D)$.

The size of a disorder patch introduces a natural lower cutoff of avalanche sizes. We will only consider as avalanches clusters of high velocity that span more than one disorder patch. This implies that the minimum avalanche size is $A_{min} = 0.4 \times 0.4$ mm^2.

5.2.1 Statistical characterization of local avalanches

In this section we analyse the statistical properties of sizes, durations, and morphologies of local avalanches.

We first study the effect of the clip v_c on the statistical distributions. In earlier experimental works on imbibition (Planet, 2009; Santucci et al., 2011) the threshold for the velocities was defined as $\tilde{v}_c = c\langle v \rangle$. This corresponds to considering as avalanches regions of large velocity compared to $\langle v \rangle$. However, as shown earlier in Fig. 5.4, the distributions of $v/\langle v \rangle$ for different experiments do not collapse. This indicates that the underlying statistics of $v/\langle v \rangle$ is different for each (μ, v). If we instead consider the distributions of the normalized variable:

$$Y = \frac{v - \langle v \rangle}{\sigma}, \tag{5.6}$$

the pdfs for all experimental conditions explored almost collapse for $Y > 1$, as previously shown in Fig. 5.6. The choice $v_c = \langle v \rangle + c\sigma$ is thus more appropriate, since fixing c is equivalent to examine avalanches of velocities above a given value of Y. Then, in order to consider local avalanches of statistically-equivalent local velocities, we choose clip levels $c > 1$. This will allow us to compare experiments performed at very different conditions (μ, v).

Distributions of sizes $P(A)$ and durations $P(D)$ of local avalanches are shown in Fig. 5.14 for one experimental condition and various clip levels c. All distributions follow a power law with a decaying cutoff at large values. The power-law exponent, α_A for sizes and α_D for durations, is the same in all cases independently of the clip within the

range of c explored. However, c plays a role in the cutoff of the distributions. As we increase the clip level we reduce the size of the high-velocity clusters, and also their durations. Increasing c cuts the largest avalanches and, thus, the power-law range of the distributions is also reduced.

Having checked that the clip v_c only affects the cutoffs of the distributions but it does not modify the scaling of the power-law regime, we select $c = 2$ in all subsequent analysis in order to compare experiments performed with different (μ, v).

As it is shown throughout this section, the distributions of the various properties of the avalanches –size, duration, lateral extents– can be approximated by a power-law with an exponential cutoff, i.e. have the general form $P_x(x) = a_x x^{-m_x} e^{-x/\xi_x}$. The cutoff depends on the controlling parameters of the experiment and the clip level, and $\xi_x \sim \langle x \rangle^{1/(2-m_x)}$ when $m_x < 2$. As previously described in detail in Sec. 1.5, to obtain a reliable value for the power-law exponent of the distributions, a good procedure –as described by Pruessner (2010) and Planet et al. (2010)– is to find the value m_x^* that provides the best collapse of $\mathcal{Y} = P(x)\langle x \rangle^{m_x/(2-m_x)}$ vs $\mathcal{X} = x/\langle x \rangle^{1/(2-m_x)}$. This method is applied here to obtain the exponents for the distributions of A, D, L_x, and L_y. For some particular experimental conditions, however, the pdfs may only display the exponential decay. The corresponding data will be discarded to extract a power-law exponent.

Distributions of sizes and durations

Figure 5.15 shows the distributions of sizes for various experimental conditions. $P(A)$ follows a power law with an exponential cutoff. The power-law exponent is independent of the imposed mean velocity of the front or the viscosity of the fluid, as observed on the left and the right panels of the figure, respectively. In all cases the power-law regime displays the same exponent

$$\alpha_A = 1.09 \pm 0.08. \tag{5.7}$$

This exponent is compatible with the value reported earlier in the literature for experiments of imbibition in open fracture models, $\alpha_A = 1.08 \pm 0.05$ (Santucci et al., 2011). However, it differs from $\alpha_A = 1.54 \pm 0.05$ obtained in phase-field simulations by Pradas (2009), Pradas et al. (2009) and López et al. (2010).

The scaling range of the distributions, and thus the cutoffs, however, do depend on v and μ. The evolution of ξ_A with v is quite clear and systematic. The slower the fluid is pushed through the medium, the bigger the avalanches can be. On the contrary, the evolution of ξ_A with viscosity is less clear. Nevertheless, in general we observe that the smaller μ the bigger the avalanches can be. The evolution of the cutoffs with both experimental parameters is analysed quantitatively at the end of this section.

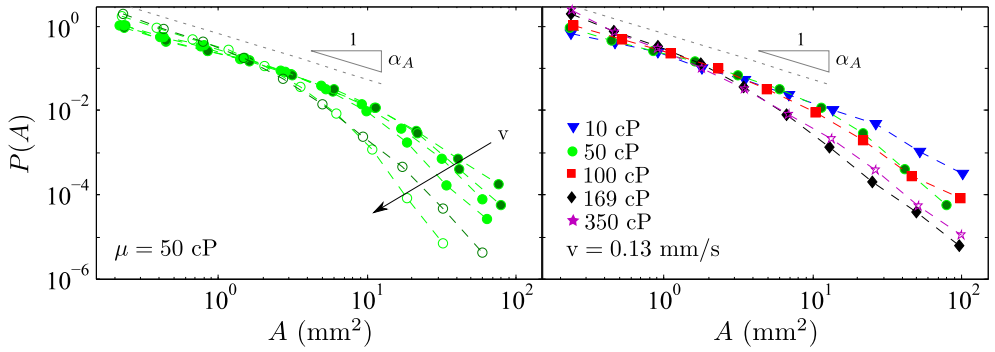

FIGURE 5.15: Distributions of sizes of local avalanches. Left: evolution of the pdfs with the imposed mean velocity v = 0.036, 0.053, 0.11, 0.16, 0.22, 0.35, 0.55 mm/s. Open symbols correspond to ill-behaved distributions. Right: evolution of the pdfs with oil viscosity μ. In both cases $\alpha_A = 1.09 \pm 0.08$.

The distributions of durations of local avalanches are displayed in Fig. 5.16 for the same experimental conditions shown in the previous figure. Again, the distributions show a power-law regime with an exponential cutoff. The power-law exponent is the same for all distributions irrespectively of the experimental conditions:

$$\alpha_D = 1.03 \pm 0.10. \tag{5.8}$$

In this case the exponent differs from the value obtained from earlier experiments where $\alpha_D = 1.24 \pm 0.10$ (Santucci et al., 2011), although they are almost compatible within error bars. The result from phase-field simulations is very different, $\alpha_D = 1.62 \pm 0.06$ (Pradas et al., 2009).

The effect of the controlling parameters (v, μ) on the avalanche durations is manifested in the evolution of the cutoffs, which measure the maximum duration of the bursts of fast motion. ξ_D evolves systematically with the mean velocity of the front, as clearly observed on the left panel of Fig. 5.16. The faster the front, the shorter the avalanches. On the contrary, the evolution of ξ_D with viscosity is not obvious. The scaling of ξ_D with μ and v is analysed and discussed at the end of this section.

Morphology of avalanches

The shape of local avalanches is not isotropic. High-velocity clusters are larger in the lateral direction x than in the direction of front advancement y, as can be observed in Fig. 5.13.

The statistical distributions of lateral extents L_x and L_y, perpendicular and parallel to the advancement of the front, are displayed in Fig. 5.17 for a number of experimental conditions. Both $P(L_x)$ and $P(L_y)$ are power-law distributed with exponential cutoffs.

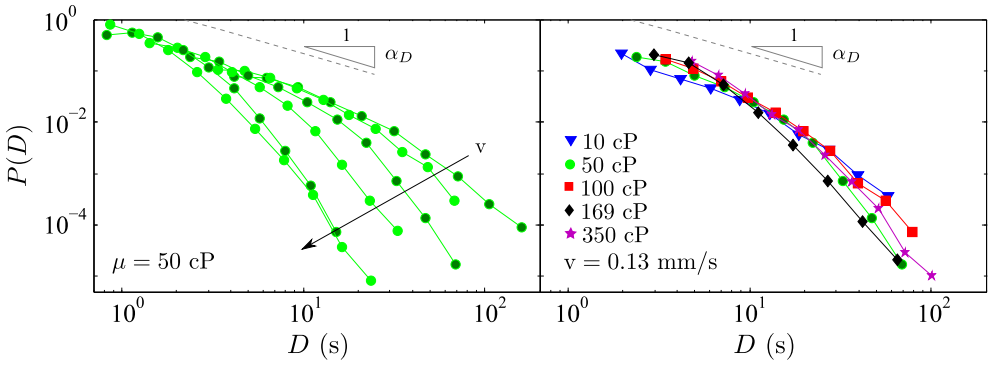

FIGURE 5.16: Distributions of durations of local avalanches. Left: evolution of the pdfs with the imposed mean velocity v = 0.036, 0.053, 0.11, 0.16, 0.22, 0.35, 0.55 mm/s. Right: evolution of the pdfs with oil viscosity μ. In both cases $\alpha_D = 1.03 \pm 0.10$.

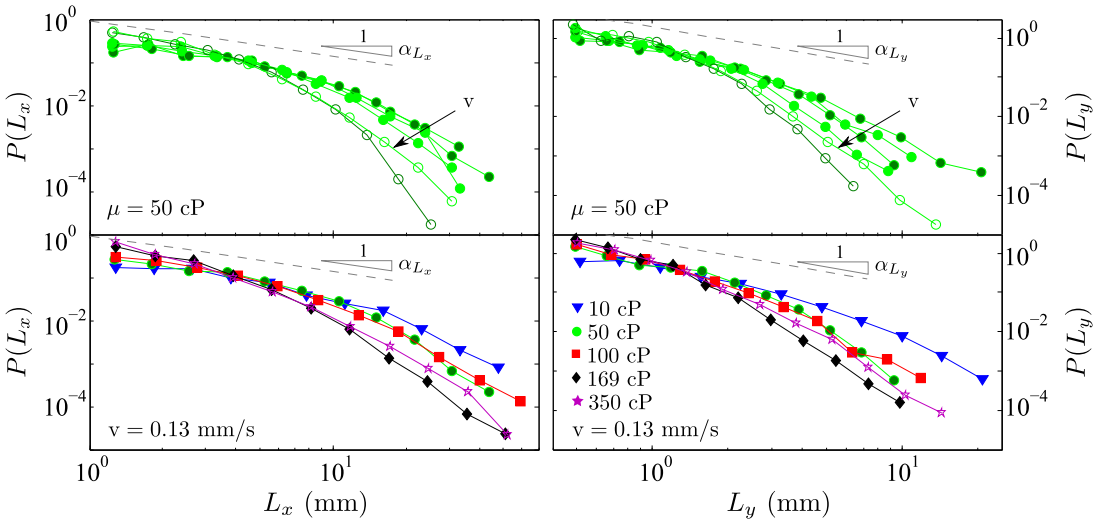

FIGURE 5.17: Distributions of lateral extents L_x (left) and L_y (right) of local avalanches. The range of velocities shown in the top panels is v = 0.036, 0.053, 0.13, 0.23, 0.35, 0.55 mm/s. The bottom panels show the evolution of the pdfs with viscosity. The exponents obtained are $\alpha_{L_x} = 0.83 \pm 0.10$, and $\alpha_{L_y} = 1.08 \pm 0.15$.

The power-law exponents α_{L_x} and α_{L_y} do not depend sensibly on the experimental conditions. Their values are

$$\alpha_{L_x} = 0.83 \pm 0.10, \quad \text{and} \quad \alpha_{L_y} = 1.08 \pm 0.15. \tag{5.9}$$

The exponent of $P(L_x)$ is in very good agreement with earlier experimental results (Santucci et al., 2011) where $\alpha_{L_x} = 0.82 \pm 0.15$ was obtained. As for α_{L_y}, experimental values are only reported in (Planet, 2009) who obtained $\alpha_{L_y} = 0.75 \pm 0.20$.

Contrary to the power-law exponents, the range in which these distributions follow a power law depends on both v and μ. Therefore, the cutoffs ξ_{L_x} and ξ_{L_y} evolve with experimental conditions. This evolution is discussed at the end of the section.

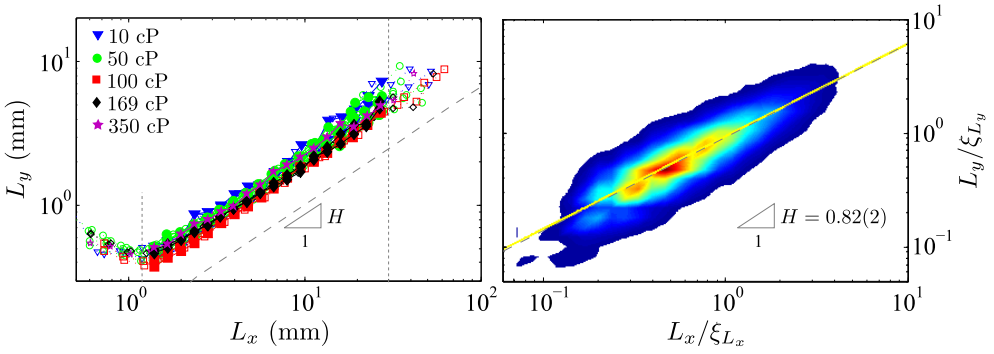

FIGURE 5.18: Left: Joint distributions of $P(L_x, L_y)$. Results for all experiments are shown, but different velocities are not distinguished. Full symbols represent data used to obtain H. Vertical dotted lines show the lower and upper limits of the range of L_x considered. Right: rescaled joint distributions of the data within the scaling range. The power-law exponent is obtained from a linear fit of the log-log data. The colour code corresponds to the density of events and increases from dark blue to red.

In order to quantify the anisotropic shape of the local clusters of high velocities we analyse the joint distribution $P(L_x, L_y)$. We expect a scaling relation $L_y \sim L_x^H$ between the most probable values, where the exponent H is a measure of the anisotropy, and $H = 1$ corresponds to isotropic shape. The joint distributions $P(L_x, L_y)$ corresponding to all experiments studied in the present chapter are shown in Fig. 5.18. The left panel displays the average of the 2D histograms of the distributions for each experiment. We observe a scaling range where $L_y \sim L_x^H$. At small values of L_x the distributions clearly bend. This is a consequence of windowing, resulting from the fact that we consider only avalanches larger than the size of a disorder patch $A_d = 0.4 \times 0.4$ mm^2. Not taking into account avalanches of $A < A_d$ implies that very narrow avalanches –small L_x– are underrepresented and, therefore, must be disregarded. We choose to consider avalanches with $L_x > 1.2$ mm, i.e. two times ℓ_d, the characteristic length of the medium heterogeneities (defined in Sec. 2.2). Bending of the joint distribution is also observed at large values of L_x. We cut the distributions for $L_x > 30$ mm, which corresponds to $2\ell_c$ for the largest ℓ_c explored. Data within these two limits are represented using full symbols in the figure, while the excluded points are shown in open symbols.

To obtain a more reliable value of H, we consider the joint distribution of L_x and L_y rescaled by their cutoffs ξ_{L_x} and ξ_{L_y}. The right panel of Fig. 5.18 shows the 2D histogram corresponding to all the avalanches within the range of L_x chosen. A linear fit to the data in log-log scale is used to obtain the exponent:

$$H = 0.82 \pm 0.02. \tag{5.10}$$

This result is in very good agreement with the value $H = 0.81 \pm 0.05$ reported earlier for the same kind of imbibition displacements using one single oil viscosity (Santucci et al.,

2011).

Characteristic sizes and durations of avalanches

The cutoffs ξ_A, ξ_D, ξ_{L_x}, and ξ_{L_y} represent characteristic values of the maximum size, duration, and extent in the x and y directions of the local avalanches.

Let us recall now that the correlation length along the front ℓ_c defines the extent of the correlations of the fluctuations of the interface height in the x direction. Planet (2009) and Santucci et al. (2011) showed that the lateral extent of the local avalanches is also bounded by ℓ_c. They observed that $\xi_{L_x} \sim 1/\sqrt{\mathrm{v}}$ for one single viscosity. Then, given that $\ell_c \sim 1/\sqrt{\mu \mathrm{v}}$, they concluded that $\xi_{L_x} \sim \ell_c$. We extend this result now by including the effect of viscosity. The dependence of the cutoffs of L_x on capillary number is shown in the top left panel of Fig. 5.19. Given that $\mathrm{Ca} \sim \mu \mathrm{v}$, this representation of the data allows us to compare the dependence on both μ and v on the same plot. We observe that the cutoffs diverge as $\mathrm{Ca} \to 0$, and that the evolution is compatible with $\xi_{L_x} \sim 1/\sqrt{\mu \mathrm{v}} \sim 1/\sqrt{\mathrm{Ca}}$. In the bottom left panel of the figure we compare the cutoffs (solid symbols) with the distance $\Delta\ell^*$ of maximum anticorrelation of the front obtained in Sec. 5.1.2 (open symbols). ξ_{L_x} and $\Delta\ell^*$ are plotted vs the nominal value of ℓ_c. Both quantities show a linear relation with ℓ_c, reflecting that the lateral extent of local avalanches is indeed bounded by the correlation length ℓ_c. However, the actual values are slightly larger (ξ_{L_x}) or smaller ($\Delta\ell^*$) than the nominal ℓ_c, as a consequence of the dependence on the clip level of the former or on the particular criterion chosen to define the latter. Nevertheless, this result reinforces the notion that μ and v play the same role in controlling the lateral extent of the avalanches.

It is worth noting that for the largest v and μ (largest Ca) the smallest avalanches may be underrepresented in Fig. 5.17. In these cases the nominal correlation length can be as small as 2.6 mm. Given that their maximum size is bounded by ℓ_c, we expect a large number of tiny avalanches. However, because of the constraints arising from the size of the disorder patches, that impose a minimum size $A_d = 0.16$ mm^2 of the local avalanches, and the windowing effect, we only consider events whose lateral extent is $L_x > 1.2$ mm. Hence the expected tiny avalanches are disregarded. Since the pdfs are normalized, the occurrence of large events might be overestimated, and the distributions distorted. In summary, we probably overestimate the cutoffs of the distributions of sizes, durations, and lateral extents for the largest capillary numbers.

Having established that $\xi_{L_x} \sim \ell_c \sim 1/\sqrt{\mathrm{Ca}}$, several scaling relations between the cutoffs of the other properties of the local avalanches can be derived (Santucci et al., 2011).

From the anisotropic shape of the avalanches, characterized by $L_y \sim L_x^H$, we can infer that the cutoffs of these distributions will also scale as $\xi_{L_y} \sim \xi_{L_x}^H$, and thus $\xi_{L_y} \sim \ell_c^H \sim$

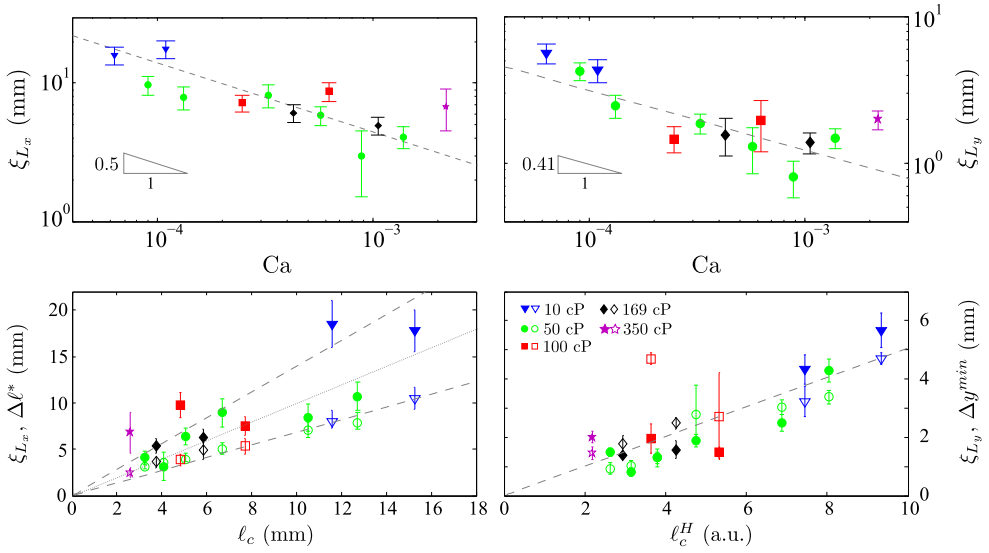

FIGURE 5.19: Top panels: evolution of the cutoffs of $P(L_x)$ (left) and $P(L_y)$ (right) with capillary number in double-logarithmic scale. Dashed straight lines are guides to the eye with the exponents shown in the figure. Bottom left: cutoffs ξ_{L_x} and maximum lateral anticorrelation lengths $\Delta\ell^*$ vs the nominal correlation length ℓ_c. Bottom right: cutoffs ξ_{L_y} and decorrelation lengths in the direction of propagation Δy^{min} vs ℓ_c^H, where $H = 0.82$ is the anisotropy exponent. Dashed straight lines are guides to the eye. The dotted line has slope 1. Different symbols correspond to different viscosities.

$\mathrm{Ca}^{-H/2} \sim \mathrm{Ca}^{-0.41}$. The cutoffs ξ_{L_y} vs Ca are shown on the top right panel of Fig. 5.19. The data are compatible with the expected scaling. We can also compare ξ_{L_y} to the correlation lengths in the direction of propagation Δy^{min} obtained in Sec. 5.1.2. These quantities are plotted vs ℓ_c^H in the bottom right panel of the figure. The proportionality of both ξ_{L_y} and Δy^{min} with ℓ_c^H shows that the local dynamics is strongly controlled by the avalanches.

The size of local avalanches can be approximated by the product of their lateral extents $A \sim L_x L_y$. Therefore, their maximum value is expected to scale as $\xi_A \sim \xi_{L_x}\xi_{Ly} \sim \xi_{L_x}^{1+H} \sim \mathrm{Ca}^{(1+H)/2} \sim \mathrm{Ca}^{-0.91}$. The evolution of ξ_A with Ca is shown in the left panel of Fig. 5.20. The result is consistent with the scaling proposed. It reinforces the results of Santucci et al. (2011), and extend them to a larger range of velocities and also to different viscosities.

Finally, we consider the cutoff ξ_D of the durations of the local clusters of high velocity. This boundary can be estimated as the time spent on average by the front in advancing a distance ξ_{L_y}, the maximum extent of an avalanche in the direction of propagation. The average velocity of the front is v. Therefore, we expect $\xi_D \sim \xi_{L_y}/\mathrm{v} \sim \ell_c^H/\mathrm{v} \sim \mu^{-H/2}\mathrm{v}^{-(1+H/2)}$. The right panel of Fig. 5.20 displays the evolution of ξ_D with Ca. The behaviour of ξ_D is compatible with the scaling relation proposed, even though the error bars for this observable are specially large. In Fig. 5.21 we compare the evolution of ξ_D

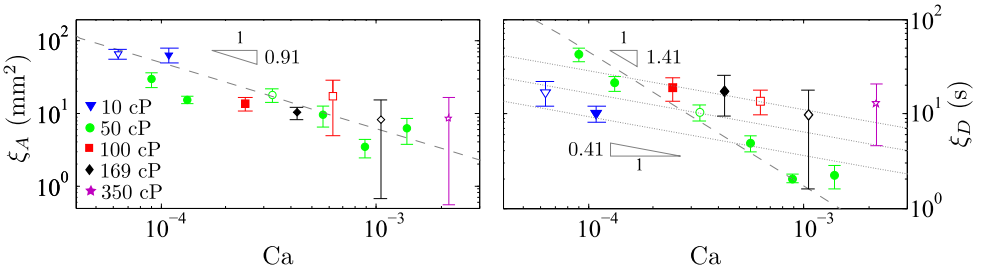

FIGURE 5.20: Evolution of the cutoffs of $P(A)$ (left) and $P(D)$ (right) with the capillary number in log-log scale. Dashed and dotted straight lines are guides to the eye with the exponents shown in the figure. Different symbols (either open or solid) correspond to different viscosities. The values of the experiments performed at v = 0.13 mm/s are represented by open symbols.

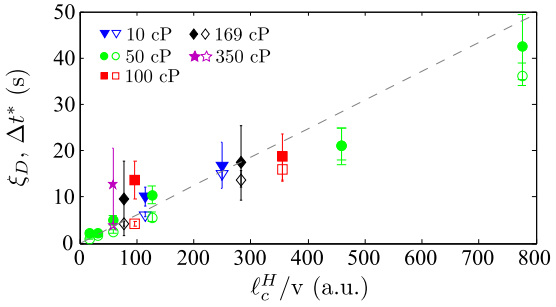

FIGURE 5.21: Cutoffs of $P(D)$ (solid symbols) and maximum anticorrelation time Δt^* (open symbols) vs ℓ_c^H/v, an estimation of the maximum duration of local avalanches. The dashed line is a guide to the eye. Different symbols correspond to different viscosities. For the same viscosity, slower experiments have larger ℓ_c^H/v.

(solid symbols) and the correlation time Δt^* (open symbols) with ℓ_c^H/v, estimation of the maximum duration of the avalanches. ξ_D and Δt^* are of the same order and show proportionality with ℓ_c^H/v. This result indicates that the temporal correlations of the local velocities –at the scale of the spatial resolution– are controlled by the dynamics of the local bursts of fast motion of the interface.

5.2.2 Scaling relations

We have shown that slowly-driven imbibition interfaces advancing through our laboratory model of an open fracture display avalanche dynamics. The statistical properties of the local avalanches –sizes, durations and lateral extensions– are power-law distributed with a cutoff that diverges as Ca $\to 0$. Such behaviour is understood in the framework of a pinning-depinning transition, where avalanches are expected to be scale invariant at the critical pinning point (Alava et al., 2004).

Close to the critical point, avalanches are also expected to be scale invariant but only up to the cutoff scale imposed by a finite correlation length ℓ_c. If we consider a transformation $L_x \to bL_x$, sizes and durations of avalanches scale as $A \to b^{d_{av}} A$ and $D \to b^{z_{av}} D$, where d_{av} is the avalanche dimension exponent and z_{av} the avalanche dynamic exponent (Pradas, 2009; López et al., 2010; Santucci et al., 2011). Since $A \sim$

$L_x L_y \sim L_x^{1+H}$, the avalanche dimension exponent can be also written as $d_{av} = 1 + H$. From the scaling of these observables it follows that:

$$L_x \sim D^{1/z_{av}} \quad \text{and} \quad A \sim D^{\gamma_{av}}, \tag{5.11}$$

where $\gamma_{av} = (1 + H)/z_{av}$.

The top and middle panels of Fig. 5.22 show the joint distributions $P(L_x, D)$ and $P(A, D)$ in double-logarithmic scale. In both cases, the distributions have been rescaled by their cutoffs to include all experiments.

We observe a clear scaling of A/ξ_A with D/ξ_d (top panel of Fig. 5.22). The exponent obtained from the fit is $\gamma_{av} = 1.8 \pm 0.1$. This value agrees within error bars with the experimental result obtained by Santucci et al. (2011), $\gamma_{av} = 1.6 \pm 0.2$. It however differs significantly from the exponent $\gamma_{av} = 1.28 \pm 0.04$ obtained by Pradas et al. (2009) from phase-field simulations.

The scaling of L_x/ξ_{L_x} with D/ξ_D gives an exponent $z_{av} = 1.10 \pm 0.12$ (middle panel of Fig. 5.22). The value is in very good agreement with previously reported results by Santucci et al. (2011), $z_{av} = 1.1 \pm 0.1$. A value $z_{av} \simeq 1$ corresponds to a ballistic lateral propagation of the avalanches $L_x \sim D$. Again, the measured value differs from the one obtained in phase-field simulations, $z_{av} = 1.59 \pm 0.15$ Pradas et al. (2009).

Using the exponents obtained experimentally, the scaling relation $\gamma_{av} = (1 + H)/z_{av}$ is then fulfilled within error bars.

We finally show the joint distribution $P(A, L_x)$ in the bottom panel of Fig. 5.22. A power-law scaling of the most probable values of the joint distribution is observed again. In this case the power-law behaviour is compared to the expected $A \sim L_x^{1+H}$. The value $H = 0.82$ obtained earlier in Sec. 5.2.1 is compatible with the scaling of the joint distribution.

If we consider that the joint distribution of sizes, durations and lateral extents is scale invariant, $P(A, D, L_x) = b^{\sigma} P(b^{1+H} A, b^{z_{av}} D, b L_x)$ for any factor $b > 0$. The marginal distributions $P(A)$, $P(D)$ and $P(L_x)$ are obtained by integration over the other two arguments. The following scaling relations among exponents are then obtained (Pradas et al., 2009):

$$\alpha_D - 1 = \frac{1 + H}{z_{av}}(\alpha_A - 1), \quad \text{and} \quad \alpha_D - 1 = \frac{1}{z_{av}}(\alpha_{L_x} - 1). \tag{5.12}$$

Given that the values $\alpha_A = 1.09 \pm 0.08$, $\alpha_D = 1.03 \pm 0.10$, and $\alpha_{L_x} = 0.83 \pm 0.10$ obtained experimentally are only slightly different from 1, it is very difficult to fully validate these scaling relations.

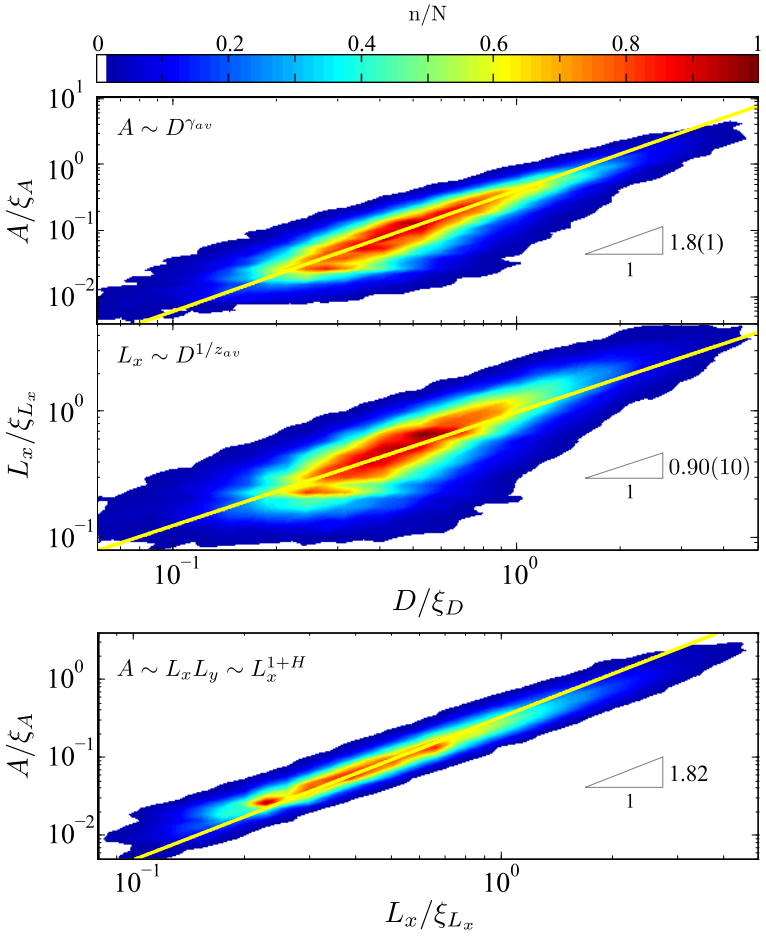

FIGURE 5.22: Joint probability distributions of A (top) and L_x (middle) with D, rescaled by the cutoffs of their individual pdfs. All experimental data are shown. The power-law exponents are obtained from a least-square linear regression in double-logarithmic scale. The bottom panel shows the joint distribution of A and L_x rescaled by their respective cutoffs. The solid line is a power law with exponent $1+H = 1.82$.

All in all, we have shown that local avalanches of motion of the forced-flow imbibition fronts in our model of disordered medium fulfil the scaling relations expected close to a critical depinning transition. However, the actual values of the exponents differ significantly from the numerical values obtained in phase-field simulations of the problem (Pradas et al., 2009; López et al., 2010). As pointed out by Santucci et al. (2011), this could arise from the nature of the disorder. In our case the disorder patches have a finite size, while in phase-field simulations the disorder is point-like. The fact that we are not right at the critical pinning point –the lateral correlation length extends only up to 11 % of the system size– may also have en effect on the scaling behaviour of the local velocities.

5.2.3 Effect of the disorder on the dynamics of the interface

Thanks to the very high control of the disorder in our setup and the high spatial resolution of our image acquisition system, we are able to compare directly disorder patches with local bursts of velocity.

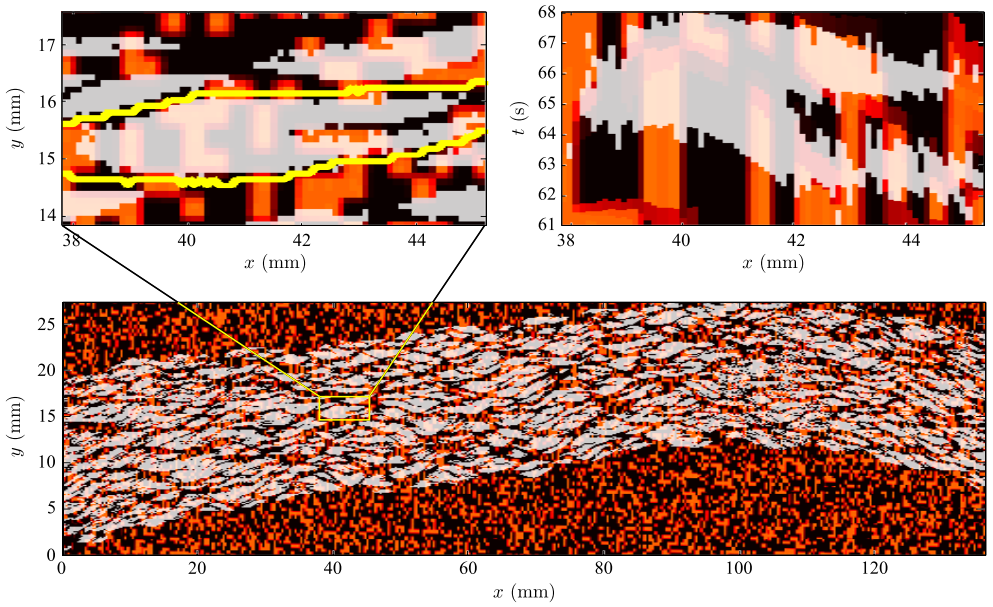

FIGURE 5.23: Comparison of local avalanches with the disorder patches in the plate underneath. Bottom panel: Velocity map in (x, y) space. Top panels: close-up of a single avalanche in the (x, y) (left) and (x, t) spaces (right). Local avalanches are depicted in white. The colour code for the disorder ranges from orange (no disorder patch in the pixel) to black (disorder occupying the whole pixel).

Figure 5.23 displays the clipped velocity map corresponding to an experiment with v = 0.13 mm/s and $\mu = 50$ cP, on top of the disorder landscape explored by the front. Velocities above $v_c = \langle v \rangle + 2\sigma_v$ are shown in white, while velocities below are not displayed. Then, the white clusters observed in the figure correspond to local avalanches –as defined in Fig. 5.13. Disorder patches –copper islands that reduce the gap spacing of the cell– are represented in black, and the disorder-free regions in orange. Since the disorder matrix does not coincide with the matrix of pixels of the image, some pixels are only partially filled by disorder patches. For this reason the pixel colour scale ranges from orange (no disorder patch) to black (disorder). The bottom panel shows the whole velocity map (x, y) of the experiment. The top panels show a close-up of a single avalanche on the velocity map (x, y) and on the activity map (x, t) (left and right, respectively).

We observe that the geometry of the local disorder bears no direct correlation with the clusters of high velocities. To quantify this effect we measure the amount of disorder swept by the front during a local avalanche, i.e. the amount of copper patches within a cluster of fast motion. Figure 5.24 shows the area of disorder swept by each local avalanche vs the area of the corresponding avalanche. These magnitudes are proportional to each other with a proportionality coefficient 0.35. This means that the amount of disorder below a local avalanche is 35 % on average. This value corresponds to the nominal filling fraction of the disorder patches –as detailed in Sec. 2.2. Therefore,

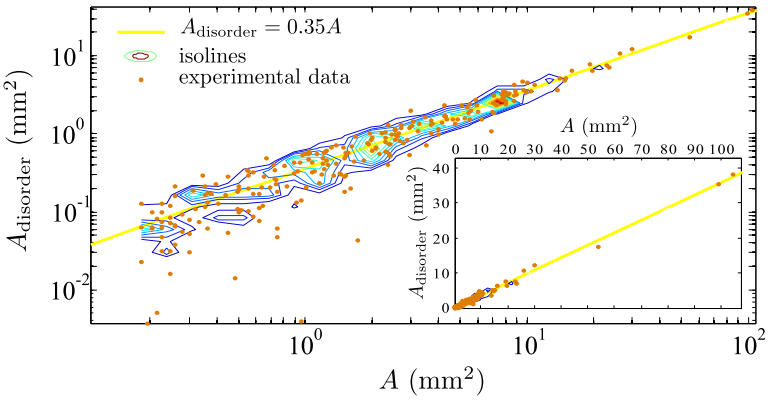

FIGURE 5.24: Area of disorder swept by each local avalanche as a function of size of the corresponding avalanche, in double-logarithmic scale (main plot) and in lin-lin scale (inset). Data correspond to the experiment shown in Fig. 5.23.

avalanches occupy any region of the cell with no particular preference for the underlying disorder patches. This result also reflects the fact that the front dynamics on a single site is highly dependent on the dynamics at all other sites. Non-locality makes forced-flow imbibition intrinsically different (and substantially more complex) than most other dynamic problems involving slowly driven fronts in disordered landscapes.

5.3 Conclusions

We have analysed the local spatio-temporal dynamics of forced-flow imbibition fronts in a model open fracture. A wide range of experimental conditions has been explored. We have used different oils with dynamic viscosities $\mu = 10$ to 350 cP, and imposed flow rates that produced mean velocities of the front ranging from v = 0.036 to 0.55 mm/s. Corresponding capillary numbers ranged from 6×10^{-5} to 2×10^{-3}, and the lateral correlation length along the front took values $3 < \ell_c < 15$ mm. The large number of experiments for each set of parameters (μ, v) with different disorder realizations has led to large data sets, allowing an accurate statistical analysis.

Local velocities of the front fluctuate around the imposed mean value due to the heterogeneities of the medium, and have been shown to be widely distributed. The range of amplitudes of the velocities and the specific shape of the distributions are controlled by the capillary number Ca. In particular, the velocities span a wider range as Ca decreases, approaching the critical pinning-depinning transition.

We have shown that imbibition fronts exhibit large spatial and temporal correlations. The two parameters of the system (μ, v) play the same role in controlling the correlations in space. Specifically, we have experimentally shown for the first time that $\ell_c \sim 1/\sqrt{\mathrm{Ca}}$ for both μ and v. The dependence of the correlations in time, however, is much stronger on the mean imposed velocity than on the viscosity of the fluid.

The interfaces display avalanche dynamics controlled by the correlation length ℓ_c (Santucci et al., 2011). In the present work we extend this result to a larger range of v, and verify its validity also for different μ.

The statistical properties of the local avalanches –sizes, durations and lateral extents– are power-law distributed with an exponential cutoff that diverges as Ca $\to$ 0, understood in the framework of the pinning-depinning transition (Santucci et al., 2011). We have also extended the validity of these observations to a larger range of v, and to different μ. It has allowed to corroborate experimentally for the first time the different evolution of ξ_D with μ and v, $\xi_D \sim \ell_c^H/\mathrm{v} \sim \mu^{-H/2}\mathrm{v}^{-(1+H/2)}$.

The power-law exponents that characterize the different properties of local avalanches fulfil the scaling relations proposed in the literature. However, the actual values of the power-law exponents differ from those obtained in phase-field simulations. We attribute this difference to the different nature of the disorder.

We have finally observed that local avalanches are not directly correlated with the disorder landscape. We have checked that the amount of disorder patches swept by the front during a local avalanche corresponds to a 35 % of the area of the avalanche. This value corresponds to the nominal filling fraction of disorder, indicating that local avalanches occur at any region of the cell.

Chapter 6

Global spatio-temporal dynamics

In the previous chapter we have analysed the burst-like dynamics of the front at local scale. Our high-resolution setup allows us to measure the velocity of the front at scales much smaller than the lateral correlation length ℓ_c of the interface. However, this information is not accessible in a wide variety of systems showing an equivalent intermittent dynamics. As explained in Sec. 1.5.2, in those cases a spatially-averaged, *global* signal is analysed instead.

This global observable is known as *crackling noise* when the system response to a slow, external driving is in the form of intermittent avalanche dynamics (Sethna et al., 2001). Those avalanches are scale-free at the critical or near-critical point of the system, and have a typical average shape. The fluctuations of those global quantities in spatially-correlated systems has attracted much attention in recent years, triggered by the seminal work of Bramwell, Holdsworth and Pinton (1998). As described in detail in Sec. 1.5.2, the distributions of those fluctuations are not Gaussian and are well fitted by a generalized Gumbel distribution (Portelli et al., 2001).

In this chapter we study the properties of the spatially-averaged (global) velocity of the oil-air interface in forced-flow imbibition experiments. Specifically, we analyse the effect of the two physical controlling parameters explored, viscosity μ and imposed mean velocity v, and the scale of observation ℓ on a number of observables: the fluctuations of the global velocity $V_\ell(t)$, the temporal correlations of the signal, and the properties of the avalanches including the distribution of sizes and durations, and their average shape. The intermittent character of the front is analysed in detail in Ch. 7.

We have used the D disorder cells, velocities ranging from v = 0.036 to 0.55 mm/s, and five viscosities μ = 10, 50, 100, 169, and 350 cP. Details regarding the setup and the properties of the oils used are described in Ch. 2.

6.1 Fluctuations of $V_\ell(t)$

The *spatially-averaged (global) velocity* of the front over a window of size ℓ is given by

$$V_\ell(t) = \frac{1}{\ell}\int_\ell v(x,t)dx. \tag{6.1}$$

The local activity map $v(x,t)$ is obtained via the waiting-time-matrix procedure described in Sec. 2.6. As a consequence of the avalanche dynamics of the front at the local scale with large fluctuations of v, and spatial and temporal correlations, the global signal also displays a burst-like dynamics.

Results presented in this chapter correspond to forced-flow imbibition experiments, that is, experiments in which the fluid is driven through the system at a constant flow rate. This implies a global conservation of mass per unit time in three dimensions. However, we study the two-dimensional projection on the plane of the cell $(x-y)$ of the actual three-dimensional interface. Therefore, fluctuations in the available volume in the direction perpendicular to the plates of the cell allow temporal variations in the mean velocity of the interface –which otherwise would be constant. Moreover, the maximum window of observation $L = 136$ mm is smaller than the width of the model open fracture (190 mm) to minimize the influence of the boundaries. This can also introduce fluctuations in the averaged signal $V_\ell(t)$.

We have explored different experimental conditions varying two controlling parameters –imposed mean velocity v and dynamic viscosity of the oil μ– and analysed the interfaces at different windows of observation ℓ.

To observe the effect of each parameter v, μ, ℓ, six typical signals of $V_\ell(t)$ are shown in Fig. 6.1 in groups of two. Each group corresponds to setting two of the parameters constant, and changing the third one. The top panel shows the effect of changing the window of observation ℓ on analysing the same experiment (μ, v fixed). On the left panel the front is observed at the smallest window considered $\ell = L/50 = 2.7$ mm, while on the right panel it is observed at the largest window $\ell = L = 136$ mm. Middle panel displays the signals for the most different viscosities studied, $\mu = 10$ cP on the left, and $\mu = 350$ cP on the right. In both cases v = 0.13 mm/s and $\ell = L/8 = 17$ mm. Finally, the signals corresponding to the two extreme values of v are shown in the bottom panel of the figure, for $\mu = 50$ cP and $\ell = L/8 = 17$ mm. In all cases shown, $V_\ell(t)$ is a jerky signal that strongly fluctuates around its mean value. The magnitude of the fluctuations is larger when the fluid is injected faster, but also when the system is observed at smaller ℓ or the fluid has lower μ, keeping the other parameters constant. However, the relative magnitude of the fluctuations (compared to the mean velocity of the front) is larger whenever v, μ, or ℓ are smaller and the other parameters are fixed (left panels of the figure). The shape of the fluctuations of the three signals on the left

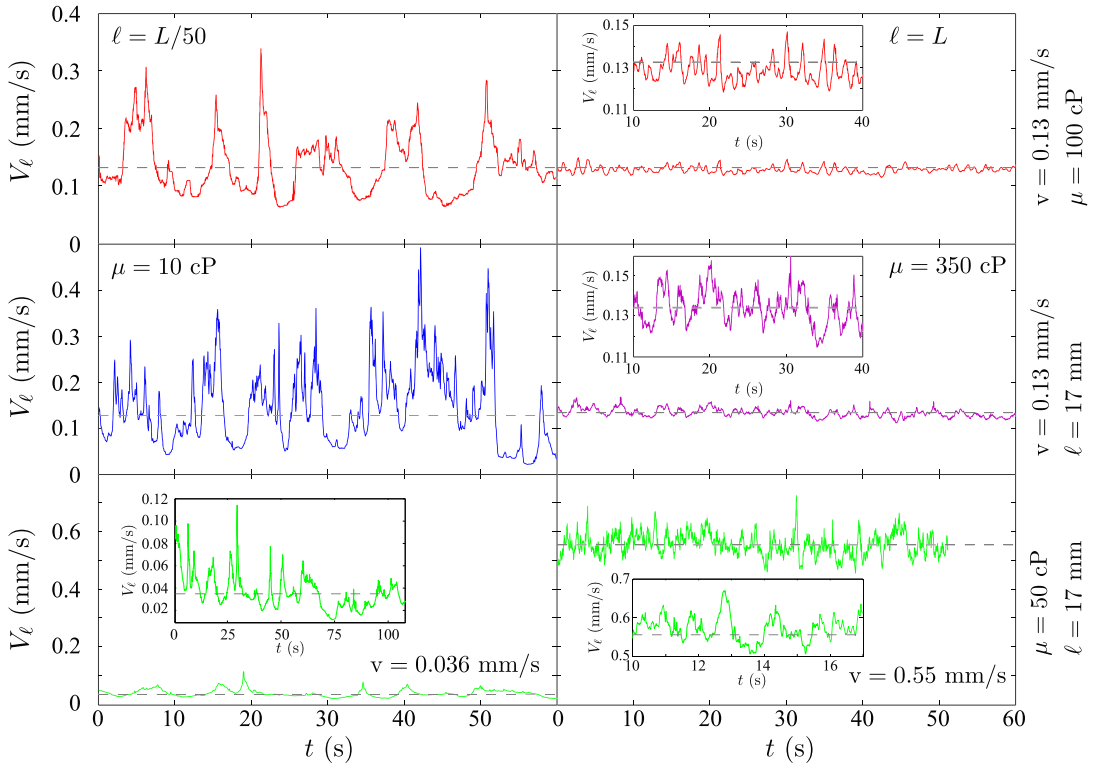

FIGURE 6.1: Examples of spatially-averaged (global) velocities of the front as functions of time. Six limiting cases are shown to identify the effect of the window of observation ℓ (top), the dynamic viscosity μ (medium), and the imposed mean velocity v (bottom) on the actual form of the signal. Each panel (top, middle, bottom) corresponds to setting two of the parameters (v, μ, ℓ) constant, and changing the third one (smaller value on the left than on the right plots). The insets show $V_\ell(t)$ corresponding to the same mean advancement of the front (30 s at v = 0.13 mm/s). Dashed lines indicate the time-averaged velocity $\langle V_\ell(t) \rangle$ in each experiment.

panels (small ℓ, μ, or v) looks alike, when they are observed at the appropriate scale of velocities. Similarly, the signals on the right also seem to resemble each other. The properties of these signals are analysed quantitatively in the following sections.

6.1.1 Statistical analysis of $V_\ell(t)$

We first study the amplitude of the fluctuations of the spatially-averaged velocity $V_\ell(t)$. We have shown in Ch. 5 that interfaces propagating through the disordered medium develop lateral correlations up to a distance given by ℓ_c. Thus, local velocities $v(x,t)$ are also spatially correlated. $V_\ell(t)$ is then a spatial average of a spatially-correlated signal. In this situation, non-Gaussian fluctuations of the global signal are usually expected (Bramwell et al., 1998; Bertin, 2005). As introduced in Sec. 1.5.2 statistics of averaged (global) observables in correlated systems can be related to Gumbel statistics, and in particular this relationship naturally leads to distributions that are well described by

the generalized Gumbel (GG) distribution $P_a(Y)$ (Bertin, 2005), also defined in Sec. 1.5.2. When the variable analysed Y is normalized, the only free parameter describing the shape of the GG distributions is a. This parameter is related to the asymmetry of the distributions by (Portelli et al., 2001):

$$Sk = \langle Y^3 \rangle \sim 1/\sqrt{a}. \tag{6.2}$$

For forced-flow imbibition experiments Planet et al. (2009) showed that when the global velocity of the front is measured at a scale comparable to or smaller than the lateral correlation length, the fluctuations of $V_\ell(t)$ take a GG shape. In addition, the skewness of the distributions measures the effective number of degrees of freedom probed in the experiment, given by ℓ/ℓ_c. Those experiments were performed at different imposed mean velocities v, and analysed at different windows of observation ℓ in the same setup than in this Thesis, but using only one oil (of viscosity $\mu = 50$ cP).

In the present work we expand this earlier research in various ways. First, we increase substantially the range of capillary numbers explored and, thus, of lateral correlation lengths ℓ_c. Second we include experiments performed with oils of different dynamic viscosities, that allows us to check the scaling of the GG distributions with ℓ/ℓ_c with respect to both v and μ.

Figure 6.2 shows the evolution of the probability distributions of the rescaled global velocity

$$Y = \frac{V_\ell(t) - \langle V_\ell(t) \rangle}{\sigma_{V_\ell}} \tag{6.3}$$

with the experimental controlling parameters, v and μ, and the window of observation ℓ. We observe the same qualitative evolution of the tails upon varying either of the three parameters while keeping the other two constant. As ℓ, μ, or v decrease, the distributions become more asymmetric and both positive and negative tails increase. On the other hand, as either ℓ, μ, or v get large the distributions evolve towards a Gaussian pdf, which is only achieved for large enough values of these parameters. Generalized Gumbel distributions with the asymmetry of the data fit well the experimental pdfs. This implies that the evolution of the distributions is determined only by their skewness, Sk.

Figure 6.3 displays the evolution of Sk with ℓ for all the experimental conditions explored. In all cases, Sk is significantly larger than zero at small ℓ. It decays monotonously with ℓ towards $Sk = 0$ (symmetric distribution). Also, for a given ℓ, Sk is larger at low v and small μ.

As mentioned before, the asymmetry of GG-like distributions of averages of correlated variables is related to the number N_{eff} of effective degrees of freedom of the system under study (Portelli et al., 2001; Noullez and Pinton, 2002). In our case, the effective number

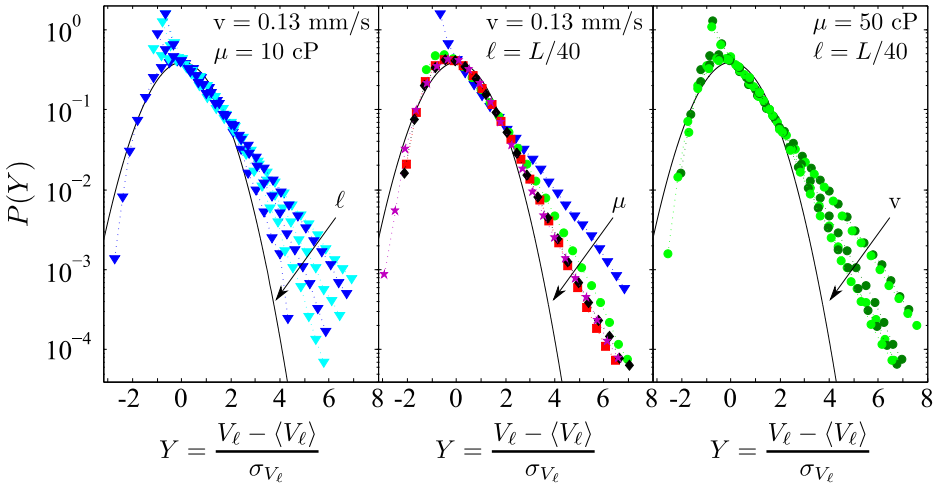

FIGURE 6.2: Evolution of the distributions of the rescaled global velocity with window of observation ℓ (left), dynamic viscosity μ (middle), or imposed mean velocity v (right). In the left panel, data for $\ell = L/n$ with $n = 1$, 8, 11, 16, 27, 50 are plotted. Data in the middle panel correspond to $\mu = 10$, 50, 100, 169, 350 cP. Data in the right panel correspond to v = 0.036, 0.053, 0.13, 0.23, 0.35, 0.55 mm/s. The solid lines correspond to a normal distribution.

of statistically independent domains of the interface can be estimated by the ratio of the window of observation to the lateral correlation length:

$$N_{\text{eff}} = \ell/\ell_c. \tag{6.4}$$

Planet et al. (2009) verified this relation for experiments at various v, analysed at different ℓ. We now test this relation in a wider range of Ca and changing also the oil viscosity. In the inset of Fig. 6.3 we show that the skewness of the distributions for the available combinations of experimental parameters reasonably collapse into a common functional form when Sk is plotted as function of the reduced variable ℓ/ℓ_c. This result validates that Sk is a measure of the effective number of degrees of freedom of the imbibition fronts. Since Sk determines the shape of the distributions of $V_\ell(t)$, $N_{\text{eff}} = \ell/\ell_c$ appears as the only controlling parameter of the fluctuations of $V_\ell(t)$. Moreover, this result confirms that μ plays the same role as v in controlling N_{eff} in our system –as expected since $\ell_c \sim 1/\sqrt{\text{v}\mu}$.

6.1.2 Controlling parameter ℓ/ℓ_c

Having checked that ℓ/ℓ_c is the only controlling parameter of the non-Gaussian fluctuations of $V_\ell(t)$ opens a way to improve the quality of our statistical data analysis. We can study data sets containing data from all experiments performed at different μ and v, and analysed at different ℓ, provided that ℓ/ℓ_c remains constant.

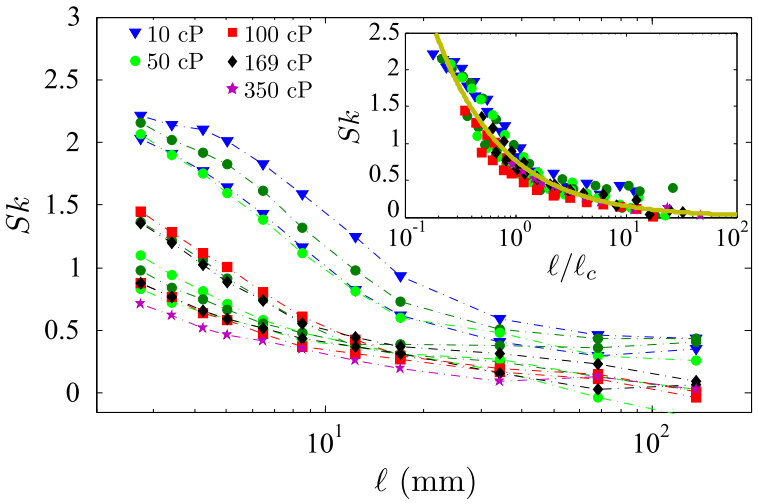

FIGURE 6.3: Skewness of the velocity distributions in a semilog plot as a function of ℓ. Different symbols correspond to different viscosities. For the same viscosity, the larger the velocity the smaller Sk. The curves obtained for different μ and v collapse when plotted as a function of ℓ/ℓ_c (inset). The solid thicker line is a guide to the eye.

Figure 6.4 displays the resulting distributions of velocities for different values of ℓ/ℓ_c. Top panels compare the pdfs obtained from separate experiments (μ, v) analysed at ℓ/ℓ_c constant. The distributions resulting from considering together all available data with ℓ/ℓ_c constant are also plotted (full symbols). All distributions collapse remarkably. In addition, distributions corresponding to all available data are compared to (not fitted by) GG distributions using relation (6.2) and the skewness of the experimental distributions. An extremely good agreement between experimental data and the corresponding GG distributions is observed in all cases. The bottom panel shows the distributions for various ℓ/ℓ_c from 0.5 to 20 using data from all compatible experiments. The evolution of the shape of the distributions with the effective number of degrees of freedom is clear. While for $\ell/\ell_c = 20$ the distributions are nearly Gaussian, they become more and more non-Gaussian and asymmetric as ℓ/ℓ_c is reduced.

The evolution of the asymmetry of the distributions with the effective number of degrees of freedom of the interfaces is presented quantitatively in Fig. 6.5, where Sk is plotted versus ℓ/ℓ_c. Again, for small ℓ/ℓ_c the skewness is significantly different from zero. Sk then decays with ℓ/ℓ_c towards the symmetric case, $Sk = 0$. The skewness of the distributions that include all compatible data is compared to the fit obtained in Fig. 6.3 for all the experiments separately: the results are equivalent.

6.1.3 Temporal correlation of $V_\ell(t)$

To study the fluctuations of the spatially-averaged (global) velocity of the front in time, we analyse the autocorrelation function:

$$C_{V_\ell}(\Delta t) = \overline{\left\langle \Big(V_\ell(t+\Delta t) - \langle V_\ell(t)\rangle\Big)\Big(V_\ell(t) - \langle V_\ell(t)\rangle\Big)\right\rangle_t}. \tag{6.5}$$

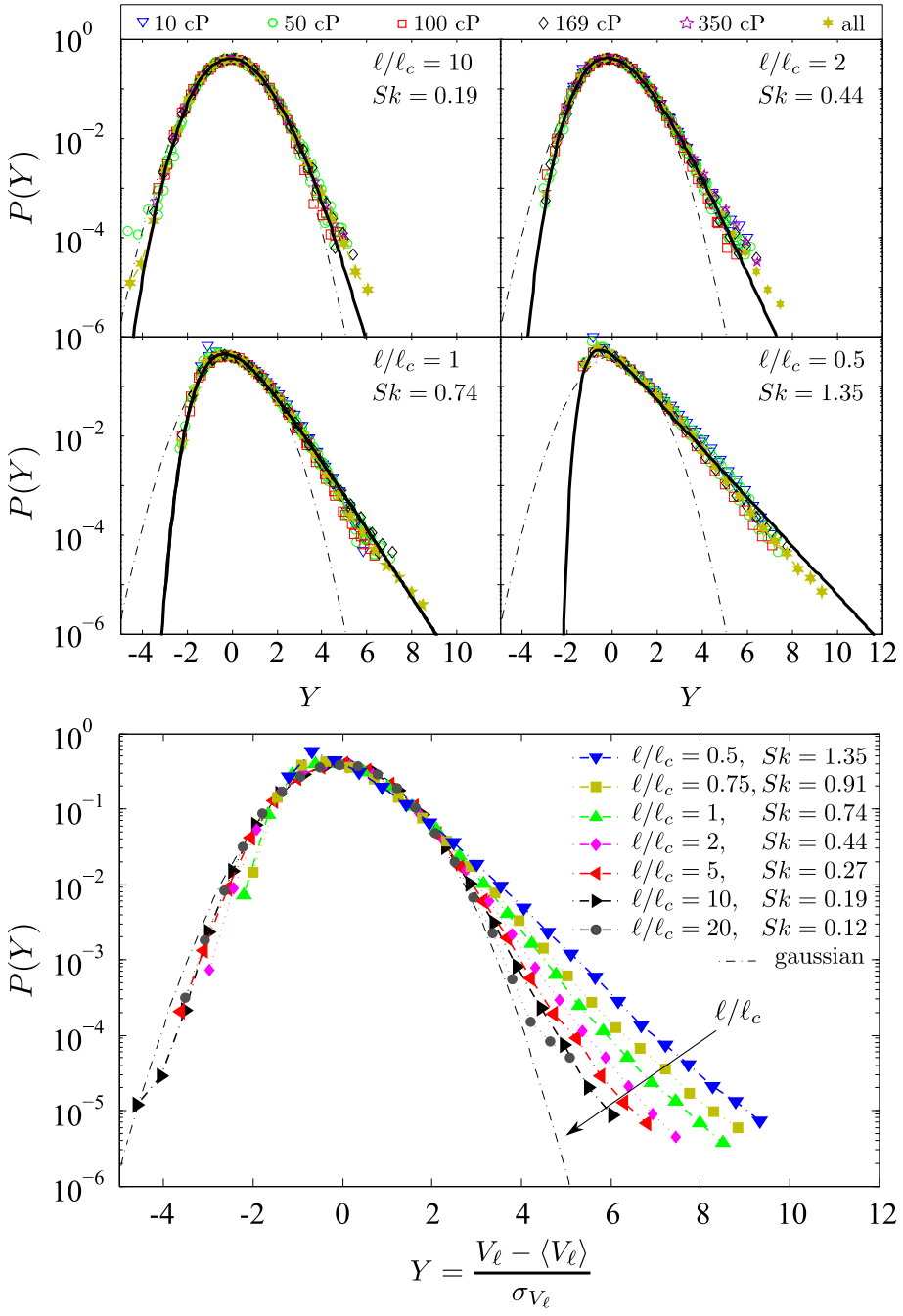

FIGURE 6.4: Statistical distributions of the normalized global velocity $Y = (V_\ell(t) - \langle V_\ell(t) \rangle) / \sigma_{V_\ell}$ for various values of ℓ/ℓ_c. Top panels show $P(Y)$ for all the experiments with different (μ, ν) compatible with $\ell/\ell_c = 10$, 2, 1, and 0.5. Distributions for each experiment separately, and for data sets containing data from all experiments are shown. Solid lines correspond to Generalized Gumbel distributions with the value of Sk of the experimental distributions. The bottom panel displays $P(Y)$ for data sets containing data from all experiments compatible with ℓ/ℓ_c from 0.5 to 20. Dashed-dotted lines in all plots correspond to the normal distribution.

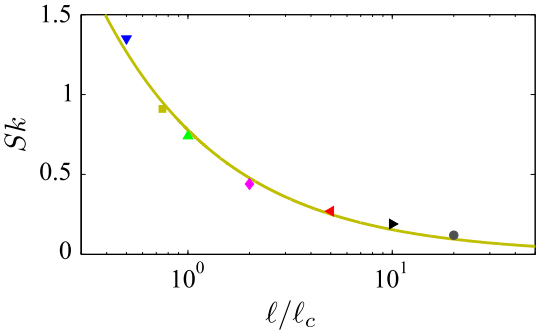

FIGURE 6.5: Skewness of the velocity distributions in a semilog plot as a function of ℓ/ℓ_c for data sets containing data from all compatible experiments. The solid line corresponds to the fit of Sk vs ℓ/ℓ_c presented in Fig. 6.3.

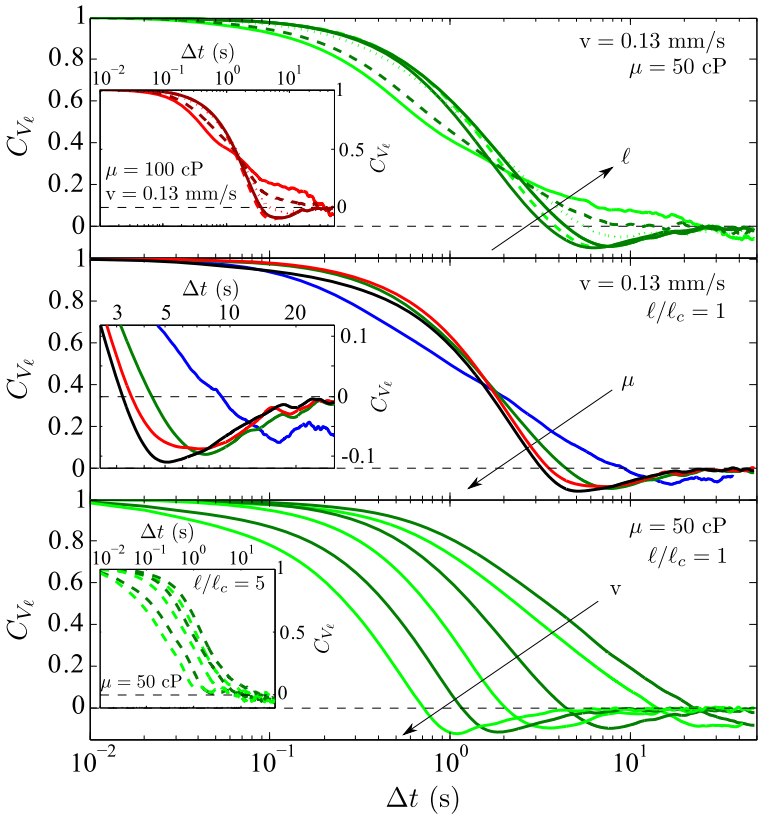

FIGURE 6.6: Autocorrelation functions of $V_\ell(t)$ as a function of the time increment Δt. Top: evolution with ℓ for ℓ/ℓ_c = 10, 5, 2, 1, 0.75, 0.5 and two different values of μ. Middle: evolution with μ = 10, 50, 100, 169 cP for ℓ/ℓ_c = 1. A zoom of the minima is shown in the inset. Bottom: evolution with v from 0.036 to 0.55 mm/s for two values of ℓ/ℓ_c.

Here $\langle \cdots \rangle_t$ is an average over the duration of every experiment, and $\overline{\cdots}$ the ensemble average over different experimental realizations.

The results are shown in Fig. 6.6 for a number of conditions. In all cases C_{V_ℓ} decays monotonously in time until it reaches a maximum anticorrelation –minimum value of C_{V_ℓ} below zero– at Δt^*. Above Δt^*, C_{V_ℓ} increases towards zero.

The temporal correlations of the velocity signal show a systematic evolution with ℓ, μ, and v, as displayed on the panels of the figure. The smaller the window of observation, the shorter Δt^*. On the contrary, the maximum anticorrelation is achieved at larger Δt as μ or v decrease. Moreover, these three parameters do not play the same role in the sense that the differences in Δt^* are much larger when varying v rather than μ or ℓ.

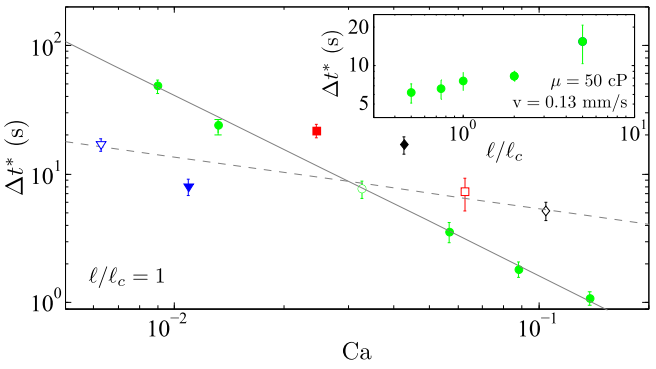

FIGURE 6.7: Evolution of the maximum anticorrelation time Δt^* with the capillary number Ca. The solid line $\Delta t^* \sim \mathrm{v}^{-1.4}$ follows the results for various velocities but one viscosity $\mu = 50$ cP (green circles). The dashed line $\Delta t^* \sim \mu^{-0.4}$ passes through data for various viscosities but one velocity v = 0.13 mm/s (open symbols). Inset: evolution with ℓ/ℓ_c for one set (μ, v).

The evolution of Δt^* with the capillary number Ca is displayed in Fig. 6.7 for $\ell = \ell_c$. Δt^* varies differently with either v or μ. For different imposed mean velocities we observe that $\Delta t^* \sim \mathrm{v}^{-1.4}$, while for different viscosities $\Delta t^* \sim \mu^{-0.4}$. This behaviour can be understood by considering the maximum duration of the local avalanches. As shown in the previous chapter, the distance advanced by the front in the direction of propagation during a local avalanche scales as $L_y \sim L_x^H$, where L_x is the lateral size of the burst. We measured $H = 0.83 \pm 0.02$ for all local bursts. Then, considering the largest avalanches –of lateral size ℓ_c–, the maximum extension in the direction of propagation is proportional to ℓ_c^H. Since v is the mean velocity of the front, the quantity ℓ_c^H/v is an estimation of the maximum duration of local bursts of activity (Santucci et al., 2011). This estimation is proportional to $\mu^{-H/2} \simeq \mu^{-0.4}$ and $\mathrm{v}^{-(1+H/2)} \simeq \mathrm{v}^{-1.4}$. Therefore, the behaviour of Δt^* is compatible with $\Delta t^* \sim \ell_c^H/\mathrm{v}$.

The results presented in Fig. 6.7 indicate that the temporal correlations of the spatially-averaged (global) signal, observed at the correlation length scale ℓ_c, are controlled by the longest-lasting local avalanches –via a proportionality coefficient. This characteristic time, however, is larger if the front dynamics is analysed at larger scales, as shown in the inset of the figure. At these scales larger than ℓ_c simultaneous overlapping local avalanches contribute to the global advancement of the front. The proportionality between Δt^* and the maximum duration of a local avalanche ℓ_c^H/v may not hold then. At windows of observation below ℓ_c, Δt^* is slightly smaller. This is compatible with observations at the local scale in Ch. 5. It results from observing local bursts in windows ℓ which may cut their lateral extension.

6.2 Global avalanches

Events of fast motion of the average position of the front can be distinguished from slower advancements. This allows us to define *global avalanches* as events of $V_\ell(t)$ that occur above an arbitrary threshold V_c. Size S and duration T of global avalanches are defined

by the area enclosed and the time elapsed between two consecutive threshold-crossings of the signal $V_\ell(t)$, as shown in Fig. 6.8.

It is worth noting that S is the extra advancement of the front with respect to the distance advanced at velocity V_c. The threshold used is

$$V_c = \langle V_\ell(t) \rangle + c\sigma_V, \qquad (6.6)$$

where $\langle V_\ell(t) \rangle$ is the temporal average of the signal over the duration of the experiment, σ_V its standard deviation, and c is an arbitrary constant. Therefore, size and duration of avalanches depend on V_c.

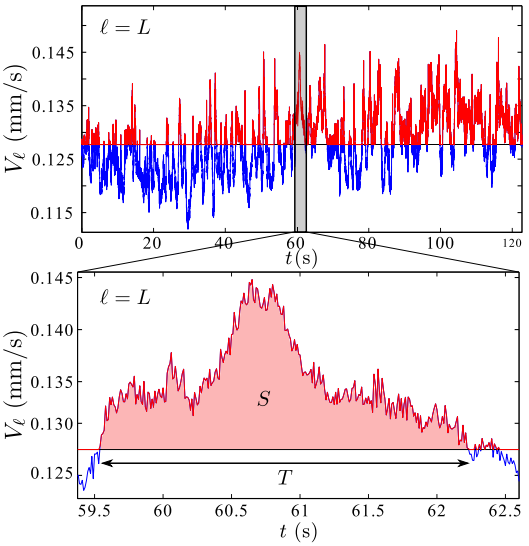

FIGURE 6.8: The top panel shows an example of the global velocity signal for $\ell = L$, clipped by its average value. In the bottom panel a single avalanche is depicted, and its size S and duration T are defined.

The temporal resolution δt of image acquisition introduces a natural cutoff for the shortest avalanches. However, to avoid artefacts arising from the discretization of time, we will only consider avalanches longer than $T_{min} = 10 \times \delta t$. The size of the disorder patches also introduces a cutoff size for the smallest avalanches, S_{min}, which corresponds to the avalanche produced by the advancement of the front over a single patch of disorder in the position x. $S_{min} = (\ell_d/\ell)r$, where $\ell_d = 0.4$ mm is the lateral size of a disorder patch, ℓ is the lateral size of the window of observation, and $r = 0.106$ mm the spatial resolution.

We first check qualitatively the effect of the arbitrary threshold V_c on the statistical properties of global avalanches. Figure 6.9 shows the distributions of sizes and durations for different values of c. Both $P(S)$ and $P(T)$ display a power-law regime with an exponential cutoff, that will be analysed quantitatively and in detail in following sections. We observe that the clip level c does not change the behaviour of the distributions, but shifts the cutoff. The smaller c, the larger the cutoff of the pdfs and hence the larger the power-law regime. Distributions corresponding to the smallest value displayed $c = -0.5$, however, start to show deviations in the power-law regime, that would imply a decrease in the exponent. Therefore we have to consider clip levels larger than $c = -0.5$. We have checked the robustness of the results presented in this section for various clip levels from -0.25 to 0.5. However, all the analysis presented are shown for a single value, $c = 0$.

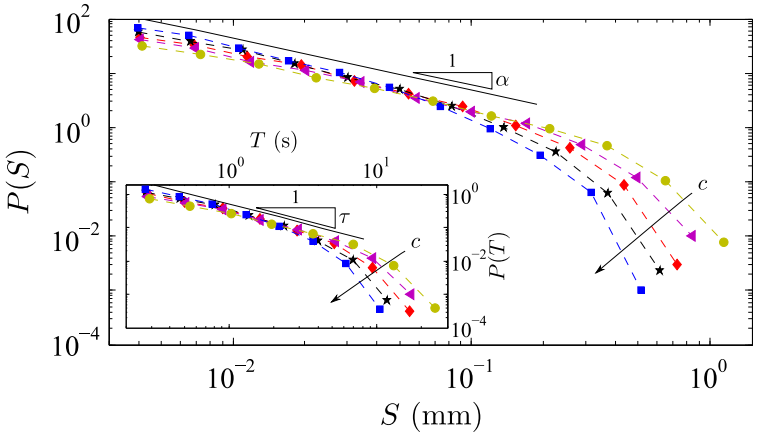

FIGURE 6.9: Effect of the clip level c on $P(S)$ (main plot) and $P(T)$ (inset) for experiments with v = 0.13 mm/s, $\mu = 50$ cP, and $\ell = 2\ell_c$. Here $c = -0.5, -0.25, 0, 0.25, 0.5$. Solid lines are guides to the eye corresponding to a power law with exponent $\alpha = 0.96$ for sizes and $\tau = 1.15$ for durations.

6.2.1 Effect of the experimental conditions on the statistics of avalanches

In this section the statistics of avalanche sizes and durations are analysed as a function of the experimental controlling parameters, v and μ, and the window of observation ℓ. In order to avoid the effect on the distributions of considering windowed data (Chen et al., 2011), we first study velocity signals $V_\ell(t)$ computed at $\ell \geq \ell_c$, the correlation length along the front. Results for velocities averaged over $\ell < \ell_c$ are addressed afterwards.

Spatially-averaged velocities measured at scales larger than ℓ_c

Figure 6.10 shows the evolution of the distributions of sizes (left) and durations (right), with ℓ, μ, and v (top, middle, bottom) when the other two parameters are fixed. In all cases, $P(S)$ and $P(T)$ follow the general form $P_x(x) = a_x x^{-m_x} e^{-x/\xi_x}$ corresponding to a power-law distribution with an exponential cutoff.

The power-law exponent for the sizes of the avalanches is the same irrespective of the experimental conditions or the window of observation. However, the cutoff of the distributions, which controls their scaling range, evolves with the three parameters. The smaller ℓ, μ, or v, the larger the power-law range.

The effect of the controlling parameters on the cutoffs can be understood in terms of the correlation length along the front, and the number of statistically-independent domains of the interface considered to compute $V_\ell(t)$. ℓ_c diverges as v $\to 0$ or $\mu \to 0$. When approaching this limit, the correlation length becomes larger and, therefore, local avalanches –analysed in detail in Ch. 5– occupy a larger fraction of the window of observation. The bigger the underlying local avalanches, the larger the extra advancement of the interface within a given window ℓ and hence the size S of the global avalanches. Similarly, when $V_\ell(t)$ is computed at progressively smaller scales ℓ, more regions of the front are correlated, and then local avalanches are large compared to the window of observation. In summary, the sizes of the spatially-averaged (global) avalanches seem

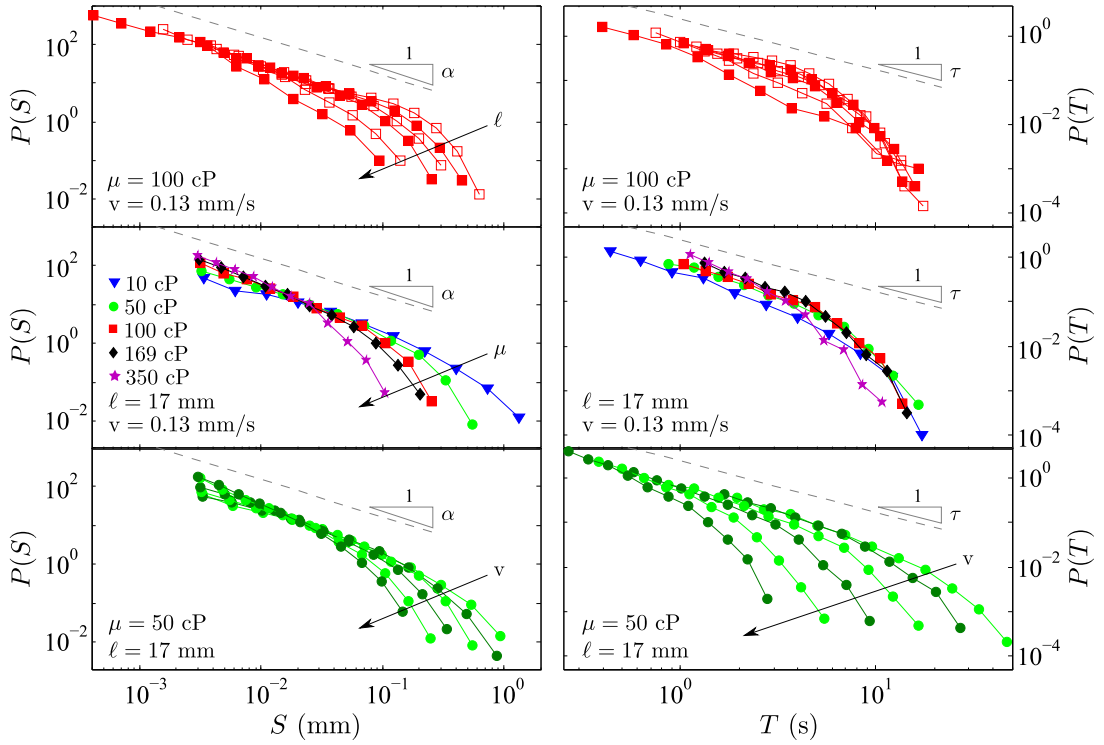

FIGURE 6.10: Distributions of sizes (left) and durations (right) of the global avalanches for velocities analysed at $\ell \geq \ell_c$. The top, middle and bottom panels show the evolution of the distributions with ℓ, μ, and v respectively when the other two parameters are not changed. The top panels show the results for $\ell = 136$, 34, 17, 12.4, 8.5, and 5 mm, and the bottom panels for v = 0.036, 0.053, 0.13, 0.23, 0.35, 0.55 mm/s. Dashed lines are guides to the eye corresponding to power laws with exponents $\alpha = 0.96$ for sizes and $\tau = 1.15$ for durations.

to be controlled by the number of statistically independent domains of the front, ℓ/ℓ_c. This hypothesis is verified in Sec. 6.2.3.

Regarding the distributions of durations, all $P(T)$ also follow the same power law at the scaling regime regardless of the controlling parameters. In this case, however, unlike for $P(S)$, the cutoffs of the distributions do not evolve with either ℓ or μ but they do evolve with v. The cutoffs of the distributions, which provide an estimation of the maximum duration of the avalanches, increase as $v \to 0$. This reveals that avalanches behave differently in space than in time. The evolution of the cutoffs is analysed in more detail in Sec. 6.2.3.

Spatially-averaged velocities measured at scales smaller than ℓ_c

The evolution of the distributions of sizes and durations of global velocities computed at scales smaller than the correlation length are shown in Fig. 6.11.

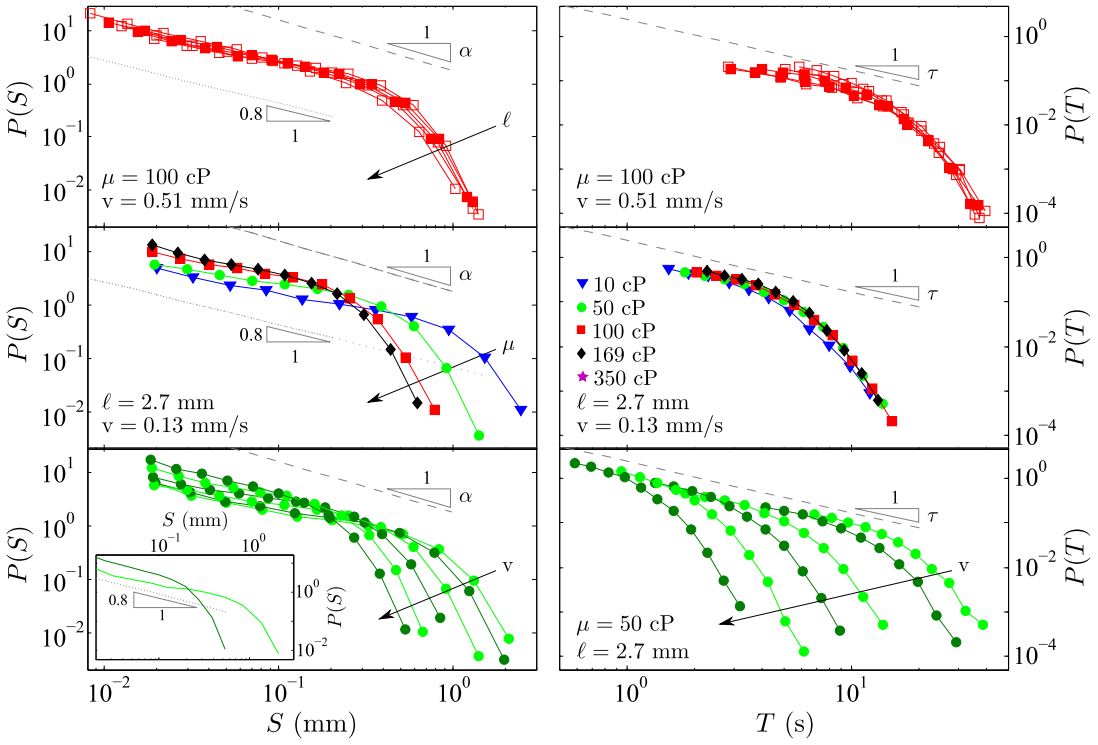

FIGURE 6.11: Distributions of sizes (left) and durations (right) of the global avalanches for velocities computed at $\ell < \ell_c$. The top, middle and bottom panels show the evolution of the distributions with ℓ, μ, and v respectively when the other two parameters are not changed. The top panels show results for $\ell = 6.5$, 5, 4.3, 3.4, and 2.7 mm, and the bottom panels for v = 0.036, 0.053, 0.13, 0.23, 0.35, 0.55 mm/s. The inset shows the results for the lowest and highest velocity in the main plot. Dashed lines are guides to the eye corresponding to power laws with exponents $\alpha = 0.96$ for sizes and $\tau = 1.15$ for durations, and dotted lines a power law with exponent 0.8.

Distributions of sizes (left panels of the figure) can be approximated again by a power law with an exponential cutoff. However, the value of the exponent α compatible with the data is smaller. In addition, the distributions show a bump near the cutoff, before the decay. These two effects, the decrease of the power-law exponent and the appearance of a bump, are signatures of windowed data, i.e. that local avalanches are cut laterally when the global signal is computed (Chen et al., 2011).

The evolution of $P(S)$ with ℓ is tiny but systematic (top left panel of Fig. 6.11). The smaller the window of observation, the slightly larger the cutoff. The effect of μ and v is more clear (two other left panels of the figure). The cutoffs increase when either μ or v decrease. The behaviour of the bump of the distributions is also systematic with the three parameters. Again, the effect is more evident for small μ and v because ℓ_c is larger, the data is more heavily windowed, and therefore the bump is more pronounced.

Distributions of durations of the global avalanches are shown in the right panels of Fig. 6.11. $P(T)$ can be approximated by a power-law distribution with an exponential

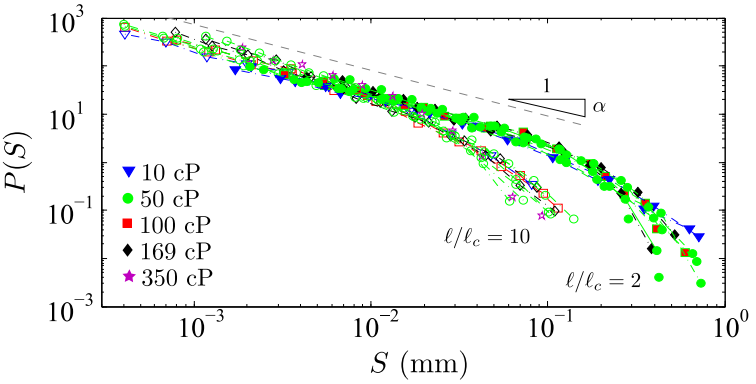

FIGURE 6.12: Distributions of avalanche sizes for $\ell/\ell_c > 1$. Experiments compatible with $\ell/\ell_c = 2$ (solid symbols) and $\ell/\ell_c = 10$ (open symbols) are shown. μ ranges from 10 to 350 cP and v from 0.036 to 0.55 mm/s. The dashed line corresponds to a power law with exponent $\alpha = 0.96$.

cutoff. In this case, the (small) scaling regime is compatible with the value of τ obtained for $\ell > \ell_c$. Moreover, the bump observed in $P(S)$ close to the cutoffs is less clear in these distributions. This reveals that data windowing affects much less the avalanche durations and thus, once again, shows that the properties of the global avalanches in space and in time evolve differently with v and μ. Furthermore, experiments are grouped again by the imposed mean velocity v independently of μ and ℓ.

6.2.2 Effect of ℓ/ℓ_c on the distributions of sizes and durations

In Sec. 6.1 we have shown that the fluctuations of the spatially-averaged velocity of the front are controlled by the ratio ℓ/ℓ_c, a measure of the statistically independent domains along the front. Then, in order to compare the statistics of the bursts of fast motion of the front among the very different experimental conditions explored, we analyse $V_\ell(t)$ at windows of observation such that ℓ/ℓ_c is constant.

We first analyse the cases $\ell > \ell_c$. Figure 6.12 shows the distributions of avalanche sizes for data corresponding to $\ell/\ell_c = 2$ and 10. All the distributions $P(S)$ show a power-law regime with the same exponent α. In addition, experiments performed at different v or μ but analysed at given ℓ/ℓ_c decay exponentially with a very similar cutoff for large S. The scaling range of the distributions is controlled by the ratio ℓ/ℓ_c; the smaller ℓ/ℓ_c the larger the cutoff ξ_S. However, tiny differences for different experimental conditions analysed at the same ℓ/ℓ_c are still observed. They are studied quantitatively in Sec. 6.2.3.

As for $P(T)$, shown in Fig. 6.13, we recover a power-law distribution with an exponential cutoff. Again, the power-law exponent does not depend on ℓ/ℓ_c. The behaviour of the distributions shows no clear dependence on ℓ/ℓ_c either. However, the cutoff ξ_T seems to evolve with the imposed mean velocity. The slower the fluid is injected through the system, the larger the maximum duration of the avalanches. The behaviour of the cutoffs is analysed quantitatively in Sec. 6.2.3.

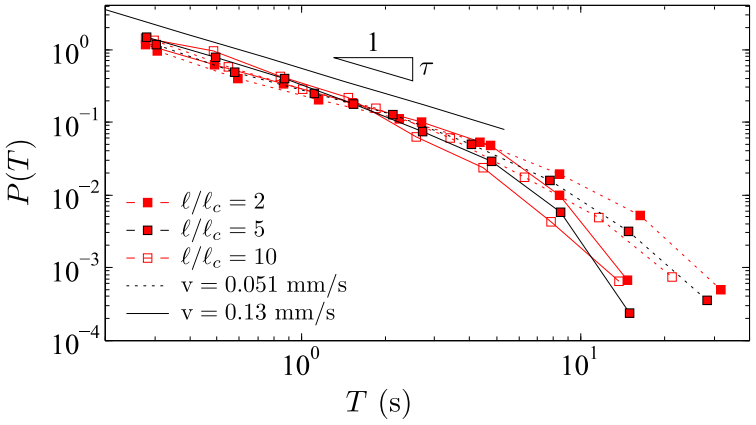

FIGURE 6.13: Distributions of avalanche duration for two experimental conditions: $\mu = 100$ cP and v = 0.051, 0.13 mm/s, analysed at three different values of ℓ/ℓ_c. The solid straight line corresponds to a power law with exponent $\tau = 1.15$.

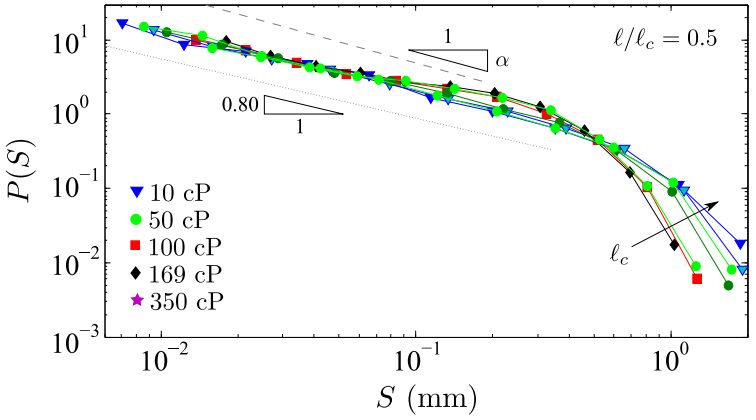

FIGURE 6.14: Distributions of $P(S)$ for $\ell/\ell_c = 0.5$. Different symbols correspond to different viscosities. The dashed and dotted lines are guides to the eye that correspond to power laws with exponents $\alpha = 0.96$ and 0.8 respectively.

We finally show the distributions obtained when the front is analysed at windows of observation smaller than the correlation length ℓ_c. Distributions of sizes for $\ell/\ell_c = 0.5$ are displayed in Fig. 6.14 for various experimental conditions (μ, v). As we noticed in the left panels of Fig. 6.11, the distributions $P(S)$ are compatible again with a power-law distribution with an exponential cutoff. The exponent of the scaling region, compatible with 0.8, is smaller than $\alpha = 0.96$. Distributions show a bump before the exponential decay that is more pronounced the smaller ℓ_c. We also observe a small dispersion of the cutoffs: ξ_S increases with ℓ_c.

Distributions of durations for $\ell/\ell_c = 0.75$ and 0.5 are shown in Fig. 6.15. The pdfs are well approximated by a power law with an exponential cutoff. The power-law regime is compatible with the exponent $\tau = 1.15$ obtained for $\ell > \ell_c$. However, $P(T)$ displays a bump at the beginning of the decay in all cases. The bump is more important the slower v. It is also worth noting that different experiments are grouped again by the imposed mean velocity at which they have been performed, regardless of μ and ℓ/ℓ_c.

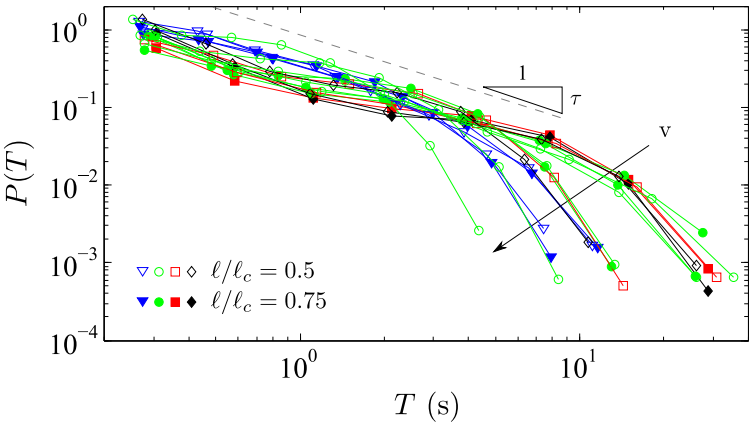

FIGURE 6.15: Distributions of $P(T)$ for $\ell/\ell_c < 1$. Different symbols correspond to different viscosities. $P(T)$ are grouped by velocity, with v = 0.35, 0.23, 0.13, 0.053 and 0.036 mm/s. The dashed line is a guide to the eye that corresponds to a power law with exponent $\tau = 1.15$.

6.2.3 Collapse of the distributions

In order to avoid spurious effects arising from data windowing, in this section we will consider only avalanches from experiments analysed at windows of observation $\ell > \ell_c$.

Figure 6.16 shows the rescaled distributions of sizes (top) and durations (bottom) and their respective fits for experiments analysed at $\ell > \ell_c$. Thirty-four different experimental sets (μ, v, ℓ) are considered, showing a remarkable data collapse in both cases. Experiments at the highest mean velocities, v = 0.35, 0.55 mm/s for the oil of $\mu = 50$ cP, and experiments with the oil of largest viscosity, $\mu = 350$ cP, have not been considered in the data collapse. The pdfs in these cases display a very small range of power law –they are dominated by the exponential cutoff– which makes the method used to extract α and τ inaccurate. Nevertheless, the exponents obtained considering these faster experiments or using the largest viscosity, $\alpha = 0.95(5)$ and $\tau = 1.27(15)$, are compatible with the values shown in the figure. The power-law regimes are robust and extend for almost two decades of sizes and durations. However, small deviations at the right-end tails –where statistics is poorer– are observed. The error functions ϵ and their minima are shown in the insets.

From these data collapses we have been able to extract reliably size and duration exponents:

$$\alpha = 0.96 \pm 0.05, \quad \tau = 1.15 \pm 0.15. \tag{6.7}$$

These values are in excellent agreement with previous results found by Planet et al. (2009) and Planet et al. (2011) in a setup equivalent to the one used in this Thesis, i.e. $\alpha = 1.00 \pm 0.15$ and $\tau = 1.25 \pm 0.25$. These earlier results are now extended with the use of oils of five different viscosities, showing that the scale-invariant picture of the dynamics that emerges from the previous analysis is very robust. The result also agrees with phase-field simulations of the same kind of forced-flow imbibition displacements, where $\alpha = 1.03 \pm 0.05$ and $\tau = 1.10 \pm 0.11$ were found (Pradas, 2009).

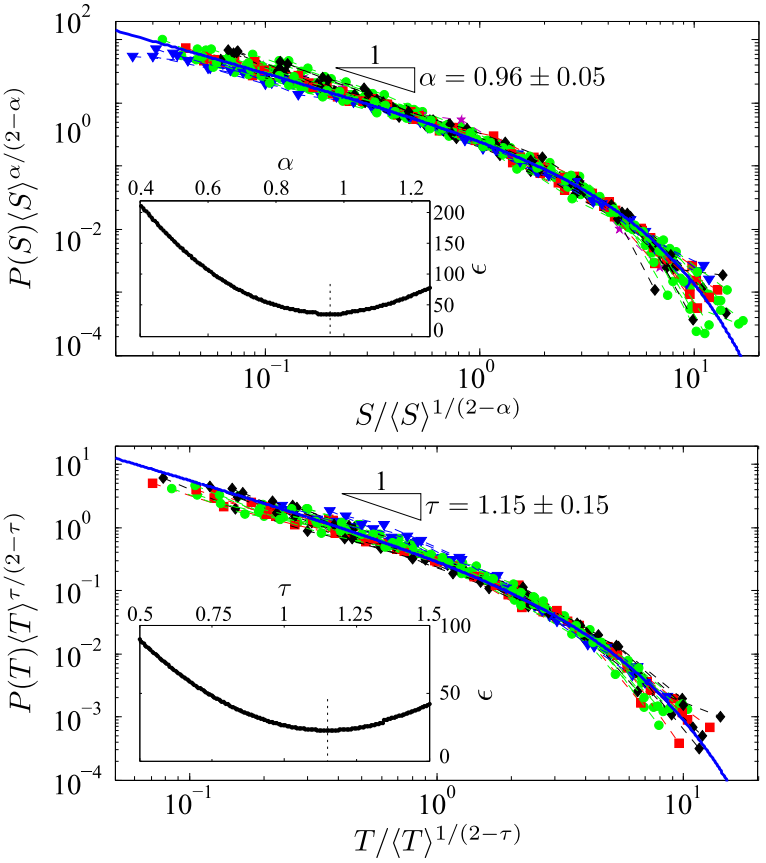

FIGURE 6.16: Data collapse of the probability distributions of sizes (top) and durations (bottom) of the global avalanches, for experiments analysed at $\ell/\ell_c > 1$. Different symbols correspond to different viscosities. The best fits to a power law with an exponential cutoff are achieved with $\alpha = 0.96$ and $\tau = 1.15$ (solid lines). The insets show the error of the fits as a function of α or τ.

Having extracted the power-law exponents of the distributions, we can obtain the cutoffs ξ_S and ξ_T of the pdfs by considering only their exponential decay. In order to do so, we fit an exponential function to the distribution $P(x)x^m$ vs x.

The exponential decays of $P(S)$ are displayed in the top panel of Fig. 6.17. Specifically, $P(S)S^\alpha$ are shown as functions of S. Distributions for different experiments (μ, v) are grouped by ℓ/ℓ_c –shown in different colours– as previously observed in Fig. 6.12. Small deviations of the cutoffs are still observed. These small fluctuations, however, do not evolve systematically with any of the parameters, indicating that they may result from a lack of statistics. $P(S)S^\alpha$ are well fitted by a decaying exponential from which the cutoff ξ_S is obtained. The inset displays the divergence of ξ_S and thus the increase of the power-law range of $P(S)$, as ℓ approaches ℓ_c from above, revealing that the system becomes more and more critical.

The cutoffs of the distributions of durations are extracted from $P(T)T^\tau$ vs T. The bottom panel of Fig. 6.17 displays the pdfs for experiments analysed at $\ell/\ell_c = 2$. Distributions are sorted by the imposed mean velocity –shown in different colours. The slower the fluid is injected, the larger the cutoff time. We find that $\xi_T \sim 1/\mathrm{v}$, as shown in the inset.

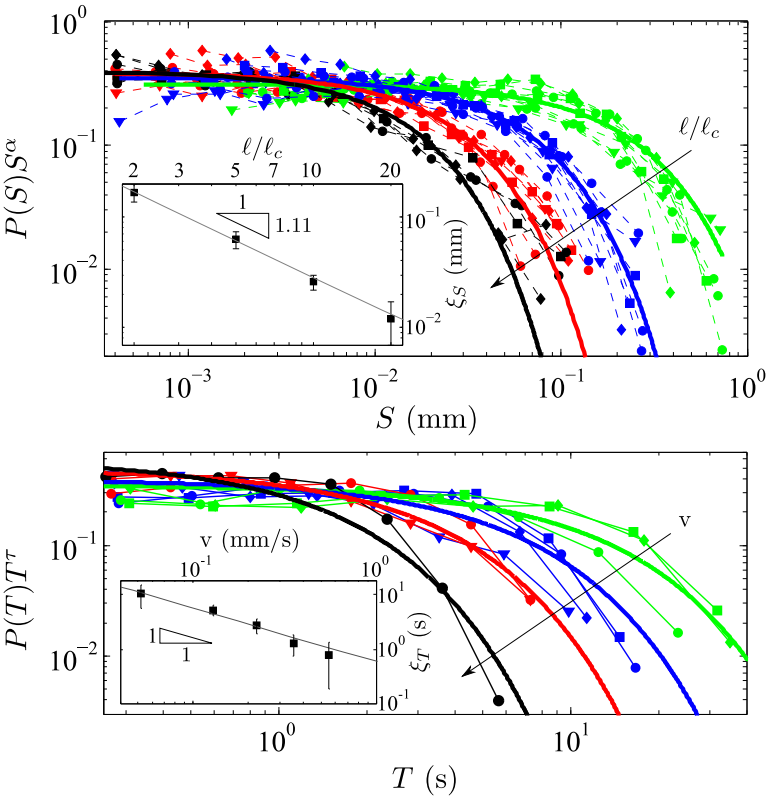

FIGURE 6.17: Top: pdfs of avalanche sizes rescaled by S^α vs S. Colours stand for ℓ/ℓ_c = 2, 5, 10, 20. Solid lines are exponential fits of the data for each ℓ/ℓ_c. Bottom: pdfs of the durations rescaled by T^τ for experiments analysed at $\ell/\ell_c = 2$. Colours stand for v = 0.052, 0.13, 0.22, 0.35 mm/s. In both cases different symbols correspond to experiments with different viscosities –we do not distinguish different v for the same μ. Solid lines are exponential fits of the data for each v. Insets: evolution of the cutoff values obtained from the previous fits with ℓ/ℓ_c (top) and v (bottom). Solid lines are guides to the eye.

The evolution with ℓ/ℓ_c and v of the mean size $\langle S\rangle$ and mean duration $\langle T\rangle$ of the avalanches parallels the corresponding evolutions of the cutoffs. This allows us to extract a characteristic size and duration of distributions without having to specify their actual shape –specially convenient for $\ell < \ell_c$, where the distributions display a bump close to the beginning of the decay. The comparison of the cutoffs ξ_S and ξ_T to $\langle S\rangle$ and $\langle T\rangle$ is displayed in Fig. 6.18. Cutoffs are an upper limit for the characteristic sizes and durations and thus their values are larger than $\langle S\rangle$ and $\langle T\rangle$. However, the evolution of both $\langle S\rangle$ and ξ_S is perfectly compatible with $(\ell/\ell_c)^{-1.1}$ for $\ell/\ell_c \geq 1$. As for the durations, $\langle T\rangle$ and ξ_T are both consistent with an scaling 1/v. In addition, these characteristic durations are compared to the time needed to advance a distance ℓ_d (the characteristic size of the disorder) at the imposed mean velocity, $\tau_c = \ell_d/\text{v}$. Although the cutoffs of $P(T)$ depend on the velocity threshold V_c chosen for defining avalanches (Eq. (6.6)) they are of the same order of magnitude as τ_c. Specifically, for the value of V_c chosen in Fig. 6.18 they are equal within error bars. This reveals that the maximum durations of the global avalanches seem to be controlled by the spatial extent of the disorder. Further insight into this possibility will be provided in Ch. 7.

The clear evolution of the cutoffs for both $P(S)$ and $P(T)$ is observed for the first time in our setup thanks to the large data sets, required for accurate statistics. Using

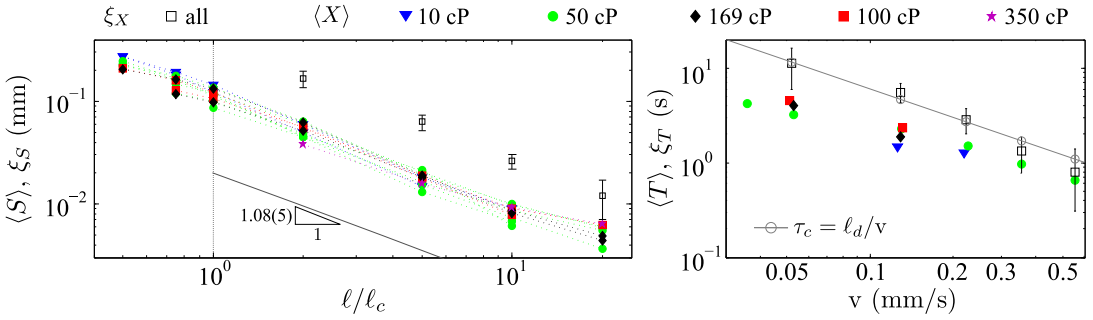

FIGURE 6.18: Dependence of the mean value and the cutoff of the distributions of sizes (left) and durations (right) with ℓ/ℓ_c and v respectively. The solid line in the left panel is a power-law fit to $\langle S \rangle$ vs ℓ/ℓ_c down to $\ell = \ell_c$. In the right panel, the experimental values are compared to $\tau_c = \ell_d/\mathrm{v}$, with $\ell_d = 0.6$ mm.

oils of different viscosities has also allowed us to distinguish the role played by v, μ, and $\ell/\ell_c \sim \ell/\sqrt{\mathrm{v}\mu}$ independently on the behaviour of the different observables.

The results presented show that sizes and durations of the global avalanches of the front are not controlled by the same mechanism. While the maximum size of the avalanches is restrained by the lateral correlation length ℓ_c, their maximum duration is controlled by the mean velocity of the interface. This conclusion is also reached in the next chapter (Ch. 7), in which the intermittent properties of the global velocity are studied.

6.2.4 Joint distribution $P(S,T)$

The distributions of sizes and durations $P(S)$ and $P(T)$ are the marginal pdfs of the joint distribution $P(S,T)$. Figure 6.19 shows the joint distribution for the rescaled variables $S^* = S/\langle S \rangle^{1/(2-\alpha)}$ and $T^* = T/\langle T \rangle^{1/(2-\tau)}$, which depend on the exponents α and τ previously obtained, for $\ell/\ell_c = 1$ and 10 (left and right). In both cases the crest of the joint distribution follows a power law, limited by an upper and lower cutoff indicated by the vertical dashed lines. The upper cutoff reflects the upper cutoffs of $P(S)$ and $P(T)$. The lower cutoff is associated with the minimum possible size of a global avalanche and the discretization of time.

In the scaling regime the most probable values follow $S \sim T^\gamma$. We have obtained γ from a linear fit of the whole data set. We consider only avalanches within $T^* = T/\langle T \rangle^{1/(2-\tau)} \in [10^{-0.9}, 1]$ and $T > 0.2$ s to ensure that $T_{min} > 10\delta t$, where δt is the temporal resolution. The values obtained for $\ell/\ell_c = 1$ and 10 are displayed in the figure. γ is slightly larger when the interface is observed at scale ℓ_c than at larger windows. The behaviour with ℓ/ℓ_c is systematic: the smaller the effective number of degrees of freedom, the higher γ. However, the maximum variation of measured exponents between

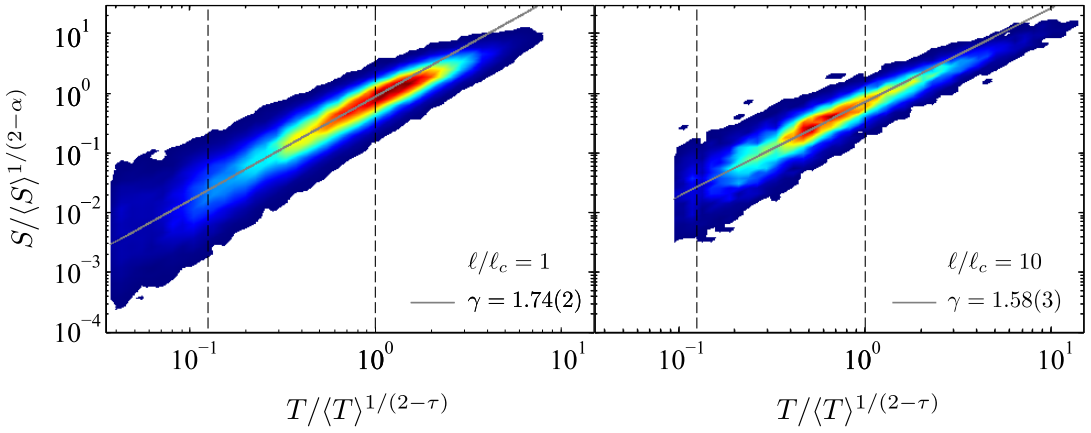

FIGURE 6.19: Probability density plots of the joint distribution of rescaled variables S^* and T^* for $\ell/\ell_c = 1$ (left) and 10 (right). Vertical dashed lines show the scaling regime chosen to extract the power-law exponent γ. The solid straight lines are the best fits $S^* \sim (T^*)^\gamma$ (statistical error of the fit quoted in the figure). The probability density of points increases from blue to red.

$\ell/\ell_c = 1$ and 20 is smaller than 10 %. The evolution of γ with ℓ/ℓ_c is shown later, in the top right panel of Fig. 6.24.

The exponent γ can be related to the exponents α and τ of the distributions of sizes and durations. Since $P(S)$ and $P(T)$ are marginal distributions of the joint probability distribution $P(S,T)$, given by power laws $P(S) \sim S^{-\alpha}$ and $P(T) \sim T^{-\tau}$ up to the cutoff scales ξ_S and ξ_T, it follows that $\tau - 1 = \gamma(\alpha - 1)$. This scaling relation is compatible with the exponents quoted earlier, within error bars. However, since α and τ are close to one, the value of γ derived from the scaling relation is subjected to a very large uncertainty.

6.2.5 Shape of avalanches

We have shown that global avalanches are power-law distributed in sizes and durations, and that the joint distributions of S and T are scale invariant as well. In this section we show that global bursts also have a typical average shape.

It has been proposed that avalanche shapes provide more information about the dynamics of crackling noise than the power-law distributions of sizes and durations (Papanikolaou et al., 2011; Laurson et al., 2013), as explained in detail in Sec. 1.5.2. Specifically, the analysis of the shape of the avalanches allows for testing various theoretical models on experimental data. Accelerations (and decelerations) of the signal, as well as possible inertial effects, are directly observed on the average shape of avalanches.

From the spatially-averaged velocity $V_\ell(t)$ we extract the signals corresponding to excursions of duration T above a clip level V_c, i.e. $V_\ell(t|T)$. Sizes and durations of bursts of $V_\ell(t)$ above V_c have been defined in Fig. 6.8. Typical shapes are shown in the left panel

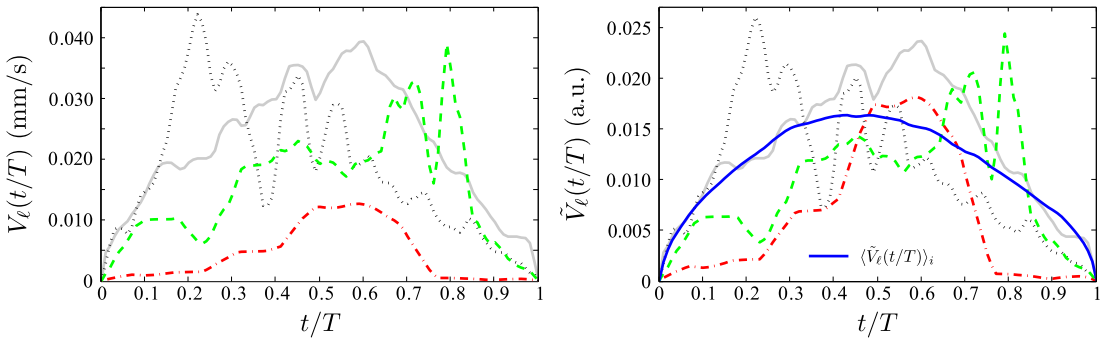

FIGURE 6.20: Four typical avalanche shapes before rescaling (left) and after rescaling by $T^{\gamma-1}$ (right) as a function of rescaled time t/T. The solid blue curve in the right plot shows the average shape of all avalanches within the scaling range of S vs T (more than 2200) for these experimental conditions $\mu = 50$ cP, v = 0.053 mm/s and $\ell = 10.5$ mm $= \ell_c$.

of Fig. 6.20 with the time axis rescaled by avalanche duration, t/T. We find all kind of shapes: from small to high fluctuations of V_ℓ, and maximum values at the beginning, middle or end of the avalanche.

The size of an avalanche $V_\ell(t|T)$ is given by

$$S(T) = \int_0^T V_\ell(t|T)dt. \tag{6.8}$$

In the previous section we have seen that the average size and duration of the bursts scale as $S \sim T^\gamma$. Then, the amplitude of the average avalanche shape scales as

$$\langle V_\ell(t|T) \rangle \sim T^{\gamma-1}. \tag{6.9}$$

Therefore, to compare among bursts of different sizes and durations, we rescale each avalanche signal $V_\ell(t|T)$ by its expected size $T^{\gamma-1}$, and we rescale time by the avalanche duration T. Then, for each avalanche we have a rescaled signal

$$\tilde{V}_\ell(t/T) \equiv \frac{V_\ell(t/T)}{T^{\gamma-1}}. \tag{6.10}$$

The average avalanche shape for a given experimental condition i (defined by μ and v) analysed at scale ℓ is then obtained by averaging over the N rescaled bursts within a given range of durations:

$$\langle \tilde{V}_\ell(t/T) \rangle_i = \frac{1}{N} \sum \tilde{V}_\ell(t/T). \tag{6.11}$$

The right panel of Fig. 6.20 displays the rescaled $\tilde{V}_\ell(t/T)$ corresponding to the raw shapes shown in the left panel. For the experimental condition considered ($\mu = 50$ cP, v = 0.053 mm/s and $\ell/\ell_c = 1$) the average shape out of all avalanches within the

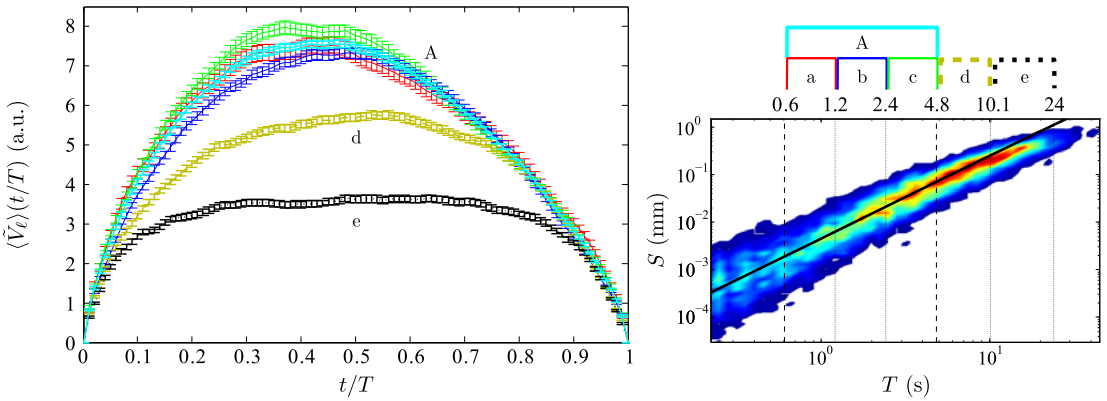

FIGURE 6.21: Avalanche shape obtained by averaging over the range of durations shown and quoted on the joint distribution $P(S,T)$ displayed in the right panel. The average shape obtained by considering all avalanches in the scaling range A is also shown. Experimental conditions: $\mu = 100$ cP, v = 0.13 mm/s and $\ell = \ell_c$.

scaling range of S vs T (more than 2200) is also displayed. $\langle \tilde{V}_\ell(t/T) \rangle_i$ is much smoother than each single avalanche. The maximum velocity is reached around $t/T = 0.4$. Thus, the signal shows a slight inclination towards short times, indicating that avalanches are consequence of a fast acceleration followed by a slower relaxation. This asymmetry of the shape is discussed below.

In the left panel of Fig. 6.21 we compare the avalanche shape obtained by averaging over various ranges of durations, which are shown on the joint distribution in the right panel. We observe that the shapes corresponding to duration T within the scaling range of the joint distribution of S and T (a, b, and c) are equivalent, i.e. they do not evolve with T. However, average shapes $\langle \tilde{V}_\ell(t/T) \rangle_i$ obtained for larger durations, beyond the scaling regime of $P(S,T)$, flatten as T increases (d and e curves). In addition, these average signals become also more symmetric. In these cases, several shorter local avalanches can contribute to those long bursts, thus changing their resulting shape.

Therefore, it is justified to consider only avalanches in the scaling regime of the joint distributions $P(S,T)$ for each experiment. Durations of avalanches, then, have to fulfil $T^* = T/\langle T \rangle^{1/(2-\tau)} \in [10^{-0.9}, 1]$, as seen in the previous section. In addition, to ensure that $T_{min} > 10\delta t$, bursts of durations $T < 0.2$ s are disregarded, as discussed at the beginning of Sec. 6.2.

The relation (6.9) gives the scaling of the amplitude of the average avalanche shape, but it does not set the prefactor. Then, in order to compare average shapes of signals from different experimental conditions we need to normalize them. We choose to set the maximum velocity of the shape equal to 1. Then, for each experimental condition i we

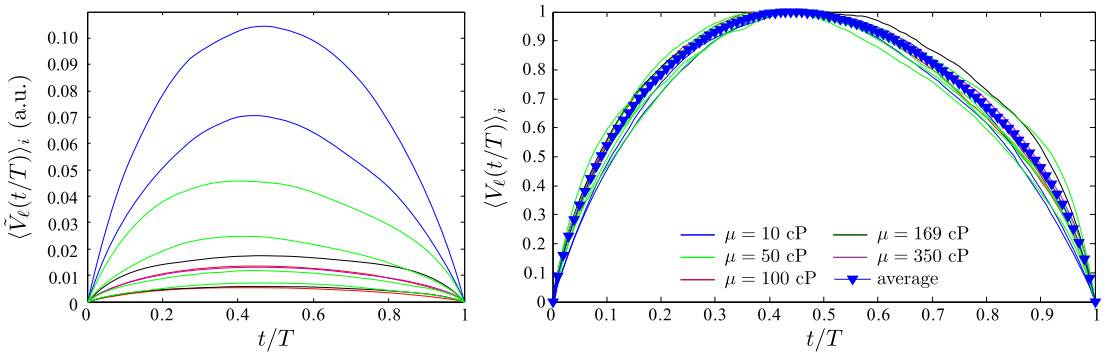

FIGURE 6.22: Average avalanche shape before rescaling by their maximum velocity (left) and after rescaling (right) for a variety of experimental conditions, with dynamic viscosities ranging from $\mu = 10$ to 350 cP (different colours), and velocities from v = 0.036 to 0.35 mm/s (not distinguished). In all cases the fronts are analysed at $\ell/\ell_c = 2$. The average over the different (μ, v), $\langle V_\ell(t/T)\rangle$, is also shown in the right panel.

obtain the normalized shape:

$$\langle V_\ell(t/T)\rangle_i \equiv \frac{\langle \tilde{V}_\ell(t/T)\rangle_i}{\langle \tilde{V}_\ell(t/T)\rangle_i^{\max}}. \tag{6.12}$$

Consistently with the results shown for the fluctuations of $V_\ell(t)$ –Sec. 6.1.2– and for the scaling of the global bursts –Sec. 6.2.2–, the average shape of the avalanches also evolves systematically with the effective number of degrees of freedom of the interface. Figure 6.22 shows the average shapes of the avalanches corresponding to experiments performed at different (μ, v) and analysed at $\ell/\ell_c = 2$. Before rescaling by their maximum value, burst shapes evolve with μ and v, as shown in the left panel. However, after normalizing the maximum value to one, they all display an equivalent behaviour, as shown in the right panel of the figure. This equivalence, observed for all ℓ/ℓ_c explored, allows us to average $\langle V_\ell(t/T)\rangle_i$ over all the experiments analysed at the same N_{eff}. Figure 6.23 shows the evolution of

$$\langle V_\ell(t/T)\rangle = \frac{1}{N}\sum_i^N \langle V_\ell(t/T)\rangle_i, \tag{6.13}$$

for $\ell/\ell_c = 1$ to 20. The curves show a systematic evolution with ℓ/ℓ_c: from asymmetric shapes tilted to the left towards more symmetric burst shapes. Error bars shown on the right panel account for the standard deviation of $\langle V_\ell(t/T)\rangle$. Different curves for different ℓ/ℓ_c can be still resolved.

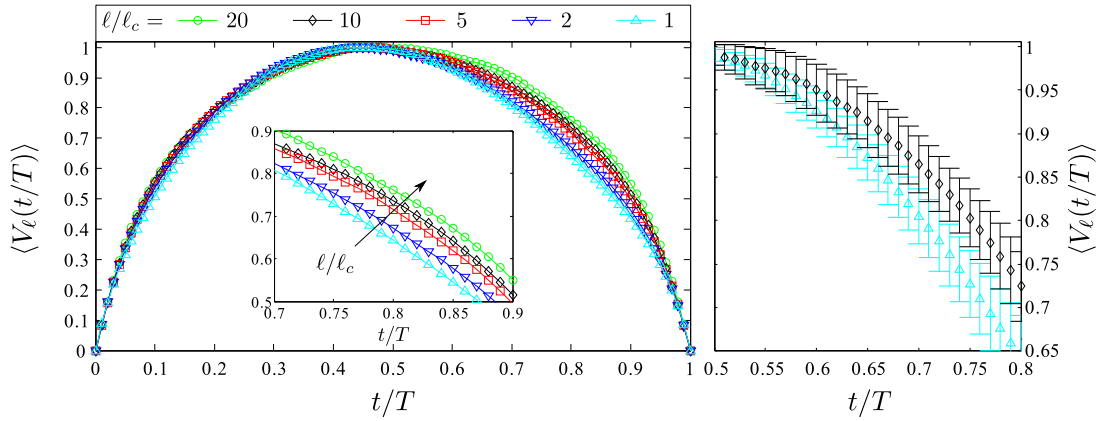

FIGURE 6.23: Average shape of the avalanches normalized to one. The left panel shows the systematic evolution of the shapes with ℓ/ℓ_c. In the right panel error bars are plotted for two cases.

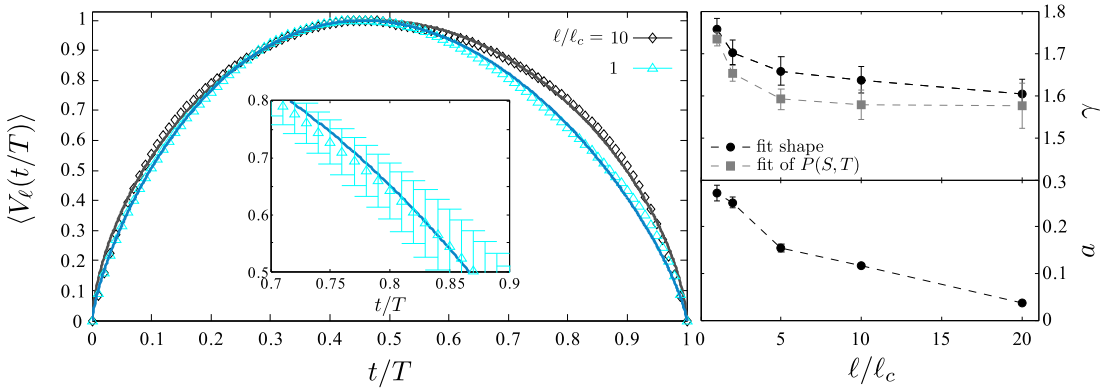

FIGURE 6.24: Left panel: average shape of the avalanches for two ℓ/ℓ_c. Solid lines correspond to a fit to Eq. (6.14). Right panel: parameters γ and a of the fit as a function of ℓ/ℓ_c. The value of γ measured for the joint distributions S vs T is also shown.

As explained in detail in Sec. 1.5.2, Laurson et al. (2013) recently proposed a general scaling form of the average avalanche shape for non-mean-field systems given by

$$\langle V_\ell(t/T)\rangle \sim T^{\gamma-1}\left[\frac{t}{T}\left(1-\frac{t}{T}\right)\right]^{\gamma-1}\left[1-a\left(\frac{t}{T}-\frac{1}{2}\right)\right]. \tag{6.14}$$

It depends on two parameters only: the scaling exponent γ relating the average avalanche size of the avalanche S to its duration T, and an asymmetry parameter a that characterizes the temporal asymmetry of the avalanches.

The average shapes of the avalanches in our system are well fitted by the universal form (6.14). Then, some physical insight can be obtained by using this formulation in relation to the interpretation given by Laurson et al. (2013).

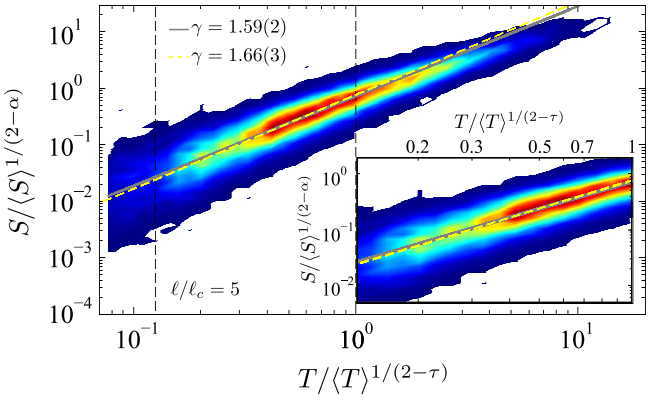

FIGURE 6.25: Rescaled joint distribution for $\ell/\ell_c = 5$. Straight lines correspond to power laws with exponents γ obtained either from $P(S,T)$ (solid) or from the shape of avalanches (dashed). The scaling regime –between the two vertical dashed lines– is magnified in the inset. Density of counts increases from blue to red.

The fits of Eq. (6.14) to the data are displayed in Fig. 6.24 for $\ell/\ell_c = 1$ and 10. The goodness of the fits is remarkable. The values of the exponent γ and the asymmetry parameter a from the fits are shown on the right panel of the figure as a function of ℓ/ℓ_c. γ is compared to the value of the exponent obtained from the joint distributions $P(S,T)$ described in the previous section. In both cases γ follows the same trend, slightly decreasing with ℓ/ℓ_c. Figure 6.25 shows that both values of γ are compatible and almost indistinguishable when fitting $S \sim T^{\gamma}$. The asymmetry parameter a is significantly different from zero at small ℓ/ℓ_c and decreases towards $a = 0$ (time-symmtric avalanches) for large ℓ/ℓ_c.

According to Laurson et al. (2013), a accounts for the time-irreversibility of the avalanche dynamics. A value $a \neq 0$ is expected in systems where the interactions mediating the avalanche dynamics are not fully non-local. As observed in Ch. 5, local activity maps of our experiments are not time-reversal since the branching of avalanches in v-shapes defines the time direction. This time-irreversibility of the system at local scale is revealed in the shape of the bursts of the spatially-averaged (global) signal.

Asymmetry of the shape of global bursts in crackling-noise phenomena has been also related to inertial effects, as described in detail in Sec. 1.5.2. In slow imbibition of an open fracture, inertial effects are usually not considered because the front is driven at low velocities. However, avalanches are events of fast motion with large velocities. Inertia could play a role in the large accelerations of the front, that would be reflected on the asymmetric shape of the avalanches.

6.3 Conclusions

We have analysed the spatio-temporal behaviour of the spatially-averaged (global) velocity of forced-flow imbibition fronts. A wide range of experimental conditions has been explored. We have used different oils with dynamic viscosities from $\mu = 10$ to 350 cP, and imposed flow rates that produced mean velocities of the front ranging from

v = 0.036 to 0.55 mm/s. Then the range of capillary numbers explored is 6×10^{-5} to 2×10^{-3}, and the lateral correlation length verifies $3 < \ell_c < 15$ mm.

Fluctuations of the global velocity $V_\ell(t)$ have been statistically characterized by their probability density functions. We have shown that the number of effective degrees of freedom $N_{\text{eff}} = \ell/\ell_c$ is the controlling parameter of such fluctuations, and thus that μ and v play the same role in controlling them. The distributions of global velocities are very well reproduced by generalized Gumbel distributions determined only by the skewness of the experimental data. Regarding the correlation in time of $V_\ell(t)$, we have shown that the time Δt^* at which the maximum anticorrelation is achieved is proportional to the duration of the longest-lasting local avalanches, when the interface is analysed at $\ell = \ell_c$.

We have defined the events of fast motion of the front as (global) avalanches, and we have characterized them. For $\ell/\ell_c > 1$ the distributions of sizes S and durations T of these avalanches follow a power law with an exponential cutoff. The power-law exponents (α and τ) are independent of the experimental conditions. We have obtained $\alpha = 0.96 \pm 0.05$ for $P(S)$ and $\tau = 1.16 \pm 0.15$ for $P(T)$. These results agree with earlier experimental results from Planet et al. (2009) and Planet et al. (2011) with only one viscosity, and with phase-field simulations of the problem (Pradas, 2009). Thanks to the large number of experiments analysed, the evolution of the cutoffs of the distributions has been studied in detail. Using oils of different viscosities has allowed us to show that maximum sizes and durations of the avalanches are not controlled by the same mechanism. The maximum size is shown to depend on ℓ/ℓ_c, while the maximum duration is only controlled by the mean velocity of the interface. Joint distributions of sizes and durations also show scale invariance, $S \sim T^\gamma$. The exponent γ evolves slightly with ℓ/ℓ_c. Finally, $P(S)$ and $P(T)$ display bumps for experiments analysed at $\ell < \ell_c$, as a result of windowed avalanches.

The average shape $\langle V_\ell(t/T) \rangle$ of global avalanches has been also studied. It shows a systematic evolution with N_{eff}: from asymmetric shapes tilted towards short times to more time-symmetric shapes as ℓ/ℓ_c is increased. Asymmetry of the avalanches can be a signature of either the time-irreversibility of the local activity maps (Laurson et al., 2013) or the presence of inertia on the dynamics (Zapperi et al., 2005). The shapes have been compared to a recently proposed universal shape (Laurson et al., 2013). The fits to our experimental data are remarkable, and the values of γ obtained from them are compatible with the exponents obtained from the joint distributions $P(S, T)$.

Chapter 7

Experimental evidence of intermittency in slow imbibition

Spatially-localized avalanches presented in Ch. 5 can lead to strong temporal fluctuations of the global advancement of the imbibition front. These fluctuations of the spatially-averaged (global) velocity $V_\ell(t)$ have been studied in the previous chapter.

We have shown that the global signal displays avalanches of velocities much faster than the mean value imposed. These avalanches alternate with periods of low velocities. In hydrodynamic turbulence, the occurrence of bursts of intense motion within more quiescent fluid flow is called intermittency (Frisch, 1996). Intermittent dynamics leads to strong deviations from Gaussian statistics, that become larger when considering fluctuations at smaller scales (Castaing et al., 1990; Chevillard et al., 2006).

As described in Sec. 1.5.3, intermittency is observed in many dynamical systems: from hydrodynamic turbulence (Castaing et al., 1990) to porous media flows (de Anna et al., 2013). However, understanding the physical mechanism of intermittency in systems which differ from high Reynolds number hydrodynamic turbulence remains a challenge (Falcon et al., 2007).

In this chapter a multi-scale analysis of the spatially-averaged velocity of the fluid front slowly invading our model disordered medium is presented. The analysis reveals all the distinguishing features of an intermittent dynamics and, more importantly, uncovers which parameters control it in this system. This work provides the first experimental evidence and detailed characterization of intermittency in fluid invasion of confined heterogeneous media.

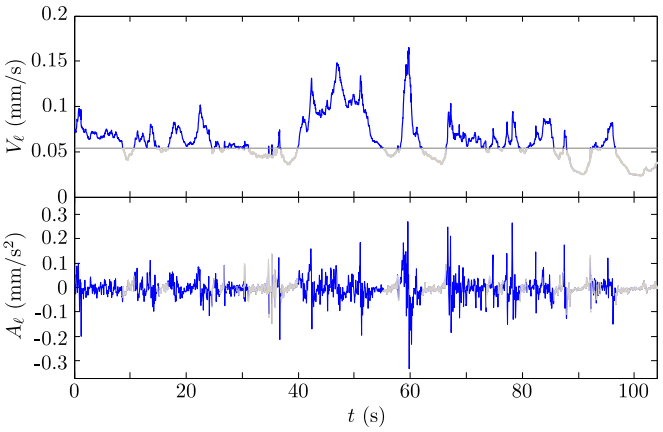

FIGURE 7.1: Typical velocity signal (top) and its corresponding time-derivative (bottom). Velocities below v are displayed in light grey. The accelerations corresponding to these periods of low velocity are plotted in the same colour. Experimental conditions v = 0.053 mm/s and $\mu = 50$ cP, analyzed at $\ell = L/8 = 17$ mm.

7.1 Velocity increments

We focus our attention on the intermittent character of the spatially-averaged velocity of the front $V_\ell(t)$. A typical example of $V_\ell(t)$ and its time derivative $A_\ell(t)$ are shown in Fig. 7.1. Regions of low velocities –below the imposed mean front velocity v– are displayed in light grey to distinguish them from high velocity regions. The corresponding accelerations are displayed using the same colour code. We observe that the acceleration strongly fluctuates during the periods of large velocities, while it is close to zero when V_ℓ is low.

To study the intermittent character of $V_\ell(t)$ we specifically perform a multi-scale analysis of the signal both in space and time. We base our analysis on the pioneering work of Frisch and Parisi (1985), described in Sec. 1.5.3. They introduced a multi-scaling description of jerky signals $v(t)$ in terms of the signal increments $\Delta v(\tau) = v(t+\tau) - v(t)$, as a function of the time lag τ. Intermittency is then characterized by analysing the statistical distributions of $P(\Delta v)$ and, specifically, the evolution of the moments of these distributions (Frisch, 1996).

Therefore, throughout this chapter we examine the statistical properties of the velocity increments defined as

$$\Delta V_\ell(\tau) = V_\ell(t+\tau) - V_\ell(t) \tag{7.1}$$

for various time delays τ and averaging length scales ℓ.

We first present the results corresponding to a given set of conditions: v = 0.053 mm/s and $\mu = 50$ cP, with a measuring window $\ell = L/8 = 17$ mm ($\simeq 1.6\ell_c$). The top panel of Fig. 7.2 shows the distributions of the normalized velocity increments

$$Y = \frac{\Delta V_\ell - \langle \Delta V_\ell \rangle}{\sigma} \tag{7.2}$$

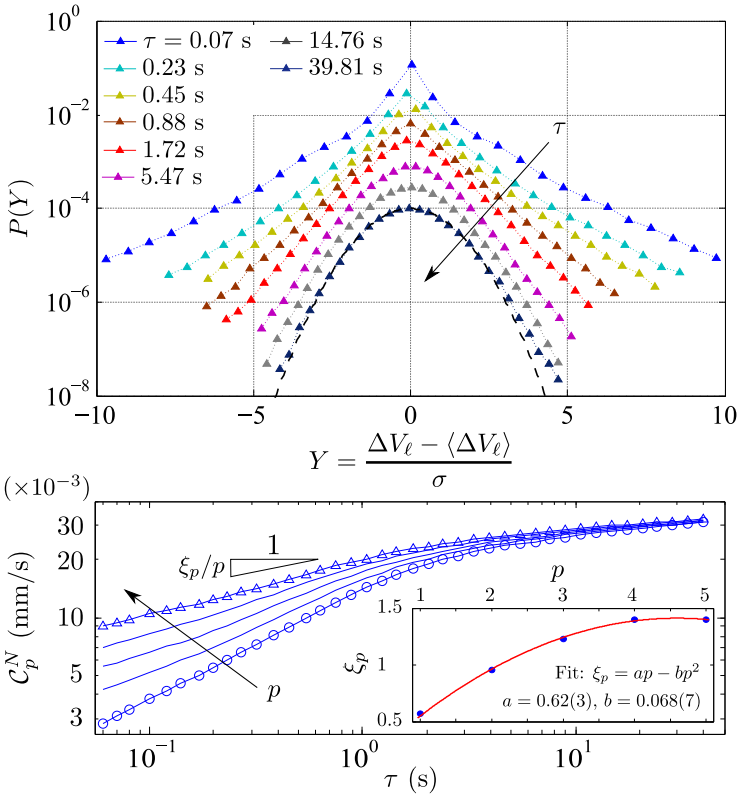

FIGURE 7.2: Top: Semi-log plot of $P(Y)$ vs $Y = (\Delta V_\ell - \langle \Delta V_\ell \rangle)/\sigma$ for increasing time lags τ, shifted vertically for visual clarity, for experiments at v = 0.053 mm/s and $\mu = 50$ cP, and analyzed at $\ell = L/8 = 17$ mm. The dashed curve represents a Gaussian distribution. Bottom: Corresponding normalized p-root structure functions $C_p^N(\tau)$ for $p = 1(\circ), 2, 3, 4, 5(\triangle)$. The evolution of the exponent ξ_p with p is shown in the inset; error bars are smaller than symbol size.

for increasing time lags τ. $\langle \Delta V_\ell \rangle$ stands for the ensemble average of ΔV_ℓ and σ for its standard deviation. Interestingly, we observe that the shape of these distributions evolves continuously through the temporal scales τ. For short time lags we measure distributions with exponential tails and a peak at $Y = 0$ (zero acceleration). This shape progressively evolves towards nearly Gaussian distributions at longer time lags. This result unveils that the dynamics of the invading front is highly intermittent, with complex temporal correlations on short time intervals (Frisch, 1996).

In order to quantify such complex temporal correlations, with strong deviations from Gaussian statistics, we analyse the scaling behaviour of the p-root structure functions $\mathcal{C}_p(\tau)$ of $\Delta V_\ell(\tau)$ given by

$$\mathcal{C}_p(\tau) \equiv \mathcal{S}_p^{1/p}(\tau) = \langle |\Delta V_\ell(\tau)|^p \rangle^{1/p}, \tag{7.3}$$

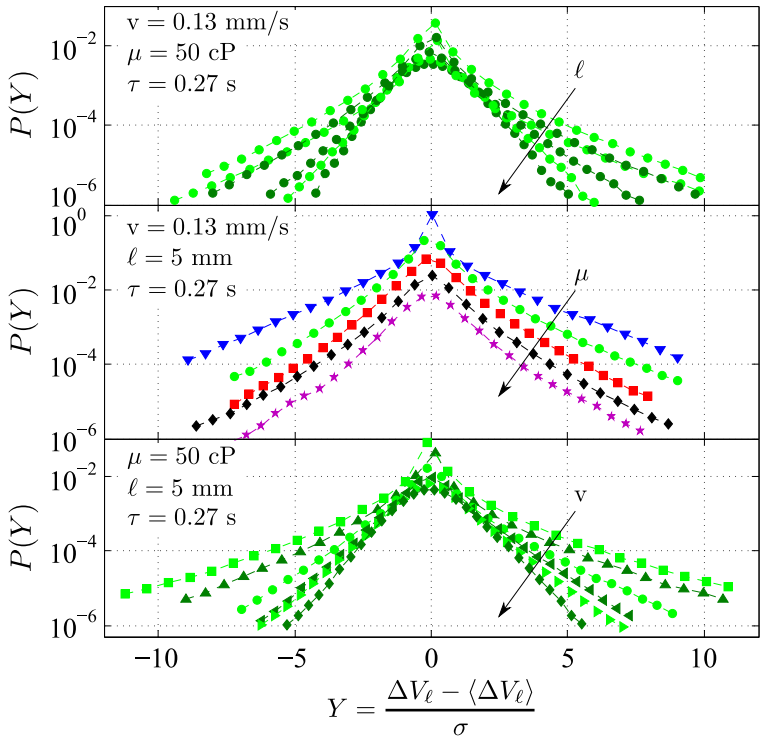

FIGURE 7.3: Statistical distributions $P(Y)$ vs $Y = (\Delta V_\ell - \langle \Delta V_\ell \rangle)/\sigma$, represented in a semilog plot and shifted vertically for visual clarity. The shape of the distributions evolves systematically with the scale of observation ℓ and the controlling parameters μ and v. Top: distributions for experiments observed at ℓ = 136, 34, 12.4, 6.5, 2.7 mm. Middle: evolution of the distributions with the viscosity μ = 10, 50, 100, 169, 350 cP. Bottom: distributions for driving velocities v = 0.036, 0.053, 0.13, 0.23, 0.35, 0.55 mm/s.

where $\mathcal{S}_p(\tau)$ are the structure functions defined in Sec. 1.5.3. The bottom panel of Fig. 7.2 shows a double-logarithmic plot of the normalized p-root structure functions

$$\mathcal{C}_p^N(\tau) = \frac{\mathcal{C}_p(\tau)}{\mathcal{R}_p^G} \tag{7.4}$$

for $p = 1, \ldots, 5$. The normalizing factor $\mathcal{R}_p^G = \mathcal{C}_p^G / \mathcal{C}_2^G$ is the ratio of p-root structure functions for a Gaussian distribution, and depends only on p (Santucci et al., 2007). At short time lags $\mathcal{C}_p^N \sim \tau^{\xi_p/p}$ over more than one decade. The non-linear dependence of ξ_p on p corresponding to the multiscaling behavior of the normalized structure functions, shown in the inset of Fig. 7.2, is a hallmark of intermittency (Frisch, 1996). It reflects non-homogeneous temporal fluctuations, which correspond to the evolution of the shape of the statistical distribution of velocity increments across time scales. The normalized structure functions collapse onto a single curve for all p at long time lags, as expected for Gaussian statistics –observed on the top panel of Fig. 7.2 at large τ.

The same behaviour of the shape of the distributions of $\Delta V_\ell(\tau)$ with the time lag is observed for all the experimental conditions explored. More interestingly, the tails of the distributions of velocity increments for a given time lag τ evolve with the scale of observation and the experimental controlling parameters, as shown in Fig. 7.3. The tails are systematically larger when the spatially-averaged velocity is measured at smaller length scales ℓ, or the oil viscosity μ, or the imposed flow rate –and hence v– are smaller, shown in the top, middle, and bottom panels respectively. This reveals a stronger intermittent character as ℓ, v, or μ are decreased. However, the effect of the parameters is not equal. Velocity has the strongest influence on the shape of the distributions, as observed in Fig. 7.3 although it is only explored in the range $\mathrm{v}_{max}/\mathrm{v}_{min} = 15$. The second most important parameter in controlling the evolution of the tails of the distributions is ℓ, which is varied in the range $\ell_{max}/\ell_{min} = 50$ in the plot. Finally, the distributions slightly evolve with viscosity, although a wide range is shown $\mu_{max}/\mu_{min} = 35$. The systematic evolution of the distributions of the rescaled ΔV_ℓ and the dependence of the pdfs on (ℓ, μ, v) are characterized in the following section.

7.2 Characterization of intermittency

In order to quantify the temporal evolution of the distributions of $\Delta V_\ell(\tau)$ and thus the intermittency of the dynamics of the invading front, we perform a statistical analysis of the scaling behaviour of the moments of $P(\Delta V_\ell(\tau)$. These methods are commonly used to study intermittency (Frisch, 1996).

Flatness of the distributions

As described in Sec. 1.5.3, together with the analysis of the structure functions of $\Delta V_\ell(\tau)$, the flatness of the distributions of velocity increments is also used to characterize the systematic evolution of the shape of the distributions and the intermittent character of the dynamics quantitatively (Frisch, 1996; Chevillard et al., 2012). Flatness is measured by the kurtosis of the distributions, $K(\tau)$, defined in Sec. 1.5.3.

The evolution of $K(\tau)$ as function of the experimental controlling parameters v and μ is shown in Fig. 7.4. The left panel of the figure shows the results for experiments with dynamic viscosity $\mu = 50$ cP, and various imposed velocities $0.036 < \mathrm{v} < 0.55$ mm/s. The right panel displays the kurtosis corresponding to experiments performed at the same $\mathrm{v} = 0.13$ mm/s but using different oils of dynamic viscosities from $\mu = 10$ cP to 350 cP. In both cases the interfaces are analysed at scale $\ell = L/16 = 8.5$ mm.

The effect of the window of observation on the distributions is quantified by measuring their kurtosis. Figure 7.5 shows the evolution of $K(\tau)$ with ℓ for a given experimental condition, $\mu = 50$ cP and $\mathrm{v} = 0.13$ mm/s.

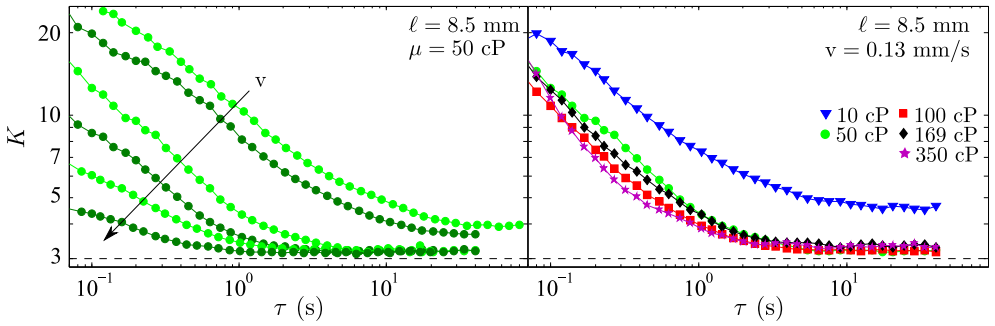

FIGURE 7.4: Kurtosis of $P(\Delta V_\ell(\tau))$ in log-log scale. Left panel shows the results for $\mu = 50$ cP, and v = 0.036, 0.053, 0.13, 0.23, 0.35, 0.55 mm/s. Right panel corresponds to experiments v = 0.053 mm/s and different μ. In all cases the interfaces are analysed at $\ell = L/16 = 8.5$ mm. The dashed line corresponds to the Gaussian value, $K_G = 3$.

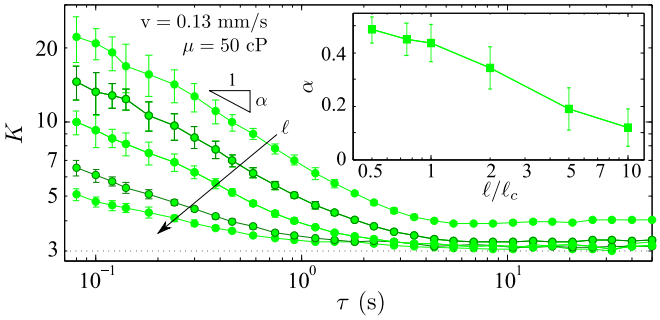

FIGURE 7.5: Double-logarithmic plot of the kurtosis of the distributions of $\Delta V_\ell(\tau)$ for $\mu = 50$ cP, v = 0.13 mm/s analysed at $\ell/\ell_c = 0.5, 1, 2, 5, 10$ ($\ell_c = 6.7$ mm). The dotted line corresponds to the Gaussian value, $K_G = 3$. The inset shows the power-law exponent α vs ℓ/ℓ_c.

In all cases K is manifestly larger than $K_G = 3$ for short time lags τ, making evident strong deviations from Gaussian statistics. The kurtosis decreases monotonically with τ, reflecting the non-similarity of the statistical distributions at different time lags. Finally, the kurtosis reaches a plateau at long τ, above a characteristic time lag τ_c. The final value of the plateau depends on the parameters ℓ, μ, and v. It reaches the expected Gaussian value $K_G = 3$ for $\ell > \ell_c$, but it is significantly larger for smaller windows of observation or larger correlation lengths, for which $\ell < \ell_c$, due to finite-size effects. We observe this effect in Fig. 7.4 for the lowest velocities and the lowest viscosity, for which ℓ_c is larger than the window of observation used. The finite-size effects are directly observed also in Fig. 7.5, where the size of the windows of observation used to compute $K(\tau)$ is measured in units of the correlation length.

The kurtosis is found to evolve systematically with v and ℓ, as observed in the behaviour of the distributions in Fig. 7.3. The slower the front is injected or the smaller the window of observation, the larger the resulting K. The evolution with μ appears less clear although a similar trend can be also observed. The lower the viscosity, the larger K.

As pointed out, K decreases with τ from short temporal increments until it reaches a plateau above a characteristic time τ_c. Near τ_c the behaviour can be approximated

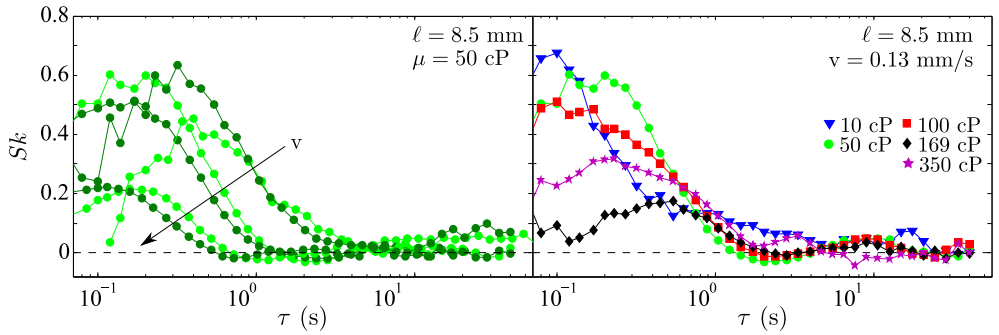

FIGURE 7.6: Skewness of $P(\Delta V_\ell(\tau))$ in log-log scale. Left panel shows the results for $\mu = 50$ cP, and v = 0.036, 0.053, 0.13, 0.23, 0.35, 0.55 mm/s. Right panel corresponds to experiments v = 0.053 mm/s and different μ. In all cases the interfaces are analysed at $\ell = L/16 = 8.5$ mm. The dashed line corresponds to the symmetric value, $Sk = 0$.

by a power law $K \sim \tau^{-\alpha}$. The power-law exponent α measures the intermittency of the signal within this range of τ (Chevillard et al., 2012). As shown in the inset of Fig. 7.5, α increases systematically as ℓ approaches ℓ_c, and saturates to a nearly constant value for $\ell \leq \ell_c$. This behaviour of the exponent α, and thus of the intensity of the intermittency, with ℓ/ℓ_c is observed in all experimental conditions (v, μ) explored.

Asymmetry of the distributions

It is worth noting that the distributions of $\Delta V_\ell(\tau)$ have positive asymmetry for small τ, in addition to being fat-tailed as measured by the kurtosis. In order to quantify such asymmetry we compute the skewness Sk of the pdfs, defined in Sec. 1.5.3.

The dependence of the skewness of $P(\Delta V_\ell(\tau))$ with the experimental controlling parameters (μ, v) is shown in Fig. 7.6. The left panel shows $Sk(\tau)$ for experiments performed at various imposed velocities $0.036 < \mathrm{v} < 0.55$ mm/s but one viscosity $\mu = 50$ cP. Sk for experiments using different oils of viscosities from $\mu = 10$ cP to 350 cP but performed at the same v = 0.13 mm/s are displayed in the right panel. In both cases the interfaces are analysed at scale $\ell = L/16 = 8.5$ mm. The evolution of the skewness as a function of the window of observation ℓ keeping μ and v constant is shown in Fig. 7.7.

In all cases Sk is different from zero at short time increments. As τ increases Sk decays towards zero, the symmetric value. The systematic evolution of the positive asymmetry is clear when varying v or ℓ. The slower the velocities or smaller the windows of observation, the more asymmetric are the distributions. The effect of viscosity is again less evident.

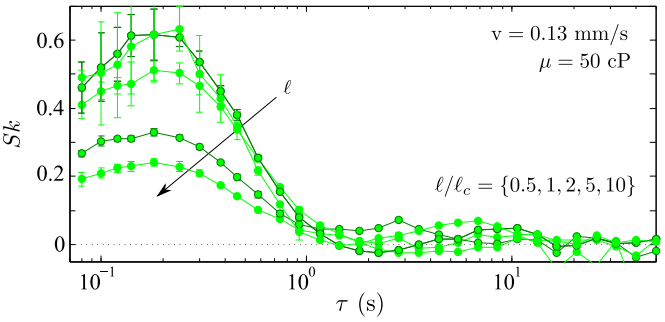

FIGURE 7.7: Double-logarithmic plot of the skewness of the distributions of $\Delta V_\ell(\tau)$ for μ = 50 cP, v = 0.13 mm/s analysed at $\ell/\ell_c = 0.5$, 1, 2, 5, 10 ($\ell_c = 6.7$ mm). The dotted line corresponds to the symmetric value, $Sk = 0$.

7.3 Controlling parameters of intermittent dynamics

To compare experiments performed in very different conditions, and avoid finite-size effects due to the correlation length scale ℓ_c (and specifically, its evolution with the imposed flow rate v and viscosity μ), we carry out this analysis for spatially-averaged velocity V_ℓ measured at scales ℓ such that ℓ/ℓ_c is constant. This ratio provides an estimate of the effective number of statistically independent domains of the invading front, which controls the non-Gaussian asymmetric shape of the distributions of velocity fluctuations, as shown in Ch. 6 (Sec. 6.1).

Interestingly, when measured at scales $\ell = \ell_c$ and a given time lag τ, we observe that the distributions of velocity increments $\Delta V_\ell(\tau)$ collapse into the same shape for experiments performed at different viscosities but same velocity (left top panel in Fig. 7.8). However, in these conditions ($\ell = \ell_c$) the shape of the distributions of the velocity increments still evolves systematically with the imposed flow rate (right top panel in Fig. 7.8). The slower the fluid is injected through the medium, the more non-Gaussian are the distributions of $\Delta V_\ell(t)$. Such behaviour, observed for one single time increment τ in top panels of the figure, is confirmed by the temporal evolution of the kurtosis K of V_ℓ measured at scales $\ell = \ell_c$, as shown in the bottom panels of Fig. 7.8. $K(\tau)$ for experiments performed using oils of different viscosities but the same v collapse within error bars (left panel of the figure). However, for experiments with a single μ, $K(\tau)$ clearly evolves with the imposed mean velocity (right panel of the figure).

Therefore, when interfaces are analysed at windows such that ℓ/ℓ_c is constant, the evolution of K and, more specifically, the characteristic time delay τ_c at which K reaches a plateau do not depend on oil viscosity. However, τ_c decreases systematically with imposed flow rate, as shown in the inset of Fig. 7.9. Moreover, the intensity of the intermittent character of the velocity signal, measured by the exponent α, appears to be the same for the various experimental conditions –given that ℓ/ℓ_c is constant. Then, we expect a collapse of the kurtosis for all experiments when time lag τ is rescaled by τ_c.

Figure 7.9 shows the kurtosis corresponding to all experiments compatible with $\ell/\ell_c = 1$ as a function of the rescaled increment of time τ/τ_c. The curves display a good

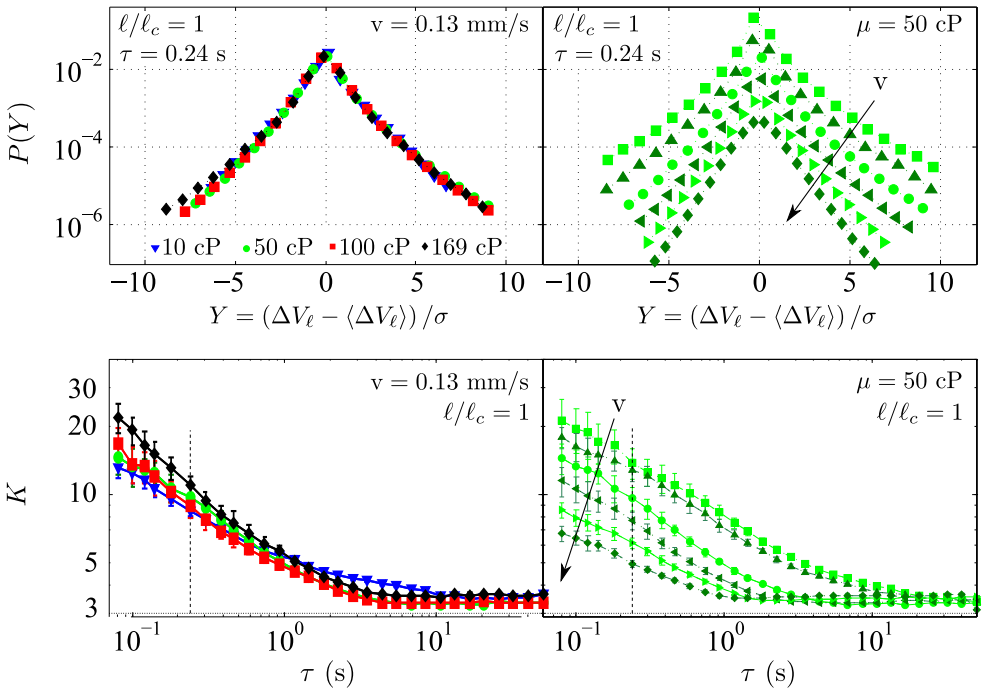

FIGURE 7.8: Top: semi-log plots of the normalized distributions of velocity increments (shifted arbitrarily for different v for visual clarity) for experiments analyzed at $\ell = \ell_c$. Bottom: log-log plots of their corresponding kurtosis for all time lags τ explored. Left panels display results for different μ but fixed v. Right panels display the systematic evolution with v (from 0.036 to 0.55 mm/s) for a single μ. Vertical lines give the value of τ used to compute the distributions shown in the top panels.

collapse. For short τ/τ_c, the error bars are larger due to poorer statistics. Nevertheless, all experimental conditions show the same behaviour with an exponent compatible with $\alpha = 0.45$.

As shown in the inset of Fig. 7.9, we find that the characteristic time scales with the velocity as $\tau_c \sim 1/\mathrm{v}$ with a proportionality coefficient around 0.6 mm –independently of ℓ, μ, v. This value coincides with ℓ_d, the mean extent of the disorder patches –described in Ch. 2. Therefore, $\tau_c = \ell_d/\mathrm{v}$ can be identified as the average time spent by the fluid front to advance over the typical distance ℓ_d.

Interestingly, while local bursts of activity –analysed in detail in Ch. 5– can extend on scales much larger than this characteristic length of the medium heterogeneities ℓ_d and last over time scales much longer than τ_c, the latter determines the temporal range of intermittency of the global (spatially-averaged) velocity signal. This effect can be observed in the temporal traces of the velocity signal $V_\ell(t)$ and how they are related to their time derivative. An example was shown in Fig. 7.1. Periods of low velocities, slightly below the imposed mean front velocity v (grey colour in the plot), alternate with periods of very large velocity excursions above v. In the former the acceleration

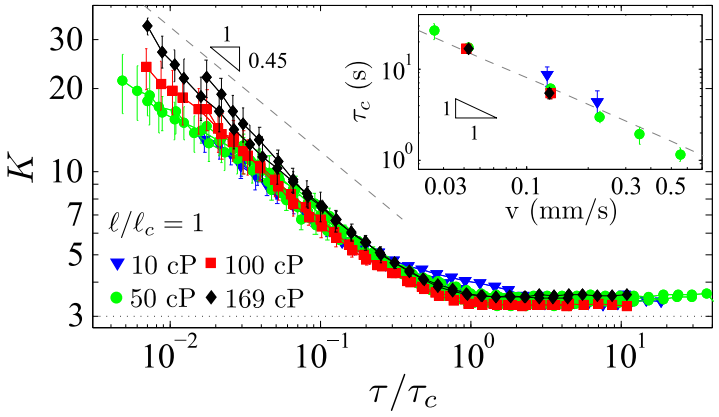

FIGURE 7.9: Kurtosis corresponding to all experiments compatible with $\ell = \ell_c$ as a function of the rescaled τ/τ_c in log-log. Different symbols correspond to different viscosities –different velocities ranging from $0.036 < \mathrm{v} < 0.55$ mm/s are not distinguishable. The dotted line corresponds to the Gaussian value, $K_G = 3$. Inset: characteristic time obtained from K as a function of the imposed mean velocity in log-log. Dashed lines correspond to power laws with the exponents quoted.

is small and strongly correlated to the velocity, while in the latter the acceleration fluctuates strongly. This behaviour can be related to the comportment of the global avalanches of the front –studied in Ch. 6 (Sec. 6.2). In that case, the maximum duration of avalanches scaled as τ_c, revealing that the temporal extension of the bursts of activity of the spatially-averaged velocity is strongly influenced by the disorder. This observation suggests that global avalanches of $V_\ell(t)$ are closely related to the intermittent character of the signal.

The statistical analysis of $\Delta V_\ell(\tau)$ shown so far allows us to reach the main result of the present Chapter, namely to identify the controlling parameters of the observed intermittent dynamics. Figure 7.10 shows the normalized statistical distributions of spatially-averaged velocity increments obtained under various experimental conditions (μ, v), but measured at length scales ℓ and time lags τ such that both ratios ℓ/ℓ_c and τ/τ_c are fixed. The data collapse is remarkable considering that up to 13 different (μ, v) are shown.

The collapse of the data from experiments analysed at windows $\ell \leq 2$, shown in Fig. 7.10 for four values of τ/τ_c, is confirmed for all range of τ explored by the collapse of the kurtosis of the distributions, as displayed in the top panels of Fig. 7.11.

Figure 7.11 shows the kurtosis for all experiments compatible with $\ell/\ell_c = 0.5$, 2, 5 and 10 as functions of the rescaled τ/τ_c. The effect of the ratio ℓ/ℓ_c is clear again. First, the intensity of the intermittency increases when the number of statistically independent domains is reduced, as revealed by the increasing slope of K for small τ/τ_c. The actual values of K also increase as ℓ/ℓ_c diminishes. In addition, finite-size effects are also observed. The value of the plateau reached by K at long τ/τ_c becomes larger than

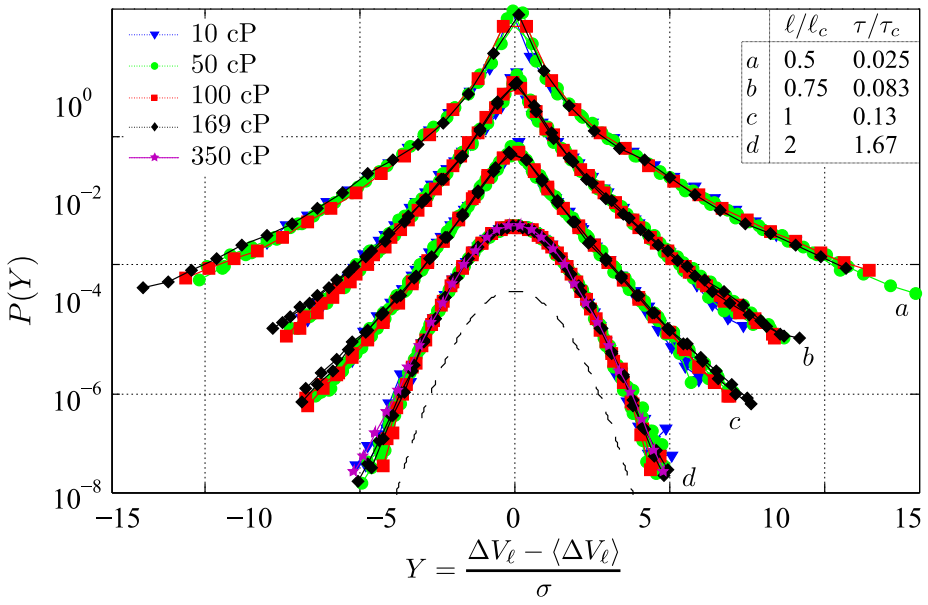

FIGURE 7.10: Semi-logarithmic plot of the distributions of $\Delta V_\ell(\tau)$ for very different experimental conditions, with v ranging from 0.036 to 0.55 mm/s and μ from 10 to 350 cP, collapsed for fixed $(\ell/\ell_c, \tau/\tau_c)$. The dashed curve represents a Gaussian distribution. Distributions are shifted arbitrarily for visual clarity

$K_G = 3$ when $\ell/\ell_c \leq 1$. For $\ell/\ell_c = 0.5$, small uncertainties in the window of observation ℓ or on the actual value of ℓ_c are turned into the small dispersion of the values $K(\tau > \tau_c)$ observed.

Finally, we notice that the collapses of K for $\ell \gg \ell_c$ are not as clear as for $\ell/\ell_c \leq 2$, specially at small rescaled time lags. In these cases the exponent α slightly differs from one experimental condition to the other, resulting in poorer collapse of the data. Nevertheless, in all cases the distributions reach the plateau at $\tau = \tau_c$.

In figure 7.12 we show the distributions of velocity increments from all experimental conditions compatible with $\ell/\ell_c = 5$ and 10 for a small τ/τ_c. Data sets involved in the analysis of large ℓ are smaller, then increasing the statistical fluctuations. Nevertheless, in both cases displayed the pdfs show a good collapse spanning more than three decades. Only the tails of the distributions, which correspond to rare, extreme events with poorer statistics, display some dispersion. This dispersion of the pdfs due to the lag of statistics is then responsible for the poorer collapse of the kurtosis observed in the bottom panels of Fig. 7.11.

All in all, the data collapses displayed in Figs. 7.10 and 7.12 show that the distributions of velocity increments depend specifically on ℓ/ℓ_c and τ/τ_c only. While the characteristic time τ_c sets the temporal range over which intermittency is observed, the ratio ℓ/ℓ_c controls its intensity.

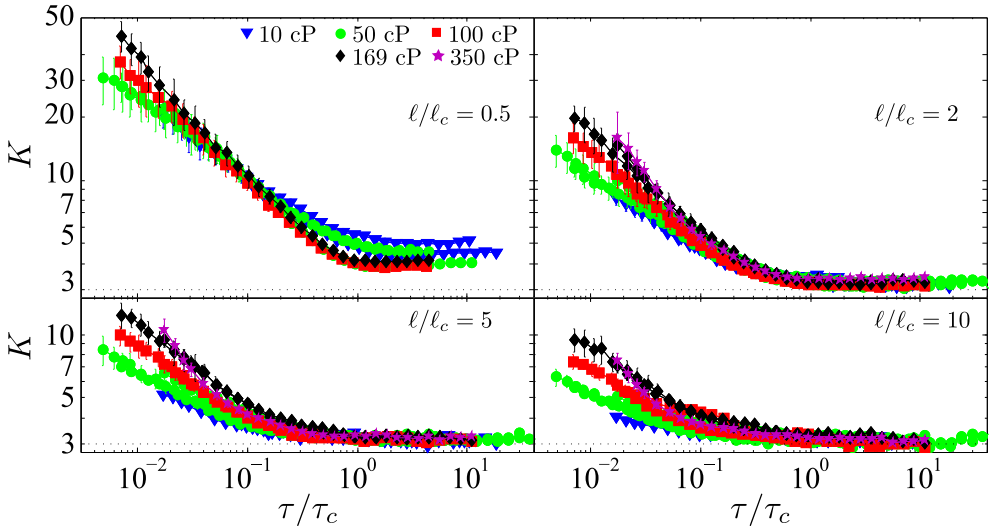

FIGURE 7.11: Double-logarithmic plots of the kurtosis corresponding to all experiments compatible with $\ell/\ell_c = 0.5$, 2, 5, 10 as functions of the rescaled τ/τ_c. Different symbols correspond to different viscosities –different velocities ranging from $0.036 < v < 0.55$ mm/s are not distinguishable.

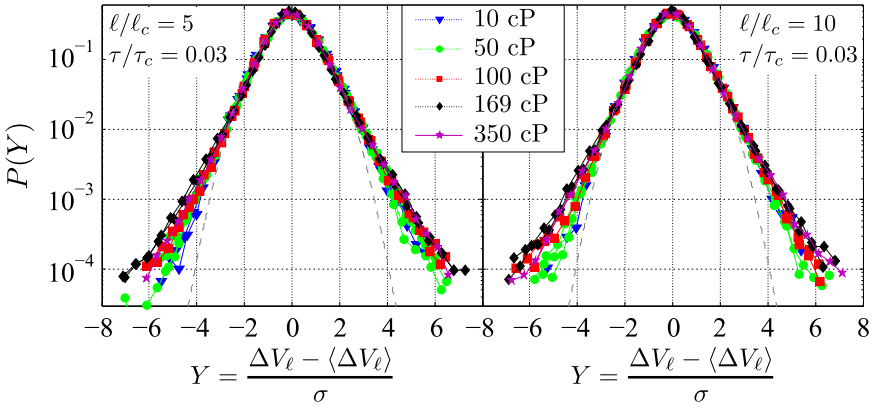

FIGURE 7.12: Semi-logarithmic plot of the distributions of $\Delta V_\ell(\tau)$ for very different experimental conditions, with imposed mean velocities ranging from 0.036 to 0.55 mm/s and viscosities from 10 to 350 cP, collapsed for fixed $(\ell/\ell_c, \tau/\tau_c)$.

7.4 Conclusions

To conclude, we have shown that the slow fluid invasion of an open fracture displays all the characteristic features of intermittent dynamics. Periods of low velocities alternate with periods of very large velocity excursions above v. In the former the accelerations are small and strongly correlated to the velocity, while in the latter the acceleration fluctuates strongly. Large velocity bursts and fluctuating accelerations have their origin in the capillary pressure fluctuations produced by the variable aperture of the model,

which heavily distort the front at the scale of the medium heterogeneities, and in the relaxation of front distortions by surface tension at larger scales up to ℓ_c.

The intermittent dynamics results from local bursts of fast cooperative motion, triggered from the smallest length scales of the medium heterogeneities up to the correlation length ℓ_c –at which viscous pressure damping becomes more effective than surface tension. Intermittency is controlled by the ratio ℓ/ℓ_c, where ℓ_c depends on material properties of the invading fluid, the permeability of the disordered medium, and the average front velocity imposed. The temporal range over which intermittency is observed is set by τ_c. Both ℓ_c and τ_c vanish at high flow rates. Hence, intermittency is present only in slow imbibition displacements in the capillary regime.

By analogy with intermittency and the flux of energy across different scales in fully developed turbulence (Frisch, 1996; Chevillard et al., 2012), we speculate with the possibility that the positive asymmetry of the pdf of velocity increments observed in our experiments is the signature of an inverse cascade resulting from fluid incompressibility, which is at the origin of the correlation length ℓ_c (Alava et al., 2004). Extension of the analysis presented here to other problems of front propagation in random media such as fluid imbibition in compact porous media (Delker et al., 1996), contact line dynamics (Le Doussal et al., 2009), and planar crack front displacements (Tallakstad et al., 2013), could bring further insight into this question. Our model experiment of fluid front invasion at low Ca, and the systems mentioned, are very different from hydrodynamic or wave turbulence. Hence, we expect that the results presented will motivate new theoretical and experimental approaches of intermittency.

Chapter 8

Conclusions and future perspectives

8.1 Conclusions

The present Thesis has focused on the spatio-temporal dynamics of the interfacial front between displaced air and invading oil, in imbibition displacements through a model open fracture.

Our model open fracture consists of a Hele-Shaw (HS) cell, i.e. two parallel plates separated by a narrow gap spacing. Two configurations have been explored: a flat HS cell, that mimics an open fracture with constant aperture; and a HS cell with a dichotomic gap spacing randomly distributed in space, that mimics an open fracture featuring a two-dimensional non-zero aperture field distributed along a plane. Silicone oils of different viscosities have been used for the first time in this setup. Two driving protocols have been studied, corresponding to spontaneous imbibition, where a constant pressure difference is imposed between the inlet and the outlet of the cell, and forced-flow imbibition, where a constant flow rate is imposed at the inlet.

The conclusions of the Thesis are drawn in the following.

Capillary rise

We have first analysed the evolution of the mean position of the interface in spontaneous imbibition, both analytically and experimentally, in Ch. 3. Two configurations of the model open fracture –constant aperture and spatially-fluctuating aperture– have been explored for two qualitatively different conditions: with and without gravity. An effective gravity opposing front advancement has been achieved by tilting the cell.

The conclusions of this study are:

- Our model open fracture behaves macroscopically as a real porous medium, in the sense that the spatially-averaged position of the fronts in spontaneous imbibition follows the LW and ES solutions. In the absence of gravity $h \sim t^{1/2}$, while in the presence of gravity the front saturates at h_{eq}, the Jurin's height.

- We have shown that any additional source of viscous dissipation in the system changes the nature of the classical LW and ES solutions. These solutions overestimate the experimental curves $h(t)$ at all times.

- Considering an additional resisting term in the pressure balance equation, proportional to the mean velocity of the front, a new analytical solution $h(t)$ has been obtained. Viscous dissipation at the preparation zone of the cell is responsible for this term.

- This new solution reproduces the experimental results at all times, with and without gravity, particularly for the constant gap configuration.

Kinetic roughening

The growing spatio-temporal fluctuations of the oil-air interface in low-viscosity, forced-flow imbibition displacements have been studied in Ch. 4. A kinetic roughening process takes place as the front evolves from an initially-flat interface to a final, statistically-invariant rough front.

The conclusions of this study are:

- The scaling scenario of kinetic roughening is anomalous, i.e. local and global scales follow different dynamics. Specifically we have characterized a super-rough scaling scenario with exponents $\alpha = 1.38(15)$, $\alpha_{loc} = 0.97(1)$, $\beta = 0.50(1)$, $\beta^* = 0.16(7)$, and $z = 2.8(4)$. These values satisfy the theoretical scaling relations $\beta^* = (\alpha - \alpha_{loc})/z$ and $\beta = \alpha/z$.

- We have proven that forced-flow imbibition at $\mathrm{Ca} = 6.3 \cdot 10^{-5}$, corresponding to v = 0.13 mm/s and $\mu = 10$ cP, is in the capillary-dominated disorder regime, where $z = 3$ is expected.

- The results presented are compatible with earlier experiments of forced-flow imbibition by Planet et al. (2014) for capillary number $\mathrm{Ca} = 3.2 \cdot 10^{-4}$.

Local spatio-temporal dynamics

The spatio-temporal dynamics of the interfaces at local scale, i.e. at the scale of the spatial resolution (typically much smaller than the lateral correlation length of the front

ℓ_c and the characteristic length of the disorder ℓ_d), has been studied in Ch. 5 in forced-flow experiments. A wide range of experimental conditions has been explored, including the use of oils of different viscosity for the first time in this setup. The imbibition front exhibits a burst-like dynamics, advancing by spatially-localized avalanches.

The conclusions of this study are:

- Local velocities $v(x, y)$ are widely distributed around their mean value. Fluctuations of $v(x, y)$ are controlled by the capillary number Ca: the range of $v(x, y)$ widens as Ca $\to 0$. We have shown that μ and v play the same role in controlling these fluctuations.

- We have studied the spatial and temporal correlations of the local velocities for the first time. The experimental parameters μ and v play the same role in controlling the lateral correlation length of local velocities, as expected from the theoretical prediction $\ell_c \sim 1/\sqrt{\mu \mathrm{v}}$. On the contrary, the maximum anticorrelation time Δt^* evolves differently with μ and v, $\Delta t^* \sim \mu^{-0.4} \mathrm{v}^{-1.4}$. The spatial correlation in the direction of propagation of the front presents two characteristic length scales: the length of maximum anticorrelation Δy^*, and the decorrelation length Δy^{min}. Δy^* is constant for all experiments and fairly coincides with the lengthscale ℓ_d at which the disorder patches become uncorrelated. On the contrary, $\Delta y^{min} \sim (\mu \mathrm{v})^{-0.4}$.

- We have confirmed for different oil viscosities that sizes A, durations D, and lateral extents L_x and L_y of local avalanches are widely distributed, following power laws with exponential cutoffs. The power-law exponents of the pdfs are independent of μ and v. On the contrary, the cutoffs diverge as Ca $\sim \mu \mathrm{v} \to 0$.

- We have obtained the power-law exponents $\alpha_A = 1.08$ of $P(A)$, $\alpha_D = 1.03(10)$ of $P(D)$, $\alpha_{L_x} = 0.83(10)$ of $P(L_x)$, and $\alpha_{L_y} = 1.08(15)$ of $P(L_y)$. The anisotropy exponent, relating the extent of local avalanches in the streamwise and spanwise directions, $L_y \sim L_x^H$, is $H = 0.82(2)$. These values are in excellent agreement with earlier experimental results by Santucci et al. (2011), but differ significantly from results obtained in phase-field simulations by Pradas et al. (2009).

- Thanks to large data sets we have been able to analyse carefully the behaviour of the cutoffs of the pdfs of sizes ξ_A, durations ξ_D, and lateral extents ξ_{L_x} and ξ_{L_y}. We have verified that $\xi_{L_x} \sim \ell_c$, $\xi_{L_y} \sim \xi_{L_x}^H \sim \ell_c^H$, $\xi_A \sim \xi_{L_x} \xi_{L_y} \sim \ell_c^{1+H}$, and $\xi_D \sim \xi_{L_y}/\mathrm{v} \sim \ell_c^H/\mathrm{v}$, with $\ell_c \sim 1/\sqrt{\mu \mathrm{v}}$, upon changing systematically both front velocity and fluid viscosity. We have also shown that $\Delta y^{min} \sim \ell_c^H$, and $\Delta t^* \sim \ell_c^H/\mathrm{v}$.

- The spread of local avalanches in space is not trivially correlated with the underlying disorder of the medium. We have shown for the first time that on average

35 % of the area swept by local avalanches corresponds to disorder patches. This value coincides with the nominal filling fraction of our disorder plates.

Global spatio-temporal dynamics

In Ch. 6 we have also analysed the spatially-averaged (or global) velocity of the front $V_\ell(t)$, observed through windows of lateral size ℓ, in the same set of forced-flow experiments. The temporal signal $V_\ell(t)$ displays avalanche-like dynamics with non-Gaussian fluctuations.

The conclusions of this study are:

- The statistical distributions of $V_\ell(t)$ are properly represented by a generalized Gumbel distribution. We have verified that the effective number of degrees of freedom of the interface, $N_{\text{eff}} = \ell/\ell_c$, controls the asymmetry of those distributions –also upon changing oil viscosity μ for the first time in this setup.

- The temporal correlations of $V_\ell(t)$ have been characterized for the first time. The maximum anticorrelation time Δt^* is controlled by the duration of the longest-lasting local avalanches, $\Delta t^* \sim \ell_c^H/\text{v}$.

- We have confirmed that sizes S and durations T of global avalanches are widely distributed. We have characterized for the first time the influence of the window of observation ℓ on the statistical properties of global avalanches, and related this influence to ℓ_c.

- For $\ell > \ell_c$, $P(S)$ and $P(T)$ are power-law distributed with exponential cutoffs. The power-law exponents $\alpha = 0.96(5)$ of $P(S)$, and $\tau = 1.15(15)$ of $P(T)$ are independent of the experimental conditions. Moreover, these values are in good agreement with the values obtained from experiments by Planet et al. (2009) and Planet et al. (2011), and remarkably also with the values obtained from phase-field simulations (Pradas et al., 2009).
  The joint distribution $P(S,T)$ also verifies a scaling relation $S \sim T^\gamma$, but γ slightly evolves with ℓ/ℓ_c.
  Using oils of different viscosities has allowed us to show that maximum sizes ξ_S and maximum durations ξ_T of global avalanches are not controlled by the same mechanism. While ξ_S evolves with ℓ/ℓ_c, $\xi_T \sim 1/\text{v}$.

- For $\ell < \ell_c$, $P(S)$ and $P(T)$ display a bump before the exponential decay, as a consequence of data windowing.

- The average shape of global avalanches has been studied for the first time in imbibition fronts. The average avalanche shape shows a systematic evolution with

increasing N_{eff}: from asymmetric shapes tilted towards short times to nearly time-symmetric shapes. Experimentally determined average shapes are well described by a recently proposed general form (Laurson et al., 2013) that depends on two parameters only, γ and a. γ is the exponent of $S \sim T^{\gamma}$, and a is an asymmetry parameter, related to inertial effects and temporal irreversibility. We have found that both parameters evolve systematically with ℓ/ℓ_c.

Intermittency in slow imbibition

In order to study in a quantitative way the intermittent character of our slow imbibition displacements, we have performed a multi-scale analysis of the spatially-averaged front velocity. The results obtained represent first experimental evidence and detailed characterization of intermittency in fluid invasion of confined heterogeneous media.

The conclusions of this study are:

- The spatially-averaged velocity $V_\ell(t)$ of a fluid front invading a model open fracture in a forced-flow imbibition displacement is intermittent. The statistical distributions of velocity increments $\Delta V_\ell(\tau) = V_\ell(t+\tau) - V_\ell(t)$ evolve continuously through time scales τ from fat-tailed to Gaussian, a hallmark of intermittency.

- Intermittency has been studied quantitatively by analysing different moments of the distributions of $\Delta V_\ell(\tau)$, specifically their kurtosis and skewness. A characteristic time τ_c has been defined as the time lag required for the kurtosis to saturate. We have found that τ_c only depends on v.

- The statistical analysis performed has allowed us to collapse data for a wide range of experimental conditions (μ, v) analysed at various ℓ. The collapse shows that intermittency is controlled by two parameters only: ℓ/ℓ_c and τ/τ_c. The former, that depends on μ, v, and ℓ, is associated with local mass conservation of the fluid. The latter, which only depends on v, may be related to the characteristic extent ℓ_d of the disorder, with $\tau_c = \ell_d/\text{v}$.

- The intensity of intermittency is controlled by ℓ/ℓ_c, while τ_c sets the temporal range over which intermittency is observed.

General conclusion

The ensemble of results presented in this Thesis supports a very general picture of the nonequilibrium dynamics of slowly-driven fronts in open fractures. The lateral propagation of interfacial fluctuations is controlled by local mass conservation, through the lateral correlation length $\ell_c \sim 1/\sqrt{\text{Ca}}$. The advancement of the interface in the direction

of propagation is controlled by the characteristic extent of the disorder ℓ_d and by the mean front velocity. These are the two basic ingredients that control the avalanche-like, intermittent dynamics of the fluid front. We propose that a minimal model of the interfacial dynamics studied here should take care of these two properties only.

8.2 Future perspectives

The results presented throughout this Thesis have brought new interesting questions regarding the dynamics of imbibition fronts in model open fractures. In the following we propose new experimental studies to answer these questions, that will widen our understanding of flow in these media.

Configuration of the disorder

Results obtained in chapters 5 to 7 have shown that the heterogeneities of the medium play a crucial role on the intermittent burst-like dynamics of the imbibition interfaces invading it. In particular, the length of maximum anticorrelation in the direction of front advancement of the local velocities fairly coincides with the characteristic size of the disorder ℓ_d. The characteristic intermittent time can be related also to ℓ_d. However, a systematic study of the relation between the dynamics of the front and the underlying disorder landscape is missing. We propose three approaches to understand this relation:

- We propose to start with modifying the persistence of the disorder in the direction of propagation by systematically modifying (reducing or enlarging) the extent of the disorder patches in the y direction.
- A step forward could be taken by considering a disorder landscape closer to a natural open fracture. In this case, a smoothly-fluctuating substrate would be used, similar to the setups utilized by Geromichalos et al. (2002) or Boschan et al. (2009, 2011).
- The setup could be adapted to study the transition from a model open fracture to a model porous medium. To model a porous medium some disorder patches should occupy the whole gap spacing of the cell, preventing the advancement of the fluid front over them.

Single defect study

In order to understand the role of the disorder on the front dynamics, another approach consists in analysing the dynamics of the front over an isolated disorder patch or defect.

A systematic characterization in terms of the lateral correlation length of the front, the characteristic extent of the disorder in the direction of propagation, and also the extent of the disorder in the lateral direction, can shed light on the dynamics of the imbibition front through our model open fracture. Given that the quenched disorder would be extremely well controlled, it could also allow a direct comparison to existing theoretical approaches (Joanny and de Gennes, 1984; Pauné and Casademunt, 2003) and, specifically, verify the relaxation of the perturbations by capillary forces and viscous dissipation. In addition, given that the evolution of the front is deterministic and a statistical analysis would not be necessary, these experiments would not require a large data set for each experimental configuration. First attempts in this direction have been carried out.

Approaching the pinning point

In chapters 5 and 6 we have shown that the dynamics of the fluid front invading our disordered medium approaches a critical pinning/depinning point when $\mathrm{Ca} \to 0$. The lateral correlation length of the interface then diverges when $\mathrm{Ca} \to 0$ as $\ell_c \sim 1/\sqrt{\mathrm{Ca}} \sim 1/\sqrt{\mu \mathrm{v}}$.

This limit cannot be directly reached simply by reducing v or μ to zero due to experimental limitations. Here we present two procedures that would allow to achieve a diverging lateral correlation length, reaching the system size.

- Controlled pressure perturbations. In this procedure the fluid penetrates the medium in spontaneous imbibition. The HS cell is slightly tilted so that an effective gravity acts against the advancement of the fluid front. Then, the interface naturally reaches $\mathrm{v} = 0$ at the equilibrium height. In this situation $\ell_c > L$, the system size. We can then perturb this critical state by slightly increasing the applied pressure difference, and study the relaxation of the front. In appendix C we present preliminary experiments in this regime.

- Destabilizing gravity. In forced-flow imbibition experiments in the presence of gravity the lateral correlation length is given by $\ell_c^* \sim 1/\sqrt{\mu \mathrm{v} + \rho\kappa g_{\mathrm{eff}}}$, where g_{eff} is the effective gravity $g \sin\psi$ in the in-plane y direction. A positive g_{eff} opposes front advancement, while a negative g_{eff} promotes front advancement. In the latter case, a diverging correlation length can then be achieved for finite v and μ. Specifically, for $\mu \mathrm{v} = \rho\kappa|g_{\mathrm{eff}}|$, $\ell_c^* \to \infty$. Inclinations of the cell $-1^\circ > \psi > -3^\circ$ are adequate considering the range of experimental parameters explored. Beyond this marginal state, e.g. for $\rho\kappa|g_{\mathrm{eff}}| > \mu \mathrm{v}$ with $g_{\mathrm{eff}} < 0$, the front is linearly unstable against the formation of viscous fingers.

Part II

Summaries

Chapter 9

Resum en català

L'objectiu de la tesi és l'estudi de la dinàmica espacio-temporal de la interfície entre aire desplaçat i oli invasor, en desplaçaments d'imbibició a través d'un model de fractura oberta. La recerca presentada combina un extens i exhaustiu treball experimental amb una anàlisi de dades acurada, basada en mètodes utilitzats en física estadística de no equilibri.

Primer de tot s'estudia l'avançament de la posició mitjana del front de fluid en condicions d'imbibició espontània. L'evolució de la interfície s'analitza tant analíticament com experimental. Seguidament es caracteritza el procés d'arrugament dinàmic (*kinetic roughening*) del front oli-aire en condicions d'imbibició forçada. Finalment, la dinàmica espacio-temporal complexa del sistema és estudiada en el règim d'avançament estadísticament estacionari, en el règim en què l'amplitud de les fluctuacions del front ha saturat.

9.1 Introducció

La dinàmica de fluxos a través de medis desordenats, com ho són els medis porosos i les fractures obertes, és rellevant en molts processos d'interès que comprenen escales de longitud del micròmetre a diversos quilòmetres (Sahimi, 2011). El flux de fluids biològics en membranes i vesícules, la irrigació de sòls (Heber Green and Ampt, 1911), l'absorció d'aigua per part del ciment en edificis (Khatib and Clay, 2004) o la difusió de partícules contaminants al subsòl (Frippiat and Holeyman, 2008) en són alguns exemples. A més a més, el flux a través de medis desordenats s'ha erigit com un bon sistema per estudiar problemes de física fonamental. L'estructura heterogènia dels medis porosos o les fractures obertes pot comportar que la seva invasió per part d'un fluid

mostri una dinàmica espacio-temporal complexa. Concretament s'han observat processos d'arrugament dinàmic (*kinetic roughening*), allaus, i fluctuacions no gaussianes de la velocitat dels fronts d'imbibició.

En aquesta tesi ens centrem en l'estudi de la dinàmica de fronts de fluid a través d'una fractura oberta. Aquest medi consisteix en una peça sòlida separada per una fissura amb una obertura petita. La separació entre les dues parets en general no és constant sinó que fluctua al llarg del medi (Sahimi, 2011). En funció de les propietats de mullat dels fluids invasor i desplaçat respecte el medi observem un procés de drenatge, quan el fluid desplaçat mulla millor el medi, o bé un procés d'imbibició en el cas contrari (Alava et al., 2004). En el darrer cas, l'efecte de la pressió capil·lar és suficient per fer penetrar el fluid dins el medi sense necessitat d'aplicar una força externa. Aquesta pressió és deguda a la curvatura del front, ja que el fluid avança per les parets del medi amb més facilitat, i a la tensió superficial, que procura disminuir aquesta curvatura. La proporcionalitat entre la velocitat mitjana del fluid a través d'un medi porós o una fractura oberta i el gradient de pressió ve donat per la llei de Darcy quan es considera un flux estacionari a un número de Reynolds baix (Guyon et al., 2001).

El nostre estudi s'ha centrat en el procés d'imbibició. N'hem explorat dos protocols d'injecció de fluid: imbibició espontània, en que es manté una diferència de pressió constant entre l'entrada i la sortida del medi, i imbibició forçada, en que el fluid s'injecta a flux de massa per unitat de temps constant.

Els processos d'imbibició espontània s'anomenen d'ascens capil·lar quan es refereixen a la propagació d'una interfície de fluid a través d'un tub de radi interior molt petit (tub capil·lar) i també en el cas de l'avançament a través d'una fractura oberta. Si el medi es troba col·locat horitzontalment, la posició mitjana del front de fluid creix proporcionalment a l'arrel quadrada del temps, seguint la llei de Lucas (1918) i Washburn (1921). Quan s'inclina el medi de manera que la gravetat efectiva actua en contra de l'avançament del front, la interfície es propaga seguint la llei de Lucas-Washburn a temps curts i satura exponencialment a l'alçada d'equilibri d'acord amb la Solució Estesa (*Extended Solution*) obtinguda per Fries and Dreyer (2008*b*).

En una part substacial dels experiments presentats en aquesta tesi s'utilitza un model de fractura oberta amb un espaiament entre parets que fluctua aleatòriament en l'espai degut al desordre introduït –descrit a la Sec. 9.2. En aquests casos, la pressió capil·lar a la interfície fluctua significativament, seguint les variacions de l'obertura de la fractura. Aquestes fluctuacions de la pressió provoquen que el front no avanci contínuament sinó que ho faci a batzegades, seguint un procés d'ancoratge/desancoratge (*pinning/depinning*). El desordre, doncs, és el responsable que el front deixi de ser pla –imposat a l'inici de l'experiment– i s'arrugui. Per altra banda, la pressió viscosa i la tensió superficial al llarg del front procuren aplanar de nou la interfície. Aquests dos sistemes d'esmorteïment

escalen diferent amb la mida lateral de les pertorbacions, fet que ens permet definir una longitud característica ℓ_c. Aquesta longitud és proporcional a $\ell_c \sim 1/\sqrt{\mu v}$, on μ és la viscositat dinàmica del fluid i v la velocitat mitjana del front, de manera que es pot ajustar modificant els paràmetres de control experimentals. La longitud ℓ_c, a més, resulta ser una fita superior per la correlació lateral del front (Alava et al., 2004).

El procés pel qual el front incialment pla es va deformant fins que assoleix una amplada estadística màxima és estudiat en termes de la teoria d'arrugament dinàmic (Krug, 1997). Aquesta teoria relaciona les fluctuacions locals (microscòpiques) que afecten la propagació de la interfície amb el seu comportament macroscòpic i les seves propietats universals d'escalament. Específicament, en aquest treball caracteritzem les propietats d'escalament de les fluctuacions de les interfícies en termes de la hipòtesi d'escalament genèric proposada per Ramasco et al. (2000).

El problema d'imbibició en un medi desordenat mostra moltes similituds amb altres fenòmens crítics fora de l'equilibri en sistemes estesos en l'espai. El motiu és que la longitud lateral de correlació del front divergeix quan la velocitat mitjana de la interfície tendeix a zero. En aquest límit el front d'imbibició avança per allaus discretes de qualsevol mida i durada possibles, limitats només per la mida del sistema. La propagació de la interfície mostra una dinàmica espacio-temporal complexa que podem analitzar a l'escala local o a l'escala global, obtinguda de la mitjana de les mesures locals. La dinàmica a batzegades observada a l'escala global és coneguda com a soroll cruixent (*crackling noise*), un tipus de resposta que s'ha observat en una multitud de sistemes, des del soroll Barkhausen en materials magnètics (Sethna et al., 2001) al transport actiu de càrrega en cèl·lules vives (Wang et al., 2013).

Resultats experimentals previs en imbibició forçada (Planet et al., 2009, 2010, 2011; Santucci et al., 2011) mostren que les propietats que descriuen les allaus tant locals com globals estan distribuïdes estadísticament en forma de llei de potències amb un truncament exponencial. També que les fluctuacions de la velocitat global del front segueixen una distribució de Gumbel generalitzada, com s'observa en altres sistemes correlacionats espacialment.

9.2 Sistema experimental

En aquesta tesi s'estudia la propagació d'un front de fluid a través d'un medi desordenat. El sistema experimental utilitzat va ser dissenyat per primera vegada per Soriano (2003) per estudiar la morfologia dels fronts en el procés d'arrugament dinàmic que es produeix quan la interfície avança pel medi desordenat. Més tard, Planet (2009) estudià la dinàmica de les interfícies gràcies a l'ús d'una càmera de captura ràpida. Planet també

introduí l'opció d'inclinar la cel·la, que permeté estudis d'arrugament dinàmic en ascens capil·lar.

El muntatge experimental modela una fractura oberta. El model consisteix en una cel·la de Hele-Shaw (HS) formada per dues grans plaques rectangulars de vidre (205 $\times$ 555 mm^2) separades un espaiat b molt més petit que la seva amplada i llargada. Nosaltres hem utilitzat dos tipus de model de fractura oberta: un en què la separació entre plaques és constant en l'espai, $b = 0.46$ mm (cel·la llisa, o S), i un altre en que l'espaiat fluctua aleatòriament entre dos valors, $b = 0.40$ i 0.46 mm (cel·la desordenada, o D). Les variacions controlades de l'obertura de la cel·la s'aconsegueixen amb una placa de fibra de vidre col·locada sobre la placa inferior de vidre. La placa de fibra de vidre és llisa en el cas S. En el cas desordenat D es col·loquen uns obstacles de coure a la placa de fibra de vidre distribuïts aleatòriament en l'espai i que redueixen l'espaiat de la cel·la en aquells punts. La cel·la és sellada de manera que el fluid només pot avançar en la direcció més llarga, entre l'entrada d'oli i la sortida d'aire.

Com a fluid invasor utilitzem olis de silicona de viscositats dinàmiques d'entre $\mu = 10$ i 350 cP, que s'han variat sistemàticament per primera vegada en aquest sistema experimental. La densitat, viscositat cinemàtica i la tensió superficial nominals es mostren a la Taula 2.2. El fluid s'injecta a la cel·la controladament en règim d'imbibició espontània o d'imbibició forçada. Pel primer cas el model de medi desordenat es connecta a un dipòsit de fluid que, mitjançant un sistema de recirculació, manté el nivell d'oli constant i per tant una diferència de pressió entre l'entrada i la sortida de la cel·la, ΔP, constant. En el segon cas s'utilitza una bomba de xeringa que injecta una quantitat constant de fluid per unitat de temps, que comporta una velocitat mitjana d'avançament del front v = ctt.

L'avançament de la interfície entre oli i aire és enregistrat mitjançant càmeres des de la part superior de la cel·la. Gràcies a un sistema d'il·luminació indirecta utilitzant LEDs, s'aconsegueix un bon contrast entre les regions envaïdes per oli i l'aire. El sistema en conjunt (cel·la i sistema d'enregistrament) es pot inclinar per tal d'introduir una gravetat efectiva en contra o a favor de la propagació del fluid a través del medi. Al llarg d'aquesta tesi s'ha millorat i automatitzat el control de la inclinació del sistema.

Nosaltres estem interessats en l'evolució de la interfície de fluid a través del medi, per això necessitem extreure els fronts de les imatges enregistrades. Per fer-ho utilitzem un mètode de detecció de vores que s'aplica sobre les imatges dels experiments prèviament binaritzades. El procés de binarització consisteix, primer, en restar una imatge de fons (capturada abans de començar l'experiment) a cada una de les imatges enregistrades. D'aquesta manera s'eliminen reflexos indesitjats o el patró de desordre de la placa inferior de la cel·la. Així també es millora el contrast entre les fases de fluid invasor i aire de manera que l'histograma de nivells de grisos mostra dos pics, un per cada fase. El mínim

entre els dos màxims és utilitzat com a nivell de gris llindar per aconseguir la imatge en blanc i negre.

Pels estudis d'ascens capil·lar i d'arrugament dinàmic s'analitzen directament els fronts obtinguts. Per l'estudi de la dinàmica s'utilitza el mètode de la matriu de temps d'espera (*waiting time matrix*) desenvolupat per Måløy et al. (2006). Aquest mètode consisteix en generar una matriu de la mida de les imatges capturades on cada element indica la quantitat de temps que el front ha passat en aquella coordenada. Invertint els elements d'aquesta matriu s'obté el mapa de velocitats locals del front. Combinant aquesta informació amb la posició del front en cada instant de temps s'aconsegueixen els valors de la velocitat local del front a cada instant en la direcció de propagació. Fent la mitjana al llarg del front per finestres d'una mida fixada ℓ s'obté el senyal de velocitat global, $V_\ell(t)$.

9.3 Resultats principals

Els resultats principals d'aquest treball es poden dividir en cinc grups, que corresponen als capítols de resultats del cos de la tesi, del 3 al 7.

Ascens capil·lar

Hem estudiat l'evolució de la posició mitjana del front en imbibició espontània tant analíticament com experimental. Hem utilitzat els dos tipus de cel·la presentats: amb obertura constant entre plaques de la cel·la (S) i amb espaiament que fluctua dicotòmicament entre plaques de manera aleatòria en l'espai (D). El desplaçament del front s'ha analitzat en dues condicions experimentals qualitativament diferents: amb presència de gravetat efectiva oposant-se a l'avançament del fluid i sense gravetat efectiva.

Hem observat que el nostre model de fractura oberta es comporta macroscòpicament com un medi porós real, en el sentit que la posició mitjana dels fronts en imbibició espontània segueix les solucions de Lucas-Washburn (LW) i la Solució Estesa (ES) – obtingudes a partir d'una equació d'equilibri de pressions. En concret, en absència de gravetat el desplaçament del front augmenta proporcionalment a l'arrel quadrada del temps, mentre que en presència de gravetat el front s'atura a l'alçada d'equilibri.

Tot i així, s'observen desviacions sistemàtiques entre les dades experimentals i les solucions clàssiques LW i ES. Específicament veiem que les prediccions teòriques sobreestimen les corbes experimentals de la posició mitjana a tots els temps. Considerant un terme de resistència addicional a l'equació d'equilibri de pressions, proporcional a la velocitat mitjana del front, hem obtingut una nova solució analítica per la posició mitjana de la interfície. La dissipació a la zona de preparació de la cel·la és la responsable

d'aquest nou terme. La solució obtinguda reprodueix els resulats experimentals a tots els temps, en presència i en absència de gravetat, i especialment bé per la configuració d'espaiat constant.

Arrugament dinàmic

Hem estudiat el creixement de les fluctuacions espacio-temporals d'una interfície oliaire en desplaçaments d'imbibició forçada amb fluid de viscositat baixa. Es produeix un procés d'arrugament dinàmic mentre el front evoluciona des d'una interfície inicialment plana a un front arrugat invariant estadísticament, a mesura que avança pel medi. Primer hem estudiat l'efecte de les correccions de línia base en els resultats i hem mostrat que una correcció linear de les dades crues està justificat en el nostre sistema experimental, mentre que descartem les correccions de forma parabòlica.

Amb les interfícies corregides hem analitzat l'escalament d'aquestes fluctuacions del front i hem vist que és anòmal, i.e. les escales globals segueixen una dinàmica diferent a les locals. En concret hem caracteritzat la dinàmica en el marc de l'ansatz d'escalament genèric i hem vist que correspon a l'escenari súper rugós. També hem comprovat que satisfà les relacions d'escala proposades teòricament. Hem comprovat que en les condicions experimentals explorades la dinàmica es troba en el règim de desordre dominat per la capil·laritat. Finalment, els resultats presentats són compatibles amb resultats anteriors d'experiments en imbibició forçada per fluids amb viscositats més altes (Planet et al., 2014).

Dinàmica espacio-temporal local

Hem estudiat la dinàmica espacio-temporal de les interfícies a l'escala local, i.e. a l'escala de la resolució espacial del sistema (molt més petita que la longitud de correlació lateral del front o de la mida característica del desordre), en imbibició forçada. Sha explorat una gran quantitat de condicions experimentals, incloent-hi l'ús d'olis de silicona de diverses viscositats per primera vegada en aquest sistema. μ i v, doncs, són els paràmetres de control d'aquests experiments (i defineixen el nombre de capil·laritat Ca $\sim \mu$v). Els fronts d'imbibició mostren una dinàmica a batzegades, avançant en forma d'allaus localitzades en l'espai.

Les velocitats locals del front estan àmpliament distribuïdes al voltant del seu valor mitjà. Hem vist que les fluctuacions d'aquestes velocitats estan controlades pel nombre de capil·laritat Ca –el rang de velocitats creix en disminuir Ca– i hem comprovat que els dos paràmetres de control, μ i v, juguen el mateix rol en controlar aquestes fluctuacions.

Per primera vegada hem estudiat les correlacions temporals i espacials de les velocitats locals. Hem pogut comprovar experimentalment que μ i v juguen el mateix paper en

controlar la longitud lateral de correlació, com s'espera de les prediccions teòriques. Pel contrari, el temps de màxima anticorrelació evoluciona diferent amb els dos paràmetres de control. Hem vist que la correlació espacial en la direcció de propagació del front presenta dues escales de longitud característiques. La longitud de màxima anticorrelació és constant en tots els experiments i coincideix amb longitud en que les illes de desordre esdevenen descorrelacionades. Per altra banda, la longitud de descorrelació de les velocitats locals en la direcció de propagació evoluciona amb Ca.

Hem estudiat el sistema en termes d'allaus locals, definides com dominis connexos al mapa de velocitats locals amb velocitats més grans que una certa velocitat llindar, i n'hem estudiat les seves propietats estadístiques. En concret hem confirmat per olis de diverses viscositats que les mides, durades i extensions laterals de les allaus locals estan distribuïdes àmpliament, seguint una llei de potències amb un truncament exponencial. Mentre que els exponents de les lleis de potències no depenen de μ i v, les escales de truncament divergeixen quan Ca tendeix a zero.

Els exponents de les lleis de potències obtinguts mostren un acord excel·lent amb resultats experimentals obtinguts prèviament per Santucci et al. (2011), però difereixen significativament dels resultats obtinguts en simulacions de *phase-field* fetes per Pradas et al. (2009).

Gràcies als grans conjunts de dades obtinguts, hem pogut analitzar curosament el comportament de les escales de truncament de les distribucions de mides, durades i extensions laterals de les allaus locals. Hem verificat les relacions esperades entre aquestes escales i la longitud de correlació tot modificant μ i v.

Finalment, hem mostrat que la propagació de les allaus locals no està trivialment correlacionada amb el desordre del medi. En concret, hem obtingut que el 35 % de l'àrea escombrada per una allau local correspon a illes de desordre. Aquesta quantitat coincideix amb el valor de la fracció d'ocupació nominal de desordre a les nostres plaques.

Dinàmica espacio-temporal global

També hem analitzat la mitjana espacial de les velocitats locals en funció de la mida de la finestra pel mateix conjunt de dades experimentals. Aquest senyal l'anomenem velocitat global. Com a conseqüència de la dinàmica intermitent del front de fluid a l'escala local, la velocitat global també mostra una dinàmica per allaus amb fluctuacions no gaussianes.

Hem vist que les distribucions de Gumbel generalitzades s'ajusten bé a les distribucions estadístiques de les velocitats globals. Hem verificat que el nombre efectiu de dominis estadísticament independents de la interfície, ℓ/ℓ_c, controla la asimetria de les distribucions, també quan es modifica la viscositat del fluid.

S'han caracteritzat les correlacions temporals del senyal global. Hem mostrat que el temps de màxima anticorrelació està controlat per la durada de les allaus locals més llargues.

Hem definit allaus en aquest senyal global com excursions de la velocitat mitjana per sobre d'un cert llindar de velocitat. Hem confirmat que les mides i durades d'aquestes allaus estan àmpliament distribuïdes. Per primera vegada hem caracteritzat la influència de la mida de la finestra d'observació ℓ sobre les propietats de les allaus, tot relacionant-ho amb la longitud lateral de correlació del front ℓ_c.

En el cas de finestres d'observació $\ell > \ell_c$, les mides i durades de les allaus estan distribuïdes en llei de potències amb truncament exponencial. Els exponents són independents de les condicions experimentals i mostren un bon acord amb els resultats obtinguts en estudis experimentals previs (Planet et al., 2009, 2011), i també remarcablement amb els valors obtinguts en simulacions de *phase-field* (Pradas et al., 2009). La distribució conjunta de mides i durades mostra la relació d'escalament en llei de potències esperada. Novament, els valors de truncament de les distribucions sí que evolucionen amb μ i v. En concret, la mida màxima de les allaus depèn de μ, v i ℓ, mentre que les màximes durades només depenen de v.

Pel que fa a finestres d'observació $\ell < \ell_c$, les distribucions mostren un bony abans del decaïment, degut a que les dades estan truncades per la mida de la finestra (*data windowing*).

Finalment, hem estudiat la forma mitjana de les allaus globals per primera vegada en fronts d'imbibició. La forma mitjana del senyal d'una allau mostra una evolució sistemàtica amb ℓ/ℓ_c: des d'una forma asimètrica inclinada cap a temps curts, a una forma pràcticament simètrica temporalment. Hem mostrat que les formes mitjanes de les allaus experimentals estan ben descrites per la forma general proposada recentment per Laurson et al. (2013). La funció proposada depèn de dos paràmetres: un que té en compte el comportament de la distribució conjunta de mides i durades i un altre que considera la asimetria de les allaus. Hem trobat que els dos paràmetres evolucionen sistemàticament amb ℓ/ℓ_c.

Evidència experimental d'intermitència en imbibició lenta

Finalment hem fet un pas més en l'anàlisi de les velocitats globals del front. En concret, hem estudiat quantitativament el caràcter intermitent dels desplaçaments de fronts d'imbibició mitjançant una anàlisi a múltiples escales temporals i espacials. Els resultats obtinguts representen la primera evidència experimental d'intermitència en la invasió d'un medi heterogeni per part d'un fluid i la seva caracterització detallada.

Ens hem centrat en l'estudi de les distribucions estadístiques dels increments de velocitat global, en funció de la mida ℓ de la finestra d'observació utilitzada per calcular la velocitat i de l'increment de temps τ. Hem observat que aquestes distribucions evolucionen contínuament a través de les escales temporals, des de distribucions de cues llargues a gaussianes, tret distintiu d'intermitència en el sistema.

L'anàlisi quantitativa ha consistit en estudiar els moments de les distribucions d'increments de velocitats i, especialment, la seva curtosi i asimetria. Hem vist que la curtosi evoluciona amb l'increment de temps fins que satura per sobre d'un temps característic τ_c. Hem trobat que aquest τ_c només depèn de v. A més a més de mostrar cues llargues, totes les distribucions també són asimètriques per increments de temps curts.

L'anàlisi estadística ens ha permès col·lapsar totes les dades per un rang ampli de condicions experimentals (μ, v) analitzades a diverses escales ℓ. El col·lapse mostra que la intermitència està controlada només per dos paràmetres: ℓ/ℓ_c i τ/τ_c. El primer quocient, que depèn de μ, v, i ℓ, està associat amb la conservació local de massa de fluid. El segon quocient, que només depèn de v, pot relacionar-se amb la longitud característica de les illes de desordre. La intensitat de la intermitència del senyal està controlada per ℓ/ℓ_c, mentre que τ/τ_c determina l'abast temporal de l'intermitència observada.

Conclusions generals

El conjunt de resultats presentats en aquesta tesi dóna suport a una descripció molt general de la dinàmica de propagació lenta de fronts fluids d'imbibició fora de l'equilibri en fractura oberta. La conservació local de massa controla la propagació lateral de les fluctuacions de la interfície, a través de la longitud de correlació lateral $\ell_c \sim 1/\sqrt{\mathrm{Ca}}$. La longitud característica del desordre i la velocitat mitjana del front, per la seva banda, controlen l'avançament del front en la direcció de propagació.

Chapter 10

Bref résumé en français

Quand un fluide mouillant visqueux (comme une huile) pénètre un milieu hétérogène tel qu'une fracture ouverte ou un matériau poreux, l'interface entre l'air déplacé et l'huile développe des corrélations à longue portée menant à une dynamique spatio-temporelle complexe. Dans cette Thèse, nous avons étudié expérimentalement et théoriquement ce processus de transport d'un fluide, appelé imbibition, pertinent dans diverses situations, comme en biologie avec l'écoulement de fluides physiologiques, ou en géophysique, avec l'irrigation des sols et la récupération du pétrole. Notre étude a combiné un travail expérimental exhaustif avec une analyse précise des données (expérimentales) basées sur des méthodes de physique statistique et physique non linéaire. L'imbibition est un processus de transport d'un fluide dans un milieu dans lequel un fluide mouillant déplace un autre fluide non miscible résident dans ce milieu. Ce processus d'invasion peut être classé suivant deux protocoles différents d'injections du fluide qui correspondent à différentes conditions aux limites du milieu imbibé: en imbibition spontanée, le fluide est entraîné par une différence de pression constante entre l'entrée et la sortie du milieu, et le débit d'écoulement est libre de fluctuer dans le temps. En imbibition forcée, un débit constant est imposé à l'entrée du milieu, et la différence de pression peut évoluer dans le temps.

Nous modélisons expérimentalement une fracture ouverte par deux plaques de verres parallèles séparées par une certaine distance, système communément appelé cellule de Hele-Shaw (HS). Deux configurations ont été considérées: une cellule avec un espacement constant (cellule lisse) et une autre avec un écart dichotomique réparti aléatoirement spatialement le long du plan de la cellule, imitant ainsi une fracture avec une ouverture variable bi-dimensionnellement (cellule désordonnée). Cet modèle a été initialement développé par Soriano (2003) et utilisé aussi par Planet (2009). Nous avons utilisé des huiles de silicone de différentes viscosités, et étudié l'imbibition spontanée et forcée de nos modèles de fracture ouverte. L'avancement de l'interface huile/air est enregistré au moyen de différentes caméras à haute résolution spatiale et temporelle (jusqu'à

0.1mm/px, 200 images par seconde). Nous avons développé nos propres outils d'analyse d'image afin d'extraire la position du front.

10.1 Principaux résultats

Evolution de la position moyenne du front en imbibition spontanée

Dans un premier temps, nous avons étudié expérimentalement mais aussi théoriquement l'évolution de la position moyenne du front au cours du temps lors du processus d'imbibition spontanée. Les expériences ont été réalisées en présence ou non de l'effet de la gravité, en inclinant la cellule contre l'avancement du front, ou en la maintenant à l'horizontale respectivement. Nous avons systématiquement exploré différents régimes d'invasion en modifiant la différence de pression entre l'entrée et la sortie de la cellule. Nos résultats expérimentaux concernant l'évolution de la position moyenne du front d'imbibition montrent des écarts systématiques par rapport aux résultats de la littérature, obtenus à partir de l'équation d'équilibre de pression (solution de Lucas (1918) et Washburn (1921) (LW), sans l'effet de la gravité, et la solution étendue (ES) de Fries and Dreyer (2008*a*), en présence de la gravité). La solution (LW) surestime la position moyenne du front à tout moment, tandis que la solution (ES) surestime la position moyenne de l'interface aux temps courts et intermédiaires. Ces écarts sont attribués à la dissipation d'énergie dans la petite zone de préparation à l'entrée de la cellule qui précède la région où nous effectuons nos mesures. En considérant ce terme résistif, proportionnel à la vitesse moyenne du front, nous avons obtenu une nouvelle équation décrivant l'évolution moyenne de l'interface. De plus, une solution analytique peut être obtenue pour les deux cas étudiés, en présence ou en l'absence de l'effet de la gravité. Cette nouvelle solution reproduit les résultats expérimentaux en tout temps, en particulier pour la cellule (HS) lisse (espacement constant).

Evolution de la rugosité du front en imbibition forcée

Lors de l'imbibition de la cellule désordonnée, les hétérogénéités du milieu (variations locales de l'espacement) entrainent des fluctuations locales de pression capillaire et de perméabilité κ qui déforment l'interface, tandis que la pression visqueuse et la tension de surface ont au contraire tendance à aplanir le front. En conséquence, l'interface huile/air développe des corrélations à longue portée, avec une longueur de corrélation latérale donnée par l'échelle de longueur $\ell_c = \sqrt{\kappa/\mathrm{Ca}}$ (où Ca est le nombre capillaire), à laquelle la viscosité devient plus efficace que la tension de surface pour amortir les fluctuations interfaciales (Alava et al., 2004). Nous observons ainsi que les fronts envahissant la cellule désordonnée deviennent rugueux.

Nous avons caractérisé l'évolution des fluctuations de la rugosité de l'interface huile/air pour des expériences d'imbibition forcée en utilisant des fluides de faible viscosité. Nous avons étudié les propriétés d'invariance d'échelle de l'interface et en particulier leur évolution au cours du processus d'imbibition, conséquence de la compétition des forces agissant sur l'interface à différentes échelles de longueur. La loi d'échelle caractérisant le développement de la rugosité suit un scénario «anormal» (plus précisément «super rugueux»): les échelles locales et globales suivent des dynamiques différentes (Ramasco et al., 2000). Nous montrons que pour la gamme de paramètres étudiée le processus d'imbibition forcée est dans un régime dominé par les effets capillaires. De plus, nos résultats sont compatibles avec des expériences antérieures réalisées à des nombres capillaires Ca plus élevés (Planet et al., 2014).

Dynamique spatio-temporelle locale du front

Ensuite, nous avons étudié la dynamique spatio-temporelle du front dans un régime où la rugosité de l'interface sature et a atteint statistiquement un régime stationnaire. Grâce à la haute résolution spatiale et temporelle de notre système d'acquisition, nous pouvons mesurer la vitesse du front à une échelle locale, i.e plus petite que la longueur de corrélation ℓ_c et la longueur caractéristique du désordre ℓ_d. Nous avons étudié une large gamme de conditions expérimentales différentes: différentes vitesses imposées v et différentes viscosités μ.

Le front d'imbibition présente une dynamique par avalanches, spatialement localisées. Nous avons étudié les fluctuations à la fois spatiales et temporelles du signal de vitesse locale. Les vitesses locales $v(x, y)$ sont largement distribués autour de leur valeur moyenne. Ces distributions de vitesse sont contrôlées par le nombre capillaire Ca: la gamme de vitesse locale mesurée s'élargit, lorsque Ca diminue. De plus, nous avons caractérisé les corrélations spatiales et temporelles de ces vitesses locales. Nous avons pu montrer notamment que la viscosité et la vitesse moyenne imposée du front v, jouent le même rôle dans le contrôle de la longueur de corrélation spatiale le long de l'interface, comme prévu théoriquement $\ell_c \sim 1/\sqrt{\mu \mathrm{v}}$ (Alava et al., 2004). Au contraire, les corrélations temporelles évoluent différemment avec μ et v. Cependant, nous avons pu toutefois mettre en évidence que dans la direction de propagation les vitesses locales sont corrélées jusqu'à une échelle de longueur $\Delta y \sim Ca^{-0.4}$, avec un maximum d'anti-corrélation correspondant à la taille caractéristique des hétérogénéités du milieu ℓ_d.

A partir de la carte des vitesse locales $v(x, y)$, nous définissons des avalanches locales comme des domaines de haute vitesse. Pour nos différentes expériences (réalisées dans diverses conditions, différentes viscosités et vitesses), nous confirmons que les tailles (aires) A, les durées D, et les extensions latérales L_x et L_y de ces avalanches locales sont largement distribuées, selon des lois de puissance avec des coupures exponentielles

qui divergent lorsque le nombre capillaire décroit Ca $\to 0$. Les exposants caractérisant les lois de puissance de ces distributions sont robustes et indépendants de μ et v. En outre, nos résultats et plus spécifiquement la valeur de ces exposants sont en bon accord avec des résultats expérimentaux antérieurs (Santucci et al., 2011), mais elles diffèrent des valeurs obtenues lors de simulations en «champ de phase» (Pradas et al., 2009). De plus, nous montrons également que ces avalanches locales ne sont pas trivialement corrélées avec le désordre sous-jacent du milieu.

Dynamique spatio-temporelle globale du front

Pour la même série d'expériences d'imbibition forcée, nous avons également analysé la vitesse «globale» –moyennée spatialement le long du front à différentes échelles ℓ. Le signal temporel $V_\ell(t)$ présente également d'importantes fluctuations, caractéristiques d'une dynamique par avalanches. L'amplitude de ces fluctuations non gaussiennes de $V_\ell(t)$ sont bien décrites par une distribution de Gumbel généralisée. Nous avons vérifié que le nombre effectif de degrés de liberté de l'interface ℓ/ℓ_c contrôle l'asymétrie de ces distributions. Les vitesses globales $V_\ell(t)$ présentent une anti-corrélation maximale pour un temps caractéristique donnée par la durée maximale des avalanches locales.

Nous avons également analysé les propriétés statistiques de ces avalanches globales, dont les tailles S et durées T sont également largement distribuées. Lorsque le signal de vitesse global est mesuré (moyenné) à une échelle de longueur ℓ plus grande que la longueur de corrélation ℓ_c, les distributions suivent des lois de puissance avec des coupures exponentielles. Leurs exposants robustes sont indépendants des conditions expérimentales. Les valeurs mesurées sont en bon accord avec des résultats expérimentaux antérieurs (Planet et al., 2009, 2011) et remarquablement aussi avec celles obtenues à partir de simulations numériques en «champ de phase» (Pradas et al., 2009). De plus, nous avons pu montrer que les coupures exponentielles des distributions de tailles $P(S)$ et durées $P(T)$ ne sont pas contrôlées par les mêmes mécanismes physiques: la taille maximale de ces avalanches est fixée par le ratio ℓ/ℓ_c, alors que leur durée maximale est donnée par $\tau_c = \ell_d/\mathrm{v}$. Lorsque le signal de vitesse global est mesuré à des échelles $\ell < \ell_c$, les distributions de tailles $P(S)$ et durées $P(T)$ d'avalanches globales présentent une bosse avant la décroissance exponentielle, conséquence du «fenêtrage» des données.

Nous avons également analysé la forme moyenne de ces avalanches globales. Cette forme moyenne présente une évolution systématique avec le ratio ℓ/ℓ_c, avec une asymétrie (correspondant à une forte accélération aux temps courts) lorsque la vitesse globale est mesurée à des petites échelles proches de ℓ_c. De plus, nous montrons que la forme moyenne de ces avalanches est bien décrite par l'ansatz récemment proposé par Laurson et al. (2013).

Caractère intermittent de la dynamique d'imbibition du front

Nous avons finalement quantifié le caractère intermittent de la dynamique d'imbibition forcée dans un milieu hétérogène, en analysant de manière détaillée les distributions d'incréments de vitesse $\Delta V_\ell(\tau) = V_\ell(t+\tau) - V_\ell(t)$ à différentes échelles temporelles τ. Nous avons en particulier caractérisé l'évolution de l'aplatissement (kurtosis) et de l'asymétrie de ces distributions à travers les échelles de temps τ. Nous avons pu démontrer que l'intermittence de la dynamique d'imbibition est contrôlée par deux paramètres uniquement: les ratios ℓ/ℓ_c et τ/τ_c. Le premier, qui représente le nombre effectif de degrés de libertés de l'interface, et dépend de μ, v, et ℓ, est associé à la conservation de la masse du fluide. Le second paramètre τ/τ_c est relié à l'échelle caractéristique du désordre, avec $\tau_c = \ell_d/\mathrm{v}$. L'intensité de l'intermittence est contrôlée par ℓ/ℓ_c, tandis que τ_c définit la plage temporelle sur laquelle l'intermittence est observée.

10.2 Conclusions générales

L'ensemble des résultats présentés dans cette Thèse soutient une image très générale de la dynamique hors équilibre de fronts d'imbibition se propageant lentement dans des fractures ouvertes. La propagation latérale des fluctuations interfaciales est contrôlée par conservation de la masse locale, via la longueur de corrélation latérale ℓ_c. L'avancement de l'interface dans la direction de propagation est contrôlé par l'échelle caractéristique du désordre ℓ_d et par la vitesse moyenne du front. Ce sont les deux ingrédients de base qui contrôlent la dynamique intermittente par avalanches du front d'imbibition.

Part III

Appendices

Appendix A

Kinetic roughening of growing interfaces

We have shown throughout this Thesis that fluid fronts invading our model open fracture become rough as they advance through the medium because of the distortion of the front by the disorder patches.

Rough surfaces or interfaces are usually generated by out-of-equilibrium competing processes acting on different length and time scales. These out-of-equilibrium processes may lead to scale-invariant rough interfaces, which can be studied in the context of kinetic roughening (Krug, 1997). In this appendix we present some examples of rough interfaces. The different scaling scenarios predicted by the generic dynamic scaling ansatz for kinetic roughening processes –proposed by Ramasco et al. (2000)– are described. Examples of systems for each scaling scenario are given. A review of previous results on kinetic roughening in imbibition is also included.

A.1 Roughness and scale invariance

Scale-invariant interfaces are formed by portions that are *similar* to the whole. Two examples are shown in Fig. A.1.

Let us consider a unidimensional ($d = 1$) interface contained in a space of $d + 1$ dimensions. It is scale-invariant if applying a scale transformation in the horizontal direction $x \to bx$ implies a transformation in the vertical direction $h \to b^{\alpha}h$. α is known as the Hurst exponent, and measures the degree of anisotropy of the surface. In processes of growing interfaces in d dimensions all directions are equivalent except the growth direction. In such cases α is called the roughness exponent. Depending on the value of α we define the interfaces as self-similar or self-affine (Barabási and Stanley, 1995).

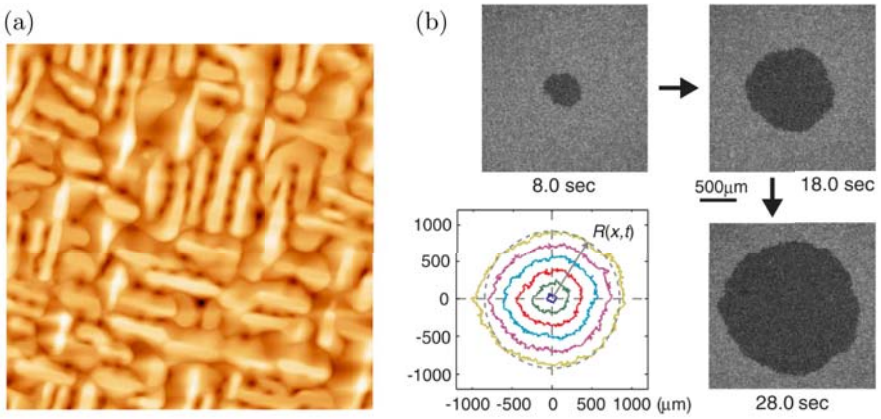

FIGURE A.1: Examples of rough interfaces. (a) Atomic force microscopy image of the surface of 600 nm Nb films. Figure from Beringer et al. (2013). Box of 2 μm $\times 2$ μm. (b) Growing interface between two turbulent states of convection of a nematic liquid crystal for three given times. Bottom-left plot: snapshots of the evolution of the interfaces taken every 5 s. Figure from Takeuchi and Sano (2010).

Self-similar or fractal structures scale their dimensions isotropically, that is, a dilation increases the size of the system uniformly in every spatial direction. In this case the roughness exponent is $\alpha = 1$.

Self-affine structures are invariant under an anisotropic transformation, i.e. a change of scale in one direction by a different factor than in the other directions. Here the Hurst exponent is $\alpha \neq 1$.

As described in Sec. 1.4, to characterize a unidimensional ($d = 1$) interface of size L that grows in time we need a single-valued function $h(x,t)$ of the interface height for each lateral position $x \in [0, L]$ and time t. For completeness, let us recall Eqs. (1.26) to (1.28) that define the mean position of the interface averaged at scale ℓ:

$$\langle h(x,t)\rangle_\ell = \frac{1}{\ell}\int_\ell h(x,t)dx, \tag{A.1}$$

and its interfacial statistical width about the mean value:

$$w(\ell,t) = \overline{\langle [h(x,t) - \langle h(x,t)\rangle_\ell]^2\rangle_\ell^{1/2}}. \tag{A.2}$$

ℓ stands for the lateral size of the window of observation, $\langle \dots \rangle_\ell$ indicates the average over the window, and the overline is an average over all the realizations of the disorder explored. In the reciprocal space, the power spectrum is defined as:

$$S(q,t) = \overline{\hat{h}_\ell(q,t)\hat{h}_\ell(-q,t)}, \tag{A.3}$$

where

$$\hat{h}_\ell(q,t) = \frac{1}{\ell^{1/2}} \int_\ell dx \, [h(x,t) - \langle h(x,t) \rangle_\ell] \, e^{iqx} \tag{A.4}$$

is the Fourier transform of $h(x,t)$ when observing the system at a scale ℓ, where the average height has been subtracted.

A.2 Kinetic roughening

The basics of kinetic roughening has been presented in Sec. 1.4.1. Here we describe the scaling functions proposed by Ramasco et al. (2000) in their generic dynamic scaling ansatz for kinetic roughening processes.

A.2.1 Scaling scenarios

As quoted in Sec. 1.4.1, from the values of the *global*, *spectral*, and *local roughness exponents*, α, α_s, and α_{loc}, one can distinguish four scaling scenarios:

If $\alpha_s < 1 \Rightarrow \alpha_{loc} = \alpha_s$	$\alpha_s = \alpha \Rightarrow$ Family-Vicsek	Ordinary scaling
	$\alpha_s \neq \alpha \Rightarrow$ Intrinsic	Anomalous scaling
If $\alpha_s > 1 \Rightarrow \alpha_{loc} = 1$	$\alpha_s = \alpha \Rightarrow$ Super-rough	
	$\alpha_s \neq \alpha \Rightarrow$ Faceted	

At the global scale, for $\ell = L$ (the system size), the interfacial width scales as

$$W(L,t) \sim \begin{cases} t^\beta & \text{for } t \ll t_s, \\ L^\alpha & \text{for } t \gg t_s, \end{cases} \tag{A.5}$$

in all scaling scenarios, where β is the *growth exponent* and t_s is the saturation time. Since the correlation length $\xi_c \sim t^{1/z}$, the stationary regime is achieved for $t \gg t_s \sim L^z$, when the correlation length has spread along the whole interface. The three global exponents verify the scaling relation $\alpha = z\beta$.

We recall also the behaviour of the power spectrum of the interfaces:

$$S(q,t) = q^{-(2\alpha+1)} s(qt^{1/z}), \tag{A.6}$$

where the scaling function $s(u)$ is defined as

$$s(u) \sim \begin{cases} u^{(2\alpha+1)} & \text{for } u \ll 1, \\ u^{2(\alpha-\alpha_s)} & \text{for } u \gg 1. \end{cases} \tag{A.7}$$

The exponent α is again the *roughness exponent* and α_s is the *spectral roughness exponent*. Their difference is usually referred to as the *anomalous exponent* $\theta = \alpha - \alpha_s$. Equations (A.6) and (A.7) also apply to all scaling scenarios.

On the other hand, for the local roughness scaling we observe differences depending on the scaling scenario. Schematic plots of $w(\ell, t)$ and $S(q, t)$ for the four scenarios are shown in Fig. A.2.

Family-Vicsek. In the ordinary or Family-Vicsek (FV) scaling, fluctuations at the global and local scale behave in the same way. Thus,

$$w(\ell, t) \sim \begin{cases} t^{\beta} & \text{for } t \ll \ell^z, \\ \ell^{\alpha} & \text{for } t \gg \ell^z, \end{cases} \tag{A.8}$$

the power spectrum scales as

$$S(q, t) \sim \begin{cases} t^{(2\alpha+1)/z} & \text{for } q \ll t^{-1/z}, \\ q^{-(2\alpha+1)} & \text{for } q \gg t^{-1/z}, \end{cases} \tag{A.9}$$

and the scaling relation $\alpha = z\beta$ holds. Then, only two exponents are independent.

The surface between two turbulent states of convection of a nematic liquid crystal (Takeuchi and Sano, 2010; Takeuchi et al., 2011), the burning fronts in slow combustion of paper (Myllys et al., 1997) or the results from the paradigmatic equations for growing interfaces EW (Edwards and Wilkinson, 1982) and KPZ (Kardar et al., 1986) show Family-Vicsek dynamic scaling (Barabási and Stanley, 1995).

Intrinsic anomalous. In this scenario the fluctuations of the front scale differently depending on the window of observation. Here $\alpha \neq \alpha_s = \alpha_{loc}$, and

$$w(\ell, t) \sim \begin{cases} t^{\beta} & \text{for } t \ll \ell_\ell, \\ \ell^{\alpha_{loc}} t^{(\alpha-\alpha_{loc})/z} & \text{for } t_\ell < t < t_s, \\ \ell^{\alpha_{loc}} L^{(\alpha-\alpha_{loc})} & \text{for } t_s \ll t, \end{cases} \tag{A.10}$$

where $t_\ell \sim \ell^z$ is the *local* saturation time and $t_s \sim L^z$ the *global* one.

In this situation an *anomalous growth exponent* $\beta^* = (\alpha - \alpha_{loc})/z (= \theta/z)$ is defined. It is only observable when small windows are analysed, as this growth regime appears in the range of times between t_ℓ and t_s.

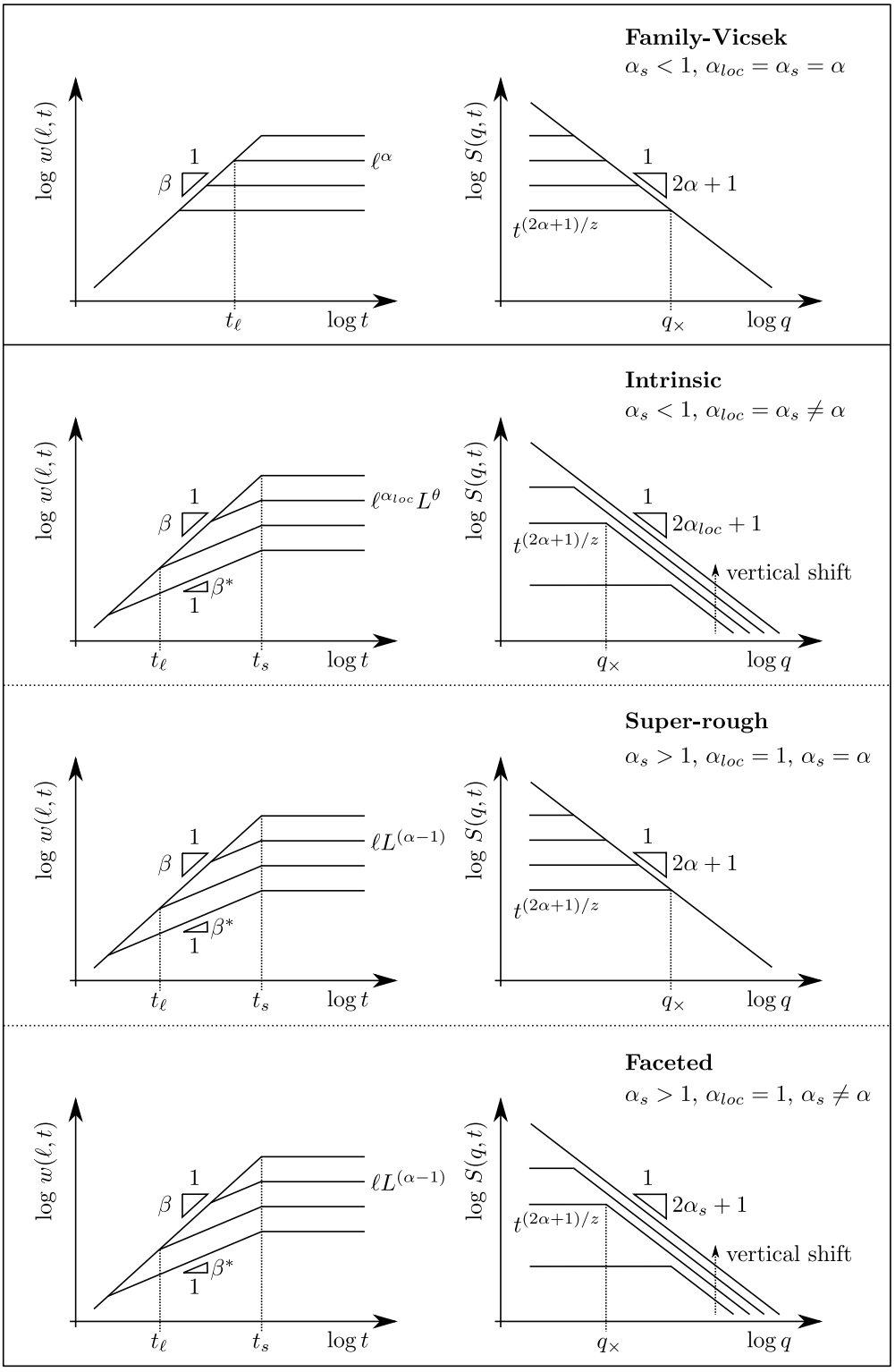

FIGURE A.2: Schematic plots of $w(\ell,t)$ and $S(q,t)$ in the four possible scaling scenarios derived from the generic scaling ansatz of Ramasco et al. (2000). Ordinary scaling is represented in the top panel and the three anomalous scenarios in the other three panels. $t_s \sim L^z$ and $t_\ell \sim \ell^z$ are the global and local saturation times. The characteristic scale $q_\times \sim t^{-1/z}$.

As for the power spectrum,

$$S(q,t) \sim \begin{cases} t^{(2\alpha+1)/z} & \text{for } q \ll t^{-1/z}, \\ q^{-(2\alpha_{loc}+1)} t^{2\theta/z} & \text{for } q \gg t^{-1/z}. \end{cases} \tag{A.11}$$

It is worth noting that for $q \gg t^{-1/z}$ –power-law regime– there is a vertical shift of the power spectra because $\theta \neq 0$. When $\alpha_s < 1$ this shift is a signature of intrinsic anomalous scaling.

In this regime we have only three independent exponents out of $\alpha, \alpha_{loc}, \beta, \beta^*, z$, since two scaling relations are fulfilled: $\alpha = z\beta$ and $\beta^* = (\alpha - \alpha_{loc})/z$.

Intrinsic anomalous roughening has been reported for either forced flow imbibition experiments with columnar disorder (Soriano et al., 2002a) or spontaneous imbibition with large negative pressure differences (Planet et al., 2007), and also for numerical simulations of a random diffusion model (López et al., 1997).

Super-roughness. When $\alpha = \alpha_s > 1$ we are dealing with a super-rough interface. The scaling of $w(\ell,t)$ and $S(q,t)$ is then

$$w(\ell,t) \sim \begin{cases} t^{\beta} & \text{for } t \ll t_\ell, \\ \ell t^{(\alpha-1)/z} & \text{for } t_\ell < t < t_s, \\ \ell L^{(\alpha-1)} & \text{for } t_s \ll t, \end{cases} \tag{A.12}$$

and

$$S(q,t) \sim \begin{cases} t^{(2\alpha+1)/z} & \text{for } q \ll t^{-1/z}, \\ q^{-(2\alpha+1)} & \text{for } q \gg t^{-1/z}. \end{cases} \tag{A.13}$$

Now the scaling relations are $\alpha = z\beta$ and $\beta^* = (\alpha - \alpha_{loc})/z$ with $\alpha_{loc} = 1$. The host-tumour interface for cell colonies *in vitro* and tumours *in vivo* (Brú et al., 1998, 2003) and the thin-film thickness of a bicrystal obtained by epitaxial growth of Nb films onto an insulating surface (Beringer et al., 2013) show this scaling behaviour.

Faceted interfaces. The last scaling scenario corresponds to the so-called faceted interfaces. This is the least observed scaling scenario. The first experimental evidence was reported by Córdoba-Torres et al. (2009) for roughening of dissolving polycrystalline pure iron. A KPZ model with columnar disorder also shows this behaviour (Szendro et al., 2007).

In this case $\alpha_s > 1$ and $\alpha \neq \alpha_s$. The scaling of the local roughness is

$$w(\ell, t) \sim \begin{cases} t^{\beta} & \text{for } t \ll t_\ell, \\ \ell t^{(\alpha-1)/z} & \text{for } t_\ell < t < t_s, \\ \ell L^{(\alpha-1)} & \text{for } t_s \ll t, \end{cases} \tag{A.14}$$

and for the power spectrum

$$S(q, t) \sim \begin{cases} t^{(2\alpha+1)/z} & \text{for } q \ll t^{-1/z}, \\ q^{-(2\alpha_s+1)} t^{2\theta/z} & \text{for } q \gg t^{-1/z}. \end{cases} \tag{A.15}$$

Again, the fact that $\theta \equiv \alpha - \alpha_s \neq 0$ results in a characteristic vertical shift of the power spectra for $q \gg t^{-1/z}$.

A.2.2 Kinetic roughening in imbibition of model open fractures

In Sec. 1.4.2 we reviewed different approaches to study kinetic roughening in model systems involving imbibition fronts. In the following we present a summary of the data obtained in imbibition experiments performed in setups similar to the one used in this Thesis, described in Ch. 2. Results from numerical simulations of imbibition fronts invading media similar to our model open fracture, and theoretical results are also quoted. We compare the roughness, growth, and dynamical exponents when available. The values are summarized in Table A.1, at the end of this appendix.

Forced-flow imbibition

Experimental and numerical results of forced-flow displacements are shown in the top panel of Table A.1. All experimental cases correspond to oil invasion of a model open fracture consisting of a Hele-Shaw cell with dichotomic gap spacing b and $b - \delta b$, with $\delta b = 0.06$ mm and typically $b = 0.40$ mm. These fluctuations in aperture were provided by copper patches randomly distributed on a plane, covering 35 % of the bottom plate of the cell. Copper patches were squares (SQ) or connected squares (SQ-n) of minimum lateral size 1.5×1.5 or 0.40×0.40 mm^2. SQ 1.5 and SQ 0.4 are described in detail in Sec. 1.1.1 (D^* and D plates). In SQ plates, disorder patches are not connected with next-nearest neighbours, contrarily to SQ-n plates. Experiments with capillary numbers $\mathrm{Ca} \leq 5.5 \cdot 10^{-4}$ operate in the capillary disorder regime, while those with larger Ca fall in the mixed capillary and permeability disorder regime, where the crossover length $\ell_\times$ that separates the influence of these two disorder types, Eq. (1.25) explained in Sec. 1.3, is smaller than the size of the system.

Roughness exponents first obtained by Hernández-Machado et al. (2001) and Soriano et al. (2002) do not correspond exactly to α_{loc}, but to exponents measured at large lengthscales (α_2 in their articles) making a general comparison difficult. However, those large-lengthscale exponents may be a good approximation of α_{loc}. We see in the table that local roughness exponents evolve systematically with Ca: they increase and finally saturate to $\alpha_{loc} = 1$ as Ca is reduced. Sharp-interface simulations (Pauné and Casademunt, 2003) and phase-field simulations (Rost et al., 2007) also measured $\alpha_{loc} = 1$. As for the global roughness exponent we can infer that in this capillary regime $\alpha > 1$.

All growth exponents measured experimentally are close to $\beta = 0.5$, while numerical results show a larger value $\beta \simeq 2/3$. Differences observed can be attributed to the actual properties of the disorder. First, disorder patches used experimentally have finite extent, while in phase-field simulations they are point-like. When persistent disorder in the direction of propagation of the front is considered, the growth exponent was also found to be $\beta = 0.5$ in forced-flow experiments (Soriano et al., 2002) and explicit analytical calculations (Pauné and Casademunt, 2003). Second, in Pauné and Casademunt (2003) the disorder landscape is smooth, while disorder patches used experimentally have sharp edges, that produce large slopes of the front height $h(x,t)$. The anomalous growth exponent is $\beta^* \simeq 0.15$ in the two experimental cases available, and the scaling scenario is super rough.

In the capillary regime power-counting arguments applied to the deterministic terms of the linearized interfacial equation predict a dynamic exponent $z = 3$. This value is found experimentally by Planet et al. (2014) and in Ch. 4 of this Thesis.

Spontaneous imbibition

Experimental and numerical results of spontaneous imbibition displacements are shown in the bottom panel of Table A.1. Experiments correspond to invasions of the same medium used in the forced-flow experiments presented earlier, but using only SQ 1.50 plates. A pressure difference ΔP applied between the inlet and the outlet allowed Soriano et al. (2005) and Planet et al. (2007) to explore three different regimes at large negative, negative, and positive ΔP. Regarding the phase-field simulations by Pradas et al. (2007, 2009) and Pradas (2009), different regimes were also observed as a function of ΔP.

In experiments performed in the capillary disorder regime (for large negative and negative ΔP) and in all phase-field simulations $\alpha > 1$ and $\alpha_{loc} \simeq 1$. In the mixed capillary and permeability disorder regime (positive ΔP) experiments display a different dynamics, with $\alpha < 1$ and $\alpha_{loc} < 1$.

Growth exponents differ again between experiments and phase-field simulations, being generally smaller in the latter. As for the anomalous growth exponent, it is different

from 0 in all cases except for a positive ΔP. In this situation the scaling scenario is Family-Vicsek, as confirmed also by the roughness exponents $\alpha \simeq \alpha_{loc}$.

Finally, the dynamic exponents obtained experimentally make clear that for positive ΔP the presence of permeability disorder strongly affects the dynamics of the system, and $z \simeq 2$. In the pure capillary disorder regime, for smaller ΔP, $z = 3$. Phase-field simulations at the smallest ΔP belong also to the capillary disorder regime with $z = 3$. However, for larger ΔP exponents change to $z = 4$ as predicted by Dubé et al. (1999). In that case, the authors assumed an infinite velocity at the beginning –which is never achieved experimentally– and disorder in the permeability was not considered in the phase-field equations.

General remarks

The results just reviewed stress the importance of the permeability disorder in the imbibition dynamics, specially when high velocities are involved (large Ca or ΔP). Planet et al. (2007) showed that the effect of the disorder in the permeability should not be neglected when studying fronts moving at velocities such that the lateral correlation length is larger than $\ell_\times$. Most numerical results shown, however, were obtained without considering permeability disorder and thus discrepancies with experimental results are expected. The actual profile of the disorder patches (e.g. with either sharp or smooth edges) and its persistence in the direction of front propagation also play an important role in the dynamics (Pauné and Casademunt, 2003).

Reference	Experimental or numerical conditions		Roughness exponents		Growth exponents		Dynamic expt.
			α	α_{loc}	β	β^*	z
Forced-flow: experimental							
	Disorder	Ca ($\times 10^{-4}$)					
Hernández-Machado et al. (2001)	SQ 1.50 & SQ-n 1.50	> 7		–	0.5		
Soriano et al. (2002)	SQ-n 1.50	$2-7$		0.5*	0.5		
	SQ 1.50	$2-7$		0.6*	0.5		
	SQ 1.50 & SQ-n 1.50	< 2		0.6* – 0.9*	0.5		
Planet et al. (2014)	SQ 0.40	3.2	1.26(11)	0.82(5)	0.42(2)	0.15(3)	3.0(2)
Chapter 4, this Thesis	SQ 0.40	0.6	1.38(15)	0.97(1)	0.50(1)	0.16(7)	2.8(4)
Forced-flow: sharp-interface and phase-field simulations							
		Disorder regime					
Pauné and Casademunt (2003)	Sharp-interface sim.	Capillary	1.20(5)	1	0.68(2)		
Rost et al. (2007)	Phase-field sim.	Capillary	1.25	1			
	Phase-field sim.	Permeability	1	1			
Spontaneous imbibition: experimental (SQ 1.50)							
Soriano et al. (2005)	Large negative ΔP		1.94(20)	0.94(10)	0.64(2)	0.33(3)	3.0(3)
Planet et al. (2007)	Negative ΔP		1.27(15)	0.97(30)	0.42(2)	0.10(3)	3.0(4)
	Positive ΔP		0.70(15)	0.59(23)	0.36(2)	0.06(3)	1.9(4)
Spontaneous imbibition: phase-field simulations							
Pradas et al. (2007)	Small positive ΔP		1.50(2)	0.95(3)	0.49(3)	0.20(4)	3.0(1)
Pradas et al. (2009)			1.50(2)	0.95(3)	0.37(3)	0.14(4)	4.0(1)
Pradas (2009)	↓		1.34(2)	1.00(3)	0.33(3)	0.12(4)	4.0(1)
	Large positive ΔP		1.25(2)	1.00(3)	0.32(3)	0.10(4)	4.0(1)

TABLE A.1: Summary of the scaling exponents obtained experimentally –in setups similar to the one described in Ch. 2– and numerically. See text for details.

Appendix B

Matlab scripts

`Matlab` is a high-level language and interactive environment for numerical computation, visualization and programming, developed by The MathWorks, Inc. Most data analysis performed in this Thesis has been carried out with `Matlab`. This appendix provides the main functions of scripts developed and used in this work.

Camera configuration and main functions required to control image acquisition via `Matlab` are explained. The script for interface extraction is discussed. Finally, a list of the main data-analysis scripts is provided.

B.1 Camera control and image acquisition

Control of the Redlake Motion Pro X3 *fast camera* (Sec. 2.5) via `Matlab` has been implemented during this Thesis. First, the computer has to be configured and the drivers installed. Specifically, the software development kit (SDK) of the camera must be installed, and a `C++` compiler[1] is required by `Matlab` to use the camera's SDK.

Camera initialization

Before performing any experiment the camera has to be initialized and configured. In the following the basic initial steps and main configuration options are quoted. The full script is included in the CD accompanying the Thesis.

The generic function to set a characteristic *property* to the camera is `SetParameter`:

```
[nResult]=XStreamML('SetParameter',cameraId,propertyKey,propertyValue);
```

[1] Microsoft Visual C++ 2010 Express, for instance.

where `propertyKey` is defined by the SDK of the camera for each property and cannot be changed, and `propertyValue` is the actual value of the property, which can be modified within the range given by the camera features.

- Open the camera. We first have to check whether the camera is well connected and can be initialized, otherwise an error is displayed. Once opened, it is important to remind that the camera must be closed after acquisition and before closing `Matlab`.

```
%% Camera OPEN
nInId=0;
[nResult,cameraId]=XStreamML('OpenCamera',nInId);
% cameraId usually = 1
if nResult ~= 0
    error('Unable to open camera');
else
    disp('Camera open')
end
```

- Exposure time and acquisition period (inverse of acquisition rate) in nanoseconds.

```
exposureKey=1;
exposureValue=10000000;
[nResult]=XStreamML('SetParameter',cameraId,exposureKey,exposureValue);
periodKey=17;
periodValue= 10000000;
[nResult]=XStreamML('SetParameter',cameraId,periodKey,periodValue);
```

- Position of the bottom-left corner of the ROI (region of interest).

```
roiXKey=13;
roiXValue=0;
[nResult]=XStreamML('SetParameter',cameraId,roiXKey,roiXValue);
roiYKey=14;
roiYValue=0;
[nResult]=XStreamML('SetParameter',cameraId,roiYKey,roiYValue);
```

- Width and height of the ROI. Maximum size (1280x1024) set by default, when Value = 0.

```
roiWidthKey=15;
roiWidthValue=0;
[nResult]=XStreamML('SetParameter',cameraId,roiWidthKey,roiWidthValue);
roiHeightKey=16;
roiHeightValue=0;
[nResult]=XStreamML('SetParameter',cameraId,roiHeightKey,roiHeightValue);
```

- Trigger mode. Different options: Internal=0, External edge high = 1, External edge low = 2, External pulse high = 3, External pulse Low = 4. Internal trigger is used by default. `CameraAcquisition.m` uses Internal, while External edge high is utilized in `PerturbationAcquisition.m` (described below).

```
syncinCfgKey=5;
syncinCfgValue=0;
[nResult]=XStreamML('SetParameter',cameraId,syncinCfgKey,syncinCfgValue);
```

- Trigger source. Different options: Pulse Train=0, Single Pulse = 1. The latter is used in `PerturbationAcquisition.m` (described below).

```
recordModeKey=6;
recordModeValue=0;
[nResult]=XStreamML('SetParameter',cameraId,recordModeKey,recordModeValue);
```

- Send configuration to camera. Finally the configuration must be sent to the camera. If there is any problem, an error is displayed.

```
[nResult]=XStreamML('SendCfg',cameraId);
if nResult ~= 0
    error('Unable to configure camera');
end
```

- Close camera. Once an experiment is finished the camera must be closed.

```
[nResult]=XStreamML('CloseCamera',cameraId);
if nResult ~= 0
    error('Unable to close camera');
else
    disp('Camera closed')
    clear cameraId
end
```

Controlled-frame-rate recording

The program `CameraAcquisition.m` allows to record images at a controlled acquisition frame-rate, including logarithmically-spaced capturing times, specially convenient for capillary rise (Ch. 3) or kinetic roughening (Ch. 4) experiments. In the following the main features of the program are described. The full script is also included in the accompanying CD.

This program is configured so that a constant, high-frame rate acquisition period is followed by logarithmically-spaced recording times[2]. We fix the number of images `nIM1` recorded at high frame rate (100 fps by default), and the number of images per decade of time, `nIMperDecade`, for the logarithmic acquisition. The program also allows to set a pausing time, when acquisition stops and the camera can be displaced along the cell to change the ROI, before resuming acquisition.

Once all parameters are set and the camera is initialized, the experiment starts. At the constant-frame-rate acquisition regime, the camera works at *memory start grab* configuration. The recording is started by the function:

```
[nResult] = XStreamML('MemoryStartGrab',cameraId,0,0,nIM1,0);
```

[2]Any variable acquisition rate could be configured. We use logarithmically-spaced time increments for convenience.

It automatically stops after recording `nIM1` images and flag `isReady` becomes 1:

```
[nResult,isReady] = XStreamML('GrabIsReady',cameraId);
```

In the logarithmically-spaced acquisition regime the camera also works at *memory start grab* configuration. However, since part of the internal memory of the camera is already full, we must indicate the position of the memory pointer to avoid overwriting previously recorded images. The pointer is given by a 64-bit number resulting from the size of the images in squared pixels (width of the image times the maximum height, 1280) times the number of previous images recorded `nIMbefore`:

```
frame_mem = uint64(IMwidth*1280*nIMbefore);
```

Then, to record new images:

```
[nResult] = XStreamML('MemoryStartGrab',cameraId,frame_mem,frame_mem,1,0);
```

Finally, the recorded images are obtained from the camera by using the *MemoryReadData* configuration of the camera:

```
[nResult,imagek] = XStreamML('MemoryReadData',cameraId,0,0,k);
```

where `imagek` is the matrix containing the information of the image number `k`. A loop for all images recorded is needed. Images are saved to the hard disk drive by using a `Matlab` function:

```
imwrite(imagek, filename,'tif');
```

where `filename` is the output name of the image, and `'tif'` sets the format of the image (in this case Tagged Image File format).

Externally-triggered recording

The program `PerturbationAcquisition.m` allows to record images each time an external sensor is activated. This recording mode has been used in the experiments with controlled pressure perturbations described in appendix C. The script is also found in the accompanying CD.

The output of the photoelectric sensor is connected to the *SYNC IN* input of the camera by a BNC cable. The recording mode of the camera is:

```
[nResult,image,~]=XStreamML('SynchGrab',cameraId,nTimeOut);
```

where `image` is the matrix containing the information of the image recorded. `nTimeOut` is the maximum time in seconds that the camera will wait for a trigger signal. If this time is exceeded the acquisition stops. In this configuration each acquired image is saved before the next image is recorded.

B.2 Interface extraction

The function `interfaces_wtmatrix.m` extracts the interfaces from raw images, generates the waiting time matrix wt, and provides the relative fraction of elements of the wt equal to zero and also of element values smaller than 10. The scripts are partially based on previous functions developed by Planet (2009).

For each experiment, the script reads the background image and subtracts it from all subsequent images to improve contrast between oil and air phases and to remove lighting inhomogeneities, undesired reflections from the top glass plate or the disorder patches, and the disorder pattern.

Each subtracted image is analysed by `getfront.m`. This script first binarizes the image by using the script `thresholdBW.m`, which computes the histogram of grey levels of the image and extracts its minimum between the two maxima corresponding to the oil and air phases. This minimum is the threshold value used to define black and white regions.

The different connected regions of the binarized image `Ibw` are then labelled and their area extracted by using the `Matlab` functions:

```
[Ilabeled, ~] = bwlabel(Ibw,8);
props = regionprops(Ilabeled,'area');
```

A new matrix `Ilabeled2` is defined whose elements are set to 1 if they correspond to the largest area of `Ilabeled`, or set to 0 otherwise. Advancing along the matrix `Ilabeled2`, the elements in which the values change from 1 to 0 (or 0 to 1) define the interface position. A new matrix `front`, of the size of the images and elements 1 or 0 if they correspond or not to the interface, is then directly obtained by using:

```
idx_Y = find(Ilabel2(:,i) == 1, 1,'first');
front(idx_Y,i) = 1;
```

where index `i` explores all elements in the x direction.

The waiting time matrix is then obtained by adding all `front` matrices.

The interface position in the y direction at time `j` is given by:

```
[y_int, ~] = find(front);
interfaces_t(:,j) = y_int;
```

B.3 Data analysis

In the following a list of the principal scripts used for data analysis is presented. Some of the functions are based on previous scripts developed by S. Santucci and R. Planet.

- `Average_LogBoxes.m`. This function considers a 2D set of data and computes the average values, $\bar{x}$ and $\bar{y}$, and their corresponding standard deviations, σ_x and σ_y, of the subset of data within logarithmically-spaced bins in x.
- `Local_Avalanches_analysis.m`. Set of scripts to obtain different observables of local avalanches.
- `AutoCorrelationGlobalSignal.m`. It computes the autocorrelation of any global signal as defined in our data set. The signal is a matrix with a number of columns given by the duration of the experiment, and a number of rows given by the number of windows n in which the front has been divided, $n = L/\ell$.
- `avalanches_global.m`. This function extracts the global avalanches from a velocity signal and provides their initial and final times, duration, and size.
- `STdistributions.m`. This script obtains the joint distribution of sizes and durations of the global avalanches. It requires `avalanches_global.m`.
- `build_PX_llc.m`. This function is used to collapse the distributions of X (either sizes S or durations T) of global avalanches, and to extract the power-law exponent of the pdfs.
- `ShapeGlobalAvalanche_ALL`. It extracts the shapes of global avalanches for a given experimental condition. All the information is saved in a structured variable `globalAv`.
- `Fit_AvShape.m`. It fits the averaged avalanche shape proposed by Laurson et al. (2013) to the experimental data, and returns the two parameters of the fit.
- `IncrementsGlobalVel.m`. This function computes velocity increments for a logarithmically-increasing time lag.

Appendix C

Controlled pressure perturbations

In chapters 5 and 6 we have shown that the lateral correlation length of the front diverges when Ca $\to$ 0 as $\ell_c \sim 1/\sqrt{\text{Ca}} \sim 1/\sqrt{\mu \text{v}}$. In addition, the cutoffs of the statistical distributions of the observables of local and global avalanches also diverge when Ca $\to$ 0, indicating that the dynamics of the fluid front invading our disordered medium approaches a critical pinning/depinning point (Alava et al., 2004).

A new experimental approach to the problem of slowly driven interfaces in disordered media is presented in this appendix. Specifically, a new driving protocol designed to explore perturbations around the critical point of the system is described, and some preliminary results shown.

C.1 Experimental setup and protocol

The driving protocol consists on bringing the oil-air interface to the critical point, at v = 0, in spontaneous imbibition. The front is then perturbed by a small increase of the applied pressure, and let to reach v = 0 again. A diagram of the protocol is shown in Fig. C.1. The front, at rest, is perturbed by a finite increase of the applied force ΔF, which sets the interface in motion. The interface reaches the new equilibrium position when the applied force relaxes to F_c.

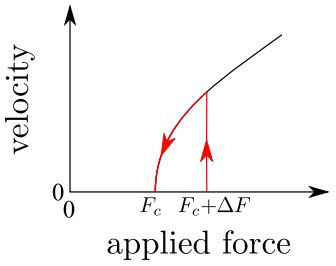

FIGURE C.1: Velocity vs applied force diagram. The front is at rest when the critical force F_c is applied. ΔF is the force perturbation.

In order to do so the HS cell, described in detail in Ch. 2, is tilted a controlled angle ψ in the sense that gravity opposes front advancement, and it is connected to a reservoir of fluid. An sketch of the setup is shown in Fig. C.2.

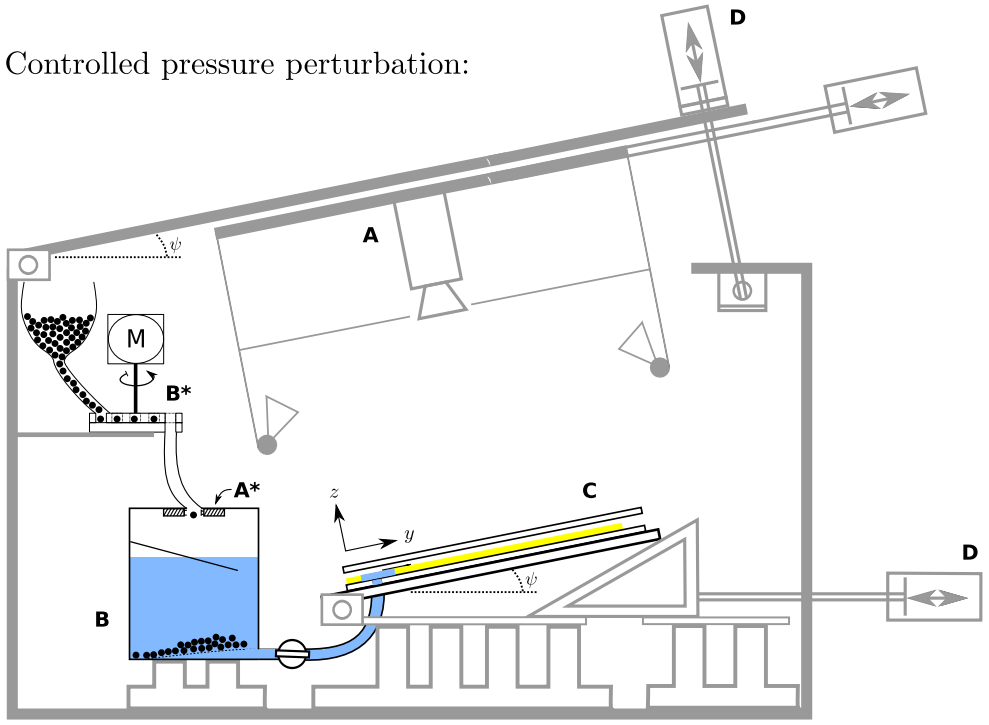

FIGURE C.2: Sketch of the experimental setup. The *fast camera* (**A**) records an image each time a bearing ball passes through the photoelectric sensor (**A***). Bearing balls are released by the revolver connected to the motor (**B***), and cause an increase in height at the oil reservoir (**B**). The cylindrical reservoir (180 mm in diameter) is connected to the Hele-Shaw cell (**C**). The cell and the acquisition system can be tilted an angle ψ by using two motors (**D**). The HS cell is illuminated by indirect lighting (LEDs pointing towards a white reflecting plate).

An initial height of the column of oil $H(t_0)$ is set, and the fluid is allowed to flow into the cell until it reaches the equilibrium height, where v = 0. H is then increased by a discrete height variation $\delta H = h_p \sin\psi$, which would correspond to a mean advancement of the front a distance h_p if no pinning forces due to disorder were present. Throwing of small bearing balls (12 mm in diameter) into the reservoir (180 mm in diameter) is responsible for controlled height increments δH, with $h_p = 0.4$ mm and $\psi = 5°$. A pool of balls is connected to the reservoir through a pipe. Release of the balls is controlled by a revolver connected to a DC motor rotating at 4 revolutions per minute. The revolver can be configured to have from one to six balls thrown to the reservoir on each complete turn of the motor. Then we can perform experiments at perturbation rates from 4 to 24 per minute, one perturbation every 15 to 2.5 s.

Following a pressure perturbation, the front position $h(x,t)$ is recorded once it has already completely stopped and just before the next perturbation. A function for MATLAB, `PerturbationAcquisition.m`, has been written to control the *fast camera* (Sec. 2.5). This function, explained in appendix B, allows image acquisition triggered by a

photoelectric sensor connected to the camera. The sensor is activated by the bearing balls just before they cause the height increment.

C.2 Preliminary results

The mean position of the fluid interface $h(t)$ can be estimated from Darcy's law (Eq. (1.11), Sec. 1.1.2), when capillary pressure fluctuations are disregarded:

$$\frac{dh}{dt} = \frac{\kappa}{\mu}\left(\frac{\Delta P}{h} - \rho g \sin\psi\right). \tag{C.1}$$

Here κ is the permeability of the medium (that takes into account the averaged effect of the disorder), μ the dynamic viscosity of the fluid, ΔP the pressure difference between inlet and outlet, ρ the density of the fluid, g the acceleration of gravity, and ψ the inclination angle of the cell.

We consider pressure perturbations δP which cause a height increment δh. Then: $\Delta P = \Delta P_0 + \delta P$ and $h = h_0 + \delta h$, where ΔP_0 and h_0 are the initial pressure difference imposed and the mean position of the front. Specifically, from Eq. (C.1) we obtain $h_0 = \Delta P_0/(\rho g \sin\psi)$ when $dh/dt = 0$.

We can now perform a linear approximation of the quotient $\Delta P/h$:

$$\frac{\Delta P}{h} = \frac{\Delta P_0 + \delta P}{h_0 + \delta h} = \frac{\Delta P_0}{h_0 + \delta h} + \frac{\delta P}{h_0 + \delta h} = \frac{\Delta P_0}{h_0} - \frac{\Delta P_0}{h_0^2}\delta h + \frac{\delta P}{h_0} + \mathcal{O}(\delta P \delta h). \tag{C.2}$$

Equation (C.1) can be then approximated by:

$$\frac{dh}{dt} = C - \frac{\kappa}{\mu}\frac{\Delta P_0}{h_0^2}\delta h. \tag{C.3}$$

The exponential solution of Eq. (C.3) reads:

$$\delta h \equiv h - h_0 = h_0 \frac{\delta P}{\Delta P_0}\left(1 - e^{-t/\tau}\right) \tag{C.4}$$

where

$$\tau = \frac{\mu}{\kappa}\frac{h_0^2}{\Delta P} = \frac{\mu}{\kappa}\frac{h_0}{\rho g \sin\psi}. \tag{C.5}$$

is a characteristic relaxation time.

We have performed preliminary experiments with a silicone oil of dynamic viscosity $\mu = 50$ cP. The HS cell has been tilted an angle $\psi = 5°$, and the disordered plate D has been used, with permeability $\kappa = 0.0146$ mm^2. The initial heights h_0 that can be explored range from 10 to 200 mm, for which the predicted relaxation times are

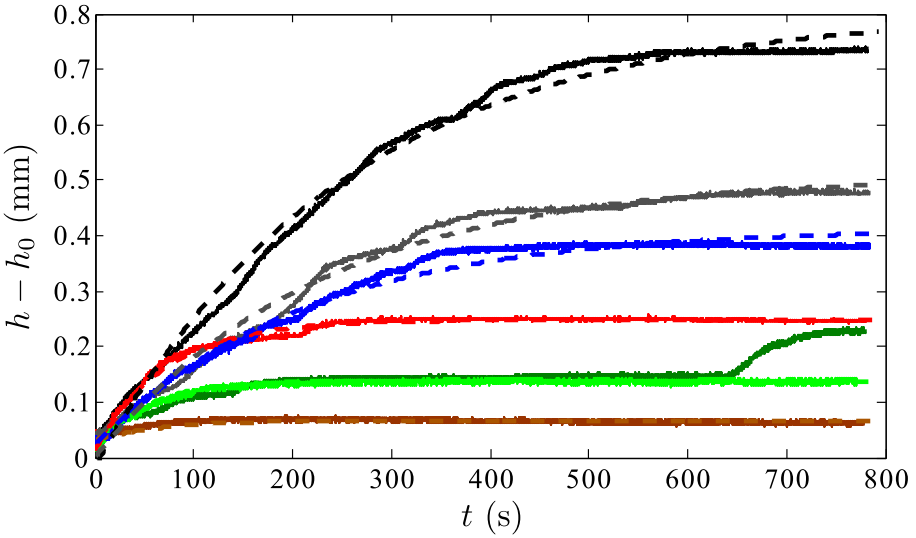

FIGURE C.3: Mean front advancement after a perturbation at $t = 0$. Experimental data (solid lines) are fitted by functions that exponentially saturate at h_{eq} (dashed lines). Characteristic times obtained from the fit of the data to $h - h_0 = A(1 - Be^{t/\tau})$ are $\tau = 250,\ 230,\ 210,\ 70,\ 50,\ 70$ s (top to bottom curves), with error bars ± 20 s. $h_0 \simeq 40$ mm in all cases.

$\tau = 40 - 800$ s. In this configuration, a single pressure perturbation corresponds to an increment in the average position of the front $\delta h = 0.4$ mm.

However, it must be noticed that the derivation above does not take the role of the disorder explicitly into account. Specifically, local pressure fluctuations due to changes in the capillary pressure at the interface are disregarded. Therefore, discrepancies between the actual equilibrium heights and relaxation times reached experimentally after a pressure perturbation, and the predictions of Eqs. (C.4) and (C.5) may be expected.

Figure C.3 shows the evolution of the mean position of the front after a pressure perturbation for seven illustrative cases with $h_0 \simeq 40$ mm. According to Eq. (C.5) the characteristic relaxation time that corresponds to the conditions explored is $\tau \simeq 160$ s. In most of the 16 experiments performed the curves display an exponential increase in time that saturates to different final heights $\delta h_{eq} = 0.1 - 0.8$ mm. In some experiments the front reaches a quasi-stationary state at a given h at intermediate times, and afterwards evolves towards a new equilibrium position at larger h (dark green curve in the figure, third curve from the bottom). Measured equilibrium heights average to $\delta h_{eq} = 0.32$ mm, with standard deviation 0.18 mm. The measured values of τ show also large fluctuations, from 50 s to 270 s, with an average value and standard deviation $\tau = 160 \pm 80$ s. These results show the important role played by the capillary forces in the dynamics of the front, in either pinning or pulling the interface below or above the equilibrium height expected without disorder, $\delta h_{eq} = h_p = 0.4$ mm.

In order to observe the critical behaviour of the pinned oil-air interface reflected on the power-law distributions of the observables of the avalanches, a very large data set is required. Specifically, at least 10000 events (pressure perturbations) are needed. Values of relaxation times in the range $40 - 800$ s, however, imply that an experiment should last more than 3 hours to record 100 events only. Measuring large data sets over a wide range of h_0 becomes therefore prohibitive from an experimental point of view. The relaxation time could be shortened by reducing the viscosity of the fluid or performing experiments only close to the inlet of the HS cell, at small h_0. Increasing the inclination of the cell would be another possibility. But it is not difficult to see that the lateral correlation length of the front is severely reduced in the presence of gravity, effectively taking the system out of criticality.

List of Publications

Part of the original work reported in this Thesis is based on the following publications:

- Clotet, X., Planet, R. and Ortín, J. (2012), Capillary rise in Hele-Shaw models of disordered media, *J. Colloid Interface Sci.*, **377**, 387-395.
- Clotet, X., Santucci, S. and Ortín, J. (2012), Intermittency of fluid imbibition in disordered media, *Revista Cubana de Física*, **29**, 1E, 62-65.
- Clotet, X., Ortín, J. and Santucci, S. (2014), Disorder-induced capillary bursts control intermittency in slow imbibition, *under second round of revision in Phys. Rev. Lett.*

List of publications currently in preparation:

- Clotet, X., Santucci, S. and Ortín, J., Asymmetric average avalanche shape in imbibition fronts, *in preparation.*
- Clotet, X., Santucci, S. and Ortín, J., Spatio-temporal dynamics of imbibition fronts: from local to global, *in preparation.*

References

Adler, P. M. and Thovert, J.-F. (1999), *Fractures and Fracture Networks*, Springer Netherlands.

Alava, M., Dubé, M. and Rost, M. (2004), Imbibition in disordered media, *Adv. Phys.*, **53**(2), 83–175.

Alessandro, B., Beatrice, C., Bertotti, G. and Montorsi, A. (1990), Domain-wall dynamics and Barkhausen effect in metallic ferromagnetic materials. I. Theory, *J. Appl. Phys.*, **68**(6), 2901.

Alexandrova, O., Carbone, V., Veltri, P. and Sorriso-Valvo, L. (2007), Solar wind Cluster observations: Turbulent spectrum and role of Hall effect, *Planet. Space Sci.*, **55**(15), 2224–2227.

Arnéodo, A., Benzi, R., Berg, J., Biferale, L., Bodenschatz, E., Busse, A., Calzavarini, E., Castaing, B., Cencini, M., Chevillard, L., Fisher, R. T., Grauer, R., Homann, H., Lamb, D., Lanotte, A., Lévèque, E., Lüthi, B., Mann, J., Mordant, N., Müller, W.-C., Ott, S., Ouellette, N., Pinton, J.-F., Pope, S., Roux, S., Toschi, F., Xu, H. and Yeung, P. (2008), Universal Intermittent Properties of Particle Trajectories in Highly Turbulent Flows, *Phys. Rev. Lett.*, **100**(25), 254504.

Balankin, A. S., García Otamendi, E., Samayoa, D., Patiño, J. and Rodríguez, M. a. (2012), Depinning and creeplike motion of wetting fronts in weakly vibrated granular media, *Phys. Rev. E*, **85**(3), 036313.

Baldassarri, A., Colaiori, F. and Castellano, C. (2003), Average Shape of a Fluctuation: Universality in Excursions of Stochastic Processes, *Phys. Rev. Lett.*, **90**(6), 060601.

Barabási, A.-L. and Stanley, H. E. (1995), *Fractal concepts in surface growth*, Cambridge Univ. Press.

Barés, J., Barbier, L. and Bonamy, D. (2013), Crackling versus Continuumlike Dynamics in Brittle Failure, *Phys. Rev. Lett.*, **111**(5), 054301.

Baró, J., Corral, A., Illa, X., Planes, A., Salje, E. K. H., Schranz, W., Soto-Parra, D. E. and Vives, E. (2013), Statistical Similarity between the Compression of a Porous Material and Earthquakes, *Phys. Rev. Lett.*, **110**(8), 088702.

Baró, J. and Vives, E. (2012), Analysis of power-law exponents by maximum-likelihood maps, *Phys. Rev. E*, **85**(6), 066121.

Barry, D. A., Parlange, J.-Y., Sander, G. and Sivaplan, M. (1993), A class of exact solutions for Richards' equation, *J. Hydrol.*, **142**(1-4), 29–46.

Barry, D. A., Wissmeier, L., Parlange, J.-Y. J., Sander, G. C. and Lockington, D. A. (2009), Comment on "An analytic solution of capillary rise restrained by gravity" by N. Fries and M. Dreyer, *J. Colloid Interface Sci.*, **338**(1), 293–295.

Batchelor, G. K. and Townsend, A. A. (1949), The Nature of Turbulent Motion at Large Wave-Numbers, *Proc. R. Soc. A Math. Phys. Eng. Sci.*, **199**(1057), 238–255.

Bear, J. (1975), Dynamics of Fluids in Porous Media, *Soil Sci.*, **120**(2), 162–163.

Bell, J. M. and Cameron, F. K. (1906), The flow of liquids through capillary spaces, *J. Phys. Chem.*, **10**(8), 658–674.

Beringer, D. B., Roach, W. M., Clavero, C., Reece, C. E. and Lukaszew, R. A. (2013), Roughness analysis applied to niobium thin films grown on MgO(001) surfaces for superconducting radio frequency cavity applications, *Phys. Rev. Spec. Top. - Accel. Beams*, **16**(2), 022001.

Berkowitz, B., Cortis, A., Dentz, M. and Scher, H. (2006), Modeling non-Fickian transport in geological formations as a continuous time random walk, *Rev. Geophys.*, **44**(2), RG2003.

Bertin, E. (2005), Global Fluctuations and Gumbel Statistics, *Phys. Rev. Lett.*, **95**(17), 170601.

Boffetta, G. and Ecke, R. E. (2012), Two-Dimensional Turbulence, *Annu. Rev. Fluid Mech.*, **44**(1), 427–451.

Bonamy, D., Santucci, S. and Ponson, L. (2008), Crackling Dynamics in Material Failure as the Signature of a Self-Organized Dynamic Phase Transition, *Phys. Rev. Lett.*, **101**(4), 045501.

Bonn, D., Eggers, J., Indekeu, J., Meunier, J. and Rolley, E. (2009), Wetting and spreading, *Rev. Mod. Phys.*, **81**(2), 739–805.

Bosanquet, C. (1923), LV. On the flow of liquids into capillary tubes, *Philos. Mag. Ser. 6*, **45**(267), 525–531.

Boschan, A., Auradou, H., Ippolito, I., Chertcoff, R. and Hulin, J. P. (2009), Experimental evidence of the anisotropy of tracer dispersion in rough fractures with sheared walls, *Water Resour. Res.*, **45**(3), W03201.

Boschan, A., Ippolito, I., Chertcoff, R., Hulin, J. P. and Auradou, H. (2011), Characterization of fracture aperture field heterogeneity by electrical resistance measurement., *J. Contam. Hydrol.*, **123**(1-2), 65–74.

Bramwell, S., Christensen, K., Fortin, J., Holdsworth, P., Jensen, H., Lise, S., López, J. M., Nicodemi, M., Pinton, J. and Sellitto, M. (2000), Universal fluctuations in correlated systems, *Phys. Rev. Lett.*, **84**(17), 3744–3747.

Bramwell, S., Holdsworth, P. and Pinton, J.-F. (1998), Universality of rare fluctuations in turbulence and critical phenomena, *Nature*, **396**(December), 552–554.

Brú, A., Albertos, S., Luis Subiza, J., García-Asenjo, J. L. and Brú, I. (2003), The universal dynamics of tumor growth., *Biophys. J.*, **85**(5), 2948–2961.

Brú, A., Pastor, J., Fernaud, I., Brú, I., Melle, S. and Berenguer, C. (1998), Super-Rough Dynamics on Tumor Growth, *Phys. Rev. Lett.*, **81**(18), 4008–4011.

Castaing, B., Gagne, Y. and Hopfinger, E. (1990), Velocity probability density functions of high Reynolds number turbulence, *Phys. D Nonlinear Phenom.*, **46**(2), 177–200.

Chebbi, R. (2007), Dynamics of liquid penetration into capillary tubes., *J. Colloid Interface Sci.*, **315**(1), 255–60.

Chen, Y.-J., Papanikolaou, S., Sethna, J. P., Zapperi, S. and Durin, G. (2011), Avalanche spatial structure and multivariable scaling functions: Sizes, heights, widths, and views through windows, *Phys. Rev. E*, **84**(6), 1–22.

Chevillard, L., Castaing, B., Arneodo, A., Lévêque, E., Pinton, J.-F. and Roux, S. G. (2012), A phenomenological theory of Eulerian and Lagrangian velocity fluctuations in turbulent flows, *Comptes Rendus Phys.*, **13**(9-10), 899–928.

Chevillard, L., Castaing, B., Leveque, E. and Arnéodo, A. (2006), Unified multifractal description of velocity increments statistics in turbulence: Intermittency and skewness, *Phys. D Nonlinear Phenom.*, **218**(1), 77–82.

Chevillard, L. and Meneveau, C. (2006), Lagrangian Dynamics and Statistical Geometric Structure of Turbulence, *Phys. Rev. Lett.*, **97**(17), 174501.

Clauset, A., Shalizi, C. and Newman, M. (2009), Power-law distributions in empirical data, *SIAM Rev.*, **51**(4), 661–703.

Colaiori, F. (2008), Exactly solvable model of avalanches dynamics for Barkhausen crackling noise, *Adv. Phys.*, **57**(4), 287–359.

Córdoba-Torres, P., Mesquita, T., Bastos, I. and Nogueira, R. (2009), Complex Dynamics during Metal Dissolution: From Intrinsic to Faceted Anomalous Scaling, *Phys. Rev. Lett.*, **102**(5), 055504.

Cottin, C., Bodiguel, H. and Colin, A. (2010), Drainage in two-dimensional porous media: From capillary fingering to viscous flow, *Phys. Rev. E*, **82**(4), 046315.

de Anna, P., Le Borgne, T., Dentz, M., Tartakovsky, A. M., Bolster, D. and Davy, P. (2013), Flow Intermittency, Dispersion, and Correlated Continuous Time Random Walks in Porous Media, *Phys. Rev. Lett.*, **110**(18), 184502.

de Gennes, P. G. (1985), Wetting: statics and dynamics, *Rev. Mod. Phys.*, **57**(3), 827–863.

de Gennes, P. G., Brochard-Wyart, F. and Quéré, D. (2004), *Capillarity and Wetting Phenomena Drops, Bubbles, Pearls, Waves*, Springer.

Deike, L., Laroche, C. and Falcon, E. (2011), Experimental study of the inverse cascade in gravity wave turbulence, *Europhys. Lett.*, **96**(3), 34004.

Delker, T., Pengra, D. and Wong, P. (1996), Interface pinning and the dynamics of capillary rise in porous media., *Phys. Rev. Lett.*, **76**(16), 2902–2905.

Delle Side, D., Velardi, L., Nassisi, V., Pennetta, C., Alifano, P., Tala, A. and Salvatore Tredici, M. (2013), Bacterial bioluminescence and Gumbel statistics: From quorum sensing to correlation, *Appl. Phys. Lett.*, **103**(25), 253702.

Dentz, M., Le Borgne, T., Englert, A. and Bijeljic, B. (2011), Mixing, spreading and reaction in heterogeneous media: a brief review., *J. Contam. Hydrol.*, **120-121**, 1–17.

Dougherty, A. and Carle, N. (1998), Distribution of avalanches in interfacial motion in a porous medium, *Phys. Rev. E*, **58**(3), 2889–2893.

Dubé, M., Rost, M., Elder, K., Alava, M., Majaniemi, S. and Ala-Nissila, T. (1999), Liquid Conservation and Nonlocal Interface Dynamics in Imbibition, *Phys. Rev. Lett.*, **83**(8), 1628–1631.

Durin, G., Colaiori, F., Castellano, C. and Zapperi, S. (2007), Signature of negative domain wall mass in soft magnetic materials, *J. Magn. Magn. Mater.*, **316**(2), 436–441.

Edwards, S. F. and Wilkinson, D. R. (1982), The Surface Statistics of a Granular Aggregate, *Proc. R. Soc. A Math. Phys. Eng. Sci.*, **381**(1780), 17–31.

Erpelding, M., Sinha, S., Tallakstad, K. T., Hansen, A., Flekkøy, E. G. and Måløy, K. (2013), History independence of steady state in simultaneous two-phase flow through two-dimensional porous media, *Phys. Rev. E*, **88**(5), 053004.

Falcon, E., Fauve, S. and Laroche, C. (2007), Observation of Intermittency in Wave Turbulence, *Phys. Rev. Lett.*, **98**(15), 10–13.

Falcon, E., Roux, S. and Audit, B. (2010a), Revealing intermittency in experimental data with steep power spectra, *Europhys. Lett.*, **90**(5), 50007.

Falcon, E., Roux, S. and Laroche, C. (2010), On the origin of intermittency in wave turbulence, *Europhys. Lett.*, **90**(3), 34005.

Falkovich, G., Gawdzki, K. and Vergassola, M. (2001), Particles and fields in fluid turbulence, *Rev. Mod. Phys.*, **73**(October), 913–975.

Family, F. and Vicsek, T. (1985), Scaling of the active zone in the Eden process on percolation networks and the ballistic deposition model, *J. Phys. A*, **75**.

Fisher, L. (1999), Physics takes the biscuit, *Nature*, **397**(6719), 469.

Fisher, L. R. and Lark, P. D. (1979), An experimental study of the washburn equation for liquid flow in very fine capillaries, *J. Colloid Interface Sci.*, **69**(3), 486–492.

Fries, N. and Dreyer, M. (2008*a*), An analytic solution of capillary rise restrained by gravity., *J. Colloid Interface Sci.*, **320**(1), 259–63.

Fries, N. and Dreyer, M. (2008*b*), The transition from inertial to viscous flow in capillary rise., *J. Colloid Interface Sci.*, **327**(1), 125–128.

Frippiat, C. C. and Holeyman, A. E. (2008), A comparative review of upscaling methods for solute transport in heterogeneous porous media, *J. Hydrol.*, **362**(1-2), 150–176.

Frisch, U. (1996), *Turbulence: The Legacy of A. N. Kolmogorov*, Cambridge University Press.

Frisch, U. and Parisi, G. (1985), Turbulence and Predictability in Geophysical Fluid Dynamics and Climate Dynamics, *in* B. R. Ghil M. and P. G., eds, "Proc. Enrico Fermi Varenna Phys. Sch. LXXXVIII", North-Holland, Amsterdam, p. 84.

Ganesan, V. and Brenner, H. (1998), Dynamics of two-phase fluid interfaces in random porous media, *Phys. Rev. Lett.*, **81**(3), 578–581.

Geromichalos, D., Mugele, F. and Herminghaus, S. (2002), Nonlocal Dynamics of Spontaneous Imbibition Fronts, *Phys. Rev. Lett.*, **89**(10), 104503.

Good, R. J. and Lin, N.-J. (1976), Rate of penetration of a fluid into a porous body, *J. Colloid Interface Sci.*, **54**(1), 52–58.

Gumbel, E. J. (1958), *Statistics of Extremes*, Vol. 114, Columbia University Press.

Guyon, E., Hulin, J.-P., Petit, L. and Mitescu, C. D. (2001), *Physical Hydrodynamics*, Oxford University Press, USA.

Hamraoui, A. and Nylander, T. (2002), Analytical approach for the Lucas-Washburn equation., *J. Colloid Interface Sci.*, **250**(2), 415–21.

Hamraoui, A., Thuresson, K., Nylander, T. and Yaminsky, V. (2000), Can a dynamic contact angle be understood in terms of a friction coefficient?, *J. Colloid Interface Sci.*, **226**(2), 199–204.

He, S., Kahanda, G. and Wong, P. (1992), Roughness of wetting fluid invasion fronts in porous media, *Phys. Rev. Lett.*, **69**(26), 3731–3734.

Heber Green, W. and Ampt, G. a. (1911), Studies on Soil Phyics., *J. Agric. Sci.*, **4**(01), 1.

Hernández-Machado, A., Soriano, J., Lacasta, A. M., Rodríguez, M. A., Ramírez-Piscina, L. and Ortín, J. (2001), Interface roughening in Hele-Shaw flows with quenched disorder: Experimental and theoretical results, *Europhys. Lett.*, **55**(2), 194–200.

Hilpert, M. (2009*a*), Effects of dynamic contact angle on liquid infiltration into horizontal capillary tubes: (semi)-analytical solutions., *J. Colloid Interface Sci.*, **337**(1), 131–137.

Hilpert, M. (2009*b*), Effects of dynamic contact angle on liquid infiltration into inclined capillary tubes: (semi)-analytical solutions., *J. Colloid Interface Sci.*, **337**(1), 138–144.

Hoffman, R. L. (1975), A study of the advancing interface. I. Interface shape in liquid–gas systems, *J. Colloid Interface Sci.*, **50**(2), 228–241.

Horvath, V. K., Family, F. and Vicsek, T. (1991), Dynamic scaling of the interface in two-phase viscous flows in porous media, *J. Phys. A. Math. Gen.*, **24**(1), L25–L29.

Hultmark, M., Aristoff, J. M. and Stone, H. a. (2011), The influence of the gas phase on liquid imbibition in capillary tubes, *J. Fluid Mech.*, **678**, 600–606.

Jeffries, J., Zuo, J. and Craig, M. (1996), Instability of kinetic roughening in sputter-deposition growth of Pt on glass, *Phys. Rev. Lett.*, **76**(26), 4931–4934.

Joanny, J. F. and de Gennes, P. G. (1984), A model for contact angle hysteresis, *J. Chem. Phys.*, **81**(1), 552.

Joubaud, S., Petrosyan, a., Ciliberto, S. and Garnier, N. (2008), Experimental Evidence of Non-Gaussian Fluctuations near a Critical Point, *Phys. Rev. Lett.*, **100**(18), 180601.

Jurin, J. (1717), An Account of Some Experiments Shown before the Royal Society; With an Enquiry into the Cause of the Ascent and Suspension of Water in Capillary Tubes. By James Jurin, M. D. and R. Soc. S., *Philos. Trans.*, **30**(351-363), 739–747.

Kardar, M., Parisi, G. and Zhang, Y.-C. (1986), Dynamic Scaling of Growing Interfaces, *Phys. Rev. Lett.*, **56**(9), 889–892.

Khatib, J. M. and Clay, R. M. (2004), Absorption characteristics of metakaolin concrete, *Cem. Concr. Res.*, **34**(1), 19–29.

Kiyono, K., Struzik, Z. and Yamamoto, Y. (2006), Criticality and Phase Transition in Stock-Price Fluctuations, *Phys. Rev. Lett.*, **96**(6), 1–4.

Kornev, K. and Neimark, A. (2001), Spontaneous penetration of liquids into capillaries and porous membranes revisited, *J. Colloid Interface Sci.*, **235**(1), 101–113.

Krug, J. (1997), Origins of scale invariance in growth processes, *Adv. Phys.*, **46**(2), 139–282.

Krug, J. and Meakin, P. (1991), Kinetic roughening of Laplacian fronts, *Phys. Rev. Lett.*, **66**(6), 703–706.

Kun, F., Varga, I., Lennartz-Sassinek, S. and Main, I. G. (2014), Rupture Cascades in a Discrete Element Model of a Porous Sedimentary Rock, *Phys. Rev. Lett.*, **112**(6), 065501.

Kuntz, M. C. and Sethna, J. P. (2000), Noise in disordered systems: The power spectrum and dynamic exponents in avalanche models, *Phys. Rev. B*, **62**(17), 11699.

Laplace, P. S. (1805), *Traité de Mécanique Céleste. Volume 4*, Courcier.

Laurson, L., Illa, X., Santucci, S., Tore Tallakstad, K., Måløy, K. and Alava, M. J. (2013), Evolution of the average avalanche shape with the universality class., *Nat. Commun.*, **4**(0316), 2927.

Le Doussal, P., Wiese, K. J., Moulinet, S. and Rolley, E. (2009), Height fluctuations of a contact line: A direct measurement of the renormalized disorder correlator, *Europhys. Lett.*, **87**(5), 56001.

LeGrand, E. E. J. and Rense, W. W. A. (1945), Data on rate of capillary rise, *J. Appl. Phys.*, **16**(12), 843–846.

Lenormand, R. (1990), Liquids in porous media, *J. Phys. Condens. Matter*, **79**, SA79–SA88.

López, J. M., Pradas, M. and Hernández-Machado, A. (2010), Activity statistics, avalanche kinetics, and velocity correlations in surface growth, *Phys. Rev. E*, **82**(3), 2–5.

López, J. M., Rodríguez, M. A. and Cuerno, R. (1997), Superroughening versus intrinsic anomalous scaling of surfaces, *Phys. Rev. E*, **56**(4), 3993–3998.

Lorenceau, E., Quéré, D., Ollitrault, J.-Y. and Clanet, C. (2002), Gravitational oscillations of a liquid column in a pipe, *Phys. Fluids*, **14**(6), 1985–1992.

Lucas, R. (1918), Ueber das Zeitgesetz des kapillaren Aufstiegs von Flüssigkeiten, *Colloid Polym. Sci.*, **23**(1), 15–22.

Magni, A., Durin, G., Zapperi, S. and Sethna, J. P. (2009), Visualization of avalanches in magnetic thin films: temporal processing, *J. Stat. Mech. Theory Exp.*, **2009**(01), P01020.

Måløy, K., Feder, J. and Jøssang, T. (1985), Viscous fingering fractals in porous media, *Phys. Rev. Lett.*, **55**(24), 2688–2691.

Måløy, K., Santucci, S., Schmittbuhl, J. and Toussaint, R. (2006), Local Waiting Time Fluctuations along a Randomly Pinned Crack Front, *Phys. Rev. Lett.*, **96**(4).

Manshour, P., Saberi, S., Sahimi, M., Peinke, J., Pacheco, A. and Rahimi Tabar, M. (2009), Turbulencelike Behavior of Seismic Time Series, *Phys. Rev. Lett.*, **102**(1), 14101.

Martic, G., Blake, T. D. and De Coninck, J. (2005), Dynamics of Imbibition into a Pore with a Heterogeneous Surface, *Langmuir*, **21**(24), 11201–11207.

Mehta, A., Mills, A., Dahmen, K. and Sethna, J. P. (2002), Universal pulse shape scaling function and exponents: Critical test for avalanche models applied to Barkhausen noise, *Phys. Rev. E*, **65**(4), 1–6.

Michelis, P. D. and Consolini, G. (2004), Time intermittency and spectral features of the geomagnetic field, *Ann. Geophys.*, **47**(December), 1713–1722.

Mier, J., Sánchez, R., García, L., Carreras, B. and Newman, D. (2008), Characterization of Nondiffusive Transport in Plasma Turbulence via a Novel Lagrangian Method, *Phys. Rev. Lett.*, **101**(16), 1–4.

Milligen, B. V., Hidalgo, C. and Sanchez, E. (1995), Nonlinear phenomena and intermittency in plasma turbulence, *Phys. Rev. Lett.*, **74**(3), 395–398.

Morrow, N. R. and Mason, G. (2001), Recovery of oil by spontaneous imbibition, *Curr. Opin. Colloid Interface Sci.*, **6**(4), 321–337.

Moulinet, S., Guthmann, C. and Rolley, E. (2002), Roughness and dynamics of a contact line of a viscous fluid on a disordered substrate., *Eur. Phys. J. E. Soft Matter*, **8**(4), 437–43.

Mumley, T. E., Radke, C. J. and Williams, M. C. (1986*a*), Kinetics of liquid/liquid capillary rise : I. Experimental observations, *J. Colloid Interface Sci.*, **109**(2), 398–412.

Mumley, T. E., Radke, C. J. and Williams, M. C. (1986*b*), Kinetics of liquid/liquid capillary rise : II. Development and test of theory, *J. Colloid Interface Sci.*, **109**(2), 413–425.

Myllys, M., Maunuksela, J., Alava, M., Ala-Nissila, T., Merikoski, J. and Timonen, J. (1997), Kinetic roughening in slow combustion of paper., *Phys. Rev. E. Stat. Nonlin. Soft Matter Phys.*, **79**(8), 1515.

Noullez, a. and Pinton, J.-F. (2002), Global fluctuations in decaying Burgers turbulence, *Eur. Phys. J. B*, **28**(2), 231–241.

Papanikolaou, S., Bohn, F., Sommer, R. L., Durin, G., Zapperi, S. and Sethna, J. P. (2011), Universality beyond power laws and the average avalanche shape, *Nat. Phys.*, **5**(12), 1–5.

Pauné, E. and Casademunt, J. (2003), Kinetic Roughening in Two-Phase Fluid Flow through a Random Hele-Shaw Cell, *Phys. Rev. Lett.*, **90**(14), 2–5.

Planet, R. (2009), Estudi experimental de la din amica dun front fluid en un medi desordenat, PhD thesis, Universitat de Barcelona.

Planet, R., López, J. M., Santucci, S. and Ortín, J. (2014), Correlated local activity and global avalanches in slowly driven interfaces., *Submitted*, .

Planet, R., Pradas, M., Hernández-Machado, A. and Ortín, J. (2007), Pressure-dependent scaling scenarios in experiments of spontaneous imbibition, *Phys. Rev. E*, **76**(5), 56312.

Planet, R., Santucci, S. and Ortín, J. (2009), Avalanches and Non-Gaussian Fluctuations of the Global Velocity of Imbibition Fronts, *Phys. Rev. Lett.*, **102**(9), 94502.

Planet, R., Santucci, S. and Ortín, J. (2010), Reply Comment on Avalanches and Non-Gaussian Fluctuations of the Global Velocity of Imbibition Fronts, *Phys. Rev. Lett.*, **105**(July), 29402.

Planet, R., Santucci, S. and Ortín, J. (2011), Roughness and intermittent dynamics of imbibition fronts due to capillary and permeability disorder., *J. Contam. Hydrol.*, **120-121**, 157–69.

Portelli, B., Holdsworth, P., Sellitto, M. and Bramwell, S. (2001), Universal magnetic fluctuations with a field-induced length scale, *Phys. Rev. E*, **64**(3), 036111.

Pradas, M. (2009), Interfaces in disordered media. Scaling growth, avalanche dynamics, and microfluidic fronts, PhD thesis, Universitat de Barcelona.

Pradas, M. and Hernández-Machado, A. (2006), Intrinsic versus superrough anomalous scaling in spontaneous imbibition, *Phys. Rev. E*, **74**(4), 041608.

Pradas, M., López, J. M. and Hernández-Machado, A. (2007), Time-dependent couplings and crossover length scales in nonequilibrium surface roughening, *Phys. Rev. E*, **76**(1), 10102.

Pradas, M., López, J. M. and Hernández-Machado, A. (2009), Avalanche dynamics in fluid imbibition near the depinning transition, *Phys. Rev. E*, **80**(5), 50101.

Pruessner, G. (2010), Comment on Avalanches and Non-Gaussian Fluctuations of the Global Velocity of Imbibition Fronts, *Phys. Rev. Lett.*, **105**(2), 029401.

Pruessner, G. (2012), *Self-Organised Criticality: Theory, Models and Characterisation*, Cambridge University Press.

Quéré, D. (1997), Inertial capillarity, *Europhys. Lett.*, **39**(5), 533–538.

Quéré, D., Raphaël, E. and Ollitrault, J.-Y. (1999), Rebounds in a Capillary Tube, *Langmuir*, **15**(10), 3679–3682.

Radjai, F. and Roux, S. (2002), Turbulentlike Fluctuations in Quasistatic Flow of Granular Media, *Phys. Rev. Lett.*, **89**(6), 5–8.

Ramasco, J. J., López, J. M. and Rodríguez, M. A. (2000), Generic Dynamic Scaling in Kinetic Roughening, *Phys. Rev. Lett.*, **84**(10), 2199–2202.

Rost, M., Laurson, L., Dubé, M. and Alava, M. (2007), Fluctuations in fluid invasion into disordered media, *Phys. Rev. Lett.*, **98**, 054502.

Rubio, M., Edwards, C., Dougherty, A. and Gollub, J. (1989), Self-affine fractal interfaces from immiscible displacement in porous media, *Phys. Rev. Lett.*, **63**(16), 1685–1688.

Ryu, K.-S., Akinaga, H. and Shin, S.-C. (2007), Tunable scaling behaviour observed in Barkhausen criticality of a ferromagnetic film, *Nat. Phys.*, **3**(8), 547–550.

Saffman, P. G. and Taylor, G. (1958), The Penetration of a Fluid into a Porous Medium or Hele-Shaw Cell Containing a More Viscous Liquid, *Proc. R. Soc. A Math. Phys. Eng. Sci.*, **245**(1242), 312–329.

Sahimi, M. (2011), *Flow and transport in porous media and fractured rock: From classical methods to modern approaches*, Wiley-VCH Verlag GmbH & Co. KGaA.

Santucci, S., Måløy, K., Delaplace, A., Mathiesen, J., Hansen, A., Haavig Bakke, J., Schmittbuhl, J., Vanel, L. and Ray, P. (2007), Statistics of fracture surfaces, *Phys. Rev. E*, **75**(1), 016104.

Santucci, S., Planet, R., Måløy, K. J. r. and Ortín, J. (2011), Avalanches of imbibition fronts: Towards critical pinning, *Europhys. Lett.*, **94**(4), 46005.

Schäffer, E. and Wong, P.-z. (2000), Contact line dynamics near the pinning threshold: A capillary rise and fall experiment, *Phys. Rev. E*, **61**(5), 5257.

Schmittbuhl, J., Vilotte, J. and Roux, S. (1995), Reliability of self-affine measurements, *Phys. Rev. E*, **51**(1), 131–147.

Sethna, J. P., Dahmen, K. A. and Myers, C. R. (2001), Crackling noise, *Nature*, **410**(6825), 242–250.

Seveno, D., Blake, T. D. and De Coninck, J. (2013), Youngs Equation at the Nanoscale, *Phys. Rev. Lett.*, **111**(9), 096101.

Sheng, P. and Zhou, M. (1992), Immiscible-fluid displacement: Contact-line dynamics and the velocity-dependent capillary pressure, *Phys. Rev. A*, **45**(8), 5694–5708.

Soriano, J. (2003), Roughness experiments of viscous fluid interfaces in disordered Hele-Shaw cells, PhD thesis, Universitat de Barcelona.

Soriano, J., Mercier, A., Planet, R., Hernández-Machado, A., Rodríguez, M. A. and Ortín, J. (2005), Anomalous Roughening of Viscous Fluid Fronts in Spontaneous Imbibition, *Phys. Rev. Lett.*, **95**(10), 104501.

Soriano, J., Ortín, J. and Hernández-Machado, A. (2002), Experiments of interfacial roughening in Hele-Shaw flows with weak quenched disorder, *Phys. Rev. E*, **66**(3), 31603.

Soriano, J., Ramasco, J. J., Rodríguez, M. A., Hernández-Machado, A. and Ortín, J. (2002a), Anomalous Roughening of Hele-Shaw Flows with Quenched Disorder, *Phys. Rev. Lett.*, **89**(2), 026102.

Spasojevic, D., Bukvic, S., Milosevic, S. and Stanley, H. E. (1996), Barkhausen noise: Elementary signals, power laws, and scaling relations., *Phys. Rev. E,*, **54**(3), 2531–2546.

Szekely, J., Neumann, A. and Chuang, Y. (1971), The rate of capillary penetration and the applicability of the washburn equation, *J. Colloid Interface Sci.*, **35**(2), 273–278.

Szendro, I., López, J. and Rodríguez, M. (2007), Localization in disordered media, anomalous roughening, and coarsening dynamics of faceted surfaces, *Phys. Rev. E*, **76**(1), 011603.

Takeuchi, K. A. and Sano, M. (2010), Universal Fluctuations of Growing Interfaces: Evidence in Turbulent Liquid Crystals, *Phys. Rev. Lett.*, **104**(23), 1–4.

Takeuchi, K. A., Sano, M., Sasamoto, T. and Spohn, H. (2011), Growing interfaces uncover universal fluctuations behind scale invariance., *Sci. Rep.*, **1**, 34.

Tallakstad, K. T., Løvoll, G., Knudsen, H., Ramstad, T., Flekkøy, E. and Måløy, K. (2009), Steady-state, simultaneous two-phase flow in porous media: An experimental study, *Phys. Rev. E*, **80**(3), 036308.

Tallakstad, K. T., Toussaint, R., Santucci, S. and Måløy, K. (2013), Non-Gaussian Nature of Fracture and the Survival of Fat-Tail Exponents, *Phys. Rev. Lett.*, **110**(14), 145501.

Tallakstad, K. T., Toussaint, R., Santucci, S., Schmittbuhl, J. and Måløy, K. (2011), Local dynamics of a randomly pinned crack front during creep and forced propagation: An experimental study, *Phys. Rev. E*, **83**(4), 1–15.

Teige, G. M. G., Thomas, W. L. H., Hermanrud, C., Øren, P.-E., Rennan, L., Wilson, O. B. and Nordgå rd Bolå s, H. M. (2006), Relative permeability to wetting-phase water in oil reservoirs, *J. Geophys. Res.*, **111**(B12), B12204.

Tóth-Katona, T. and Gleeson, J. (2003), Distribution of Injected Power Fluctuations in Electroconvection, *Phys. Rev. Lett.*, **91**(26), 264501.

Tripathy, G. and van Saarloos, W. (2000), Fluctuation and relaxation properties of pulled fronts: A scenario for nonstandard Kardar-Parisi-Zhang scaling, *Phys. Rev. Lett.*, **85**(17), 3556–3559.

Urbach, J., Madison, R. and Markert, J. (1995), Interface depinning, self-organized criticality, and the Barkhausen effect, *Phys. Rev. Lett.*, **75**(2), 276–279.

Vives, E., Ortín, J., Mañosa, L., Ràfols, I., Pérez-Magrané, R. and Planes, A. (1994), Distributions of avalanches in martensitic transformations, *Phys. Rev. Lett.*, **72**, 1694–1697.

Wang, B., Kuo, J. and Granick, S. (2013), Bursts of Active Transport in Living Cells, *Phys. Rev. Lett.*, **111**(20), 208102.

Washburn, E. W. (1921), The Dynamics of Capillary Flow, *Phys. Rev.*, **17**(3), 273–283.

Weitz, D. A., Stokes, J. P., Ball, R. C. and Kushnick, A. P. (1987), Dynamic Capillary Pressure in Porous Media: Origin of the Viscous-Fingering Length Scale, *Phys. Rev. Lett.*, **59**(26), 2967–2970.

Welling, M., Aegerter, C. and Wijngaarden, R. (2005), Self-organized criticality induced by quenched disorder: Experiments on flux avalanches in NbHx films, *Phys. Rev. B*, **71**(10), 104515.

Wolf, F. G., Santos, L. O. E. D., Philippi, P. C. and dos Santos, L. O. E. (2010), Capillary rise between parallel plates under dynamic conditions, *J. Colloid Interface Sci.*, **344**(1), 171–179.

Young, T. (1805), An essay on the cohesion of fluids, *Philos. Trans. R. Soc. London*, **95**, 65–87.

Zapperi, S., Castellano, C., Colaiori, F. and Durin, G. (2005), Signature of effective mass in crackling-noise asymmetry, *Nat. Phys.*, **1**(1), 46–49.

Zhou, M. and Sheng, P. (1990), Dynamics of immiscible-fluid displacement in a capillary tube, *Phys. Rev. Lett.*, **64**(8), 882–885.